EXPERIMENTAL ASSESSMENT, OPTIMIZATION, AND MULTI-SCALE MODELING OF ALKALI-SILICA REACTION (ASR) THROUGH MACHINE-LEARNING TECHNIQUES

A Dissertation

by

MOSTAFA JALAL

Submitted to the Office of Graduate and Professional Studies of
Texas A&M University
in partial fulfillment of the requirements for the degree of

DOCTOR OF PHILOSOPHY

Chair of Committee,	Zachary Grasley
Co-Chair of Committee,	Anol Mukhopadhyay
Committee Members,	Dan Zollinger
	Robert Lytton
	Sarbajit Banerjee
Head of Department,	Robin Autenrieth

May 2020

Major Subject: Civil Engineering

ABSTRACT

Multi-scale experimental investigation and machine-learning modeling of alkali-silica reaction (ASR) were undertaken in this research. The experimental assessment was implemented in three different levels including aggregate, mortar, and concrete. Several aggregates of different reactivity were tested to obtain their activation energy (AE), and were classified based on their reactivity. Seven different types of fly ash (FA) were characterized and investigated to determine the influencing FA indicators affecting ASR expansion. Based on the design of experiment (DOE), an accelerated mortar bar test (AMBT) was carried out on 150 mortar bars with different reactive aggregates, FA types, FA percentages, and temperatures. The ASR expansion of the mortar samples was measured at an extended time, up to 60 days, to match the test duration of the concrete test. An accelerated concrete cylinder test (ACCT) was also implemented on different mixes and at different temperatures. Based on the experimental plan, the tests were designed and the data collected on three levels of aggregate, mortar, and concrete. In order to develop multi-scale predictive models for ASR expansion of mortar and concrete at the phase of mix design, machine-learning techniques were utilized for the first time to predict the ASR expansion using Artificial Neural Network (ANN), Genetic Programming (GP), and Adaptive Inference Neuro-Fuzzy System (ANFIS). The performance of different models was evaluated using different performance criteria, and the prediction results were compared. Moreover, closed-form formulations were also derived for ANN and GP models. The results obtained indicated that the multi-scale assessment along with the machine-learning models can constitute a promising and powerful approach to predict the ASR expansion in concrete infrastructures.

DEDICATION

To my family, especially my mother, Ehteram, who dedicated and sacrificed her youth and life to raise me to be who I am and where I am now. Thank you for everything!

To my father, Mohammadreza, my older brother, Ali, my younger sister, Zahra, and my cool younger brother, Hamid.

ACKNOWLEDGEMENTS

There are several people to whom I would like to express my gratitude. I would like to thank my supervisor, Dr. Anol Mukhopadhyay, who offered me funding, constantly supported me, and patiently advised me throughout the course of my PhD. To Dr. Zachary Grasley whose constructive advice has been inspiring for me. To Dr. Robert Lytton and Dr. Dan Zollinger whose support has been appreciable. Also many thanks to Kai-Wei (Victor) Liu whose help was invaluable in my research project.

Thanks to my memorable and sincere friend, Hamed Shariatmadar, who introduced Texas A&M to me. Without his friendly suggestion, none of this may have happened.

Finally, thanks to my mother and father who have always encouraged me to achieve more in my life and education.

CONTRIBUTORS AND FUNDING SOURCES

This work was supervised by a dissertation committee of Dr. Zachary Grasley (committee chair), Dr. Anol Mukhopadhyay (committee co-chair), Dr. Dan Zollinger, and Dr Robert Lytton in Department of Civil Engineering, and Dr. Sarbajit Banerjee in department of Chemistry.

The contributions of Kai-Wei (Victor) Liu to experimental work of ASR project is highly appreciated.

The ASR research project was funded by Texas Department of Transportation (Tx DOT) and was implemented through Texas A&M Transportation Institute (TTI).

TABLE OF CONTENTS

Page

LIST OF FIGURES

LIST OF TABLES

1. INTRODUCTION

1.1. Motivation and Problem Statement

Concrete is the most widely used construction material in the world, and millions of dollars are spent every year on concrete infrastructures. Alkali-silica reaction (ASR) is a major durability issue of concrete and has been a threat to the service life of concrete infrastructures. Due to its complex nature, the mechanism of ASR has not been fully perceived, despite of extensive research endeavors since its discovery in the late 1930s (Stanton, 1940).

ASR occurs internally in concrete between reactive aggregates and the hydroxyl ions and alkalis of the pore solution. The ASR expansion mechanism is driven by three main components, namely (1) available alkalis in pore solution, (2) reactive silica present in the aggregates, and (3) sufficient moisture available to initiate the reaction.

When all the components get together, a gel, which is rich in silica, alkalis, and other ions, is formed in and around aggregates as well as within the pores of the concrete (Li, 2016). This gel is hygroscopic and expands as it imbibes available moisture from the interior of the concrete (Shafaatian, 2012). When the expansive pressure exceeds the tensile capacity of the concrete, cracking may occur. Once cracking is initiated, the external water can more easily penetrate the concrete, thereby exacerbating ASR and increasing the potential for other durability issues such as freeze-thaw attack, sulfate attack and corrosion, which leads to further deterioration of the concrete (Schwing, 2010). Due to the problems ASR has caused over years, the need to prevent ASR has generated an urgency within the engineering community.

FHWA ASR Development and Deployment Program was initiated in 2006 (Davis et al., 2018). This plan was initiated to help state transportation agencies assess ASR issues in concrete

infrastructures. FHWA provides tools, guidelines, and protocols for recognizing ASR in the field and protocols for the prevention, diagnosis, and repair of ASR. Several projects have been funded by departments of transportation (DOTs) to discover mitigation strategies for the complicated durability issues presented in ASR (Davis et al., 2018).

The main mitigation measures used thus far have been low-alkali cement, non-reactive aggregate, supplementary cementitious materials (SCMs) or lithium nitrates (Li, 2016). Researchers have investigated various aspects and techniques such as aggregate classification, accelerated mortar bar tests (AMBT), concrete cylinder tests, and exposure blocks. However, since ASR is a multifaceted problem comprising different aspects and different levels, a comparative study of different steps with proper connection of the steps is of huge importance and represents the main gap of the current literature. It requires a multi-scale assessment of the problem to scrutinize the different scales such as the nano/micro level, aggregate level, mortar level, concrete level, and field level, such as exposure clocks. Thus, two key factors to this approach are the assessment of the steps (scales) and the connections. The former can be achieved by comparative study and cross-validation through different supporting tools, and the latter by techniques or models that can connect the outcome of different steps to capture the overall behavior while handling the uncertainty and variability involved in the process.

1.2. Research Significance and Objectives

Several research projects have been carried out on ASR assessment and mitigation over years. Some of them are focused on aggregate reactivity assessment and classification (Mukhopadhyay, 2006), while many of them deal with ASR mitigation using supplementary cementitious materials (SCM). Two main tests have been adopted in most of the studies for ASR

expansion assessment, namely ASTM C 1260 and ASTM C 1293. The former, due to severe exposure condition and short time, does not represent the real-world situation well while still giving a criterion of ASR expansion. The latter, is flawed due to a long wait time, which makes it less desirable in practical applications. Instead, a recently developed test called the accelerated concrete cylinder test (ACCT) has proved to be a rather fast and accurate ASR concrete test (Mukhopadhyay et al., 2018). Several models have also been developed to predict ASR, which are mostly mechanistic or deterministic, among which kinetic (Kim et al., 2014), thermodynamic (Guthrie and Carey, 2015), mathematical (Bazant and Steffens, 2000; Samua et al., 2015), and mechanical (Charpin and Ehrlacher, 2012) models can be mentioned. However, the main drawbacks of the current models include one or some of these : (1) failure to address multi-scale effect, (2) failure to connect different steps (scales), (3) forcing limited number of variables to the model, or (4) failure to handle uncertainty, variability, and multicollinearity.

In this research, experimental assessment of ASR is implemented in three different levels, aggregate, mortar, and concrete. Several aggregates of different reactivity were tested to obtain their activation energy (AE) by modifying the classification method. Seven different types of fly ash (FA) were characterize and investigated (Mukhopadhyay et al., 2019) to determine the influencing FA indicators affecting ASR expansion. Based on design of experiment (DOE), AMBT was implemented on 150 mortar prisms of different aggregate reactivities, FA types, FA percentages, and temperatures. The ASR expansion of mortar samples was measured at an extended time up to 60 days to match the time of concrete test. ACCT was also implemented on different mixes and at different temperatures. Based on the experimental plan, the data were collected on three levels of aggregate, mortar, and concrete.

In order to fill the current ASR modeling gap in the literature, machine-learning techniques were employed for the first time to implement multi-scale modeling on ASR to develop predictive

models for concrete and mortar expansion due to ASR (Jalal et al. 2019). Two variables from the aggregate level, (AE at 0.5N and 1N), three variables from the micro level (FA indicators, FA percentage, and temperature), and time were taken into account to predict ASR expansion. Three different machine-learning techniques, Artificial Neural Network (ANN), Genetic Programming (GP), and Adaptive Neuro-Funny Inference System (ANFIS), were utilized to develop predictive models on ASR expansion. The performance of different models was evaluated using different performance criteria and the prediction results were compared. Another significance of this research is that closed-form formulation is also derived and presented for the ANN model, which other available studies in the literature lack. Figure 1 shows the flowchart representing the steps of this research.

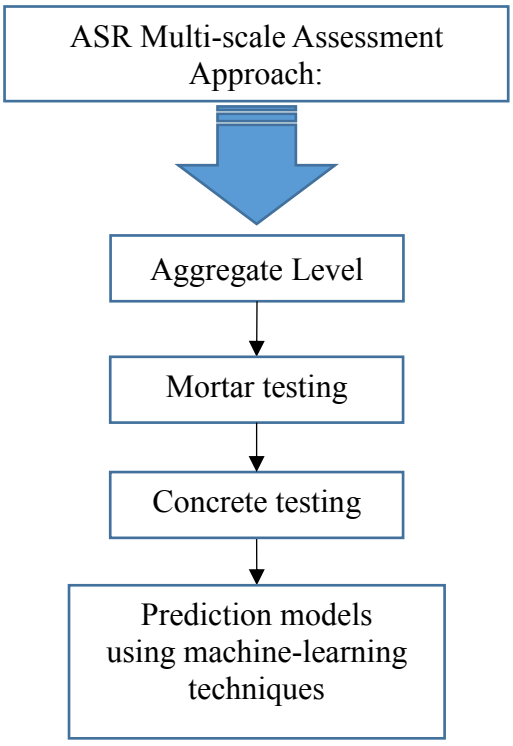

Figure 1. Flowchart of the ASR assessment steps

1.3. Organization of the Research

The research was performed in several steps described in the following chapters:

Chapter 1: Introduction – Presents the motivation and problem statement, research significance and objectives, and organization of the research

Chapter 2: Literature review — Provides the background information based on a literature review of ASR assessment by experiment and modeling

Chapter 3: Materials and experimental procedure — Presents the materials' selection, characterization, and experimental procedures

Chapter 4: Modeling and optimization techniques — Briefly describes some details and theoretical background of machine-learning techniques and optimization algorithms

Chapter 5: Results of experimental assessment — Results of the experimental assessment of aggregate, mortar, and concrete testing

Chapter 6: Results of prediction models — Results of prediction models and comparison of different models, parametric study, and closed-from formulation for ANN and GP models

Chapter 7: Summary, conclusions and recommendations

2. LITERATURE REVIEW

This chapter provides a comprehensive literature review on alkali-silica reaction (ASR) relevant to this study in several sections including introduction, ASR chemistry, diagnosis, test methods, mitigation, theories, and modeling techniques.

2.1. Introduction on Alkali-Silica Reaction (ASR)

In a general term, Alkali-aggregate reaction (AAR) is the reaction between some types of aggregate and alkali hydroxides, which can result in excessive expansion and cracking of concrete. AAR includes alkali-silica reaction (ASR) and alkali-carbonate reaction (ACR) (Thomas et al., 2013). The deterioration caused by a reaction between cement and aggregate was first identified by Stanton in 1940 (Stanton, 1940). By investigating the failures of Bradley pavement in Salinas Valley, CA it was discovered that the failure was caused by excessive expansion of concrete slabs. The subsequent laboratory investigation revealed that aggregates containing a high content of shale and chert mixed with a cement with high alkali content could cause the deleterious expansion (Stanton, 2008). It raised the doubt that the cement in concrete may react with minerals in cement and cause expansion of concrete and then further deterioration (Stanton, 2008). In following studies, the reaction was named as ASR, which indicated the nature of this reaction. Since then, researchers started the assessment of alkali-silica reaction and the potential deterioration of Portland cement concrete structure due to ASR. This discovery also placed further importance on aggregate selection and mitigation measures for construction. ASR has been reported by over 50 countries all over the world (Fournier and Berube, 2000), however, due to its complexity, the its mechanism is still under investigation. Even though the concrete suffering from ASR may show

some symptoms such as cracking, expansion, gel exudation, and pop-outs, nevertheless, none of these features can be used to confirm ASR occurrence (Poole, 1992).

2.2. Factors Affecting ASR and Its Mechanism

ASR is a chemical reaction between alkali hydroxides in a pore solution and the reactive form of silica in aggregates. It is widely accepted that three essential conditions (Figure 2) are necessary in order to create ASR-induced damage in concrete structures:

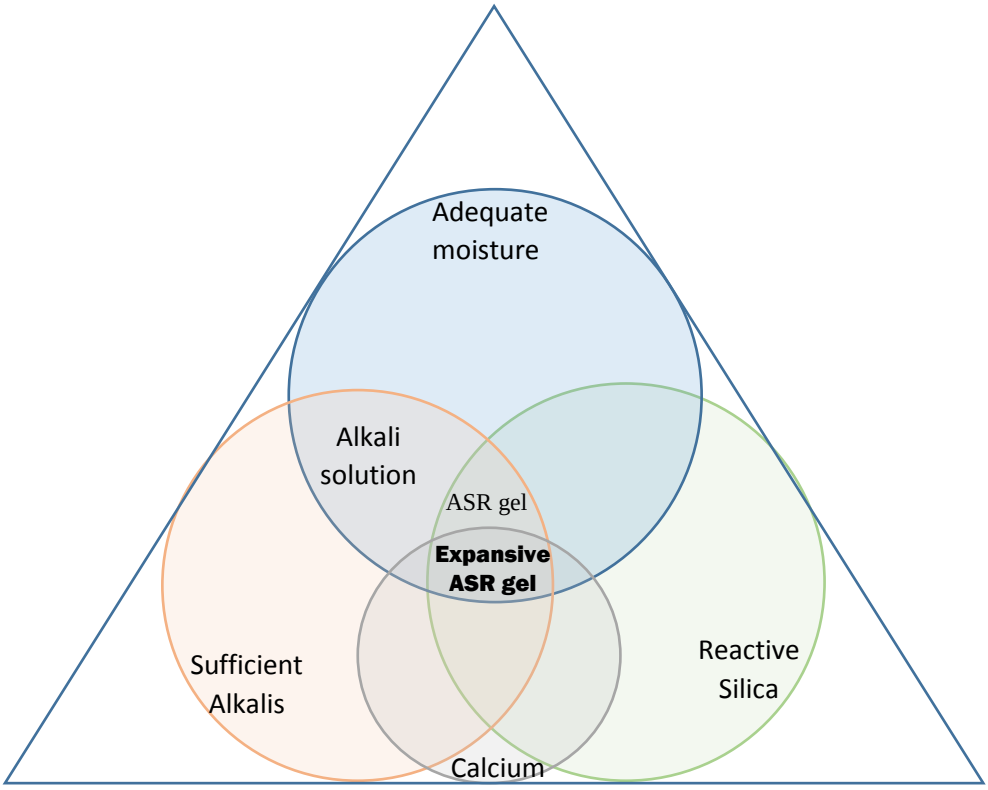

Figure 2. Components of expansive ASR gel formation

1. Sufficient availability of OH- ions and alkalis (Na+ and/or K+) – a highly alkaline concrete pore solution (pH > 13.2) ensures enough supply of alkali hydroxides.

2. Presence of a reactive siliceous component(s) in aggregates (both coarse and fine aggregates) at optimum level (i.e., pessimum proportion).

3. Sufficient moisture (> 80 percent RH) (Chatterji et al. 1989; Ponce and Batic 2006; and Mukhopadhyay et al. 2006).

The optimum combination of conditions 1 and 2 is essential to initiate ASR, whereas condition 3 is essential to make ASR expansive (i.e., deleterious). If any one of the three factors is not present in the concrete, then the reaction will either not proceed or not become deleterious. The higher the temperature the higher the rate of ASR is. Increasing temperature causes higher expansion at early age but lower ultimate expansion (Diamond et al. 1981).

The product of this reaction is a gel known as ASR gel. In the presence of sufficient moisture (> 80 percent RH), the gel absorbs moisture due to its hygroscopic nature and swells. Swelling leads to tensile stresses in concrete. When these stresses exceed the tensile strength of concrete, cracks develop. Typical visual manifestation of ASR includes map cracking, misalignment of structural elements, and expansive features such as joint closure and heaving/blow-ups, etc. ASR cracks act as open passages for moisture and other chemicals (chloride ions, sulfate ions, etc.), leading to more damage. In addition to the three requirements listed above, the presence of calcium hydroxide [Ca(OH)2] in concrete pore solution also found to be an important factor. Chatterji et al. (1989) believed that sufficient Ca2+ concentration in the pore solution (vicinity of the aggregate) is needed for ASR gel to be expansive inside aggregate.

2.2.1. Reaction Chemistry

Whenever cement contacts with water, hydration of cement particles starts. During the process of hydration, hydrates such as C-S-H, CH, AFt and AFm form, and then the aqueous phase

become disconnected, which forms a porous structure. Any remaining fluid accommodated in the pores which is not involved in hydration is termed as pore solution. The nature of ASR in concrete is the reaction between reactive silica in aggregates and alkali dissolved from cement when pore solution functions as a transferring medium (Glasser, 1992). The dissolution of silica can be expressed by equation (1) (Glasser and Kataoka, 1981):

$$Si - O - Si + H_2O \rightarrow \equiv Si - OH \cdots OH - Si \equiv \quad (2.1)$$

In the first step, silica is dissolved by hydroxyl attack to form silanol groups on the surface (Glasser and Kataoka, 1981). Then in an alkaline environment, hydroxyl ions attack the silanol group to form the monomer as shown in equation below (Rajabipour et al., 2015):

$$\equiv Si - OH + 3OH^- \rightarrow Si(OH)_4 \quad (2.2)$$

The monomer subsequently reacts with an alkali metal, such as Na+ and K+, for ion exchange which also decreases the pH. This process can be described by the following equation (Rajabipour et al., 2015; Prezzi et al., 1997):

$$Si(OH)_4 + M^+ \rightarrow (OH)_3 \equiv Si - O^- \cdots M^+ + H^+ \quad (2.3)$$

Previous research also showed that the existence of Ca is critical to form expansive ASR gel. Therefore, this process can be described by equation given below (Rajabipour et al., 2015; Prezzi et al., 1997):

$$2(OH)_3 \equiv Si - O^- \cdots M^+ + Ca^{2+} \rightarrow (OH)_3 \equiv Si - O \cdots Ca \cdots O - Si \equiv (OH)_3 + 2Na^+ \quad (2.4)$$

Therefore, the pre-requisites of ASR gel formation are sufficient alkali content, reactive silica components in aggregates and adequate moisture, which lead to a stable expansive gel in presence of calcium (Helmuth, 1993).

2.2.2. Reactive Components in Aggregates

The occurrence of silica or silicate minerals in aggregates (both coarse and fine) is a common feature. Aggregate alkali-silica reactivity is a function of the form/degree of crystallinity, grain size, texture, and proportion of the reactive silica within the reactive aggregate (Stanton 1940, Mindess 2003). Not all forms of silica are ASR-reactive. The more disordered the structure of the silica phase, the greater the reactivity. The basic structure of silicates involves a framework of silicon-oxygen tetrahedron. Each oxygen atom is shared between two silicon atoms, where each silicon atom is bonded to four oxygen atoms (called siloxane bridge). A regular (ordered) arrangement of the basic Si-O tetrahedron creates a crystalline structure (see Figure 3a, e.g., quartz) whereas an irregular (disordered) arrangement of the tetrahedron creates poorly crystalline (e.g., chalcedony) to amorphous structure (e.g., opal, Figure 3b), depending on the degree of irregularity. Diamond (1976), Tatematsu and Sasaki (1989), and Mehta and Monteiro (1992) have designated the degree of reactivity of these reactive forms of silica, with decreasing order are: Opal, Crystobalite, Tridymite, Microcrystalline quartz, Cryptocrystalline quartz, Chalcedony, Chert, Volcanic glass, Strained quartz.

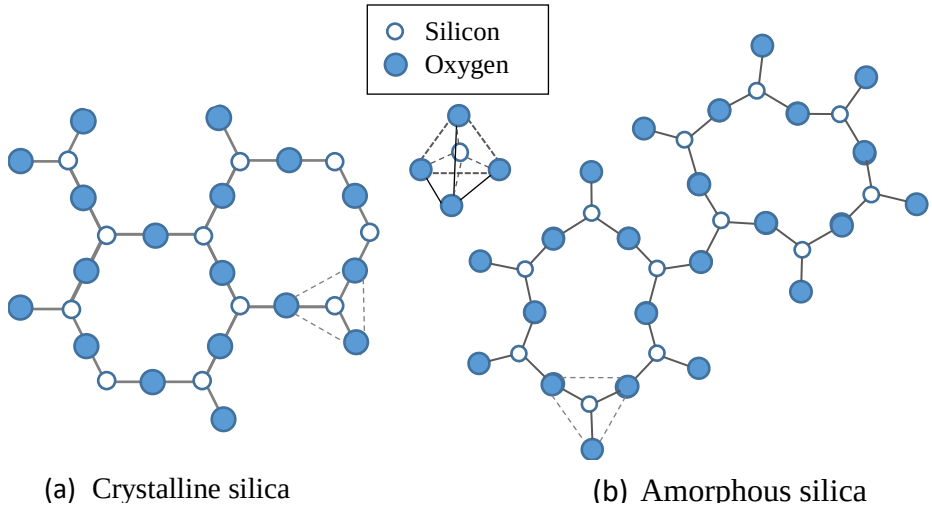

Figure 3. Molecular structure of crystalline and amorphous silica

The uncertain geological history and the complexity of mineralogy can bring difficulties on analyzing the composition of aggregates. Since there is a large proportion of silica in the earth crust, it can be expected that the majority of natural aggregates contain silica (Glasser, 1992).

However, the form of silica is not the only parameter that determines alkali reactivity of an aggregate. The other important factors that determine aggregate reactivity are as follows:

- Amount and nature of distribution of the reactive constituents inside aggregates,
- Role of aggregate porosity, pore connectivity and other internal structures (e.g., layering, schistose/foliated structures, etc.) on ingress of OH-, Na+, K+ ions into the aggregates.

An aggregate free from silica is believed to be safe from ASR as the reaction will not occur. Selecting appropriate aggregates for a specific construction project is the first step for preventing ASR. Accordingly, Table 1 shows different types of aggregates which have been identified as reactive in previous research (Fournier and Berube, 2000, Li, 2016).

Table 1. Different types of reactive aggregates (Fournier and Berube, 2000, Li, 2016)

1. ASR reactive rocks and materials	
1.1 Alkali-reactive, poorly crystalline, or metastable silica minerals and volcanic or artificial glasses (classical alkali-silica reaction)	
Reactants	Opal, tridymite, cristobalite Acidic, intermediate, and basic volcanic glass Artificial glass (e.g., common glass, steel slag, pyrex), beekite

Table 1 Continued.

Rocks	Sedimentary rocks containing opal, such as shale, sandstone, silicified rock, some chert and flint, and diatomite Glassy to vitrophyric volcanic rocks: acidic, intermediate, and basic, such as rhyolite, dacite, latite, andesite and their tuff, perlite, obsidian, all varieties with a glassy groundmass, some basalt
A. Alkali-reactive quartz-bearing rocks	
Reactants	Chalcedony, cryptocrystalline, microcrystalline quartz Macrogranular quartz: with deformed crystal lattice, rich in inclusions, intensively fractured or granulated, with microcrystalline quartz at grain boundaries
Rocks	Chert, flint, quartz vein, quartzite, quartzarenite, quarzitic sandstone, siliceous limestone Volcanic rocks such as in A1, but with devitrified, cryptocrystalline to cryptocrystalline quartz, or significant amounts of moderately to highly strained quartz: Igneous: granite, granodiorite, charnockite Sedimentary: sandstone, greywacke, siltstone, shale, siliceous limestone, arenite, arkose Metamorphic: gneiss, quart-mica schist, quartzite, hornfel, phyllite, argillite, slate
B. alkali-carbonate reactive rocks	
Reactants	Dolomite (by dedolomitization) Active clay minerals (illite) exposed after dedolomitization
Rocks	Argillaceous dolomitic limestone Argillaceous calcitic dolostone Calcitic dolostone

2.2.3. Source of Alkalis

Cement is the main source of alkalis in concrete. Alkalis such as sodium and potassium, primarily result from argillaceous materials in Portland cement (Poole, 1992; Mehta and Menteiro, 2006). Potassium could be present if mica or illitic clay is used in raw materials (Poole, 1992; Mehta and Menteiro, 2006). sodium, potassium or both are expected in clinker, should feldspar exists in the raw feed (Glasser, 1992). According to their solubility, available sodium and potassium in cement can be divided into two types: water-soluble and water-insoluble. Due to high vapor pressures at clinkering temperature during manufacturing of cement, some of the alkalis are trapped in clinker and some form a coating on the surface of the clinker grains as alkali sulfates (Glasser, 1992). alkali sulfates dissolve faster than the "trapped" alkalis when mixing in concrete, and are converted to alkali hydroxides; thereby leading to availability of the "trapped" alkalis slowly with time(Glasser, 1992). Soluble alkalis besides sulfates seldom exist in cement. equivalent sodium oxide content (Na2Oeq) is used to describe the alkali content of cement which is given by the following equation (Glasser, 1992):

$$Na_2O_{eq}=Na_2O+0.658\ K_2O \qquad (2.5)$$

In portland cement, the Na2Oeq can vary typically between 0.3% and 1.5% of the total cement content. Some researchers have shown that using low-alkali content can be an option to mitigate ASR in concrete (Fournier and Berube, 2000; Munn et al., 2003). The threshold alkali content was established in several countries. According to Canadian Standards Association (CSA), when the Na2Oeq is lower than 3.0 kg/m3, it is effective to prevent ASR for concrete with most reactive aggregate types and exposed to the most severe exposure conditions (Fournier and Berube, 2000). a range of 1.8 to 3.0 kg/m3 is also provided in the guideline to cope with a situation of

different reaction conditions (Fournier and Berube, 2000). In New Zealand, the suggested alkali threshold is 2.5 kg/m3 for normal concrete (Munn et al., 2003). The idea of alkali threshold was addressed in different studies in the previous literature. And a value of 0.30 N was reported by Kollek (Kollek et al., 1986). However, based on the research by Dunchesne, the threshold was reported to be 0.65 N (Duchesne and M. Bérubé, 1994). These discrepancies could be due to the variability of material used in research. However, using low-alkali cement on its own may not be enough to suppress deleterious expansion; other mitigation are also suggested to achieve a better effect (Malvar, 2002). Previous research also indicated that not all alkalis will cause the expansion of concrete (Lawrence and H. Vivian, 1961).

Cement having a Na_2Oe of less than 0.6 percent is generally considered as low-alkali cement. However, this kind of low alkali level in cement found to be sufficient to cause ASR in highly reactive aggregate. The bulk NaO_{eq}. of cement (0.6 percent requirement) may not always accurately define the potential of cement alkali to cause ASR and might be misleading in certain cases. Cements with similar Na_2Oeq. can have different K/Na ratios and are found to be the reason for the observed differences in concrete expansion (Leeman and Lothenbach 2008). The amount of alkalis that are soluble in the concrete pore solution and hence available for the reaction is more important than the total bulk alkali content of the concrete materials. The approach of using low-alkali cement alone does not necessarily prevent ASR-induced damage because the contribution of alkalis from other sources is not considered. Alkalis may also become concentrated in a portion of the concrete through migration with moisture. Therefore, many agencies and countries specified total permissible alkali between 2.5 and 4.5 kg/m3 (4.21 and 7.58 lbs /yard^3), and stated that the boundary of total permissible alkali is not rigid but depends on the aggregate reactivity (Nixon and Sims 1992). Sibbick and Page (1992) advocated that the alkali threshold based on CPT test is

between 3 to 5 kg/m3 (5.05 and 8.43 lbs/yard^3) for reactive aggregates but is lower for highly reactive aggregates. A value of 3.0 kg/m3 (5.05 lbs/yard^3) was reported as threshold concrete alkali based on the relationship between 2 years CPT expansion and concrete alkali content. However, the occurrence of ASR expansion has also been reported even with the total concrete alkali content less than 3 kg/m^3 (Folliard et.al. 2007).

2.2.3.1. Alkalis and Calcium

Soluble alkalis including sodium hydroxide (NaOH) and potassium hydroxide (KOH) are released into the cement pore solution during hydration (Helmuth 1993). As hydration continues some of the alkalis are used up in the reaction products; however, the water is also used up and the alkali concentration increases (Powers and Steinour, 1955, Diamond 1989). Diamond (1989) discovered a linear relationship between alkali concentration in cement pore solution and the available alkali content of the cement (Helmuth 1993). As the available alkalis within the cement increases, the concentration of alkalis within the pore solution of the concrete increases. Powers (1955) stated the importance of calcium in the formation of expansive alkali-silica gels. When excess calcium hydroxide is available within the alkali-silica gel, the gel is unstable and produces dissolved silica which will not expand. However, when the calcium-alkali-silica system produces a barrier to the transport of excess calcium to the reaction site, a stable alkali-silica gel is produced which then absorbs water and expands (Powers and Steinour, 1955, and Helmuth 1993). The process of dissolving silica minerals in the presence of highly alkaline pore solution will continue until either all of the reactive silica or all of the alkalis are consumed (Helmuth 1993).

2.2.4. Moisture Effect

Moisture is an essential ingredient for ASR to occur and become expansive. Water is the main carrier of hydroxyl and cations in a form of pore solution to the reaction site, thus facilitating ASR to occur. Subsequently, the reaction product (i.e., ASR gel) absorbs moisture, causing swelling. The swelling causes high stress inside aggregates, resulting in aggregate cracking and subsequent concrete deterioration. Although concrete looks dry during its service years, it can still maintains relative humidity (RH) in the range of 80–90 percent in the inner portions (Mukhopadhyay 2009). Pedneault (1996) found that concrete displayed very small expansion at an RH less than 80 percent, and expansion increases exponentially when RH increases above 80 percent.

The moisture level might be reduced below 80 percent in concrete by limiting the exposure of concrete structures to moisture or the use of low permeability (concrete with low water to cement ratio) concrete. In addition, improving drainage conditions can also be applied as an effective way to reduce the availability of external moisture. A higher w/c can cause both increasing and decreasing of expansion due to ASR. The following phenomena can cause increase of expansion:

- Higher porosity/permeability causing higher ionic mobility and more reaction
- Greater availability of free (capillary) water to make the gel more expansive.
- The possible mechanisms that may cause reduction in expansion are:
- Higher available space (high capillary porosity due to high w/c) for gel accommodation.
- Relatively lower pore solution concentration (dilution effects due to high w/c) may cause slower expansion rate and lower level of expansion.

2.3. ASR Diagnosis and Petrographic Assessment

ASR symptoms are analogous to other durability mechanisms, which occur in concrete (Fournier et. al, 2004). Some of the visible symptoms of ASR include map cracking at the surface of the concrete, or relative displacement of concrete elements (Stark 1991, ACI 1998, and Fournier et. al, 2004). Additional symptoms include pop-outs, surface discoloration, and/or gel exudation at the surface (Stark 1991, Fournier et. al, 2010, ACI 1998, and Fournier et. al, 2004). Often the concrete is discolored along cracks, especially when the concrete is moist (Stark 1991, Fournier et. al, 2010, and ACI 1998). It was shown by some studies that the expansion greater than 0.04 percent will lead to visible cracking in unreinforced concrete (Ideker et. al, 2012).

Map cracking occurs in concrete elements which are subjected to cyclic environmental conditions. The concrete within an element will expand more than the outer surface due to a temperature and humidity gradient which develops between the surface and interior concrete (Fournier et. al, 2004). Expansion of the concrete will produce tensile stresses and micro-cracks in the interior concrete, and drying shrinkage near the surface will cause map cracking in the exposed surfaces of the concrete (Deschenes, 2017).

Petrographic studies play an important role in understanding the above additional factors related to aggregate reactivity. The examination includes both microscopic and macroscopic identification of symptoms of ASR. Macroscopic evidence of ASR includes deposits of alkali-silica gel which is identified visually and chemically (Fournier et. al, 2004, and ACI 1998). Deposits of alkali-silica gel develop within voids in the cement pore solution and within cracked aggregate particles (Fournier et. al, 2004, and Fournier et. al, 2010).

Additionally, reaction rims are sometimes present within the interfacial transition zone around reactive aggregate particles (Fournier et. al, 2004, Fournier et. al, 2010, and ACI 1998).

Microscopic evidence of ASR may include micro-cracking within aggregates and/or the cement matrix, reaction rims, and alkali-silica gel (Fournier et. al, 2004, and Fournier et. al, 2010). Petrographic examination is necessary to provide a conclusive diagnosis of the presence of ASR and other forms of deterioration that may have occurred as a result of, or in combination to, ASR (Fournier 2004 et. al, ACI 1998, and Fournier et. al, 2010).

2.4. ASR Mitigation Strategies

Several options are available to inhibit ASR occurrence in concrete. The most efficient way of ASR mitigation involves controlling one or more of the constituents required for ASR to develop (ACI 1998). Moisture is required for ASR to develop and expansion to progress; however, limiting water is a prohibitive method of preventing ASR. using non-reactive aggregate is also a traight-forward way to avoid ASR in concrete. The most common method of prevention involves limiting the concrete pore solution alkalinity (ACI 1998). Cement alkalis are most readily available within the cement pore solution (Diamond 1989, and Thomas 1995). However, alkalis are sometimes contributed by SCMs or even aggregates (ACI 1998, and Thomas 1995). The use of low alkali cements will reduce cement pore solutions alkalinity, and a limit of 0.6 percent Na2Oe is recommended when used in combination with reactive aggregates (Thomas et. al, 2006a, ACI 1998, and Stanton 1940). However, in certain highly reactive aggregates this limit is not sufficient (Stark 1980, ACI 1998, and Swamy et. al, 1988b). In addition, SCMs dilute high alkali cements or bind the available alkalis within the hydration products (ACI 1998). Some of the SCMs which prevent or reduce ASR expansion include slag cement, fly ash, calcined clays, rice husk ash, and silica fume (ACI 1998, and Thomas et. al, 2006a). The safe replacement rate of cement with an

SCM will depend on the cement alkalis, aggregate reactivity, selected SCM, and chemical and physical composition of the SCM (ACI 1998, Thomas et. al, 2006a, and Thomas 1995).

2.4.1. Non-Reactive Aggregate and Low-Alkali Cement

Using non-reactive aggregate to mitigate ASR seems to be a straightforward option. However, several concerns arise if this option is going to be undertaken. (1) Availability of aggregates: The availability of non-reactive aggregates is usually dependent upon local geographical characterization and ease of transportation. (2) Verifying reactivity: Different experimental methods can be used to identify the reactivity of aggregates. Commonly used methods include the accelerated mortar bar test and concrete prism test. These tests can be used together to identify the reactivity of aggregates.

ASTM C1778 also includes a prescriptive way to evaluate the potential risk ASR with an aggregate source. However, the applicability of current test methods is controversial. (3) Other properties of non-reactive aggregate: For structural construction, resistance on ASR is not the only issue of concern. Other properties such as hardness, surface area and bonding with cement paste will all have impacts on concrete performance (Li, 2016).

As most of the alkalis in concrete come from cement, cement with a low content of alkali could be effective in mitigating ASR. According to ASTM C150-16, equivalent alkalis of portland cement should be kept below 0.60%. ASTM C1778 also provided the maximum alkali loading for concrete with different types of aggregates and subjected to various exposure conditions (ASTM C1778, 2014). However, limiting alkali-content of the cement on its own may not be sufficient to suppress ASR-induced expansion in some cases (Li, 2016).

2.4.2. Supplementary Cementitious Materials (SCM)

A variety of supplementary cementitious materials (SCMs) have been extensively used for durability enhancement of different types of concrete, such as nanomaterials (Jalal et al. 2012, Jalal 2012, Jalal et al. 2013, Jalal and Mansouri 2013, Hajisotoudeh and Jalal 2013, Jalal 2014, Vazinram et al. 2015), fly ash (Jalal and Mansouri 2012, Jalal and Tahmasebi 2015), silica fume (Jalal 2013, Jalal et al. 2015), slag (Teimortashlu et al. 2018, Jalal et al, 2019), Zeolite (Jalal et al. 2019), etc.

In general, SCMs such as fly ash, granulated blast-furnace slag (GGBFS), silica fume, and metakaolin are all used to reduce ASR expansion in concrete. The mechanisms are not well understood, but it is agreed that the reactive silica in SCMs combines with the cement alkalis (i.e., Na and K) more readily through pozzolanic reaction than the siliceous phase(s) in aggregate. Therefore, alkalis are rapidly consumed, and the level of hydroxyl ions is reduced to a level at which aggregates react very slowly or not at all (Carrasquillo and Farbiaz 1988, Diamond and Penko 1992). Furthermore, the pozzolanic reaction results in the formation of alkali-calcium-silicate-hydrates, which is non-expansive, unlike the water-absorbing expansive ASR gels. However, not all SCMs increase ASR resistance. Some SCMs can be a source of additional alkalis. Diamond (1981) reported that Class F fly ash is more effective in controlling ASR than Class C fly ash. Shehata and Thomas (2000) and Shon et al. (2003, 2004) supported that Class C fly ashes are less effective than Class F fly ashes in controlling ASR because some Class C fly ashes (those with Na2Oequivalent greater than the cement) actually enhance alkali ions (e.g., Na+ and K+) and OH- in pore solution.

2.4.2.1. The role of Fly Ash and its Composition

It was first shown in 1981 that fly ash can cut down on the alkalinity of pore solution. Since then, fly ash has been extensively used and investigated to mitigate ASR (Diamond, 1981). Nowadays, based on present lab results and field experiences, fly ash is accounted for as an effective pozzolan to mitigate ASR. some countries have already adopted this method to control ASR expansion (Ahlstrom, 2010; Shehata and Thomas, 2000). Dunstan observed pessimum effect of fly ash in a study, when the fly ash was utilized for partial replacement of cement (Dunstan, 1981). The ASTM C441 was used to investigate the effect of the fly ash, and an expansion increase was observed at a replacement level of below 5%. Nevertheless , the expansion decreased when the replacement level exceeded 5% (Dunstan, 1981). According to the results obtained by Shehata et al., fly ash was reported to be effective in mitigating ASR. However, the mitigation efficacy varied due to the differences in the composition of fly ash (Shehata and Thomas, 2000).

Past research has also shown that due to the presence of fly ash, a reduction in alkalinity of pore solution and a decrease of Ca/Si were observed (Shehata and Thomas, 1999; Rayment, 1982). In general, as one of the major mechanisms of fly ash addition, alkalinity reduction in concrete pore solution has been reported. Another explanation was the consumption of CH to form C-S-H, and alkalis were bound during this process.

The effects of differences in the fly ash composition have been studies by several researchers and its impact on mitigation efficacy has been investigated (Bleszynski and M.D. Thomas, 1998; Thomas, 2011). The results from these studies indicated that the CaO content in fly ash can influence the mitigation efficacy. It was reported by Dunstan (1981) that incorporation of fly ash containing a higher content of CaO into the mortar led to a higher expansion compared to a mixture with a low-CaO fly ash at the same replacement level. a higher replacement level was

reported by Shehata to be required when the fly ash with a higher CaO content was used (Shehata, M.D.A. Thomas, 1999). Furthermore, concrete with the fly ash containing a high CaO content was reported to show high alkalinity in pore solution. Calcium gels were reported by Bleszynski et al. (Bleszynski and M.D. Thomas, 1998) to be more solid when compared to silica gels, which were more dispersible to alleviate the internal pressure. It was also reported by Shehata that $(CaO+10\times Na_2O_{eq})/SiO_2$ can be used to describe the concentration of OH- in pore solution.

2.4.2.2. Chemical Index

As mentioned earlier, chemical composition of SCMs has an important influence on the their performance with regard to ASR mitigation. It was reported by Chen et al. that when SCMs included a high fraction of $SiO_2+Al_2O_3+Fe_2O_3$, they were more effective in mitigating ASR (Li, 2016). Moreover, a "chemical index" was reported by Thomas (2011), in which the major chemical compositions in binder phases were considered. The chemical index which can be utilized to correlate the chemical compositions of binder with the alkalinity of pore solution was expressed as $(Na_2O_{eq} \times CaO) / (SiO_2)_2$ (Thomas, 2011). Nevertheless, the role of Al was not considered in this chemical index. Another empirical index was also reported by Thomas and given as $(Na_2O_{eq})_{0.33} \times CaO / (SiO_2)_2$, to correlate the chemical compositions to two-year expansion (Li, 2016).

2.5. Expansion Mechanisms

In spite of the fact that the chemical reaction mechanisms governing ASR are quite known, the expansion mechanisms still remain unclear and are a point of controversy. The most common and circulated theories in the literature regarding ASR expansion mechanism are briefly described below.

2.5.1. Gel Formation and Composition

Diamond showed in his research that ASR attack was mainly due to the existence of hydroxide ions but not simply due to the existence of alkali cations in pore solution. However, the content of hydroxides was largely determined by the content of alkali cations (Diamond and Thaulow, 1974). ASR gel formation mechanism and its composition is still under assessment.

The double-layer theory proposed by Prezzi (1997), is one of the most discussed theories which discusses the interaction of silica with alkalis in pore solution, silica depolymerization, and absorption of a layer of sodium and potassium onto the surface of negatively charged silicate group. Subsequent suspensions and further gel formation will then occur due to gathering of colloidal silicate particles. Repulsive forces and Van Der Waals forces are a pair of forces determining the kinetics of gel formation during this process. When particles are close enough, Van Der Waals force will be dominant to facilitate the agglomeration of ASR gel, and repulsive force dominates when particles are far apart (Prezzi, 1997). formation of ASR gel involving the recycling of alkali, which keeps the reaction going even at the later age was also shown by Thomas (2001)

ASR gel is a product with K, Na, Ca, Si, Mg and H2O. However, the stoichiometry is still not fully understood. According to previous research, the molar ratio of (Na2O+K2O)/SiO2 ranges from 0.05 to 0.6, and (CaO+MgO)/SiO2 ranges from 0 to 0.2 (Hou et al., 2004). Knudsen and Thaulow showed that the ASR gel residing in cracks far from the reaction site had about 20% CaO in it, whereas the ASR gel in aggregates showed a lower CaO content. Thomas reported that in a seven-year-old concrete, the ASR gel in the aggregates had a Ca/Si of 0.25 and the Ca/Si was observed to be up to 1.30 for the ASR gel within the paste (Thomas, 2001).

It is believed that the presence of Ca will influence the expansion properties of ASR gel. One theory purports that when Ca exists in the system, it creates a more expansive gel; for a system with little Ca, even if ASR occurred, little expansion can occur (Hou et al., 2004). It was shown by Leemann et al. that the presence of Ca accelerated the dissolution of Si (Leemann, 2011). According to this study, with an increase of portlandite, the percentage of Q4 sites (by NMR) showed a significant decrease, which means less unreacted silica was detected (Leemann, 2011). Hou et al. found that the gel formation process included multiple stages, which included the formation of C-S-H gel and A-S-H gel. The expansive A-S-H gel was not be able to form unless the Ca in the system was consumed to generate C-S-H (Hou et al., 2005).

Another theory was developed based on the double-layer theory, in which, Ca2+ replaced Na+ and K+ on the double layer, and less expansion was expected due to smaller pressure and smaller cation radius. Based on the double-layer theory, Monteiro et al. showed that the higher the CaO / Na2Oeq was, the more lowly-expansive gels formed (Prezzi et al., 1997; Monteiro et al., 1997). However, the conclusions were made based on the usage of supplementary cementitious materials (SCMs).

2.5.2. Expansion Theories

Hansen (1944) proposed that the cracking that occurred in the concrete was due to the formation of an osmotic pressure cell surrounding the aggregate. In the theory, hardened cement paste act as a semi-permeable membrane on silicate ions passage. The membrane allows water molecules and alkali hydroxides to diffuse in, but prevents silicate ions to diffuse out. The alkali-silicate that formed on the surface on an aggregate surface would draw solution from the cement paste to form a liquid-filled pocket. The liquid that was drawn in would then exert an osmotic pressure against the confining cement paste, leading to cracking.

McGowan and Vivian (1952) postulated that cracking in concrete should relieve the osmotic pressure and prevent any further expansion. Instead, they proposed the "Swelling theory" in which alkali silica gel (a product of reacted aggregates) absorbs water, leading to swelling in the gel, which causes expansive pressure and eventually causes concrete cracking. Other researchers (Tang 1981) also agreed with this theory.

Some similar swelling theory controlled by lime was proposed by Powers and Steinour (1955), Hansen (1944) and McGowan and Vivian (1952). When a silica particle is exposed to a strong base, the hydroxyl ions attack the surface and gradually penetrate the particle. If the attack occurs in the presence of excess lime, then a non-swelling lime-alkali-silica complex is formed when chemical equilibrium with the lime is reached. However, if the alkali-silica complex is not in equilibrium with the lime, then swelling will occur.

Another theory regarding a diffusion controlled by calcium was proposed by Chatterji et al. (1986, 1989). This theory states that when hydroxyl ions are placed in a solution with a pH of 7 or greater, these ions penetrate reactive siliceous particles, in amounts increasing with solution pH and ionic strength. At a constant solution pH and ionic strength, the absorption of OH- decreases with the increasing size of the associated hydrated cation (OH- absorption decreases in the series K+, Na+, Li+, Ca2+). In a pore solution with mixed ionic species (e.g., Ca(OH)2 and NaCl), the cations will penetrate into the reactive silica grain following the penetrating OH- ions; however, more of the smaller hydrated cations will do so than the larger ones (in this example, hydrated Na+). After that, penetrating OH- ions attack siloxane bonds, and this reaction further opens up the reactive silica grain to attack. Silica ions are liberated from their original sites, enabling them to diffuse out of the reactive grains. Ca2+ controls the rate of silica diffusing out of reacting grains in the immediate vicinity. A higher Ca2+ ion concentration lowers or impedes silica

diffusion away from the reactive grains. Finally, when the net amount of materials (Na+, K+, Ca2+, OH-, and H2O) entering a reactive silica grain exceeds the amount of materials leaving (SiO2 2-), expansion occurs.

Diffuse Double Layer is another theory which is based on electrostatic repulsion between diffuse double layers (DDLs) as responsible for generating expansive forces (Prezzi 1997 and Rodrigues et al. 1999). Very high negative charges are observed at the surface of the silica grains (Bolt 1957 and Rodrigues et al. 1999). To counterbalance the negative silica charges, an electric double layer of positive charges (cations) develop and adsorb around the silica surface. Two layers defined as the Gouy-Chapman layer or the Stern layer has a collective thickness of a few nanometers that can be calculated from the ionic strength of the pore solution electrolyte. The double layers are composed of calcium, potassium and sodium, and some other anions, but the net charge of the whole system (sum of negative charges of silica + anions + sum of all cations) is equal to 0. This system will form a colloidal suspension and then conglomerate into a gel (Prezzi 1997). Diamond (1989) indicated that the expansive pressures because of gel swelling are in the range 6–7 MPa, but expansive pressure of 10.3 MPa was calculated using conventional double layer equations (Rodrigues et al. 1999).

Expansive pressure theory due to the formation of reaction rim was also proposed by Ichikawa and Miura in 2007. Their research showed that the alkali silicate does not develop expansive pressure unless an insoluble, dense reaction rim surrounds the aggregate. The reaction rim acts like a barrier, which allows the penetration of alkaline solution but prevents the leakage of alkali silicate. Aggregate swelling associated with siloxane bond breaking is another theory that was proposed by Garcia-Diaz et.al. (2006). Two reaction steps considerd in this process include the Q3 tetrahedrons formation by breaking up siloxane bonds and the dissolution of these Q3

tetrahedrons. They observed significant increase of the aggregate pore volume associated with this transition and found a linear relationship between the mortar bar swelling and the aggregate swelling due to this transition (Mukhopadhyay and Liu, 2014).

2.6. ASR Modeling Techniques

Different types of models have been developed by researchers to simulate and predict ASR behavior. These models can be mainly categorized as kinetic, thermodynamic, mathematical, and mechanical models. From the literature review on ASR models presented below, three main points can be noticed: (1) limited number of variables or the only ones that are able to be modeled are used to develop the model, and hence the compound effect is missing, (2) available models typically address only one scale, while ASR phenomenon includes multi scales, and (3) in few models wherein multi scales were taken into account, either the connection of the scales is not well-defined or the modeling technique is not able to handle multi-scale modeling.

Goltermann (1995) proposed mechanical model to predict concrete deterioration due to ASR. His research mainly seems to lack experimental verification of the proposed model. Bezant et al. (2000) developed a mathematical model to simulate ASR behavior. They mentioned two basic problems of a comprehensive model as: (a) including the kinetics of chemical and diffusional processes, and (b) modeling of the mechanical damage which calls for fracture mechanics. Their model is solely based on single spherical reactive particle and no experimental validation was reported. Samua and Perotti (2006) proposed constitutive model to predict the ASR expansion. This model which was referred to as thermos-chemo-mechanical model, requires several parameters which are obtained from the experiment and was used for ASR prediction of Dam structure. However, no validation with experimental results was presented in their paper. A

discrete element model was proposed by Alnaggar et al. (2013). In this mesoscale model, several parameters were assumed and calibration parameters were eventually obtained through curve-fitting method.

A computational linear elastic fracture mechanics-based model for alkali–silica reaction was proposed by Charpin and Ehrlacher in 2012. This model deals with the case of a concrete made up of dense spherical aggregates, and chemistry and diffusion (of ions and gel) are not modelled. The focus of their model is on the mechanical consequences of the progressive replacement of the aggregates by a less dense gel.

Pignatelli et al. (2013) developed a coupled mechanical and chemical model to simulate the ASR-induced degradation in concrete. they formulated a poro-mechanical model with two isotropic internal variables, namely chemical and mechanical damage. They utilized the double layer model as a function of pH and pore solution to simulate the expansion caused by chemical reaction. Nevertheless, the effect of SCM, which is of great importance has not been investigated in their research. A multi-scale analysis of ASR with alkali leaching effect was performed by Multon and Sellier (2016). They investigated the alkali transport and consumption in aggregate and concrete scales. The alkali threshold according to temperature and calcium concentration was assessed in their study.

Guthrie and Carey (2015) proposed a thermodynamic model for paste-aggregate interactions and ASR. This model is based on geochemical principles tied to aqueous speciation, silica solubility, kinetically controlled mineral dissolution, and diffusion. They stated that their model can also explains why pozzolans do not generate ASR, which was attributed to the fine-grained character of pozzolan that precludes formation of chemical gradients.

3. TEST METHODS AND MATERIALS CHARACTERIZATION

In this chapter, the test methods used for ASR testing are briefly described. More details on some of the modified test methods will be also presented. As presented earlier in Chapter one in Figure 1, tests were performed at three different scales including aggregates, mortar bar, and concrete cylinder.

3.1. Aggregate Testing: Volume Change Measuring Device (VCMD) Method

This test method is a kinetic-based test method that was developed in Texas A&M transportation Institute (Mukhopadhyay et al. 2009). VCMD simulates the aggregate-pore solution reaction that exists in concrete and measures net solution volume change due to ASR over time. This test is performed with as-received aggregates (the error due to crushing is eliminated) and within a short period of time (approximately 5 days including sample preparation).

By using this test, the compound activation energy (CAE) of the aggregates can be determined which provides an indicator of aggregates reactivity for ASR. Since there are several parameters affecting the aggregates' reactivity such as composition, shape, size, surface area, etc., an indicator such as activation energy that takes into account the combined effect of all those was adopted to as the aggregate reactivity indicator. In fact, The activation energy is the energy barrier that has to overcome to initiate ASR taking into account the combined effect of alkalinity, temperature, and time. The concept of ASR Ea can be considered as a composite single parameter of alkali silica reactivity of different reactive component(s) in aggregate (Mukhopadhyay et al. 2018). The use of term "composite activation energy" will be more appropriate than "activation

energy" for heterogeneous and multi-phase aggregate materials. Schematic presentation of the test setup is illustrated in Figure 4.

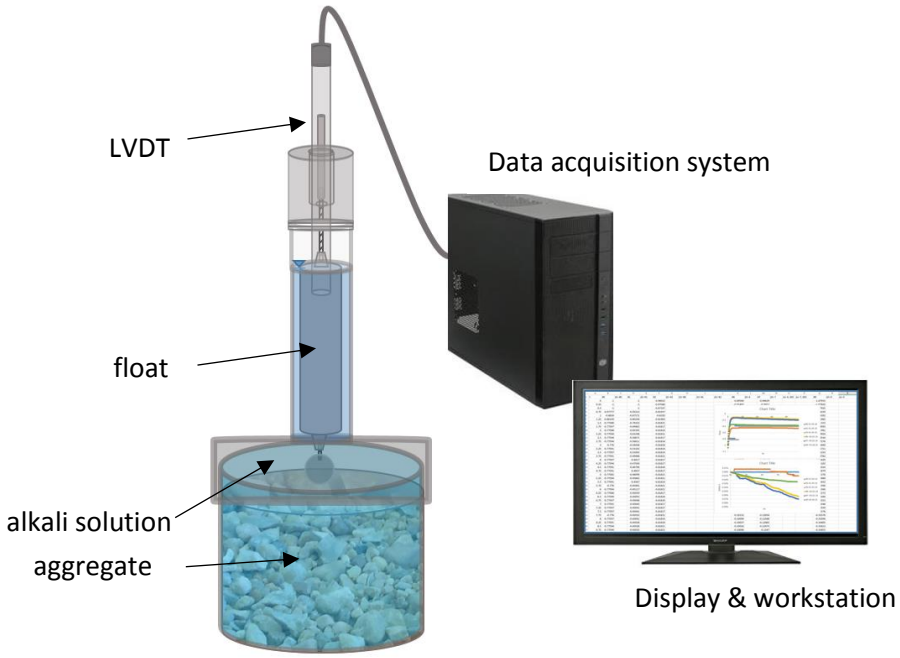

Figure 4. Schematic of modified VCMD test setup

3.1.1. Test Procedure

alkaline solution of different concentrations [e.g., 1N and 0.5N NH + CH] and tested at different temperatures (e.g., 60°, 70°, and 80°C) inside an oven according to the experimental design in Section 4.4.1. The weight of the oven-dried material corresponded to the 80 percent volume of the VCMD pot. Researchers used a constant aggregate/solution volume ratio and gradation for all the aggregate testing. The VCMD test procedure is summarized below:

- Keep the VCMD filled up with clean and dried aggregate and alkaline solution overnight at room temperature to allow maximum saturation of voids in the alkaline solution.

- Place the VCMD on a vibrating table and conduct vacuuming under vibration for 2 hours in the next day to mainly remove entrapped air bubbles in the solution. This also helps to saturate the unfilled voids (likely to be present) in aggregates after overnight saturation.
- Place the VCMD inside an oven and heat it to the selected target temperature (~ 2.5 hours).
- Apply a second stage vacuuming under vibration of around 45 minutes to facilitate further removal of air bubbles (may be generated during heating at target temperature) from solution.
- The VCMD was placed inside an oven, whose temperature was then raised to the selected target temperature (i.e. 60 or 70 or 80°C). It takes around 4–5 hours to reach the target temperature.
- Solution volume changes as the chemical reaction between aggregate and alkaline solution progresses; make the float move. As the float moves inside the tower, the stainless steel rod attached with the float also moves inside the LVDT. Through the data acquisition system, the computer records LVDT displacement readings over time.

LVDT displacement readings at the stable target temperature represents the reference (initial) LVDT reading for calculating displacement due to ASR. This ensures separation of thermal solution volume expansion from solution volume change due to ASR. All subsequent LVDT readings (i.e., after reference reading) minus the reference LVDT reading represent displacement due to ASR over time. The percent volume change of solution due to ASR is calculated by using following equation:

$$V(\%) = \frac{\Delta V_{ASR}}{V_{Aggregate}} \times 100 \qquad (3.1)$$

V(%)= Percent volume change of solution due to ASR

ΔV_{ASR}= Solution volume change due to ASR

$V_{aggregate}$= Initial volume of aggregate

3.1.2. Kinetic Model and Parameter Estimation

The modified equation of the kinetic-type model used in this method is as given below:

$$\varepsilon = \varepsilon_0 e^{(\frac{\rho}{t-t_0})^{\beta}} \quad (3.2)$$

where:

ε_0 = ASR ultimate volume change.

β = Rate constant.

t_0 = Theoretical Initial time of ASR (hr).

ρ = Time corresponding to a volume change ($\varepsilon_0/\varepsilon$).

By fitting a kinetic type of performance model to measured volume change data over time, rate constant (β) is calculated. Rate constants at multiple temperatures (a minimum of three temperatures, e.g., 60°C, 70°C, and 80°C) are then determined, and the activation energy (Ea) is calculated by plotting ln(β) versus (1/T). Based on the rate theory (Callister 2007), the slope of the linear regression is equal to (−Ea/R) where R is the universal gas constant and Ea is the activation energy. The VCMD has been used to measure the alkali-silica reactivity of selective minerals and aggregates in terms of their activation energy (Mukhopadhyay et al. 2006, Shon et al. 2007).

3.1.3. Threshold Alkalinity Level

A relationship between compound activation energy (CPA) and alkalinity can be used to determine the threshold alkalinity. The higher the alkalinity, the lower the CAE. An attempt was made to establish a mathematical relationship between CAE and alkalinity. The following model (Equation 5.2) was used to establish a relationship between CAE and alkalinity:

$$CAE = E_{a_0} + \frac{C_1}{C^n} \quad (3.3)$$

where,

CAE is compound activation energy (KJ/mol),

E_{ao} is Activation energy – theoretical threshold (KJ/mol),

C_1 is Activation energy curvature coefficient (KJ/mol $^{(n-1)}$),

N is Activation energy curvature exponent,

C is Alkalinity (mol).

The above equation was used to calculate the threshold alkalinity for different aggregates in this study.

3.1.4. Improved VCMD Method

Two main areas of improvement in VCMD that can greatly improve the final results include (1) the data acquisition system, and (2) parameter estimation of the kinetic model. In this research, at attempt was made to improve these areas by optimizing the data acquisition system of the test setup through designing a new float, and facilitating the parameter estimation of the model by using optimization techniques of Excel Solver.

Once volume change (V%) vs. time is calculated (Texas A&M Report, 2014) , the following procedure is recommended for improved parameter estimation of the model:

1. Paste the time (up to 96 hours) in column A and calculated volume change in column B.

2. Put the initial guess values (ε0: -0.0001; ρ: -20; Beta: 1; t0: 5 in cells O5 to R5) in 60, 70, and 80.

3. Go to “DATA” tab and click “Solver”. Uncheck “Make Unconstrained Variables Non-Negative” and click “Solve” for 60, 70, and 80. Click “ok.” You should be able to see a fit between the model curve (blue color) and experimental curve (orange color) in 60, 70, and 80.

4. Copy the value of zo, Ro, Beta, and t0 from the best R2 value in the plot of y vs. y' among 60, 70, and 80 as the initial guess value for another two temperatures. Run item 3 again.

5. The R2 value in the plot of y vs. y' at three temperature should be greater than 0.95, the R2 value of plot 1/T vs. Ln(beta) in Ea should be greater than 0.9, and Ea value should be positive.

a. If so, go to item 14

b. If not, go to item 6

6. Add or Remove "-" for the value of z0, R0, Beta, and t0 to ensure (i) z0 and R0 are negative and (ii) Beta and t0 are positive. If t0 is not less than 5, put t0=5. Run item 3 again.

7. The R2 value in the plot of y vs. y' at three temperature should be greater than 0.95, the R2 value of plot 1/T vs. Ln(beta) in Ea should be greater than 0.9, and Ea value should be positive.

a. If so, go to item 14

b. If not, go to item 8

8. Use the value of Beta and t0 from the best R2 value in the plot of y vs. y' among 60, 70, and 80 as the initial value of Beta and t0 for another two temperatures. Run item 3 again.

9. The R2 value in the plot of y vs. y' at three temperature should be greater than 0.95, the R2 value of plot 1/T vs. Ln(beta) in Ea should be greater than 0.9, and Ea value should be positive..

a. If so, go to item 14

b. If not, go to item 10

10. Go to the temperature containing best R2 value in the plot of y vs. y'. Adjust initial value of Beta in another two temperatures with an increase and/or decrease rate of 0.5. For example, if the best R2 is at 70C, decrease 0.5 to the Beta at 60C and increase 0.5 to the Beta at 80C. Run item 3 again.

11. Check the R2 value of plot 1/T vs. Ln (beta) in Ea. The R2 value should be greater than 0.9 and the Ea value should be positive.

a. If so, go to item 14

b. If not, go to item 12

12. Go to the temperature containing best R2 value in the plot of y vs. y'. Adjust initial value of t0 in another two temperatures with an increase and/or decrease rate of 1. For example, if the best R2 is at 70C, decrease 1 to the t0 at 60C and increase 1 to the t0 at 80C. Run item 3 again.

13. Check the R2 value of plot 1/T vs. Ln (beta) in Ea. The R2 value should be greater than 0.9 and the Ea value should be positive.

a. If so, go to item 14

b. If not, go to item 10

14. Report CAE value and the plot of 1/T vs. Ln (Beta) from the sheet of CAE.

3.1.4.1. Float Design and Optimization

The details of the VCMD test setup is displayed in Figure 5. Structural configuration of the float system is displayed in Figure 6. As can be seen from the figure, the main body part is a hollow cylinder with thickness of *t* which can be made out of two alternatives i.e., Low Density poly Ethylene (LDPE) and PVC, depending on which one can meet the design requirements (Jalal et al. 2018, Jalal et al. 2019). Two truncated cones on the top and bottom are used as holders which are of the same material. At the bottom, there is a small threaded rod which connects and holds a steel weight at the bottom of the plastic cylinder. Three geometries namely spherical, conical, and cylindrical are assessed for the bottom weight in design section to find out which one can be used

in the float structure (Jalal and Goharzay 2019). A PVC rod sits on the top that holds an LVDT on the top. Depicted in Figure 6 are the details of the float to be designed.

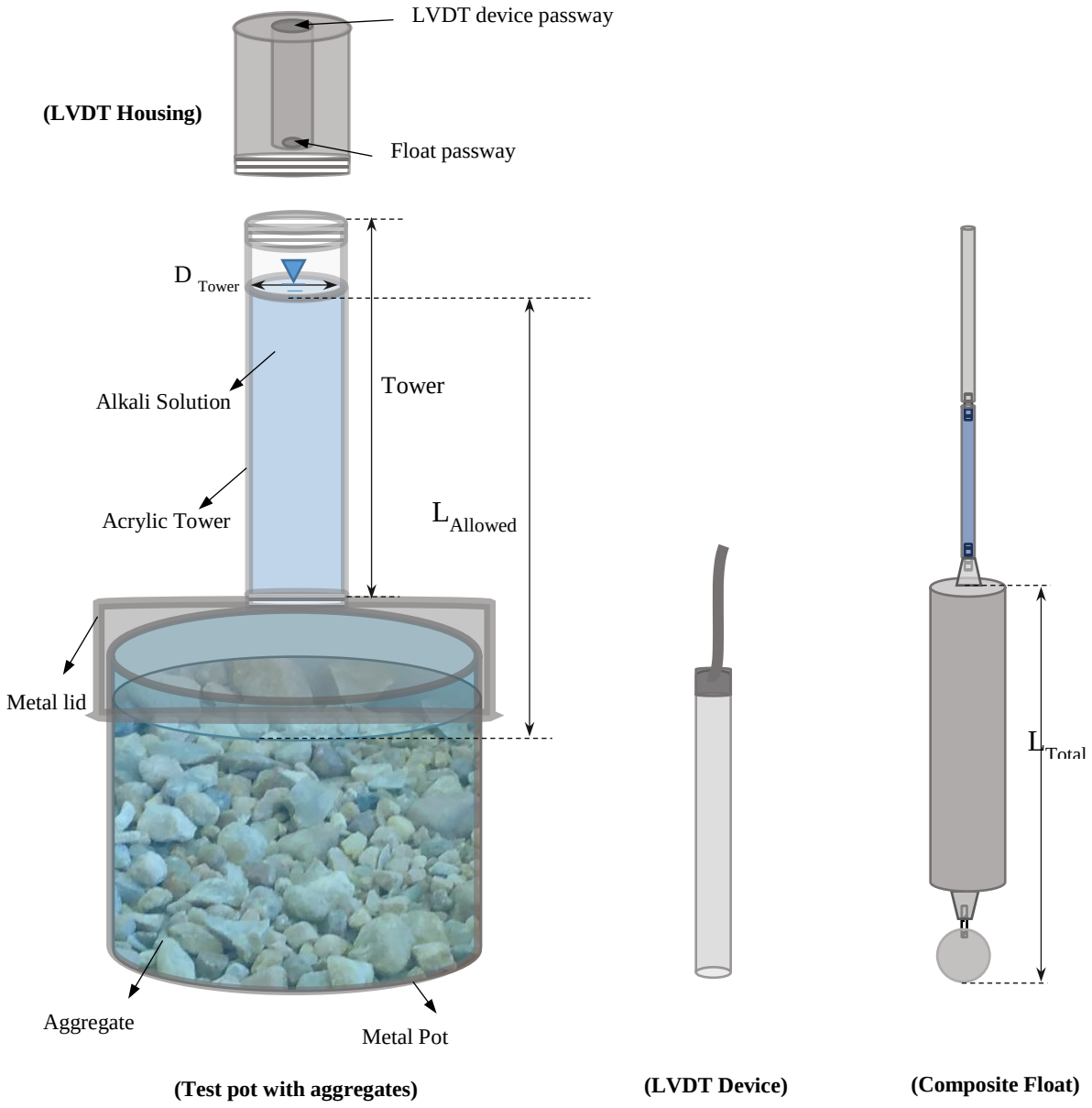

Figure 5. Details of VCMD test setup

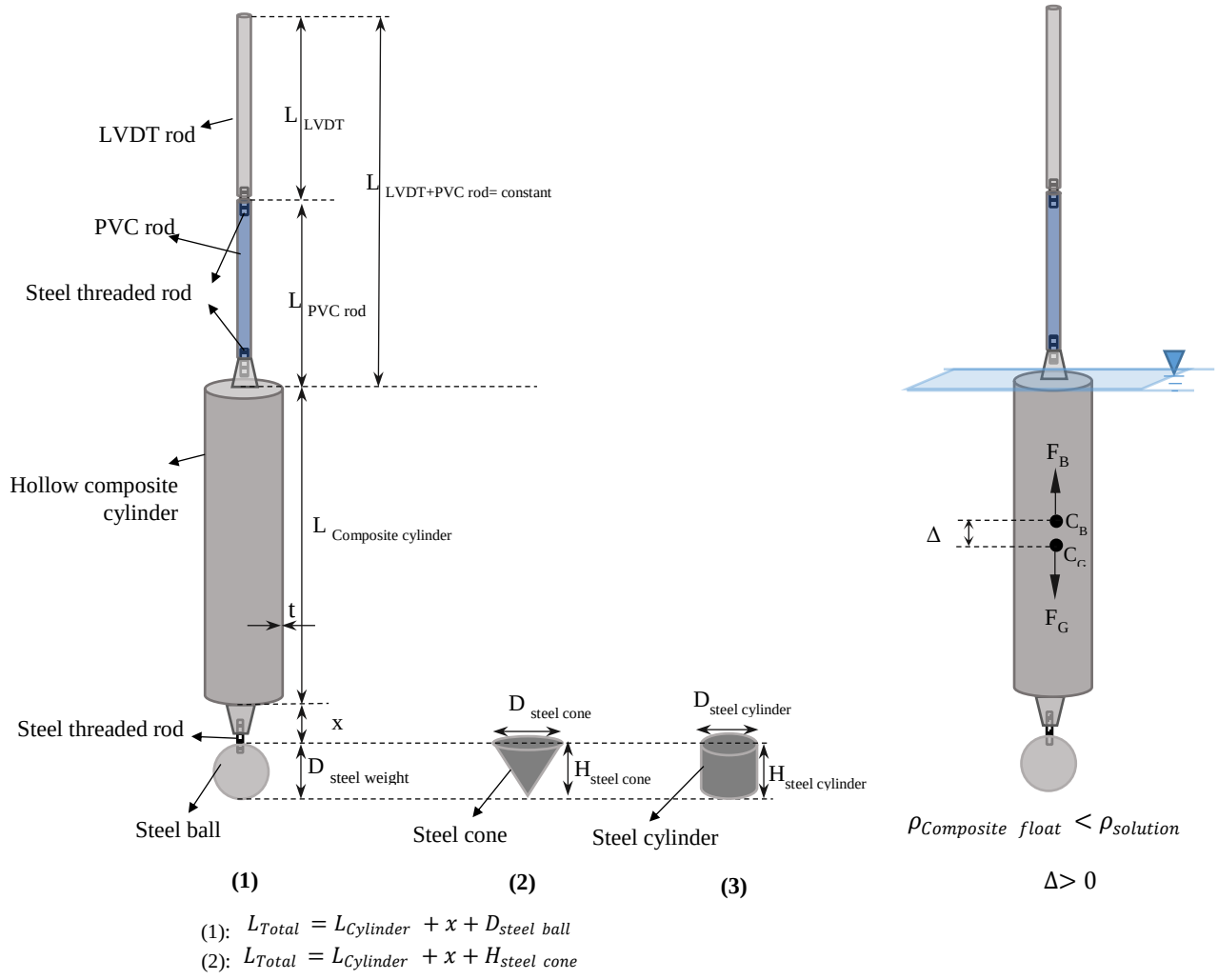

Figure 6. Details and structural configuration of the float

The float is intended to be designed in such a way that the whole height of the hollow composite cylinder is placed inside the solution so that the upper face of the composite cylinder is aligned with solution level, as shown in Figure 6. For design of the composite float, two main criteria should be met:

- The total density of the float system should be less than the solution (or water),
- In order for the float to stay up-right in the solution, its center of buoyancy (C_B) should be higher than its center of gravity (C_G), as shown in the figure.

Since the float is considered to be a composite system comprising different parts made of different materials, its total density (ρ_{float}), center of buoyancy (CB), and center of gravity (CG) are calculated using the following equation:

$$\rho_{composite\ float} = \frac{\sum_1^n m_i}{\sum_1^n V_i} \tag{3.4}$$

$$y_G = \frac{\sum_1^n m_i y_i}{\sum_1^n m_i} \tag{3.5}$$

$$y_B = \frac{\sum_1^n V_i y_i}{\sum_1^n V_i} \tag{3.6}$$

Then the two above-mentioned design criteria can be written as:

$$\Delta = y_B - y_G > 0 \tag{3.7}$$

$$\rho_{composite\ float} < \rho_{solution} \tag{3.8}$$

As displayed in Figure 6, the total length of the float system can generally be written as:

$$L^*_{Total} = L_{LVDT\&Threaded\ Rod} + L_{Cylinder} + x + H_{steel\ weight} \tag{3.9}$$

However, since in this problem $L_{LVDT+PVC\ Rod}$ is considered to be constant, the total length of the float with spherical and conical weights can be rewritten as Eq. (7) and (8) respectively:

$L_{Total} = L_{Cylinder} + x + D_{steel\ weight}$, for spherical weight (3.10)

$L_{Total} = L_{Cylinder} + x + H_{steel\ weight}$, for conical weight (3.11)

The total length of the float (L_{Total}) which is placed inside the solution should be less than the available length ($L_{Allowed}$) in the setup (Figure 5), which can vary depending on the solution level needed in the tower and testing requirement. In this case, the total allowable length was taken as 17 cm.

$$L_{Total} < L_{Allowed} = 17\ cm \tag{3.12}$$

Another important practical parameter that affects the design and also production of the float is the thickness of the hollow cylinder, *t*. Since for float production, some heating process

such as welding is needed (whether the cylinder is made of metal or polymer), the thickness cannot practically be less than a certain value.

The diameter of the tower is 1.275 in (≈32.4 mm). In order to ensure free movement of the float and also avoid sticking issues, the maximum diameter of the hollow composite part was considered about 1 in (25 mm). The minimum allowable thickness of the cylinder determined based on experience to be temperature resistant, since as mentioned earlier, some heating process will also be needed through float manufacturing. The same constraint as cylinder diameter was also applied for steel weight diameter due to space limitation of the setup. The parameter x can range from zero (when the steel ball touches the cylinder) to any positive values (when there is a distance between the cylinder and the steel weight). The allowed length was chosen with some practical considerations as 17cm (Figure 5), which is the distance between water level in the tower and aggregate level in the pot.

3.1.4.2. Kinetic Model Parameters Estimation

In order to facilitate the parameter estimation of the model which involves a curve-fitting process. For this purpose, Least Square Method can be used to find the model parameter. However, in this research, make the modeling process faster and more user-friendly, all the calculations, curve fitting and visualization were implemented in Excel. To do so, based on the following equations, the Sum of Square Error (SSE) between the experimental and modeling results were calculated and then Excel Solver was utilized to find the model parameters by minimizing the SSE.

$$y = \frac{\Delta V_{ASR}}{V_{Aggregate}} \times 100 \quad (3.13)$$

$$\hat{y} = \varepsilon_0 e^{(\frac{\rho}{t-t_0})^{\beta}} \quad (3.14)$$

$$SSE = \sum_1^n (y - \hat{y})^2 \quad (3.15)$$

$$SSE = f(\varepsilon_0, t_{0,} \rho, \beta) \quad (3.16)$$

GRG Nonlinear is one the methods provided in Excel Solver which was used to find the optimum values of the model parameters. GRG Nonlinear Solving Method for nonlinear optimization uses the Generalized Reduced Gradient (GRG2) code, which was developed by Leon Lasdon, University of Texas at Austin, and Alan Waren, Cleveland State University, and enhanced by Frontline Systems, Inc (1998).

At best, the GRG Solving method alone – like virtually all "classical" nonlinear optimization algorithms – can find a *locally optimal* solution to a reasonably *well-scaled,* non-convex model. At times, Solver will stop before finding a locally optimal solution, when it is making very slow progress (the objective function is changing very little from one trial solution to another) or for other reasons.

3.2. Accelerated Mortar Bar Test (AMBT)

This test is a modification of ASTM C 227 for assessing the potential reactivity of aggregates. Aggregates are crushed to meet specific grading requirements. Prepared mortar bars are soaked in 1N NaOH solution at 80°C for 14 days. The purpose of using severe test conditions such as high level of alkalinity and temperature along with crushing aggregate is to accelerate ASR in mortar bars. As a result, expansions of mortar bars are obtained within as little as 16 days. The test method was developed because of the shortcomings of ASTM C 227 and ASTM C 289.

Earlier research indicates that the AMBT method should be used with caution when rejecting aggregates. The test conditions (i.e., 1N NaOH and 80°C) are severe and the test results are unrelated to field performance. Aggregates with a good field track record in terms of ASR can sometimes be classified as reactive when tested according to this method. This is supported by the

observation that some aggregates failed by the AMBT method actually passed by the CPT method (i.e., false negatives). A heterogeneous distribution of reactive constituents within the aggregate is common for certain aggregates (e.g., reactive cementing materials in sandstone, reactive siliceous impurity in limestone, etc.). Losing the reactive phases during crushing and sieving of these aggregates (part of sample preparation in C 1260) sometimes causes aggregates passed by the AMBT but failed by the CPT (i.e., false positives).

ASTM C 1567 utilizes the same testing procedures as ASTM C 1260; however, combinations of Portland cement, SCMs, and a reactive aggregate are used instead of only Portland cement with a reactive aggregate. The cementitious materials are comprised of various proportions of Portland cement, pozzolans and/or ground granulated blast furnace slag (slag) or other SCMs. Pozzolans and slag may be tested in combination or individually to determine the appropriate amount required to reduce expansion to an acceptable level (ASTM C1567, 2008)

In this study, the ASTM standard was followed for mortar bar test with only difference in duration which was extended till 60 days. There are mainly two reasons that the time was extended to 60 days:

1. To better investigate the mortar expansion behavior at longer time, because it is believed that 14 days of testing may not be sufficient to show the real ASR behavior of some aggregates.
2. In order to match the test duration of ACCT and better comparison with the concrete expansion, as well as better time coverage of the mortar and concrete data-driven models.

3.3. Concrete Prism Test (CPT)

The ASTM C 1293 test is considered a more reliable test method than the ASTM C 1260 test as it tests a larger specimen, uses a full scale concrete mixture, and the testing environment is

far less harsh than ASTM C 1260 (ASTM C1567, 2008) This test is generally referred to as the concrete prism test (CPT). In this test, concrete prisms are cast with square cross sections of 3.00 ± 0.03 in. (75.0 ± 0.7 mm) and are 11.25 in. (285 mm) in length. Stainless steel gage studs are cast in both ends of each prism to give an effective gage length of 10.00 ± 0.10 in. (250 ± 2.5 mm). An ASTM C 150 Type I Cement with a 0.9 ± 0.1 Na_2O_{eq} is specified for this test method. Sodium hydroxide solution is added to the mixing water, as specified by ASTM C 1293, to raise the alkali content to 1.25 Na_2O_{eq}. Prisms are demolded after 23.5 ± 0.5h and are measured for an initial reading. Prisms are then stored at 100.4 ± 3.6 °F (38.0 ± 2.0 °C) for a period of 1 year for concrete containing no SCMs (ASTM C1567, 2008). Although the current version of ASTM C 1293 does not cover the use of SCMs within this test method, it is included in the Canadian Standards Society (CSA) Test Method A23.2-28A. The storage length is increased to 2 years for mixtures containing SCMs.[24] Prior to any length change measurements prisms are brought to 73.4 ± 3.6 °F (23 ± 2.0 °C) for 16 ± 4h. Length change measurements are performed at 1, 4, 8, 13, 26, 39 and 52 weeks; additional readings are taken at 78 and 108 weeks for mixtures containing SCMs. (CSA, 2004).

Expansions are recorded to the nearest 0.0001 in. and the average of at least three prisms (often four are cast) for each test is reported to the nearest 0.001%. Expansion criteria, as stated in the non-mandatory appendix of the standard, indicate that a concrete mixture with expansion equal to or greater than 0.04% at one year is to be considered potentially deleteriously reactive. This test method can also be used to determine the efficacy of using SCMs and/or chemical admixtures, namely lithium nitrate, to mitigate deleterious ASR. The expansion limit is retained at 0.04% at 2 years of age for prisms incorporating mitigation measures (CSA, 2004).

3.4. Accelerated Concrete Cylinder Test (ACCT)

ACCT is a new VCMD-based concrete cylinder test developed at Texas A&M transportation Institute (Mukhopadhyay, 2018) that can be done in a relatively short time, i.e. two months. In this procedure, an automatic LVDT-based length change measurement system is used which eliminates the error due to human measurement. The soak solution used in this test is simulated to be close to pore solution, thereby inhibiting the potential alkali leaching. relatively high temperature (60°C) of the test condition reduces the testing time due to faster reaction.

The device used in this study to measure length change of cylindrical concrete specimen over time is the same VCMD that was described earlier. The ACCT test setup is illustrated in Figure 7. A 3×6 inch concrete cylinder with cast-in place threaded rod is placed inside the container (pot). The specimen is then immersed with soak solution of specific alkalinity (equal to or lower than pore solution alkalinity of the specimen). The LVDT rod is connected to the threaded rod attached to the specimen, which moves inside the LVDT during ASR expansion of the specimen and creates electrical signals. These signals are converted to LVDT displacements (inch) through the data acquisition system and recorded by the attached computer through the LabVIEW program.

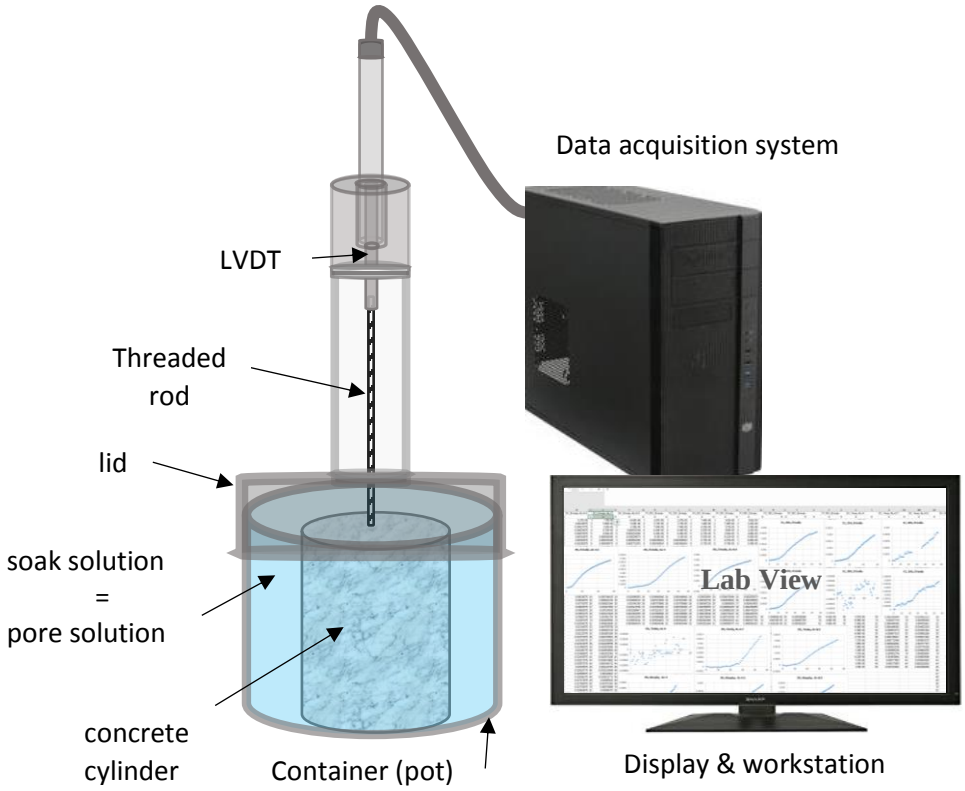

Figure 7. Schematic representation of ACCT test setup

3.5. Materials Characterization

3.5.1. X-ray Diffraction (XRD)

A table top XRD with CuKα radiation was used to determine amorphous content as well as identification and quantification of crystalline phases for the selected fly ashes studied for ASR mitigation in this research. A view of the XRD apparatus is illustrated in Figure 8.

Figure 8. Illustration of XRD apparatus used in the research

Scans were run from 7 to 70 degrees 2θ, with increments of 0.02 degrees and a counting time of 0.4 seconds per step. The identification and quantification of crystalline phases was performed using Rietveld refinement with a TOPAS 5.0 structure analysis program. Amorphous content of each fly ash was determined using the PONKCS method.

3.5.2. X-Ray Fluorescence (XRF)

X-ray fluorescence (XRF) is an analytical technique used to determine the elemental composition of materials. XRF analyzers determine the chemistry of a sample by measuring the fluorescent (or secondary) X-ray emitted from a sample when it is excited by a primary X-ray source. Each of the elements present in a sample produces a set of characteristic fluorescent X-rays that is unique for that specific element, which is why XRF spectroscopy is an excellent technology for qualitative and quantitative analysis of material composition. A view of the XRF machine is illustrated in Figure 9. This techniques was sued mainly in two part of this research: (a) characterization of the alkali solution obtained from VCMD aggregate testing to assess the Na+ concentration, (b) characterization of the pore solution extracted of cement pastes with and without fly ash to determine the Na+ K+ concentrations.

Figure 9. Illustration of XRF apparatus

3.5.3. X-Ray Computing Tomography (CT)

makes use of computer-processed combinations of many X-ray measurements taken from different angles to produce cross-sectional (tomographic) images (virtual "slices") of specific areas of a scanned object, allowing the user to see inside the object without cutting. Digital geometry processing is used to further generate a three-dimensional volume of the inside of the object from a small series of two-dimensional radiographic images taken around a single axis of rotation (Herman, 2009). Industrial CT scanning has been used in many areas of industry for internal inspection of components. Some of the key uses for industrial CT scanning have been flaw detection, failure analysis, metrology, assembly analysis and reverse engineering applications (Flisch et al., 1999). In this research, x-ray CT machine model ZEISS Xradia 520 Versa was used a supporting tool for non-destructive assessment of some of the ASR-affected samples. A view of the x-ray CT machine is illustrated in Figure 10.

Figure 10. Illustration of x-ray CT used in this research

3.5.4. Particle Size Analyzer (PSA)

The fineness test specified in ASTM C618 determine the amount of material retained on a 45-μm sieve, which only provide an overall indication of particle fineness. However, for better comparison and more accurate characterization, a laser particle size analyzer (PSA) was used to determine the particle size distribution (PSD) of the studied fly ashes in this research.

3.5.5. Additive Manufacturing (3D Printing)

In order to make the float used in aggregate reactivity measurement, different materials were investigated in the materials selection step, especially for density and alkali resistance, such as LDPE, PVC, Nylon, polypropylene filament, carbon fiber filament, standard resin, and high temperature resin. Two additive manufacturing techniques using filament and resin were investigated and the floats were 3D printed using the two different techniques and different materials. It was found that the 3D printed float using high temperature resin had the best performance.

4. OPTIMIZATION METHODS AND MACHINE-LEARNING TECHNIQUES

Complex engineering systems typically include multiple variables and rather high uncertainty due to unknown factors, which makes it difficult to find the optimum design to the problem or predicting the behavior of the system. To overcome the former obstacle, optimization techniques can be of huge advantage, which cut down on the time and effort, and help find the optimum practical solution. To handle the latter, machine-learning techniques seem to promising modeling tools to predict the behavior of complex systems, by taking into account different factors and handling the inherent uncertainty involved. ASR is one the complex problems in civil engineering, inflicting serious damages on concrete infrastructures, and has been fully understood despite several years of research. Consequently, optimization methods and machine-learning modeling techniques can be of huge significance to deal with ASR prediction and mitigation as a complex civil engineering problem.

This chapter describes the optimization methods and machine-learning techniques used in this research to investigate ASR. Optimization was mainly used in this study for designing the float to improve the aggregate test setup and subsequent kinetic model. Optimization was also performed to come up with the optimum percentage of each fly ash to control ASR expansion. Comparative study of various machine-learning techniques was also conducted in this study to predict the ASR expansion of mortar bars and concrete cylinder. The basics of the optimization algorithms and machine-learning techniques used in this study are presented in the following.

4.1. Optimization Methods

The main goal of optimization is to either maximize or minimize a property of a given engineering system. Any system that is to be optimized include several decision variables as well as an objective function that is affected by the variables (Rao, 1996). The procedure by which the optimal solutions are found to satisfy an objective function is called optimization method or algorithm (Chonh and Zak, 2008). Optimization algorithms are generally divided into two groups as *deterministic* and *stochastic* algorithms. Stochastic algorithms are preferred for multimodal functions, as they can escape from local minima easily in spite of their slower convergence speed, while deterministic algorithms are better for unimodal functions having one global optimum (Yang, 2010; Noe, 2012). *Heuristic* and *metaheuristic* algorithms are two groups of stochastic algorithms. Algorithms leading to high quality results by trial and error methods in an acceptable computational time are referred to as Heuristic. Higher level of heuristics are called *metaheuristic*, to which most of the new stochastic algorithms are referred (Blum and Roli, 2003; Yang, 2013). Since the metaheuristic algorithms are often derived from nature, they are also called nature-inspired algorithms.

4.1.1. Design of Experiment (DOE)

The design of experiments (DOE, DOX, or experimental design) is the design of any task that aims to describe or explain the variation of information under conditions that are hypothesized to reflect the variation. The term is generally associated with experiments in which the design introduces conditions that directly affect the variation, but may also refer to the design of quasi-experiments, in which natural conditions that influence the variation are selected for observation.

Experimental design involves not only the selection of suitable independent, dependent, and control variables, but planning the delivery of the experiment under statistically optimal conditions, given the constraints of available resources. Main concerns in experimental design include the establishment of validity, reliability, and replicability. For example, these concerns can be partially addressed by carefully choosing the independent variable, reducing the risk of measurement error, and ensuring that the documentation of the method is sufficiently detailed (Teimortashlu et al. 2018). Related concerns include achieving appropriate levels of statistical power and sensitivity.

In order to conduct the design of experiment for ASR expansion through mortar bar test, several experiments were designed to include the main variables such as aggregate activation energy (AE), temperature, fly ash (FA) type, and FA percentage. The flowchart of DOE in this case is depicted in Figure 11.

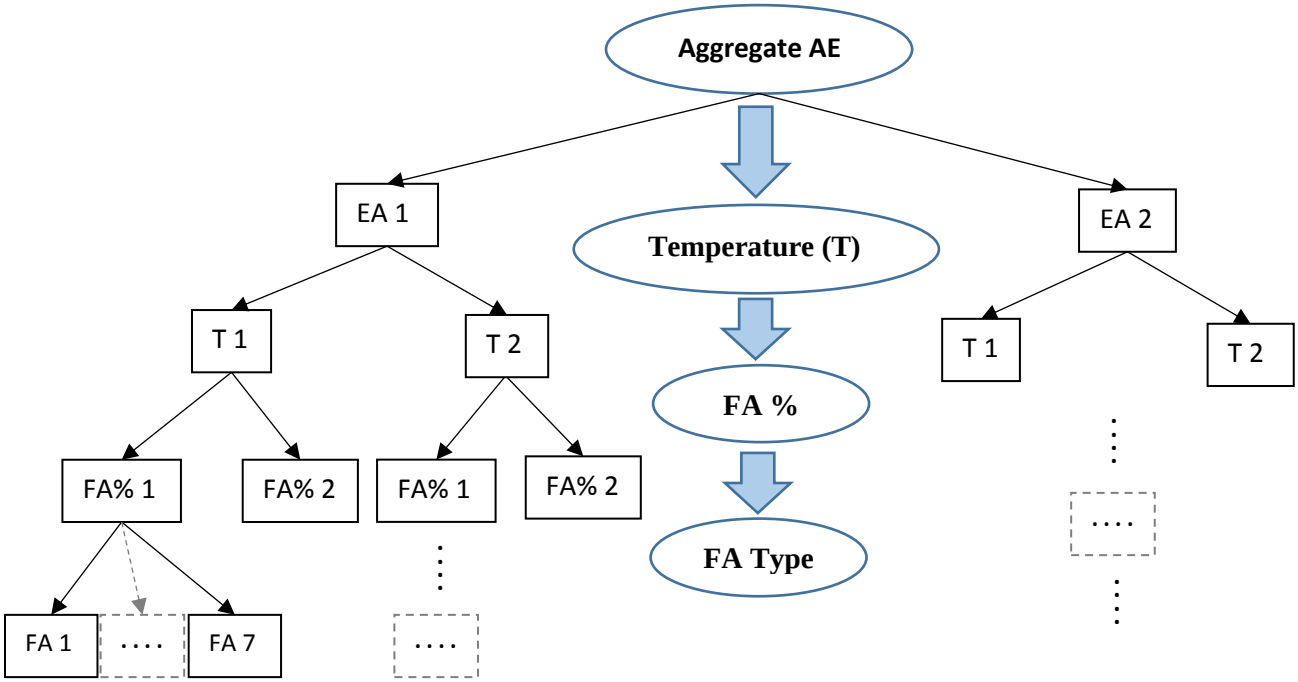

Figure 11. Flowchart of Design of Experiment for AMBT

4.1.2. Classic (Deterministic) Optimization Algorithms

A deterministic algorithm computes a mathematical function; a function has a unique value for any input in its domain, and the algorithm is a process that produces this particular value as output. a deterministic algorithm is an algorithm which, given a particular input, will always produce the same output, with the underlying machine always passing through the same sequence of states. According to some comparative studies, the generalized reduced gradient (GRG) methods and the sequential quadratic programming (SQP) methods are two of the best deterministic local optimization methods (Kao, 1998). GRG Nonlinear provided in Excel Solver is one of the deterministic algorithm that can be used for optimization problems.

The basic steps in a GRG approach is as following (Drud, 1985) :

1. Read the model input
2. Find a feasible solution, x^0. Set the iteration counter *k* to *0*.
3. Compute the Jacobian $J = \partial f / \partial x_b^k$
4. Separate the variables into *n* basic (subscripted by b) and *m-n* non-basic variables (subscripted by n) such that the current basis $J = \partial f / \partial x_b^k$ is nonsingular.
5. Compute the multipliers, $u^T = e_{jb}^T (J_b^k)^{-1}$, and reduced gradient $g_n^T = e_{jn}^T - u^T J_n^k$ (Subscript T denotes transpose, e_j is an m-dimensional unit vector with +1 in position j, and e_{jb} and e_{jn} are the basic and non-basic components of e_j, respectively.)
6. Stop if the current point satisfies the Kuhn-Tucker conditions.
7. Separate the non-basic variables into super-basics, subscripted by s, and fixed non-basic variables.

8. Compute a search direction for the super-basics, d_s, based on g_s, the super-basic part of the reduced gradient, and an estimate of the Hessian of the reduced objective, $H_s = \partial^2 x_j / \partial {x_s}^2$.
9. Perform a one-dimensional search alongd_s. For each step length, Θ, solve $f(x_b, s_s^k, \Theta d_s, x_n^k) = b$ for x_b using $(J_b^k)^{-1}$in a newton-type procedure, and extract the value of the objective.
10. Save the best solution in step 9 at x^{k+1}, set k=k+1, and go to 3.

4.1.3. Metaheuristic (Stochastic) Optimization Algorithms

Stochastic algorithms are preferred for multimodal functions, as they can escape from local minima easily in spite of their slower convergence speed, while deterministic algorithms are better for unimodal functions having one global optimum (Yang, 2010; Noe, 2012).

Heuristic and *metaheuristic* algorithms are two groups of stochastic algorithms. Algorithms leading to high quality results by trial and error methods in an acceptable computational time are referred to as Heuristic. Higher level of heuristics are called *metaheuristic,* to which most of the new stochastic algorithms are referred (Blum and Roli, 2003; Yang, 2013). Since the metaheuristic algorithms are often derived from nature, they are also called nature-inspired algorithms.

4.1.3.1. Genetic Algorithm (GA)

Genetic Algorithms are computer algorithms that search for good solutions to a problem from among a large number of possible solutions. They were proposed and developed in the 1960s by John Holland, his students, and his colleagues (Holland, 1992; Mitchell, 1998). These

computational paradigms were inspired by the mechanics of natural evolution, including survival of the fittest, reproduction, and mutation. These mechanics are well suited to resolve a variety of practical problems, including computational problems, in many fields.

The population is defined to be the collection of all the chromosomes. A generation is the population after a specific number of iterations of the genetic loop. A chromosome is composed of genes, each of which reflects a parameter to be optimized. Therefore, each individual chromosome represents a possible solution to the optimization problem. The dimension of the GA refers to the dimension of the search space which equals the number of genes in each chromosome. Steps of GA can be outlined as following:

1. Start: Randomly generate a population of N chromosomes.

2. Fitness: Calculate the fitness of all chromosomes.

3. Create a new population: a. Selection: According to the selection method select 2 chromosomes from the population. b. Crossover: Perform crossover on the 2 chromosomes selected. c. Mutation: Perform mutation on the chromosomes obtained. Figure 12 a and b demonstrates the crossover and mutation process.

4. Replace: Replace the current population with the new population.

5. Test: Test whether the end condition is satisfied. If so, stop. If not, return the best solution in current population and go to Step 2.

It should be mentioned that scaling and elitism are respectively preprocessing and post processing adjustments to control the algorithm convergence.

The flowchart of the GA steps is presented in Figure 13.

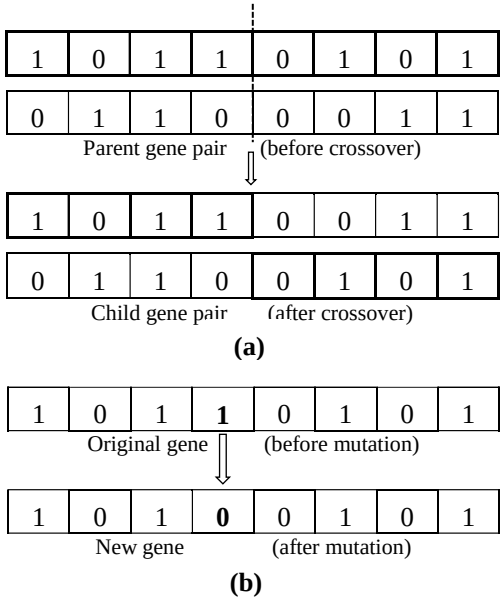

Figure 12. Representation of (a) crossover at a random point and (b) mutation at a single site in GA

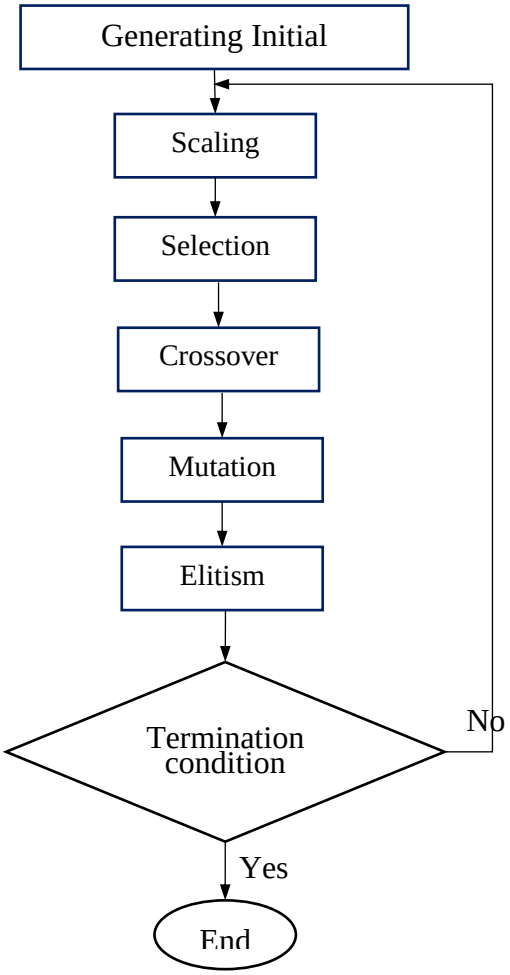

Figure 13. Flowchart of GA steps

4.1.3.2. Particle Swarm Optimization (PSO)

Particle swarm optimization (PSO) is a bio-inspired metaheuristic that was proposed by James Kennedy and Russell Eberhart in 1995. PSO performs a population-based search, using particles to represent potential solutions within the search space. Each particle is characterized by its position, velocity, and a record of its past performance. Initially, the PSO algorithm chooses candidate solutions randomly within the search space. It should be noted that the PSO algorithm has no knowledge of the underlying objective function, and thus has no way of knowing if any of

the candidate solutions are near to or far away from a local or global maximum. The PSO algorithm simply uses the objective function to evaluate its candidate solutions, and operates upon the resultant fitness values.

Each particle maintains its position, composed of the candidate solution and its evaluated fitness, and its velocity. Additionally, it remembers the best fitness value it has achieved thus far during the operation of the algorithm, referred to as the individual best fitness, and the candidate solution that achieved this fitness, referred to as the individual best position or individual best candidate solution. Finally, the PSO algorithm maintains the best fitness value achieved among all particles in the swarm, called the global best fitness, and the candidate solution that achieved this fitness, called the global best position or global best candidate solution. The PSO algorithm consists of just three steps, which are repeated until some stopping condition is met (van den Bergh, 2001):

1. Evaluate the fitness of each particle
2. Update individual and global best fitnesses and positions
3. Update velocity and position of each particle

The velocity and position update step is responsible for the optimization ability of the PSO algorithm. The velocity of each particle in the swarm is updated using the following equation:

$$v_i(t+1) = \omega v_i(t) + c_1 r_1[\hat{x}_i(t) - x_i(t)] + c_2 r_2[g(t) - x_i(t)] \quad (4.1)$$

The index of the particle is represented by *i*. Thus, $v_i(t)$ is the velocity of particle *i* at time t and $x_i(t)$ is the position of particle *i* at time *t*. The parameters ω, c_1, and c_2 ($0 \leq w \leq 1.2$, $0 \leq c_1 \leq 2$, and $0 \leq c_2 \leq 2$) are user-supplied coefficients.

The values r_1 and r_2 ($0 \leq r_1 \leq 1$ and $0 \leq r_2 \leq 1$) are random values regenerated for each velocity update. The value $\hat{x}_i(t)$ is the individual best candidate solution for particle *i* at time *t*,

and $g(t)$ is the swarm's global best candidate solution at time *t*. The first, second, and third terms are called inertia component, cognitive component, and social component respectively. The random values r_1 and r_2 cause stochastic influence on the velocity update, causing each particle to move in a semi-random manner heavily influenced in the directions of the individual best solution of the particle and global best solution of the swarm.

Once the velocity for each particle is calculated, each particle's position is updated by applying the new velocity to the particle's previous position:

$$x_i(t+1) = x_i(t) + v_i(t+1) \tag{4.2}$$

This process is repeated until some stopping condition is met. Some common stopping conditions include: a preset number of iterations of the PSO algorithm, a number of iterations since the last update of the global best candidate solution, or a predefined target fitness value. Pseudo code for PSO is given in Figure 14.

Objective function $f(x)$, $x = (xi, ..., x_p)^T$
Initialize locations *Xi* and velocity *Vi* of *n* particles.
Find g^* from min{ $f(xi), ..., f(x_n)$} (at $t = 0$)
while (criterion)
$t = t + 1$ (pseudo time or iteration counter)
for loop over all *n* particles and all *p* dimensions
Generate new velocity v_i^{t+1}
Calculate new locations $x_i^{t+1} = x_i^t + v_i^{t+1}$
Evaluate objective functions at new locations x_i^{t+1}
Find the current best for each particle $\hat{x}_i$
end for
Find the current global best *g*
end while
Output the final results $\hat{x}_i$ and *g*

Figure 14. Pseudocode of PSO

4.1.3.3. Bat Algorithm (BA)

Bat algorithm was developed by Yang (2010) based on the echolocation characteristics of microbats (Colin, 2000; Richardson, 2008), using the following approximations and simplifying rules:

- Echolocation are used by all bats to sense distance, and they also recognize in some magical way, the difference between background barriers and food/prey.
- To search for pray, bats fly randomly with velocity v_i at position x_i with a fixed frequency f_{min}, with variable wavelength λ and loudness A_0. Depending on the proximity of their target, bats can automatically adjust the wavelength (or frequency) of their emitted pulses, as well as the rate of pulse emission r in the range of **[**0, 1**]**.
- Despite the loudness can vary in many ways, it is assumed that it ranges from a large (positive) A_0 to a minimum constant value A_{min}.

Ray tracing is not included in this algorithm for simplicity, however, it can be an interesting feature for future further extension of the algorithm. Even though it can be computationally extensive, nonetheless it can be of great advantage for computational geometry and some other applications. Besides, a particular frequency is intrinsically linked to a wavelength. For instance, a frequency range of **[**20 kHz, 500 kHz**]** corresponds to a range of wavelengths from 0.7*mm* to 17*mm* in the air. Thus, depending on the ease of implementation and other factors, the change either in terms of frequency 'f' or wavelength 'λ' can be described to suit different applications. Based upon the above-mentioned approximations and idealization, the main steps of the BA in terms of a pseudo code can be summarized as shown in Figure 15.

Objective function $f(x), x = (x_1, \ldots, x_d)^T$

Initialize the bat population x_i $(i = 1,2, \ldots, n)$ *and* v_i

Define pulse frequency f_i *at* x_i

Initialize pulse rates r_i *and the loudness* A_i

while *(t < Max number of iterations)*
Generate new solutions by adjusting frequency and updating velocities and locations/ solutions
if *(rand <ri)*
Select a solution among the best solutions Generate a local solution around the selected best solution
end if
Generate a new solution by flying randomly
if *(rand < Ai & f (xi) < f (x*))*
Accept the new solutions
Increase ri and reduce Ai
end if
*Rank the bats and find the current best x**
end while
post-process results and visualization

Figure 15. Pseudo code of BA

Bat Motion:

In a *d* dimensional search or solution space, a velocity v_i^t and a location x_i^t, at iteration *t*, is associated with ach bat. There exists a current best solution $x*$ among all the existing bats. Hence, the aforementioned three rules can be formulated into the updating equations for x_i^t and velocities v_i^t:

$$f_i = f_{min} + (f_{max} - f_{min})\beta \quad (4.3)$$

$$v_i^t = v_i^{t-1} + (x_i^t - x^*)f_i \quad (4.4)$$

$$x_i^t = x_i^{t-1} + v_i^t \quad (4.5)$$

where, $\beta \epsilon [0, 1]$ is defined as a random vector drawn from a uniform distribution.

x^* is considered here as the current global best location (solution), which is located after comparing all the solutions among all the *n* bats. Since the product $\lambda_i f_i$ is the velocity increment, depending on the domain size of the problem of interest, either f_i or λ_i can be sued to adjust the

velocity change while fixing the other factor λ_i or f_i. In this approach, $f_{min} = 0$ and $f_{max} = 100$ can be used. At firts, a frequency that is drawn uniformly from [f_{min}, f_{max}] is randomly assigned to each bat. Regarding the local search, a new solution for each bat is generated locally using a local random walk, once a solution is selected among the current best solutions:

$$x_{new} = x_{old} + \varepsilon A^t \tag{4.6}$$

where, $\varepsilon \in [-1, 1]$ is a random number, while $A^t \leq \langle A^{t_i} \rangle$ is the average loudness of all the bats at this time step. BA can serve as a frequency-tuning algorithm to provide a balanced combination of exploration and exploitation, i.e. a mechanism for automatic control and auto zooming into the region with promising solutions is provided through the loudness and pulse emission rates.

Variations of loudness and pulse emission:

To vary the loudness A_i and the rate r_i of pulse emission during the iterations is essentially necessary to provide an effective mechanism to control the exploration and exploitation and switch to exploitation stage when necessary. Since the loudness typically decreases once a bat finds its prey, when the rate of pulse emission increases, the loudness can be selected arbitrarily between A_{min} and A_{max}, with the assumption that $A_{min} = 0$ means that a bat has just found the prey and temporarily stops emitting any sound. With these assumptions, we have

$$A_i^{t+1} = \alpha A_i^t,\ r_i^{t+1} = r_i^0[1 - e^{-\gamma t}] \tag{4.7}$$

where, α and γ are constants. Herein, α is basically similar to the cooling factor in simulated annealing. For any $0 < \alpha < 1$ and $\gamma > 0$, we have:

$$A_i^t \to 0,\ r_i^t \to r_i^0,\ as\ t \to \infty \tag{4.8}$$

To simplify the problem, $\alpha = \gamma$ as well as $\alpha = \gamma = 0.9$ can be used in the simulations. The choice of parameters requires some experimenting. Initially, different values of loudness and pulse emission rate should be assigned to each bat, and this can be achieved by randomization. For

instance, the initial loudness A_i^0 can usually be chosen in the range of **[**1, 2**]**, while the initial emission rate r_i^0 can be chosen around zero, or any value $r_i^0 \in [0, 1]$, provided that the equation (4.7) is used. The loudness and emission rates will be updated only if the new solutions are improved, indicating the fact that these bats are moving towards the optimal solution.

4.1.3.4. Cuckoo Search (CS) Algorithm

Cuckoo search (CS) is a nature-inspired which is categorized as an evolutionary or meta-heuristic algorithm. It was derived based on the breed behavior of certain cuckoo species. Hence, the description of this natural behavior of the bird is briefly presented in the following to help better understand the basics upon which the algorithm is developed.

Cuckoo breeding behavior:

Cuckoos are interesting birds due to beautiful sounds they can make, but more importantly because of their special reproduction plan. Some species such as the *ani* and *guira* choose to lay their eggs in communal nests, but to boost the hatching chance of their own eggs, they may remove others' eggs in order (Yang and Deb, 2009). The obligate brood parasitism is employed by some species through laying their eggs in the nests of other host birds (often other species). There exist three main types of brood parasitism including nest takeover, intraspecific brood parasitism, and cooperative breeding. Some host birds may choose to adopt direct conflict with the intruding cuckoos. Should a host bird finds out that the eggs are not its own, it will either simply abandon its nest and build a new nest elsewhere, or throw the alien eggs away. In some other species, namely the new world brood-parasitic *Tapera*, female parasitic cuckoos are often very skillful in the mimicry in pattern and color of the eggs of a few selected host species (Payne et al., 2005).

Hence, the chance of their eggs being abandoned is reduced, thereby leading to their higher chance of reproducibility.

Moreover, the timing of egg-laying of some cuckoo species is also stunning. Parasitic species typically target a nest where the host bird just laid its eggs. The cuckoo eggs typically hatch a little earlier than their host eggs. The first instinctive action that the newly hatched cuckoo chick will take is blindly propelling the eggs out of the nest to evict the host eggs. In this way, the share of food provided by its host bird for cuckoo chick's is increased (Payne et al., 2005). Studies also indicate that to acquire more feeding opportunity, a cuckoo chick can also mimic the call of host chicks.

Lévy flights:

Animals seek for food in a random or quasi-random way in nature. Generally, a random walk is an effective foraging path of an animal, because the next move is determined based on the current location/state and the transition probability to the next location. The chosen direction depends implicitly on a probability that can be modeled mathematically. For instance, it has been shown by various studies that the flight behavior of many animals and insects has demonstrated the typical characteristics of Lévy flights (Brown et al, 2007; Pavlyukevich, 2007; Yang, 2009).

Reynolds and Frye (2007) have shown that Drosophila melanogaster or fruit flies search their landscape using a series of straight flight paths punctuated by a sudden 90^{o} turn, leading to a Lévy-flight-style intermittent scale-free search pattern. Human behavior studies such as the Ju/'hoansi hunter-gatherer foraging patterns also indicate the typical feature of Lévy flights. Even light can be related to Lévy flights (Barthelemy et al., 2008). Therefore, such behavior has been

employed in optimization, and its promising potential have been reflected in the preliminary results obtained by researchers (Shlesinger 2006, Yang 2010).

Cuckoo search:

To simplify the CS approach, the following three idealized rules can be used as:

• Each cuckoo lays one egg at a time, and puts it in a randomly chosen nest.

• The best nests containing the high-quality eggs (solutions) will carry over to the next generations.

• There are a fixed number of available host nests, and a host can discover an alien egg with a probability $P_a \in [0, 1]$. In this case, the egg can be thrown away by the host or the host can abandon the nest so as to build a new nest in a new location.

Based on the above-mentioned rules, the pseudo code for CS is given in Figure 16.

begin
Objective function f(**x**), **x** = (x_1, ..., x_d)^T
Generate initial population of n *host nests* $\mathbf{x}_i$ (i = 1, 2, ..., n)
while *(*t <*Max Generation) or (stop criterion)*
Get a cuckoo randomly by L´evy flights
evaluate its quality/fitness F_i
Choose a nest among n *(say,* j*) randomly*
if *(*F_i > F_j*),*
replace j *by the new solution;*
end
A fraction (p_a*) of worse nests are abandoned and new ones are built;*
Keep the best solutions (or nests with quality solutions);
Rank the solutions and find the current best
end while
Post process results and visualization
end

Figure 16. Pseudo code of Cuckoo Search algorithm

For simplicity, a fraction P_a of the *n* nests being replaced by new nests can be used to approximate the last assumption (with new random solutions at new locations). If maximization is of interest, the quality or fitness of a solution can simply be considered as the objective function. Other forms of fitness can also be defined in a similar way to the fitness function in GA. According to the three rules, the main steps of the CS algorithm can be formulated as follows:

A Le´vy flight is performed when generating new solutions $x^{(t+1)}$ for cuckoo i,

$$x_i^{(x+1)} = x_i^{(x)} + \alpha \oplus \text{Lévy}(\lambda) \quad (4.9)$$

where, $\alpha > 0$ is the step size based the scales of the problem of interest. In most cases, $\alpha = 1$ can be used. The product $\oplus$ means entry-wise multiplications. Le´vy flights essentially generate a random walk, with the random steps being drawn from a Le´vy distribution for large steps:

$$Lévy \sim u = t^{-\lambda}, (1 < \lambda \leq 3) \quad (4.10)$$

The Le´vy distribution has an infinite variance with an infinite mean. The consecutive jumps/steps of a cuckoo herein create a random walk, which obeys a power-law step-length distribution with a heavy tail.

4.2. Machine-Learning Techniques

4.2.1. Artificial Neural Network (ANN)

As is almost widely known today, artificial neural networks (ANNs) are computer models that simulate the basics of biological nervous system. They can, in other words, be described as parallelly distributed processors with capability of storing experimental data and information, and making it available for future applications (Haykin, 2000). ANN has been successfully used as a powerful predictive model in several engineering applications (Jodaei et al. 2012, Jodaei et al.

2013, Jalal and Ramezanianpour 2012, Garmsiri and Jalal 2014, Jalal 2015, Fathi et al. 2015, Jalal et al. 2019). The structure of ANN model as well as its information processing unit are considered to be the main components of the model. Components of an artificial neuron are presented in Figure 17. As can be seen form the figure, an artificial neuron is made of five main parts, namely inputs, weights, sum function, activation or transfer function, and outputs.

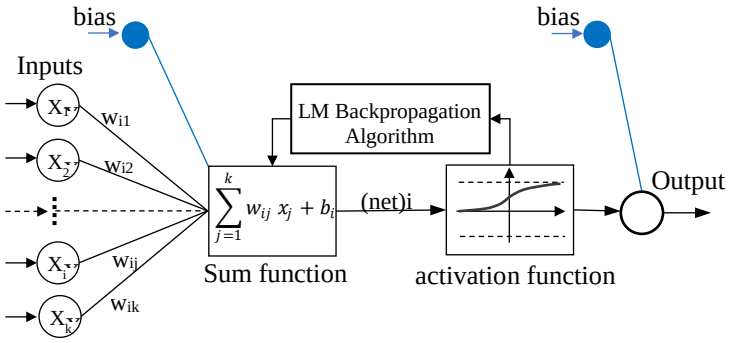

Figure 17. Components of an artificial neuron used in this study

Inputs x_1; x_2; … ; x_j enter each neuron with a weight w_{ij} corresponding to the *connection* strength for that input and the neuron (Guzelbey, 2006).

A bias b_i can be defined as a type of connection weight with a constant nonzero value which is added to the summation of inputs and corresponding weights. The weighted sums of input components (variables) are calculated using the following equation:

$$(net)_i = \sum_{j=1}^{k} w_{ij}\, x_j + b_i \qquad (4.11)$$

Then, the summation of $(net)_i$ is transformed by "activation or transfer function", $f(net_i)$, which yields the neuron output, given by the following equation:

$$Y_i = f(net_i) \qquad (4.12)$$

The significance of activation functions is that they can introduce nonlinearity into artificial neural networks, which makes them very powerful. In general, two type of activation functions are used in multilayer feed forward models, namely logarithmic and tangent sigmoid which give the outputs in (0,1) and (-1,1), respectively. They are preferred due to being continuous functions, and thereby their derivatives can be easily determined with respect to the parameters within $(net)_j$ variable (Liu, 2002).

Some factors that the neural networks are commonly characterized by are network topology and training or learning algorithms. The back propagation neural network (BPNN) is a supervised training algorithm which is based on weight correction procedure consisting of forward pass and backward pass (Rumelhart et al.,, 1986). The weights are randomly initialized in the former and are updated in the later too minimize the error between the network output and the target values (Anderson 1983, Hopfield, 1982). Back propagation is the most widely used learning algorithm due to its simplicity and applicability. The main steps of the BPNN can be formulated as following (Guzelbey et al., 2008):

$$X_i \xrightarrow{BPNN} = Y_i \tag{4.13}$$

where, *X* is the input vector and *Y* is the output vector.

The difference between the network output (δ_j^{last}) and the target value (Y_i) is calculated as the error of the output layer:

$$\delta_j^{last} = (Y_i - out_j^{last}) out_j^{last} (1 - out_j^{last}) \tag{4.14}$$

The weight correction can be done as following:

$$\Delta w_{ji}^{l} = w_{ji}^{l(new)} - w_{ji}^{l(old)} \tag{4.15}$$

By combining Eqs. (8) and (9), the weight correction in hidden layer can be written as following:

$$\Delta w_{ji}^{l} = \eta\left(\sum_{k=1}^{r} \delta_{k}^{l+1} w_{kj}^{l+1} out_{j}^{l}(1 - out_{j}^{l}) out_{i}^{l-1}\right) + \mu \Delta w_{ji}^{l(previous)} \quad (4.16)$$

which can be expressed in a short form as:

$$\Delta w_{ji}^{l} = \eta \delta_{j}^{l} out_{i}^{l-1} + \mu \Delta w_{ji}^{l(previous)} \quad (4.17)$$

where, μ is the momentum and η is the learning rate.

Levenberg-Marquardt back propagation (LMBP) is known to be a very time-efficient supervised algorithm, which is highly recommended (Suratgar , 2005), and hence was used in this study. Figure 18 shows the pseudo-code for standard LMBP training process.

1. Initialize the weights and parameter μ (μ=0.01 is appropriate)
2. Compute the sum of square errors over all inputs F(w)
   $F(w)=e^{T}e$
   where $w=[w_1, w_2, \ldots, w_n]$ consists of all weights of the network, e is the error vector comprising the error for all the training examples.
3. Solve the above equation to obtain the increment of weight Δw
   $\Delta w = [J^{t}J + \mu I]^{-1} J^{T} e$
   where J is the Jacobian matrix, μ is the learning rate which is to be updated using β depending on the outcome. In particular, μ is multiplied by decay rate β (0< β<1).
4. Using w+Δw as the trail w, and judge
   If trial F(w)<F(w) instep 2 THEN
   W=w+Δw
   μ= μ.β (β=0.1)
   go back to step 2
   ELSE
   μ= μ/β
   go back to step 4
   END IF

Figure 18. Pseudo-code for LMBP algorithm (Suratgar , 2005)

4.2.2. Genetic Programming (GP)

Genetic programming (GP) proposed by Koza (1992) is actually built based on Genetic Algorithms (GA) basics (Holland 1975, Goldberg, 1989).

GP is defined as a problem-solving method which is domain-independent. Computer programs are evolved in GP to find a solution, or approximate solution to the problems based on the Darwinian principle of reproduction and survival of the fittest and analogs of naturally occurring genetic operations such as *crossover* and *mutation* (Koza 1992). The main difference between GP and a GA is the representation of the solution. GA creates a string of numbers that represent the solution, while GP creates solutions in terms of computer programs that are represented as tree structures and expressed in a functional programming language (Koza 1992). GP optimizes a population of computer programs according to their fitness that is calculated through a fitness function. Hence, GP optimizes the fitness function as the objective function.

GP reproduces computer programs to solve problems by executing the following steps:

1. Generation of an initial population of functions and terminals of the problem (computer programs).

2. Execution of each program in the population and assigning fitness, respectively.

3. Repeating step 2 for new computer programs.

4. Selecting the best existing program which is presented as the result of genetic programming (Koza, 1992).

A population member in tree-based GP is a hierarchically structured tree comprising functions and terminals, an example of which is presented in Figure 19.

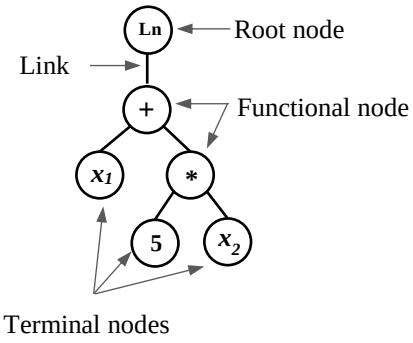

Figure 19. Tree representation of GP model *Ln* (x_1+5x_2).

Once a random population of models has been generated, the individuals are evaluated and selected for reproduction by GP. Afterwards, new individuals are generated and then the new generation is created (Koza 1992, Jalal et al., 2013). New individuals are created using mutation, crossover and direct reproduction. During this operation, a point on a branch of each program is selected at random and the set of terminals and/or functions from each program are then swapped to create two new programs. During the mutation process, a function or terminal from a model is occasionally selected at random and is mutated. A typical crossover and mutation operations are illustrated in Figure 20. Finally, the best program generated in any generation defines the output of the GP algorithm.

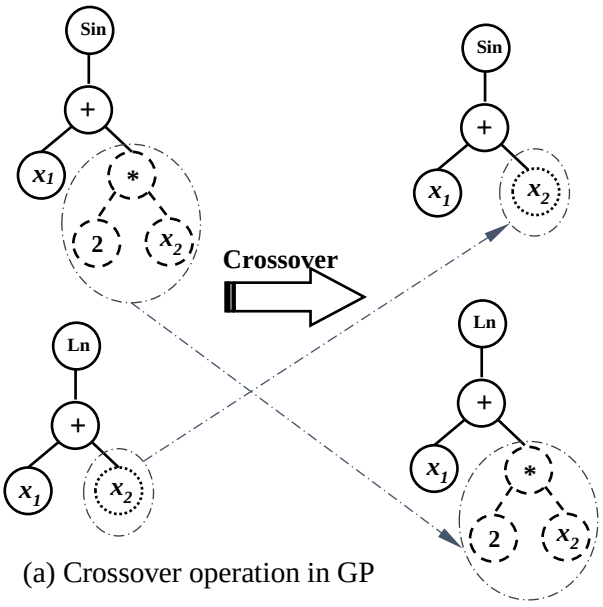

(a) Crossover operation in GP

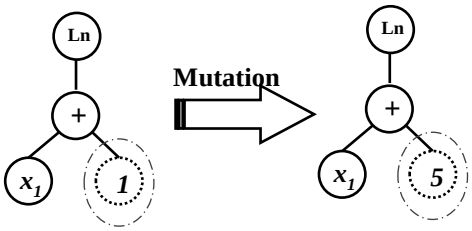

(b) Mutation operation in GP

Figure 20. A typical crossover and mutation operations in GP

GEP:

Gene expression programing (GEP) is a natural development of GAs and GP that was first invented by Ferreira (2001). GEP uses the same kind of diagram representation of GP with minor changes, providing new and efficient solutions to evolutionary computation (Ferreira, 2001). The great insight of GEP includes the invention of chromosomes capable of representing any expression tree. The new language created in GEP (Karva language or K-expression) allows reading and expressing the GEP chromosomes. Besides, the structural and functional organization of GEP genes and their interplay with expression trees (ETs), always guarantees the production of valid programs.

Five main steps are included in GEP, namely (1) fitness function, (2) terminals (T) and functions (F) sets, (3) chromosome architecture, (4) linking function, (4), and (5) genetic operators. Figure 21 displays the general flowchart of GEP algorithm.

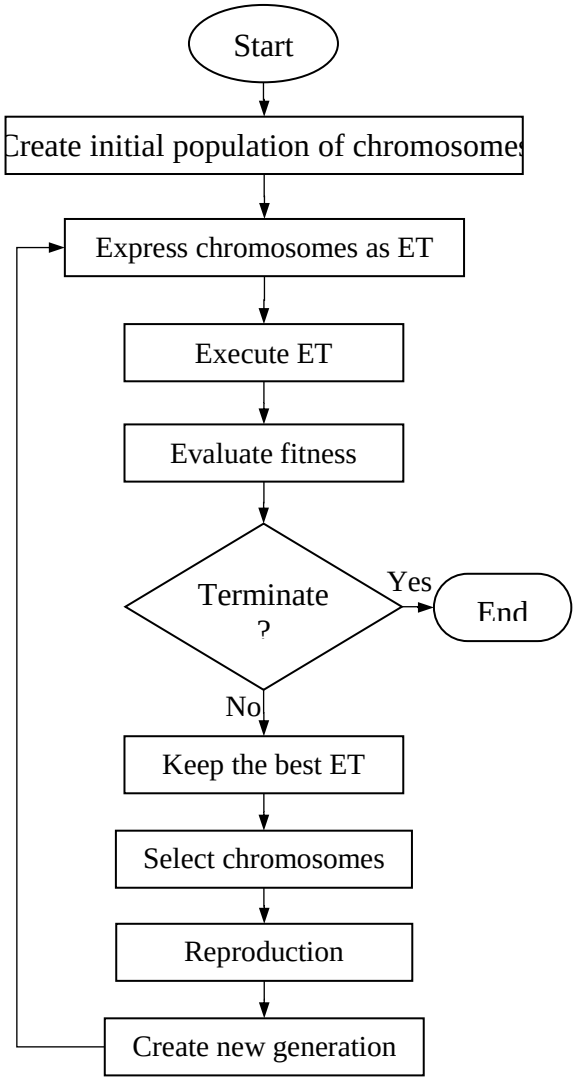

Figure 21. General Flowchart of GP algorithm

Each individual program i has a fitness function fi which is expressed as below:

$$f_i = \sum_{j=1}^{C_t}(M - \left|C_{(i,j)} - T_j\right|) \quad (4.18)$$

where, M is the range of selection, $C(i,j)$ the value returned by the individual chromosome i for fitness case j (out of Ct fitness cases) and Tj is the target value for fitness case j. This kind of fitness function has the advantage of finding the optimal solution for itself. Nevertheless, some other fitness functions can be found that suitable for different types of problems (Ferreira, 2002). The function sets can consist mathematical operations such as $F=\{-,+,*,/\}$, while the terminal sets can contain variables and constants such as $T=\{x1,x2,5\}$. Selection is made on chromosome architecture, which means selection of head sizes and the number of genes. In order to represent the solution, GEP utilizes fixed-length strings which in contrast to the conventional GP. These strings are then expressed in the form of parse trees of various shapes and sizes which are called expression trees (ETs). At the end, the sub ETs are linked though the linking functions including addition, subtraction, division, and multiplication (Ferreira, 2001). One advantage of GEP is that the genetic diversity creation is simplified to a great extent, due to the fact that genetic operators work at the chromosome level. Besides, distinctive multi-genic nature of GEP allowing the evolution of more complex programs containing several subprograms is another strength of GEP method.

The chromosome architectures of the models evolved by GEP include head size and number of genes. The head size determines the complexity of each term in the evolved model. The number of genes per chromosome governs the number of terms in the model. Each gene codes for a different sub-expression tree or sub-ET. To guarantee the validity of a randomly selected genome, GEP employs a head–tail method. Each GEP gene is composed of a head and a tail. The head may contain both function and terminal symbols, whereas the tail may contain terminal symbols only (Ferreira 2001, Baykasoglu 2008). Figure 22a, b, and c respectively represent an example including a chromosome with two fixed-length genes of 10 characters along with the K-

expression, the expression tree (ET), and the mathematical expression. GEP as one of the machine-learning techniques has been applied in different areas of engineering and has proved to be a promising predictive tool (Jalal et al. 2013, Goharzay et al. 2017).

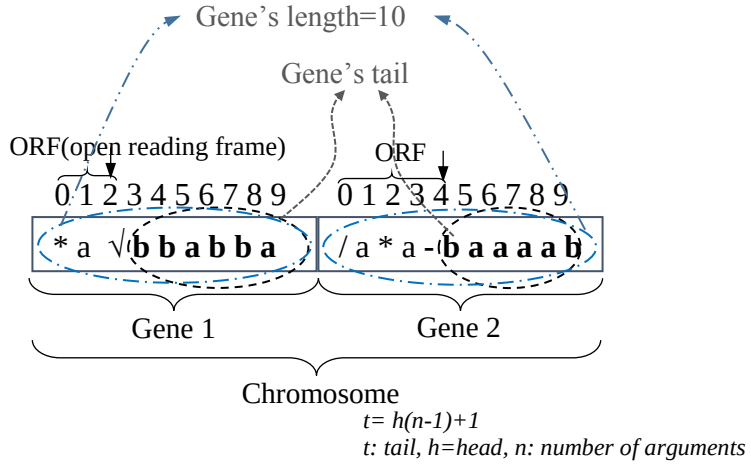

(a) Genetic structure and K- expression

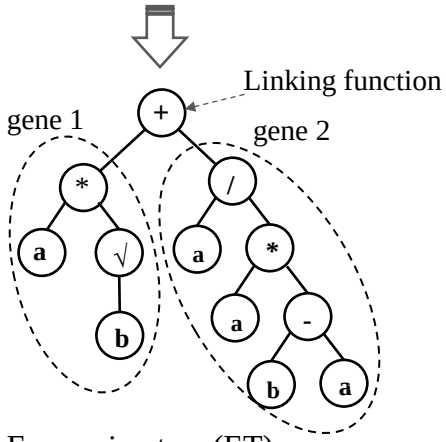

(b) Expression tree (ET)

$$(a \times \sqrt{b} + \frac{a}{a * (b - a)})$$

(c) Mathematical expression

Figure 22. Representation of (a) a chromosome with two fixed-length genes of 10 characters, (b) the expression tree (ET), and (c) the mathematical expression

4.2.3. Adaptive Neuro-Fuzzy Inference System (ANFIS)

In contrast to mathematical models, a fuzzy inference system with if-then rules is able to simulate the qualitative features that occur in human reasoning processes. However, it does not have a standard design procedure to quantify the features accurately (Walia 2015). Neural networks are able to recognize the patterns of the data, capture the relationships, and mimic the trends, which makes them able to predict the results of new combinations of data. When integrated though, the synergic benefit of both approaches can be made available to build a robust, intelligent system. With this respect, the combination of fuzzy logic and neural networks has led to a system lately that is called neuro-fuzzy. In this way, one single system imparts the advantages of fuzzy logic and ANN (Pramanik and Kumar 2009, Jalal et al. 2019). In fact, the adaptive neuro-fuzzy inference system (ANFIS) can be considered a neural network built upon a fuzzy inference system.

ANFIS is a well-known hybrid neuro-fuzzy network that can be used to model the complex systems (Jang 1993; Jang and Sun 1995). By using a set of if-then fuzzy rules, ANFIS is able to mimic a human-like reasoning style by exploiting a linguistic model and fuzzy sets. Being universal approximators with the capability of using if-then rules, is the main significance of ANFIS models (Topcu and Sarıdemir, 2008).

The architecture of an ANFIS model with two input variables is shown in Figure 23, assuming two if-then rules for fuzzy mechanism of Sugeno type, we will have the following for the ANFIS reasoning:

Rule 1: IF x is A_1 and y is B_1, THEN $f_1=p_1x+q_1y+r_1$

Rule 2: IF x is A_2 and y is B_2, THEN $f_2=p_2x+q_2y+r_2$

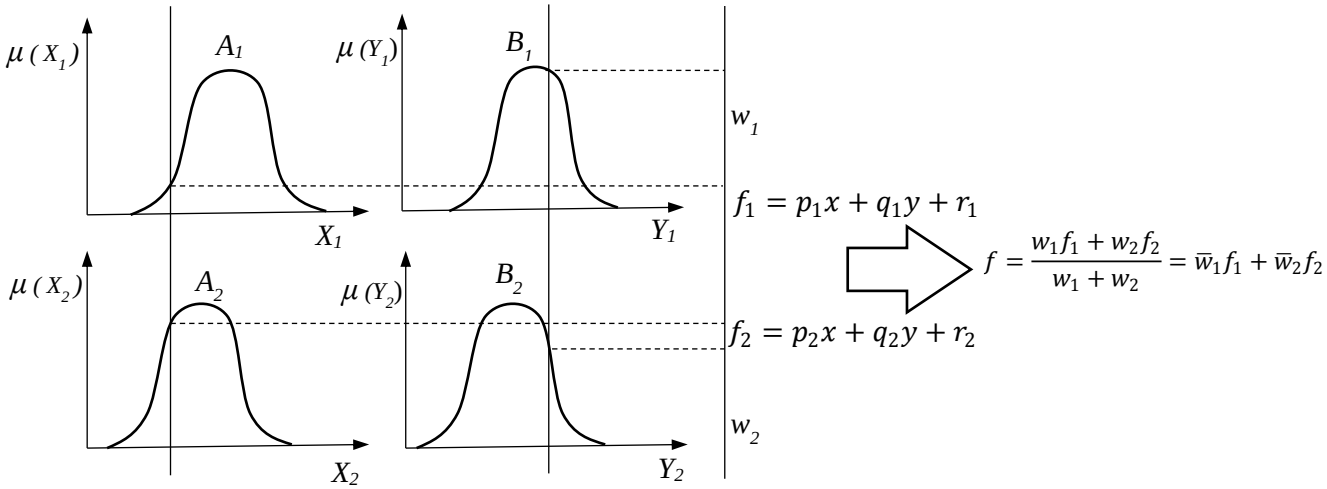

Figure 23. The Reasoning scheme of ANFIS

The ANFIS architecture corresponding to the reasoning system provided in Figure 23 is illustrated in Figure 24, for which each layer can be described as follows:

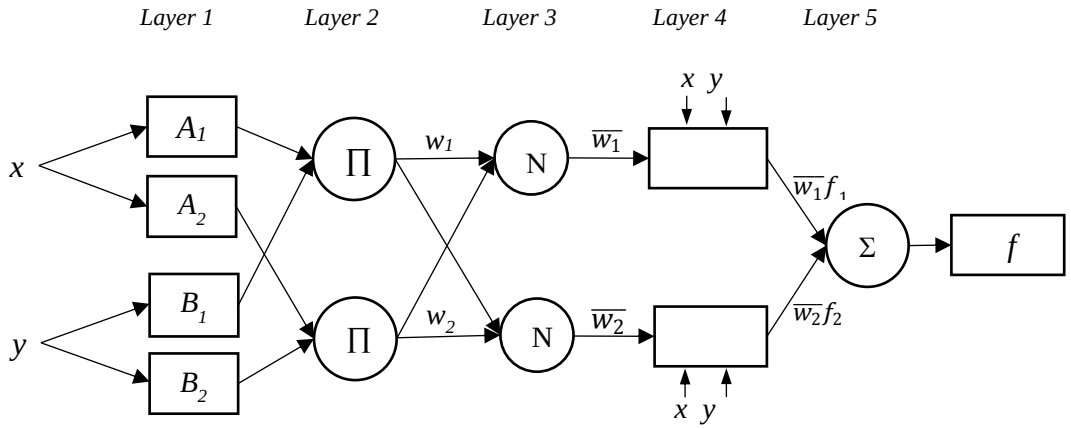

Figure 24. Schematic of ANFIS architecture

Layer 1) Every node *i* in this layer is a square node with a node function:

$$Q_i^1 = \mu_{A_i}(x) \tag{4.19}$$

where *x* is the input to node *i*, and A_i is the linguistic label (fuzzy sets: small, large, …) associated with this node function. Premise parameters change the shape of the membership function.

Layer 2) Every node in this layer is a circle node labeled ∏ which multiplies the incoming signals and sends the product out. For instance, ∏-norm operation:

$$Q_i^2 = \mu_{A_i}(x) \times \mu_{B_i}(y), i = 1, 2 \quad (4.20)$$

Layer 3) Every node in this layer is a circle node labeled *N*, representing the normalized firing strength of each rule. The *i*th node calculates the ratio of the *i*th rule's firing weight to the sum of all rule's firing weights. The outputs of this layer are called normalized firing strengths.

$$Q_i^3 = \overline{w}_i = \frac{w_i}{w_1 + w_2}, i = 1, 2 \quad (4.21)$$

Layer 4) Every node in this layer is an adaptive node with a node function, indicating the contribution of the *i*th rule towards the overall output.

$$Q_i^4 = \overline{w}_i f_i = \overline{w}_i (p_i x + q_i y + r_i), i = 1, 2 \quad (4.22)$$

where $\overline{w}_i$ is the output of layer 3, and {pi, qi, ri} is the parameter set.

Layer 5) The signal node in this layer is a circle node labeled ∑, indicating the overall output as the summation of all incoming signals calculated, i.e.

$$Q_i^5 = \sum_i \overline{w}_i f_i = \frac{\sum_i w_i f_i}{\sum_i w_i} \quad (4.23)$$

ANFIS includes a rapid learning method named hybrid-learning which utilizes the gradient descent and the least-squares method to find a feasible set of antecedent and consequent parameters (Jang and Sun, 1993, Topcu and Sarıdemir 2008). Thus, in this paper, the latter method was used to build the prediction model.

5. EXPERIMENTAL RESULTS

This chapter presents all the experimental results from ASR tests on aggregates, mortar bars, and concrete cylinders. Aggregates test results include VCMD test results, calculations of compound activation energy though old and new methods, and XRF results from the aggregate solution. Mortar results include the AMBT results obtained from 144 mortar specimens at different temperature, aggregate reactivity, FA types, and FA percentage. ACCT results conducted on various mixes similar to those of mortar bars are also presented and the effect of FA type and percentage is investigated. Besides, cement paste pore solution extraction results and analysis are also presented herein.

5.1. Aggregate Test Results

5.1.1. VCMD test and CAE Results

VCMD was conducted on 10 types of new aggregates with different reactivity in order to determine their compound activation energy (CAE) or composite activation parameter (CAP). The test was implemented as described in chapter 3. Presented in Figure 25. are the results of the model fitting to the experimental data for parameter estimation using the old and modified (new) methods. The comparative plots of the other aggregates are presented in Appendix A.

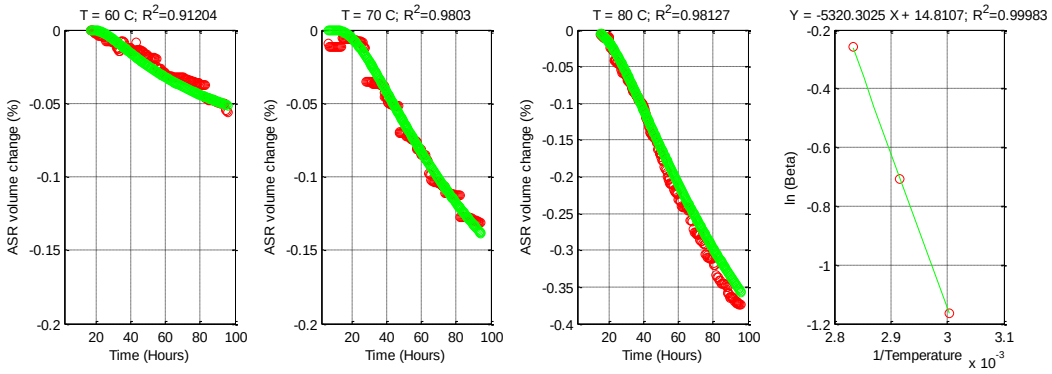

(a)

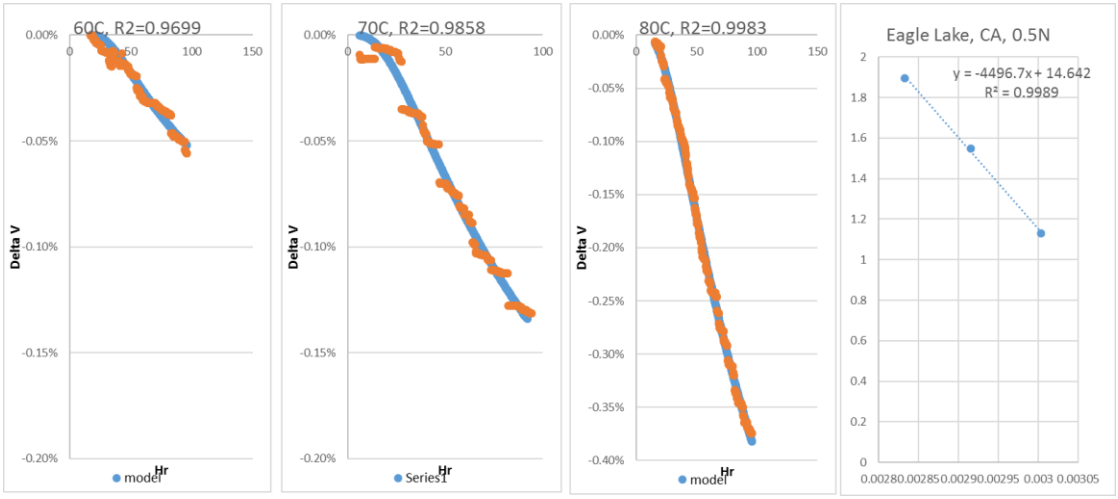

(b)

Figure 25. Model/experiment curve fitting for parameter estimation of the model for CA4 at 0.5N using (a) old procedure in MATLAB, (b) new procedure in Excel

Once VCMD was conducted on 10 types of aggregates and activation energies were calculated, threshold alkalinity was also determined for all of the aggregates. The results of CAE and threshold alkalinity of the aggregates obtained by the old and modified methods, along with the expansion results of AMBT (1260) and CPT (1293) are reported in Table 2.

Table 2. Aggregate CAE results and comparison with standards

			Old method				Modified (new method)			
Type	**1260**	**1293**	**0.5N Ea**	**1N Ea**	**THA**	**Alkali loading**	**0.5N Ea**	**1N Ea**	**THA**	**Alkali loading**
FA1	0.269	-	46.34	22.910	0.49	3.8	28.9	18.03	0.38	3.3
FA2	0.241	-	41.01	21.680	0.46	3.7	25.8	15.41	0.36	3.2
FA3	0.182	-	40.57	27.290	0.45	3.6	34.5	10.52	0.44	3.6
CA1	0.031	0.155	34.07	23.160	0.40	3.4	34.3	20.16	0.42	3.5
CA2	0.040	0.082	38.83	10.880	0.45	3.6	30.7	20.84	0.38	3.3
CA3	0.046	0.091	48.66	25.900	0.50	3.9	33.9	16.99	0.42	3.5
CA4	0.024	0.129	44.23	24.360	0.47	3.7	37.4	10.05	0.46	3.7
CA5	0.062	0.092	38.39	25.780	0.44	3.6	27.8	15.19	0.39	3.3

5.1.2. XRF Results from Aggregate Soak Solution

This test is intended to quantify the Na+ concentration change in the solution after aggregate- solution test through XRF technique. The original solutions used in the aggregate-solution tests are 1N and 0.5N, the theoretical concentration of which are 24000 and 12000 ppm respectively.

For this purpose, an attempt was made to compare and find any correlation between the Na+ concentrations change and other possibly effective parameters which are assumed to be involved in ASR phenomenon.

a. Concentration change at different temperatures:

- A clear trend of concentration change (%) by temperature cannot be found in Figure 26. However, by comparing 60C and 80C for instance, it can be said that for both cases of 0.5N and 1N, in 6 cases out of 10, the concentration change is higher for 80C.
- COVs of the 0.5N and 1N solutions are 5.14 and 4.96 respectively which can be rounded to 5. The average COV of all aggregates tested in 0.5N and 1N solutions are 13.06 and 12.91 which can be taken as 13. If average COV of standard solutions (5) is subtracted from COV of all solutions (13), the results would be 8 which is less than 10. In this way, it can be said that generally the COVs can be acceptable.

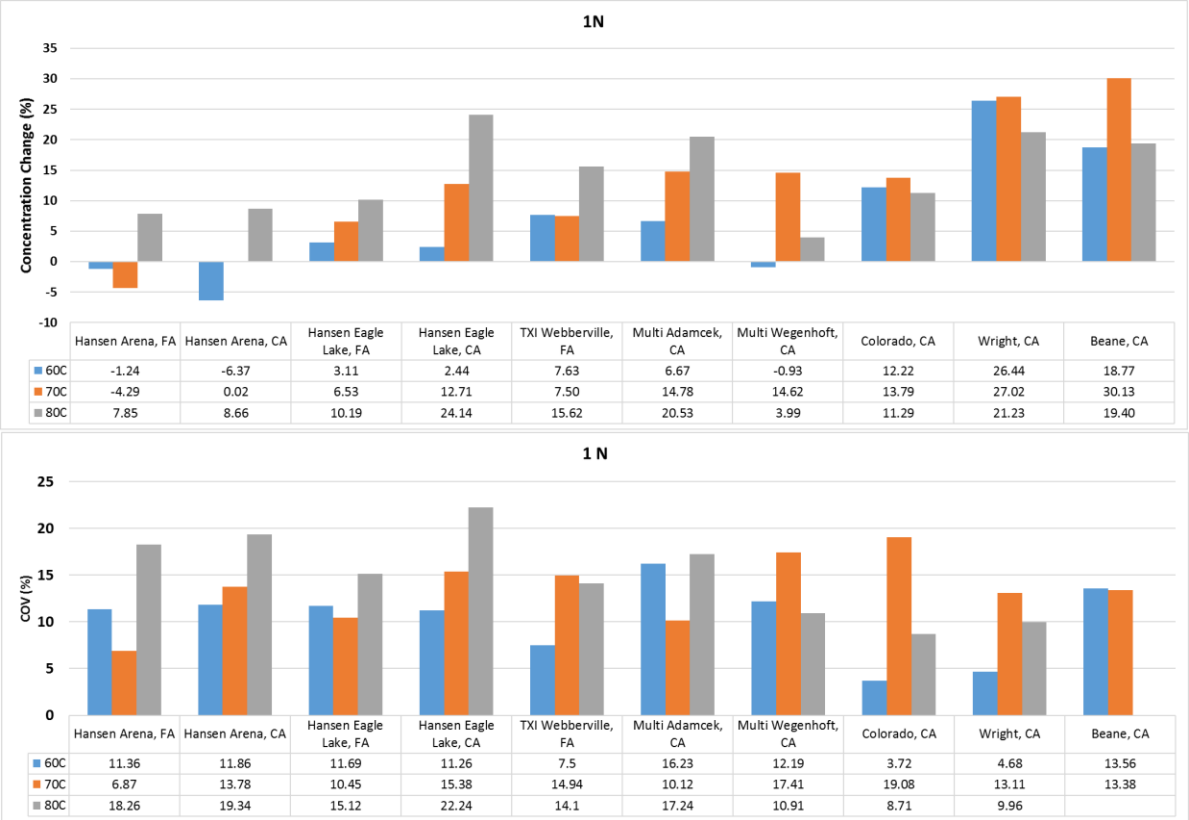

(a)

Figure 26. Variations of Na concentration change percentage of soak solution in VCMD test at different temperatures for different aggregates: (a) at 0.5N, and (b) at 1N

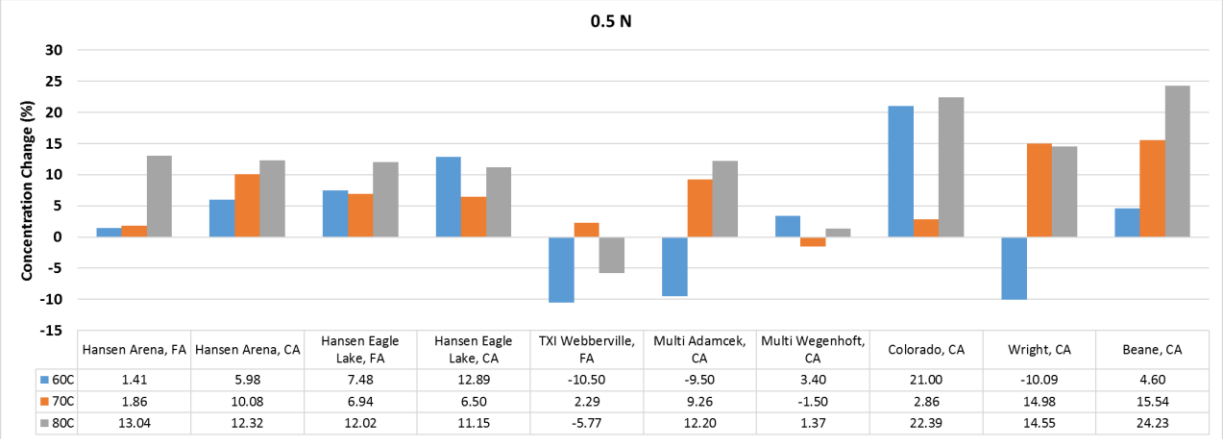

	Hansen Arena, FA	Hansen Arena, CA	Hansen Eagle Lake, FA	Hansen Eagle Lake, CA	TXI Webberville, FA	Multi Adamcek, CA	Multi Wegenhoft, CA	Colorado, CA	Wright, CA	Beane, CA
60C	1.41	5.98	7.48	12.89	-10.50	-9.50	3.40	21.00	-10.09	4.60
70C	1.86	10.08	6.94	6.50	2.29	9.26	-1.50	2.86	14.98	15.54
80C	13.04	12.32	12.02	11.15	-5.77	12.20	1.37	22.39	14.55	24.23

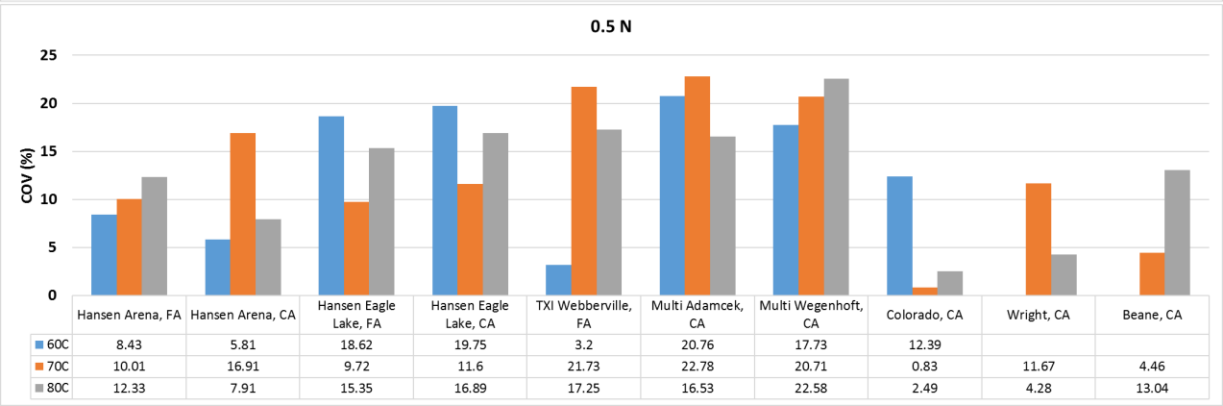

	Hansen Arena, FA	Hansen Arena, CA	Hansen Eagle Lake, FA	Hansen Eagle Lake, CA	TXI Webberville, FA	Multi Adamcek, CA	Multi Wegenhoft, CA	Colorado, CA	Wright, CA	Beane, CA
60C	8.43	5.81	18.62	19.75	3.2	20.76	17.73	12.39		
70C	10.01	16.91	9.72	11.6	21.73	22.78	20.71	0.83	11.67	4.46
80C	12.33	7.91	15.35	16.89	17.25	16.53	22.58	2.49	4.28	13.04

(b)

Figure 26 Continued.

b. Na Concentration change at different temperatures:

- Since the theoretical XRF values for 0.5N and 1N are 12000 and 24000 respectively, all results were scaled accordingly, as presented in Figure 27.
- Based on the results, concentration reduction occurred in more than 70% of the cases.

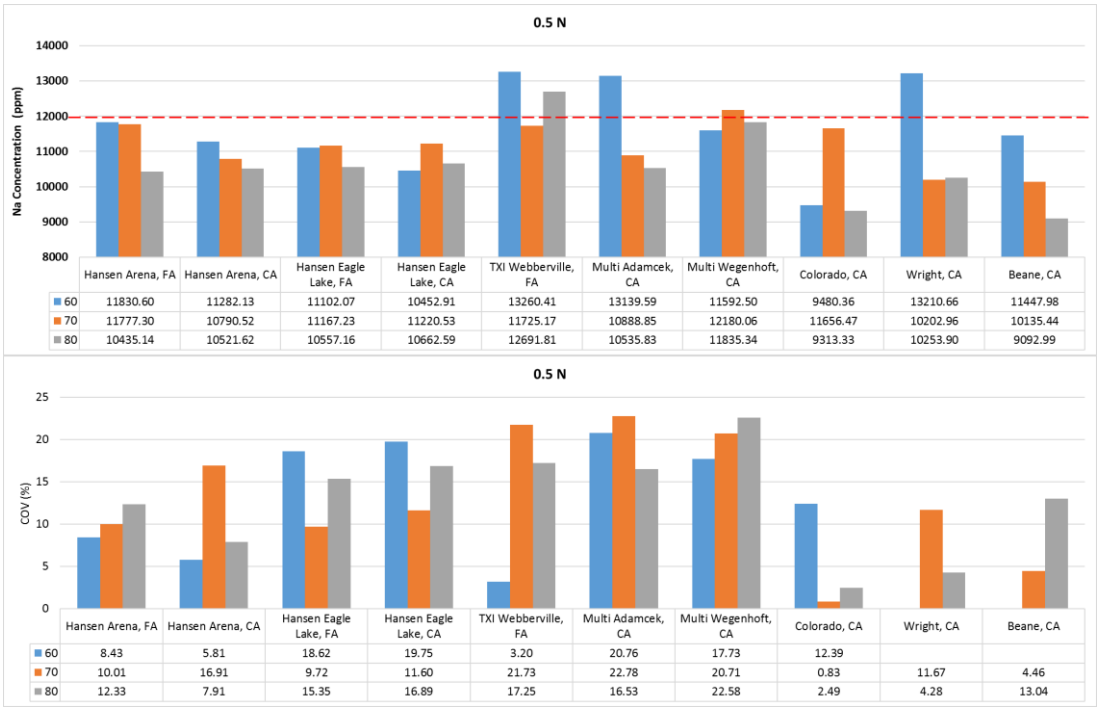

(a)

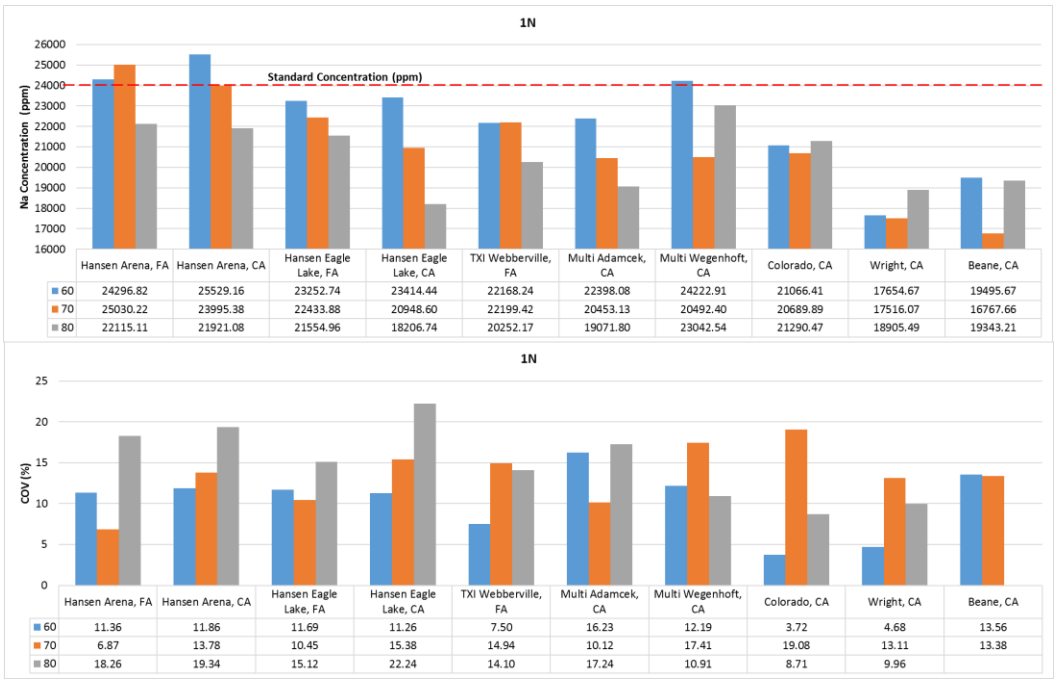

(b)

Figure 27. Variations of Na concentration change based on ppm of soak solution in VCMD test at different temperatures for different aggregates: (a) at 0.5N, and (b) at 1N

c. Concentration change with activation energy (AE):

- According to the results observed in Figure 28, the concentration change is not necessarily inversely proportional to the activation energy.
- It is observed from Figure 29 that the average Na concentration change increases by the solution normality increase and the aggregates' AE decrease.

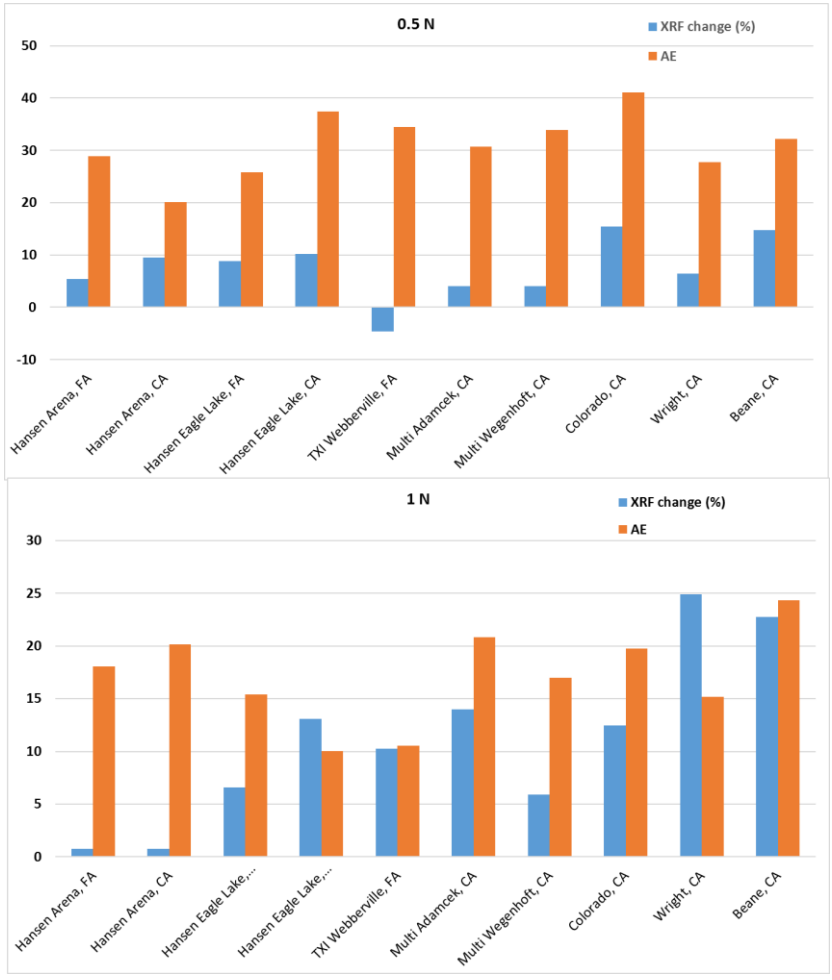

Figure 28. Variations of CAE and Na concentration change percentage of soak solution in VCMD test for different aggregates

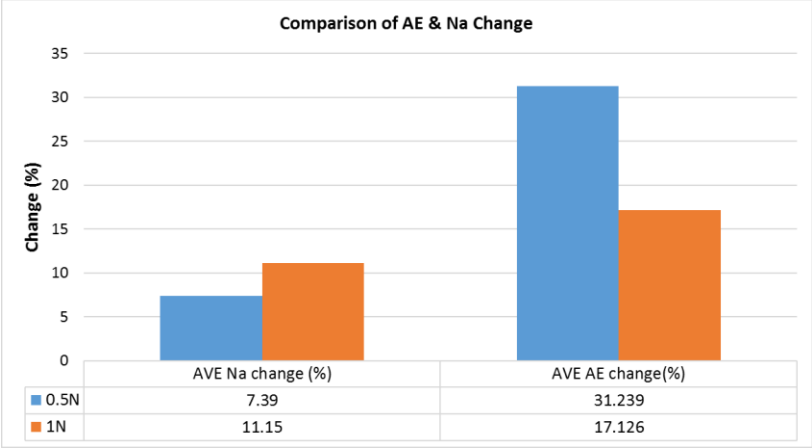

Figure 29. Average of Na concentration change vs CAE for all aggregates

d. Concentration change with normality:

- A clear trend cannot be seen for Concentration change with Normality in Figure 30.
- However, average of all concentration changes at 0.5N is 7.39 while corresponding value for 1N is 11.15. So it can be said that concentration change at 0.5N is 66% of what occurred at 1N.

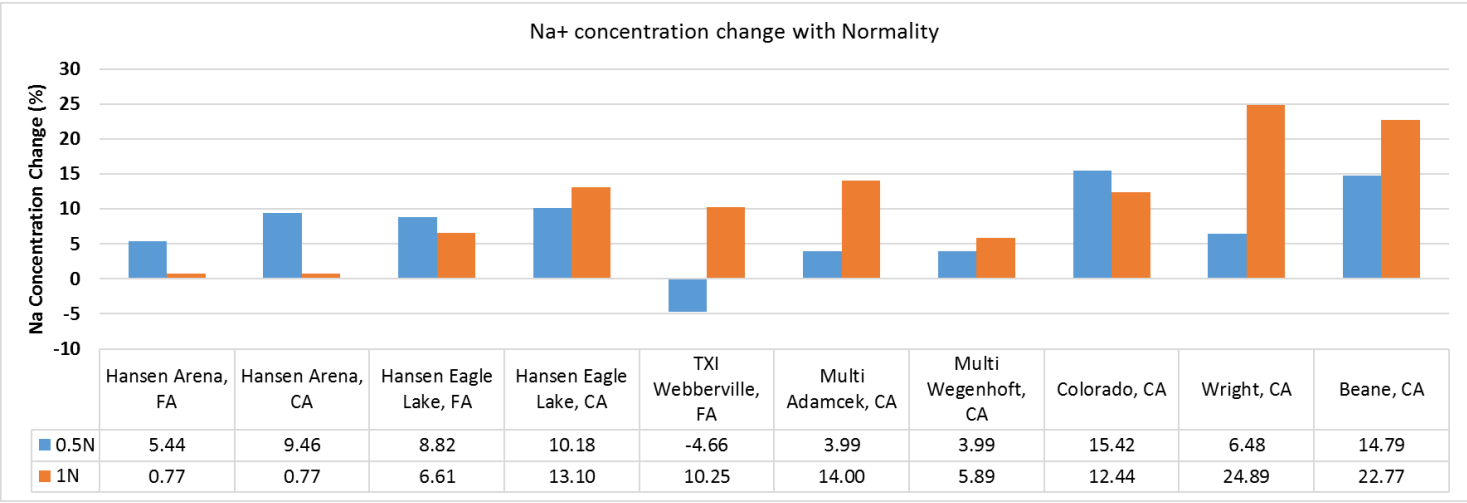

Figure 30. Na concentration change vs. normality for different aggregates.

e. Concentration change with volume change:

In Figure 31, the volume change obtained in VCMD is taken as ASR expansion.

- Clear relationship cannot be identified between concentration change and volume change.
- Interestingly enough, it is observed in Figure 32 that by taking average of the concentration changes and volume changes, interesting and significant trends can be found. Since this approach is based on compound properties, it can be said that the average values can be more significant than individual values.

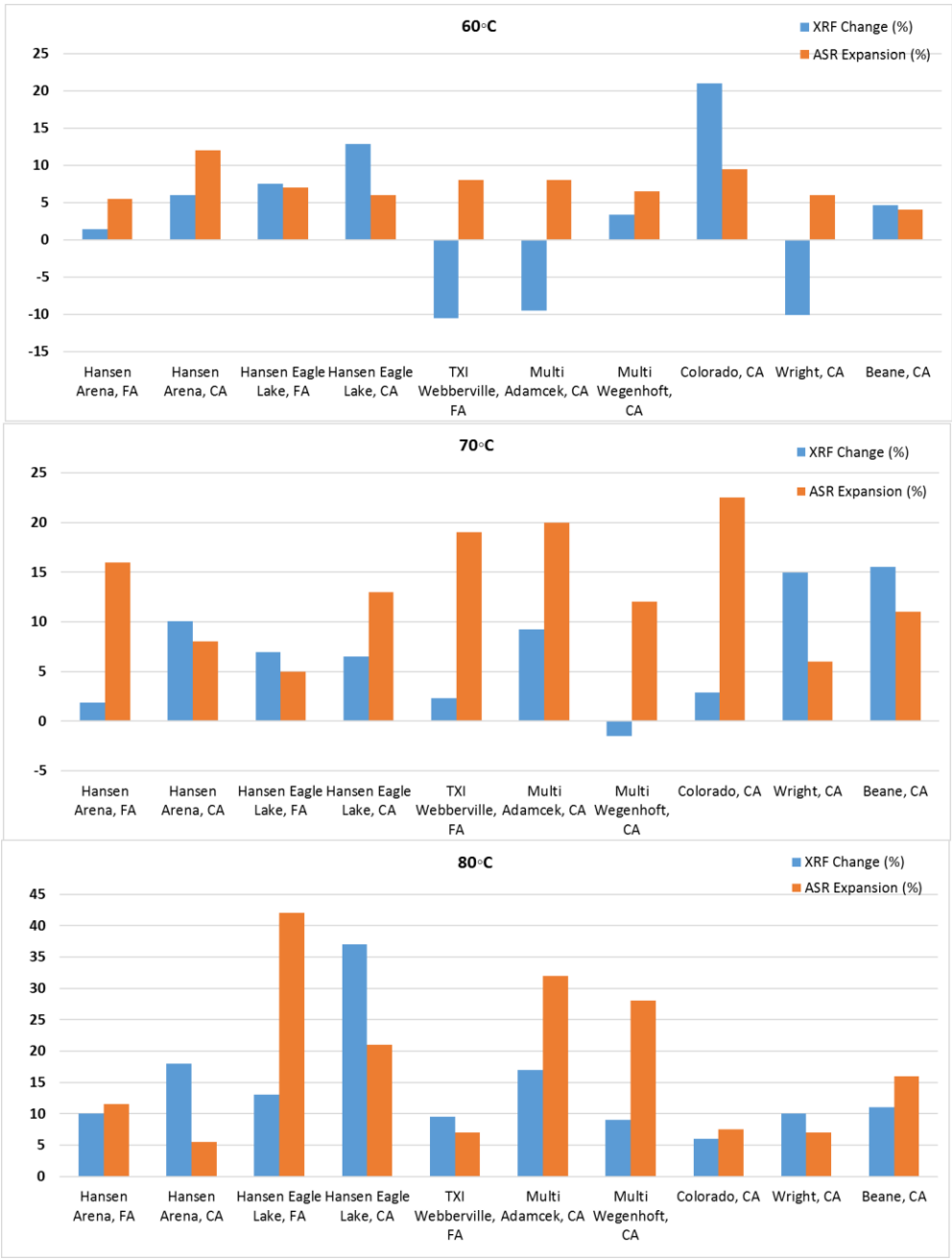

(a)

Figure 31. Variations of ASR ΔV% vs. Na concentration change percentage of soak solution in VCMD test at different temperatures for different aggregates: (a) at 0.5N, and (b) at 1N

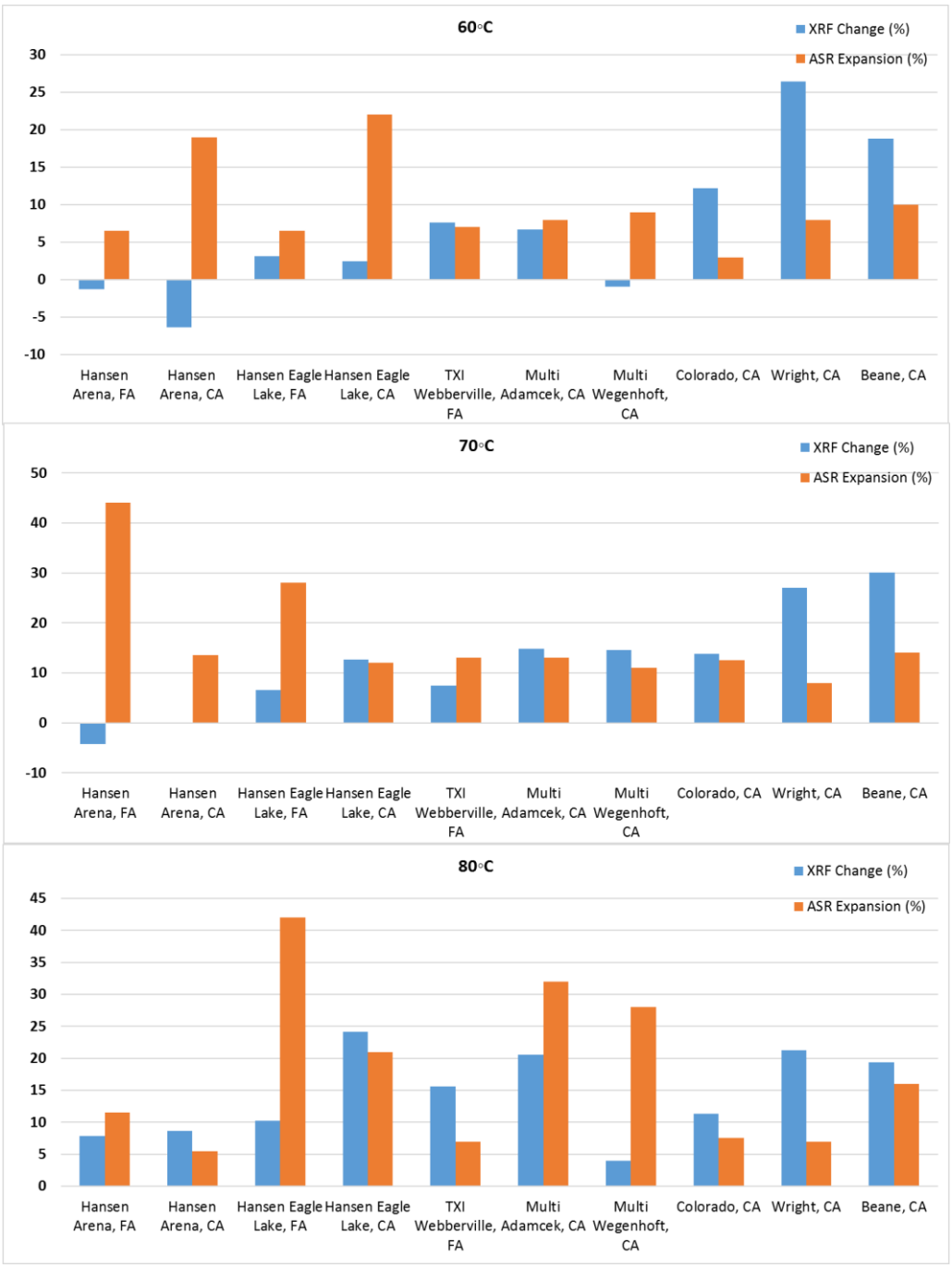

(b)

Figure 31 Continued.

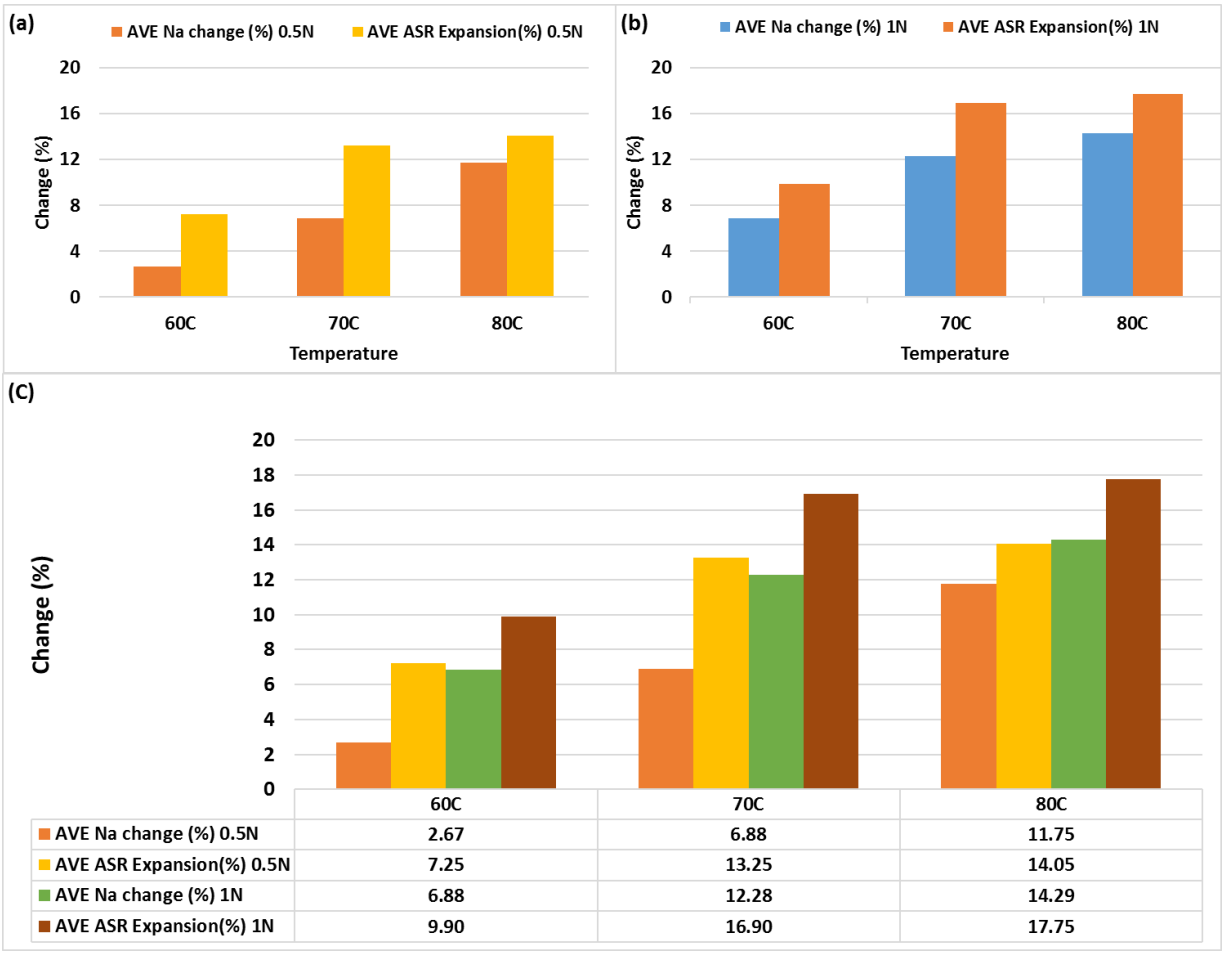

	60C	70C	80C
AVE Na change (%) 0.5N	2.67	6.88	11.75
AVE ASR Expansion(%) 0.5N	7.25	13.25	14.05
AVE Na change (%) 1N	6.88	12.28	14.29
AVE ASR Expansion(%) 1N	9.90	16.90	17.75

Figure 32. Average of Na concentration change percentage vs ASR ΔV% for all aggregates: (a) 0.5N, (b) 1N, and (c) comparative representation

5.2. AMBT Results

As mentioned earlier, design of experiment (DOE) was used to design several mixes to investigate the effect of various parameters on ASR expansion, as well as optimization of the fly ash type and percentage. Two type of aggregates of different reactivity, namely El-Indio (highly reactive) and TXI (reactive) were selected. Two replicas were made for each mix at each temperature, the average of which is reported. For the brevity, selected comparative plots of ASR expansions for different fly ashes and aggregates are presented in Figures 33 to 35.

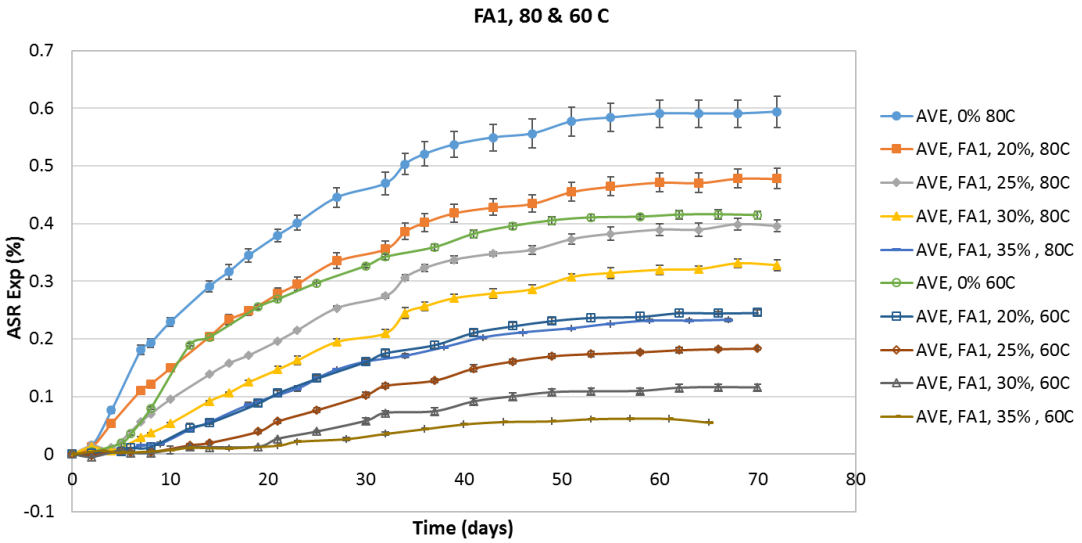

(a)

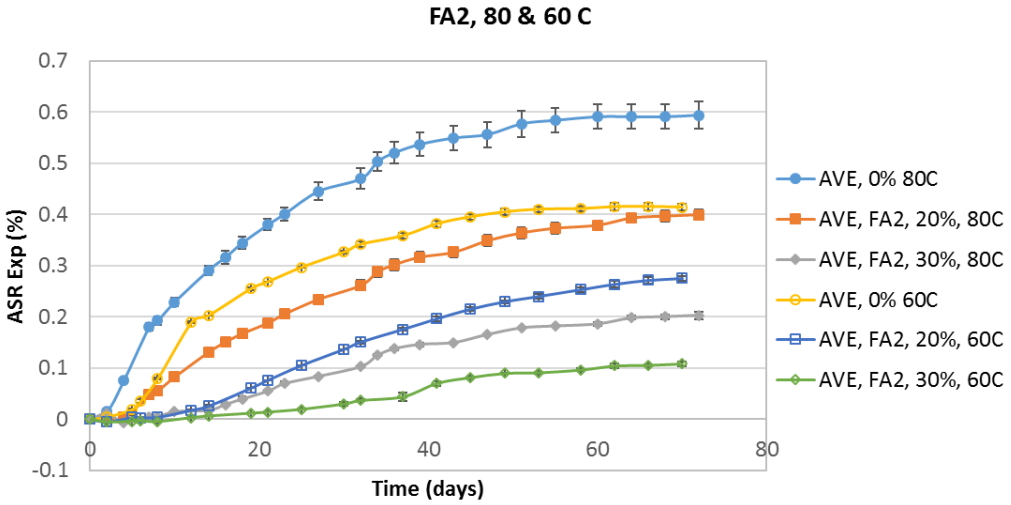

(b)

Figure 33. Comparison of the effect of different types and percentages of FA class F on expansion of a highly reactive aggregate (El-Indio)

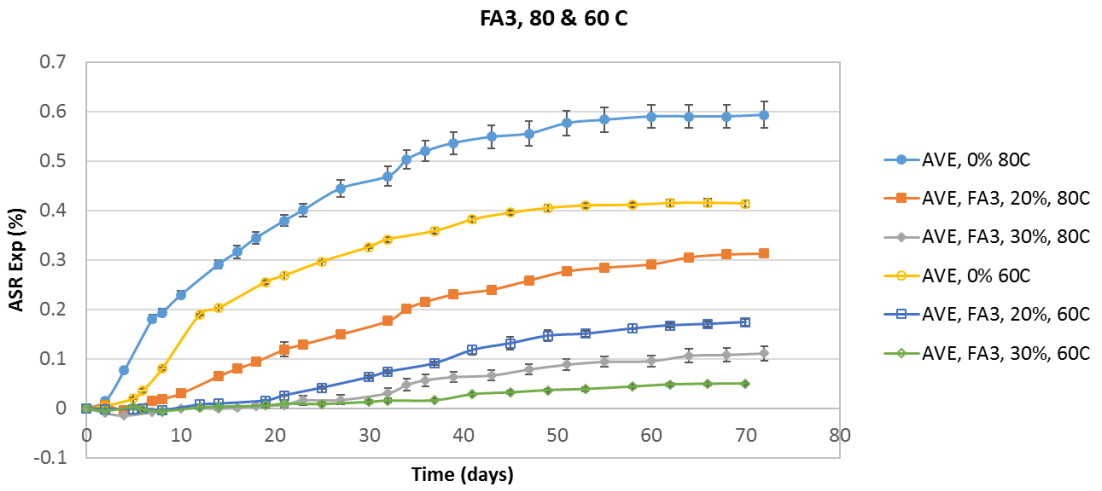

(c)

Figure 33 Continued.

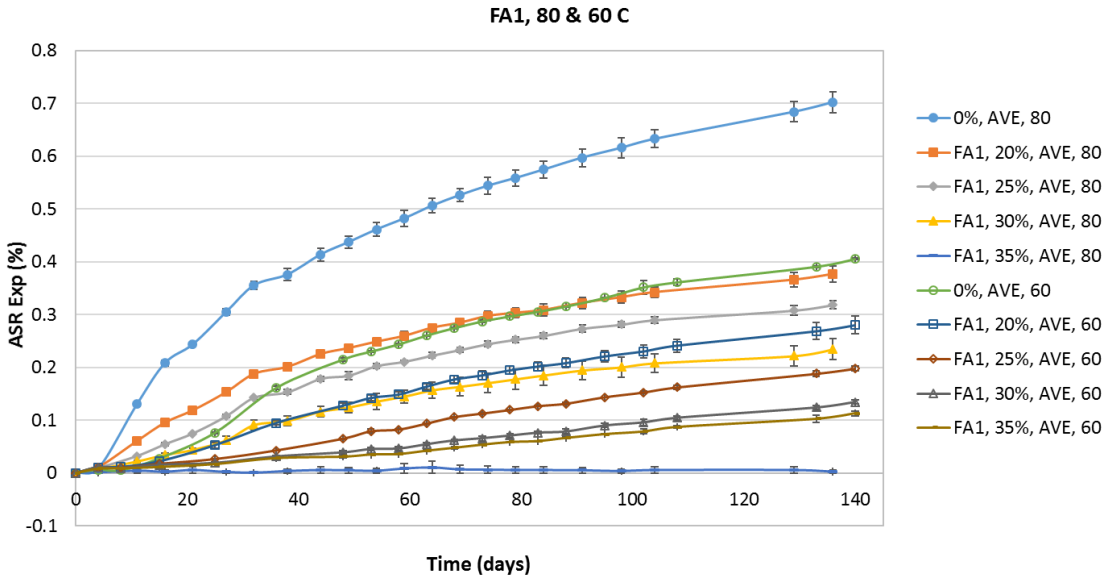

(a)

Figure 34. Comparison of the effect of different types and percentages of FA class F on expansion of a reactive aggregate (TXI)

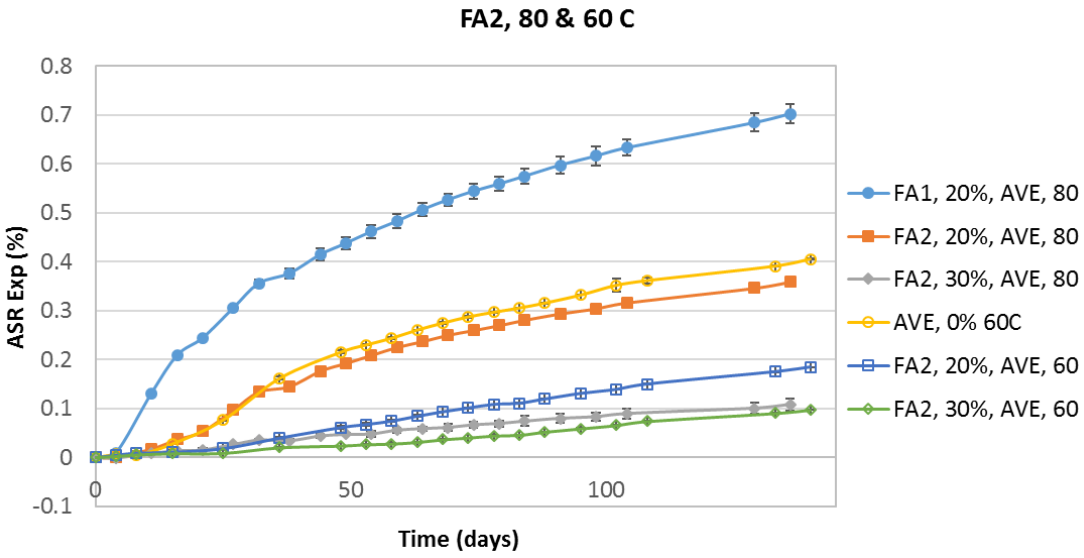

(b)

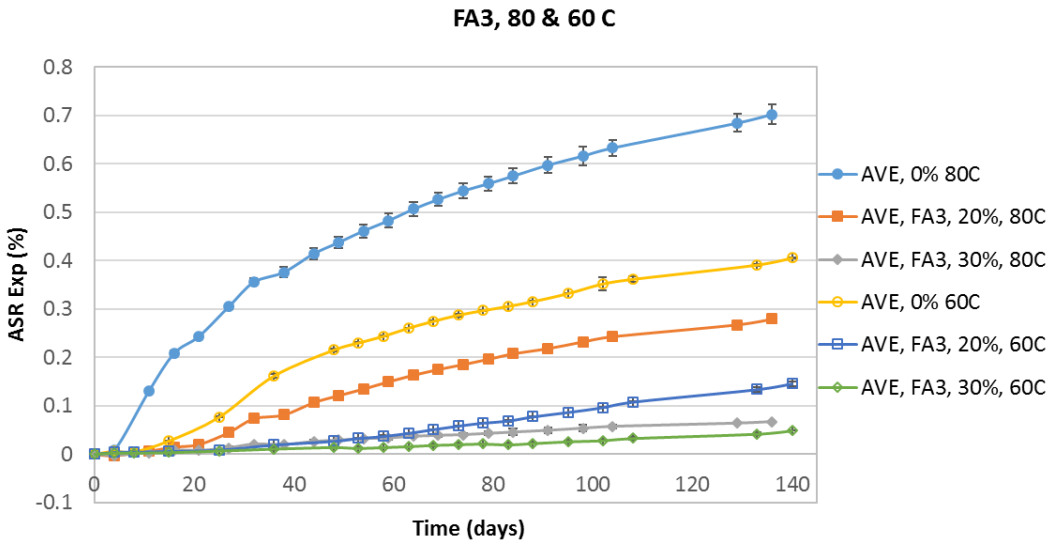

(c)

Figure 34 Continued.

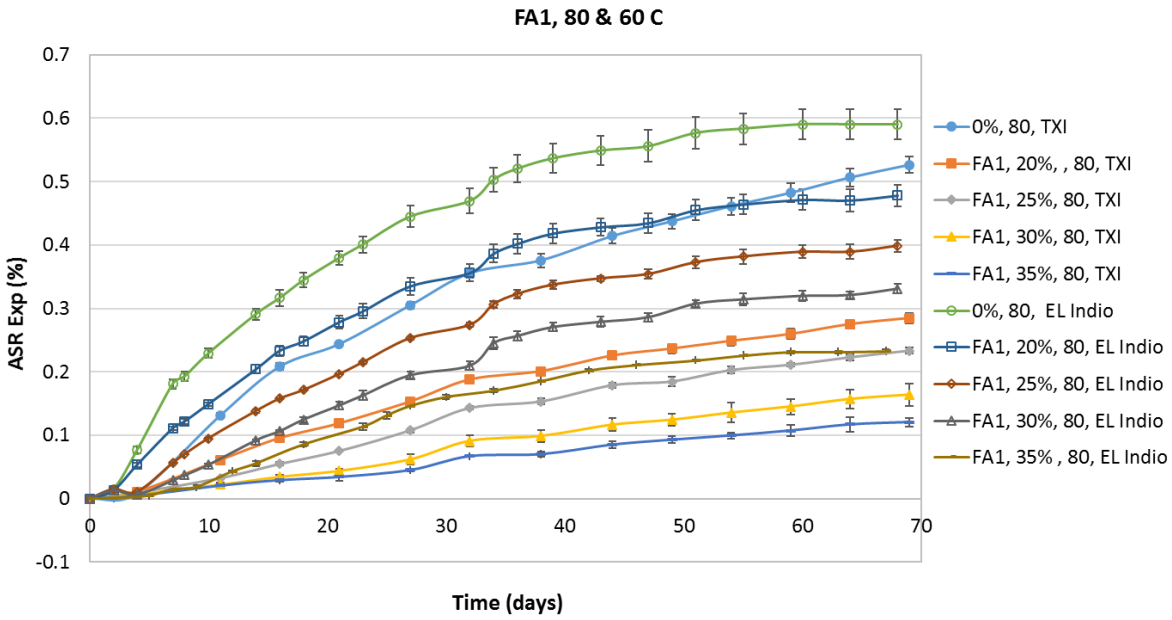

Figure 35. Comparison of ASR mortar bar expansion for different percentages of FA1 and aggregate reactivity

5.3. Determination of Threshold Alkalinity Loading

The CAE and threshold alkalinity of the aggregates used in concrete testing are presented in Table 3. If an aggregate with low THA (i.e., low level of alkali tolerance) is used in concrete, the PSA of that concrete needs to be maintained in a low level too. A reactive aggregate can practically behave as non-reactive or very slowly reactive provided the alkalinity (PSA) can be maintained below the THA.

Table 3. CAE and threshold alkalinity of the aggregates

Aggregate	CAE, KJ/Mol		THA, N
	0.5N NH + CH	1N NH + CH	
FA1	46.34	22.91	0.49
FA2	41.01	21.68	0.46
FA4	40.57	27.29	0.45
CA1	34.07	23.16	0.40
CA2	44.23	24.36	0.47
CA3	38.39	25.78	0.44
CA4	40.50	12.51	0.47
CA5	39.07	20.91	0.45
CA6	38.83	10.88	0.45
CA7	48.66	25.9	0.50

The cement paste cylinders (2 × 4 inch) using 9 levels of alkali loadings (Table 4) were cast. The use of a high-alkali (Na2Oe = 0.82%) portland cements with varying fly ash replacement and adding extra NaOH pallets (whenever needed) were adequate to achieve the different levels of alkali loadings. The cement paste cylinders were covered with plastic foil, and then stored under 98±2% relative humidity (RH) at 23±2°C for 7 days. After the 7-day curing, the specimens were de-molded and pore solutions (Barneyback and Diamond 1981) were extracted from each paste specimen. The extracted pore solution was analyzed by XRF to determine Na+ and K+ ion concentration. Table 4 presents the composition (Na^+ and K^+) of pore solution extracted from the

studied cement pastes. A minimum of three cement paste specimens for each mix was squeezed to extract pore solution followed by mixing the extracted solutions to get a representative pore solution. The Na equivalent (Na^+_e) represents the total alkali levels for each mix in this study. Figure 36 shows the correlation between PSA and alkali loading. The measured THA values were then converted using the calibration curve of PSA vs. alkali loading (Figure 36) into alkali loading. The alkali loading of all the tested aggregates were determined by applying this procedure, and are shown in Table 5.

Table 4. Cement Mix Design along with the Corresponding Pore Solution Chemistry Data.

Alkali (lb/cy)	Cement (sack/cy)	Fly ash replacement %	Add. NH (lb/cy)	PSA				
				Na^+ (ppm)	K^+ (ppm)	Na^+ (N)	K^+ (N)	Na^+_e (N)
2.47	5.83	45	-	1110	13410	0.048	0.343	0.251
2.92	5.83	35	-	1790	16700	0.078	0.427	0.327
3.15	5.83	30	-	1800	16600	0.078	0.425	0.330
3.37	5.83	25	-	2260	21800	0.098	0.558	0.427
3.60	5.83	20	-	2310	22500	0.100	0.575	0.440
4.05	5.83	10	-	2775	23825	0.121	0.609	0.480
4.27	5.83	5	-	3882	28860	0.169	0.738	0.604
4.50	5.83	-	-	4153	31562	0.181	0.807	0.657
4.99	5.83	-	0.49	5800	27420	0.252	0.701	0.666

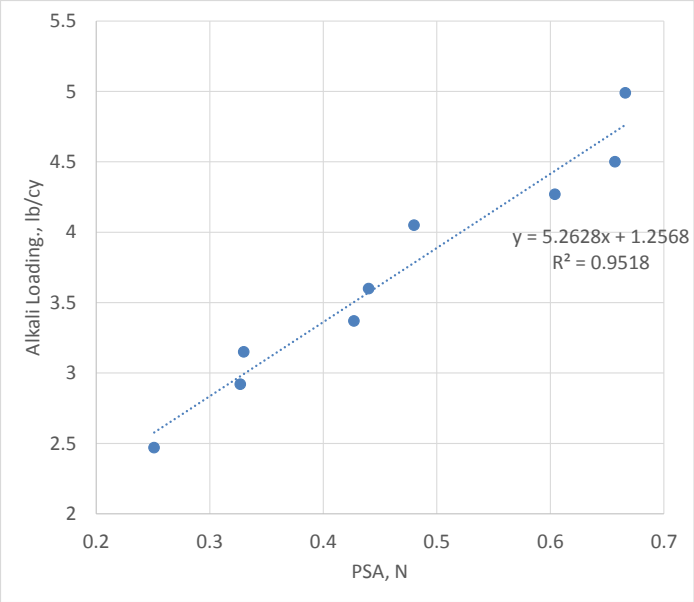

Figure 36. The Correlation between Alkali Loading and PSA

Table 5. Summary of Threshold Alkali Loading (TAL)

Aggregate	THA, N	TAL, lbs/cy
FA1	0.49	3.8
FA2	0.46	3.7
FA4	0.45	3.6
CA1	0.4	3.4
CA2	0.47	3.7
CA3	0.44	3.6
CA4	0.47	3.7
CA5	0.45	3.6
CA6	0.45	3.6
CA7	0.5	3.9

5.4. ACCT Results

Since ACCT is a test method designed to investigate ASR in concrete, which is much closer to filed performance compared to AMBT, it is of great importance to design it well enough. Several aspect were taken into account in the ACCT experiment including different reactivities, FA types, FA percentages, temperature, and the sample size. Besides, alkali loading and soak solution chemistry were also investigated to better understand their influence on ASR expansion in concrete testing. Based on the different mix designs presented earlier in chapter 3, the ACCT test results are presented here.

Mix 1 with alkaline level 4.5 lb/cy was used to verify the repeatability (within the lab) of ACCT test results. The expansion corresponding to three replicas were used to calculate the coefficient of variation (COV) and the expansion results are presented in Figure 37. The majority of expansion-based COV is within 10 percent after the 14-day expansion for the tested mixes at the level of alkalinity 4.5 lb/cy, which indicates that the repeatability (within the lab) of the ACCT method is highly acceptable.

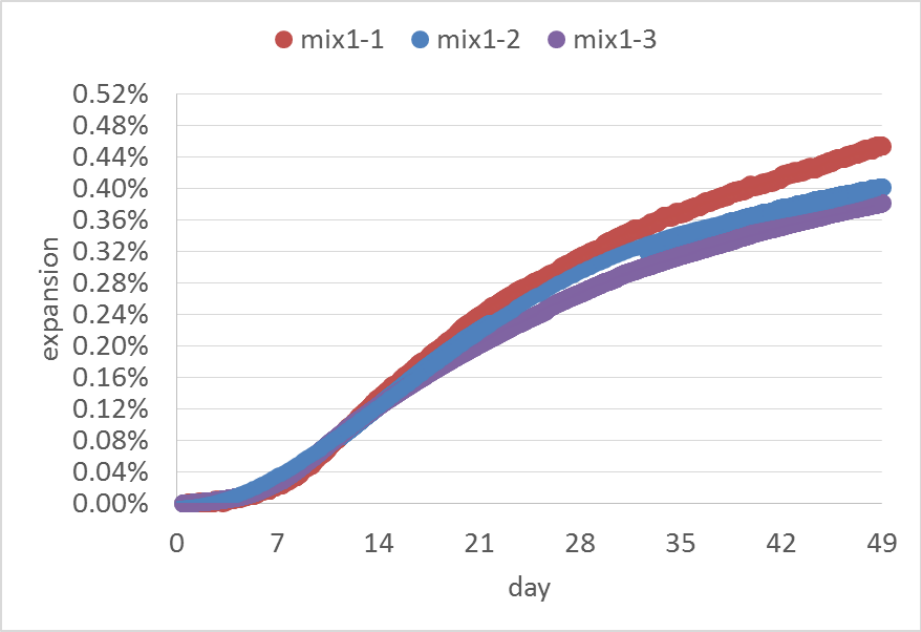

Figure 37. Expansion of Mix 1 with alkali level of 4.5 lb/cy

Several concrete mixes have been tested using the ACCT at 60°C with alkali level of 4.5 lb/cy and compared with the ASTM C1293 for validation purposes. For each test corresponding to each mix, the soak solution chemistry was equal to pore solution chemistry. For all mixes, the higher the ASR aggregate reactivity (i.e., lower CAE / higher ASTM C1293 expansion value) the higher the measured ACCT expansion is.

The ACCT plots of other mixes with different soak solutions are presented in Appendix A. The ACCT expansion data till 56 days in comparison with one year CPT (ASTM C1293) expansion data are presented in Table 6. For all the reactive mixes with alkali loading of 4.5 lb/cy, the ASTM C1293 expansion values are achieved within 56 days.

Table 6. Aggregate reactivity based on the ACCT expansion (4.5 lb/cy)

Mix	Time to Reach ASTM C 1293 1-year Expansion (Days)	Time (Days) to Cross 0.04% Expansion Limit	ASTM C 1293 1-year Exp. (%)
1	36	9	0.391
2	10/56	8	0.078/0.391
3	33	20	0.078
4	27	22	0.058
5	56	37	0.100
6*	43/50	35	0.071/0.100
7	N/A	7	-
8	None	None	0.027/0.035
9**	35	None	0.020

**: passed by C1260 but failed by C1293; **: passed by C1293 but failed by C1260*

Based on the results obtained from concrete test, it can be said that ACCT with relatively low alkali loading (i.e., 0.82% Na_2O_e, 4.5 lb/cy without alkali boosting) can achieve the 1-year ASTM C1293 value within 2 months. A concrete mix with a conventional cement content (e.g., ~ 6.0-6.5 sack/cy) will be sufficient to achieve 4.5 lb/cy alkali loadings if the Na_2O_e of the cement is relatively high (e.g., $0.6 < Na_2O_e \leq 0.82$). However, if the Na_2O_e of the cement is low (e.g., ~ 0.55), a high cement content (~ 6.5-7.5 sack/cy) with and without adding extra alkali may be needed in order to achieve 4.5 lb/cy alkali loading. It can be concluded that (i) the magnitude of expansion of direct concrete expansion measurements of these mixes depends on the reactivity of the aggregate and whether coarse or fine aggregate is reactive, and (ii) the ACCT with relatively

low alkali loadings including, but not limited to, 4.5 lb/cy and 60°C can effectively be used to pass/fail a concrete mix in a relatively short time (i.e., achieve the 1-year ASTM C1293 expansion within 1.5 months for slowly reactive aggregates and less than a month for reactive aggregates).

5.4.1. Determination of Effective Testing Period

Based on the results in sections 4.2 and 4.3, it is observed that ACCT with alkali level of 4.5 lb/cy, 0.82% Na_2O_e without alkali boosting is a good choice to pass/fail a concrete mix with the expansion limits of 0.04% at 7 to 37 days depending on the aggregate reactivity. Figure 38 shows plots of 1-year expansions in ASTM C1293 versus the 28-, 35-, 42-, 49-, and 56- day ACCT expansions at alkali level of 4.5 lbs/cy (0.82% Na_2O_e). It presents how and where expansions at 1 year of ASTM C1293 correlate well with ACCT expansion at each testing time. Based on the results, the testing period of 28 and 35 days in ACCT does not match well with the evaluation of ASR reactivity by ASTM C1293 (i.e., aggregate was identified as nonreactive aggregate by C1293 but as reactive aggregate by ACCT and vice versa), but the effective testing period of 42, 49, and 56 days is sufficient to evaluate the ASR reactivity in ACCT with the expansion limit of 0.04% at alkali level of 4.5 lb/cy.

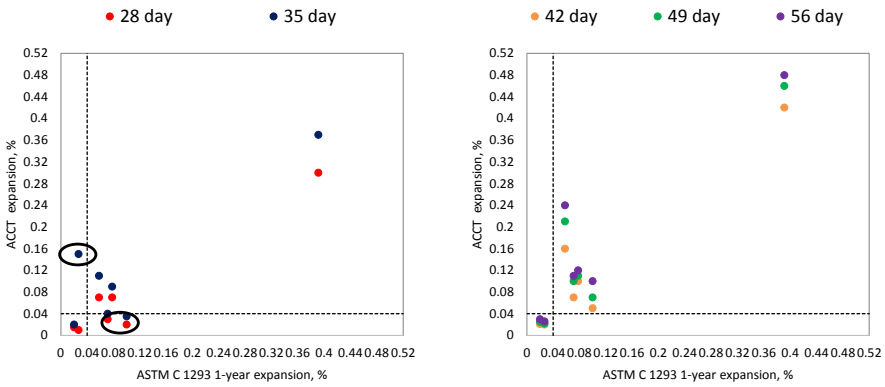

Figure. 38. Comparison of expansion at 1 year in ASTM C 1293 test versus expansion at 28, 35, 42, 49, and 56 day in the ACCT test with alkali level of 4.5 lbs/cy

5.4.2. Effect of Temperature and Sample Size

The test temperature of 38°C is used in concrete prism test (CPT) which has been considered as the best index for field performance, but the test duration imposes a major limitation. Efforts have been made by different researchers to develop an accelerated concrete prism test (ACPT) by changing the temperature of testing of CPT in order to reduce the test duration. Although the test duration is shortened by simply increasing the test temperature, a significant reduction in expansion associated with higher alkali leaching in the ACPT than the CPT was noticed (Ideker et al. 2010). ACCT has eliminated the alkali leaching from the concrete specimen during testing by matching pore solution equaling to soak solution. By doing this, it also shows that ACCT at 38 and 60°C can achieve the 1-year ASTM C 1293 value within 6 and 1.5 months respectively. Therefore, the reliability of the ACCT method is high, and ACCT can be considered as an alternative method to the current ASTM C1293. The effect of temperature, namely 38°C and 60°C on the concrete expansion behavior in ACCT with alkali loading of 4.5 lbs/cy is displayed in Figure 39.

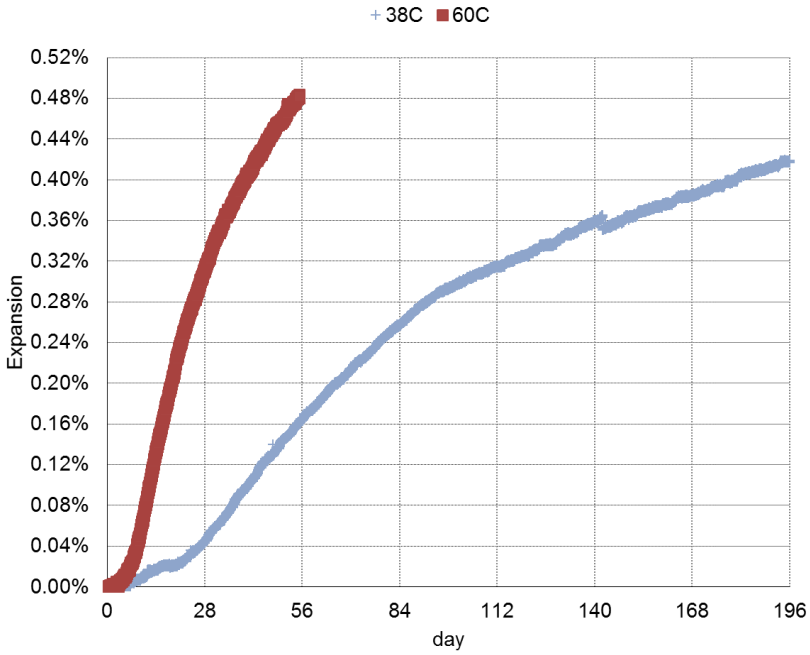

Figure 39. The effect of temperature on ACCT (Mix 1) expansion

Concrete specimens of different dimensions including, but not limited to, a cylinder of 3 x 6 inches, a cylinder of 4 x 6 inches, and a cylinder of 4 x 3.375 inches were cast using mix 1 and expansion over time was measured by the ACCT method at different temperatures including, but not limited to, 38°C and 60°C and under alkali leach-proof condition. Figures 39 and 40 show the effect of specimen sizes and temperatures on the concrete expansion behavior in ACCT with alkali loading of 4.5 lbs/cy. Figure 40 indicates the expansion difference between 3 and 4 inch diameter (regardless height) specimens is small. This is confirmed with an earlier research (Pour-Ghaz et al. 2012). The effect of specimen dimension has been studied in a similar set up, i.e., use of LVDT to measure length change of mortar cylinder in 1N NaOH solution (Pour-Ghaz et al. 2012). The expansion difference between 3 and 4 inch diameter specimens was also found to be smaller in the study. Therefore, ACCT based on 3 x 6 inch cylinder as a lowest possible dimension is acceptable.

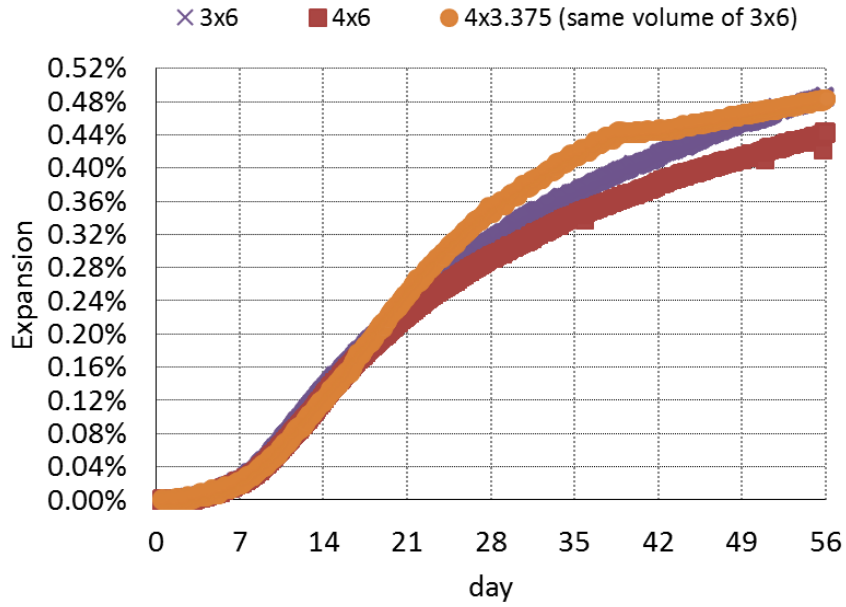

Figure 40. The effect of specimen dimension on ACCT (Mix 1) expansion at 60°C

An interesting finding from these two experiments is that the expansion in ACCT is only governed by the temperature. It is also worth mentioning that since the concentration of soak solution is equal to pore solution, there is no concentration gradient of alkalis, and hence no diffusion occurs in this test. Similar expansion of the samples of different sizes indicates the kinetics of expansion is independent of sample size (radius). Therefore, one of the great advantage of ACCT over CPT (ASTM C1293) and AMBT (ASTM C1260) is that there is not any thermal or mass diffusion involved in the expansion test.

5.4.3. Effect of Fly Ash Type and Percentage

As a part of conventional mix design practice to control ASR, several concrete mixes with different types of fly ash and different percentages were tested by ACCT. The reduction of alkali loading with increasing fly ash replacement levels was investigated as a part of this research. For

example, the alkali loading for Mix 1 without any fly ash is 4.5 lbs/cy. The alkali loading reduced to 3.6, 3.4, 3.2, and 2.9 lb/cy with corresponding fly ash replacement levels 20, 25, 30 and 35% respectively. The expansion behavior of the mixes containing fly ash is presented in Figures 41 to 44.

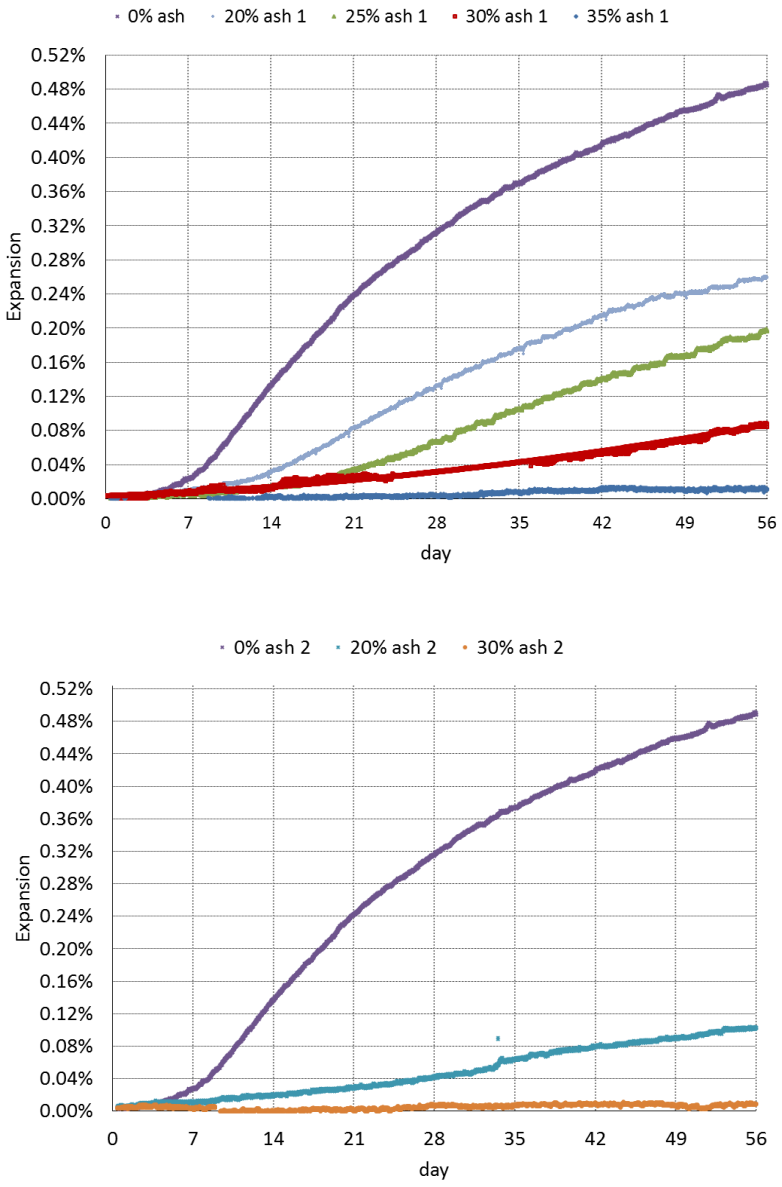

Figure 41. Expansion of mix 1 with and without fly ash replacement (s/c=3)

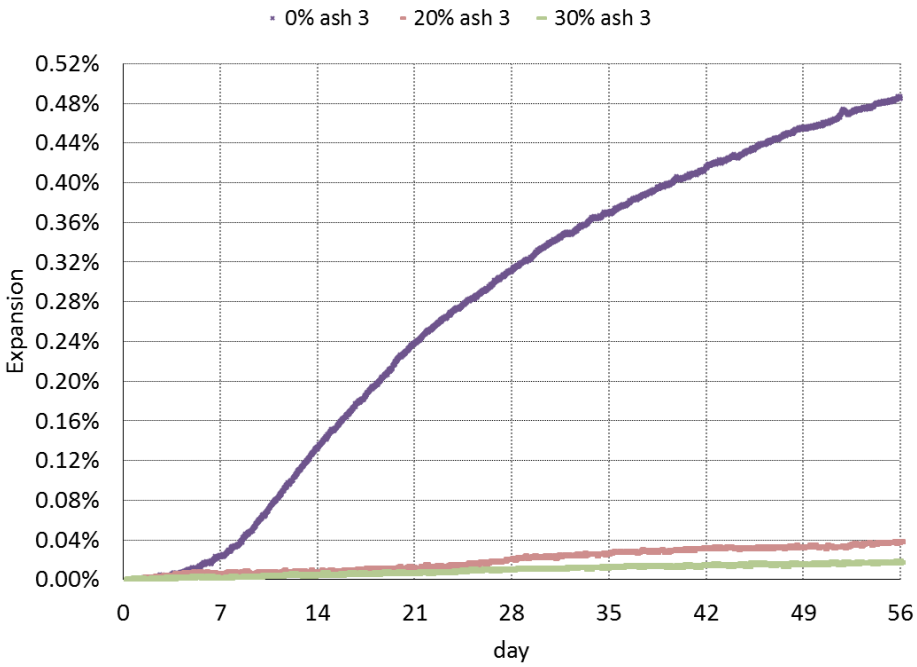

Figure 41 Continued

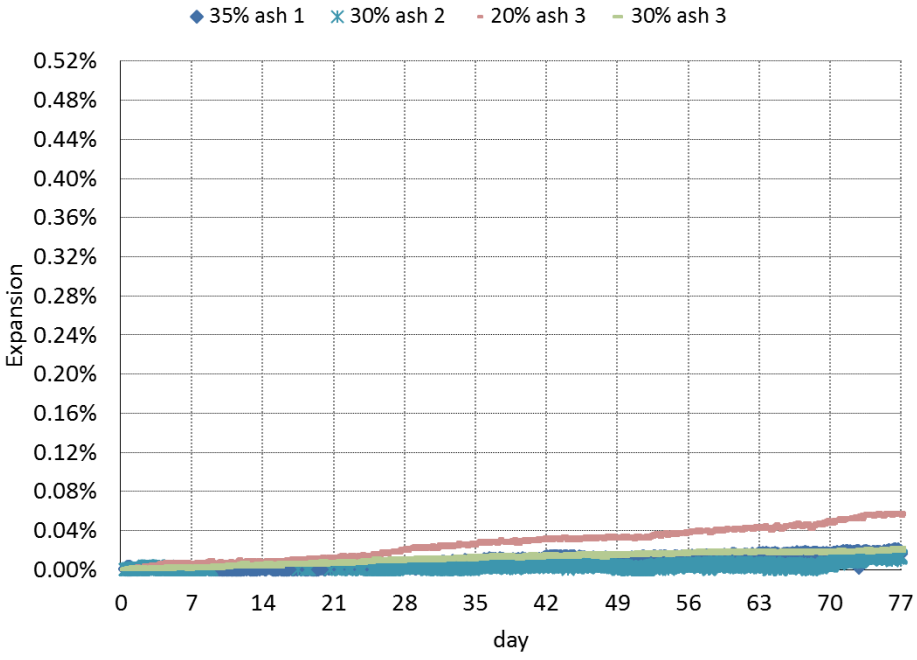

Figure 42. Expansion of mix 1 with fly ash replacement for a long period of time (s/c=3)

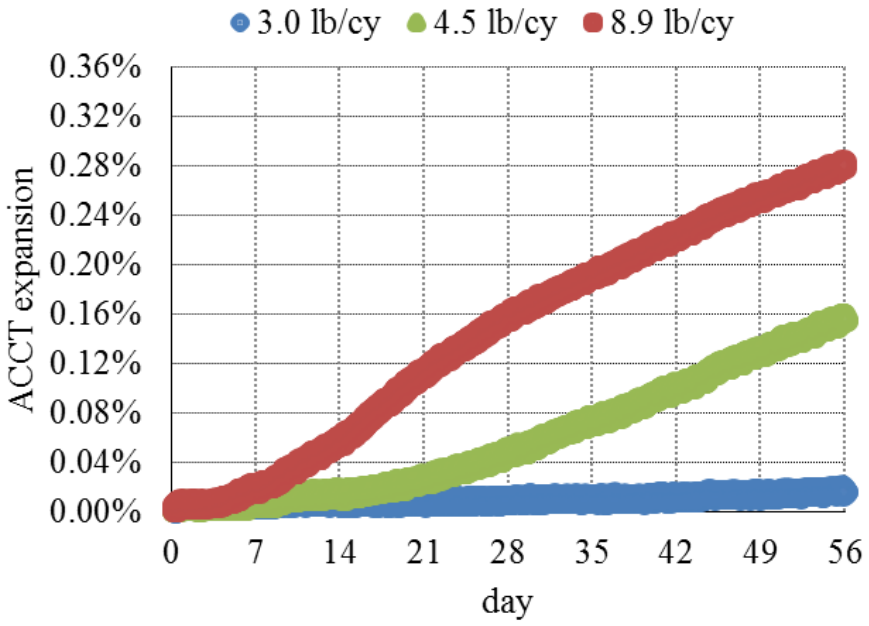

Figure 43. Expansion over time for Mix 4 (s/c = 3)

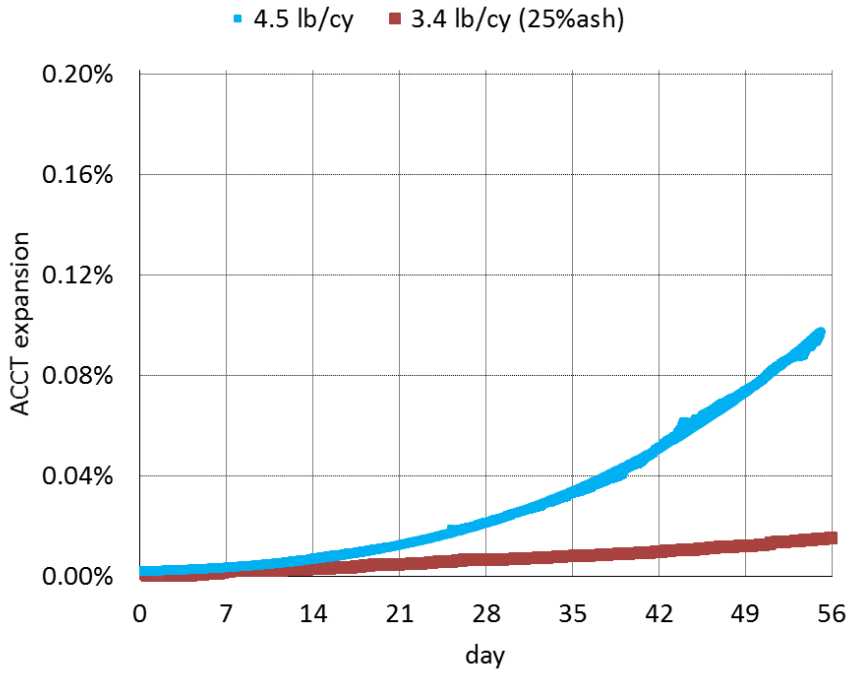

Figure 44 Expansion over time for Mix 5 (s/c = 3)

At the age of 42 days in Figure 41, the expansion reduced from 0.41% (control sample without fly ash) to 0.21%, 0.14%, 0.06%, and 0.011% for the mixes with 20%, 25%, 30%, and 35% fly ash 1 replacement respectively. The expansion reduced from 0.41% (control sample without fly ash) to 0.08% and 0.01% for the mixes with 20% and 30% fly ash 2 replacement respectively. The expansion reduced from 0.41% (control sample without fly ash) to 0.03% and 0.02% for the mixes with 20% and 30% fly ash 3 replacement respectively. For all fly ash replacement mixes (Figs. 41 to 44), the higher the level of fly ash replacement the higher is the level of alkalinity reduction in pore solution, which is correlated to higher level of expansion reduction. It is clearly observed that 20-25% fly ash replacement (conventional practice) is not sufficient to reduce the expansion below 0.04% for Mix 1 made of a highly reactive fine aggregate. 35% fly ash replacement will clearly provide sufficient protection (i.e., expansion < 0.04%) for this mix. Although, 56 days was found to be adequate for most of the mixes with fly ash but waiting till 77 days should be considered as a safe practice.

It is observed that the expansion of mix 1 with 20% fly ash 3 passes the expansion limit of 0.04% at 56 days, and the expansion of 35% fly ash 1, 30% fly ash 2 and 30% fly ash 3 remain below the expansion limit after 56 days. The expansion of mix 4 with alkaline loading of 3 lb/cy remain below the expansion limit after 56 days. The expansion of mix 5 with 25% fly ash 1 remain below the expansion limit after 56 days. The expansion of mix 6 with 20-30% fly ash 1 remain below the expansion limit after 56 days. The expansion of mix 7 with 20-30% fly ash 1 and 2 replacement (conventional practice) is not sufficient to reduce the expansion below 0.04% for Mix 7 made of a highly reactive coarse aggregate. This indicates that a job mix tested in ACCT can be

considered as an ASR-resistant mix if the expansion remains below the limit (0.04%) for 2 to 3 months.

6. RESULTS OF OPTIMIZATION AND MACHINE-LEARNING MODELING

This chapter presents the results of modeling and optimization conducted in this research. A quite comprehensive optimization and modeling using machine-learning techniques in ASR area was implemented for the in this study. The main goal here was to establish a multi-scale approach that can well-connect different scales and steps of ASR investigations and provide a powerful tool to predict and mitigate ASR. Besides, comparative study of optimization and machine-learning techniques can better demonstrate the advantages and drawbacks of each method, thereby providing a better decision-making insight based upon the needs in design, research, and applications. The optimization and modeling results obtained from this study can be categorized as below:

- Float design and optimization to improve the data-logging system of the aggregate test setup (VCMD). Different manufacturing techniques was used to make the float, out of which 3D printing techniques using high performance material led to the optimum product. It should be mentioned that this part of rehash led to a patent submission and three journal paper publications.
- Comparative modeling of ASR expansion of mortar samples using machine-learning techniques such, Artificial Neural Network (ANN), Genetic Programming (GP), and Adaptive-Inference Neuro-Fuzzy System (ANFIS). Based on Design of Experiment (DOE) presented in the earlier chapters, the mixes were designed and the necessary data were generated and used to develop the models.
- Development of different models to predict ASR expansion of concrete samples based on ACCT. The collected data on ACCT were used to develop two series of models: (a) based on

all available data obtained from ACCT, (b) based on the data of the mixes that match mortar mixes in terms of aggregate type, FA type and percentage, and temperature. The former models are concrete expansion models independent from mortar behavior. However, the latter models incorporate the mortar bar expansion as a variable to predict the concrete expansion.

6.1. Results of Float Optimization and Additive Manufacturing (3D Printing)

Based on the design formulation of the float presented in chapter 3, the optimization was implemented by several algorithms described in chapter 4. Different types of materials shown in Figure 45 were examined for design and optimization to find out which one can meet the design requirements and constraints (Jalal et al. 2018) The convergence patterns of the design variables, constraints, and cost function are displayed in Figure 46, Figure 47, and Figure 48 respectively.

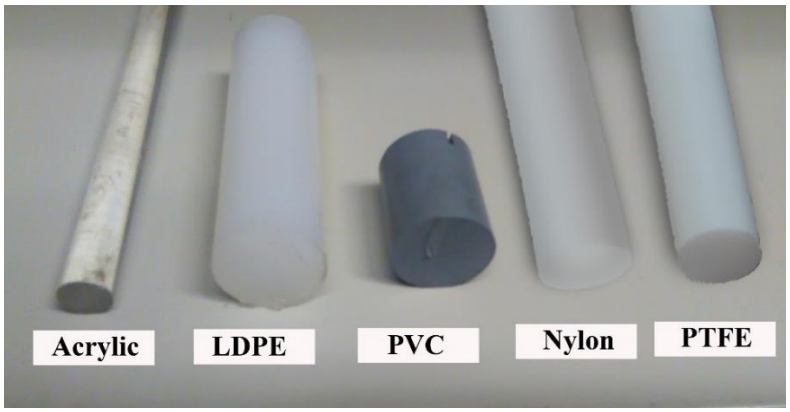

Figure 45. Materials selected for the float body

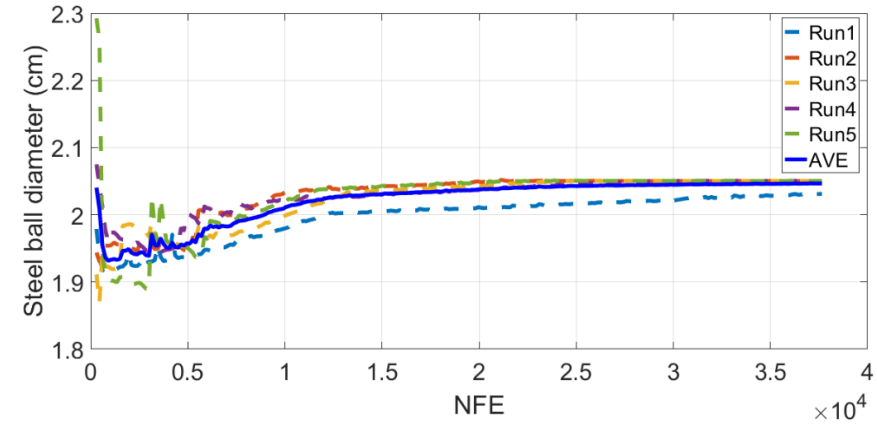

(a)

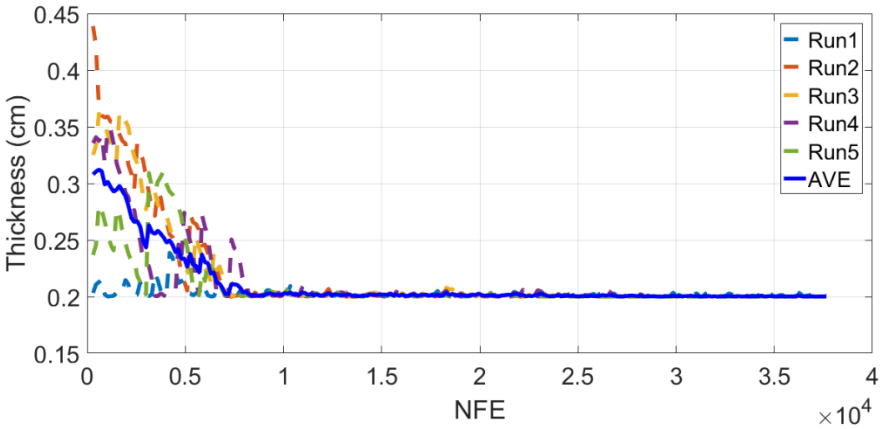

(b)

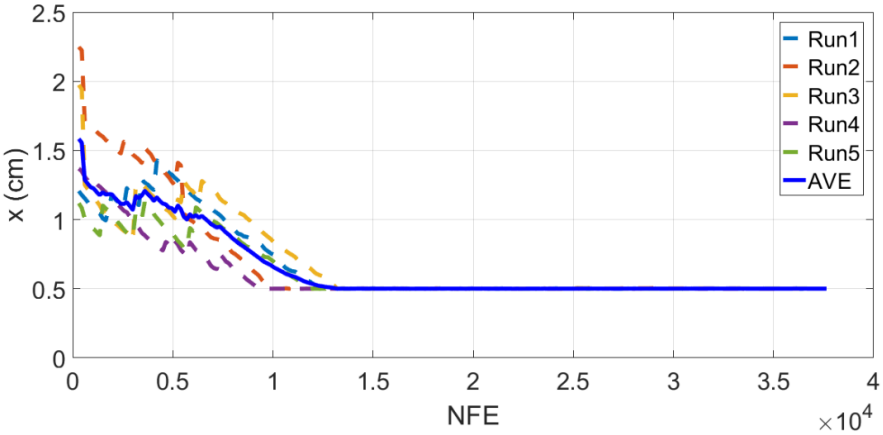

(c)

Figure 46. Convergence of BA to optimal values of design variables (NFE: Number of function Evaluation)

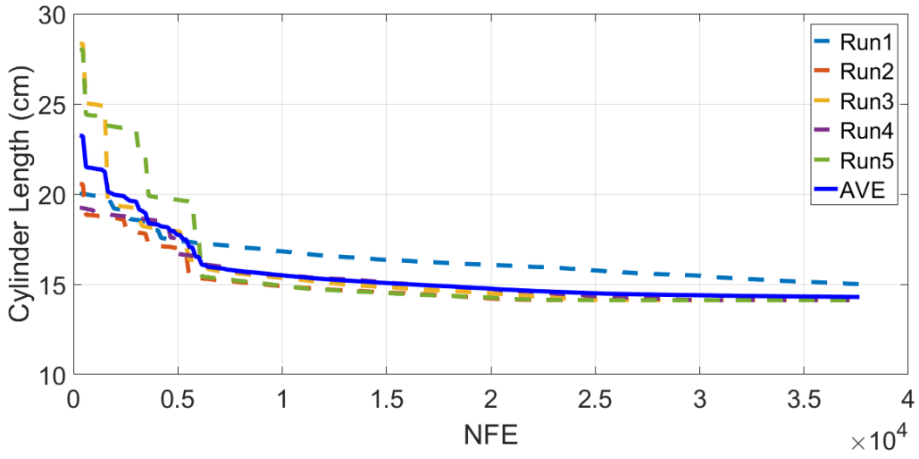

(d)

Figure 46 Continued

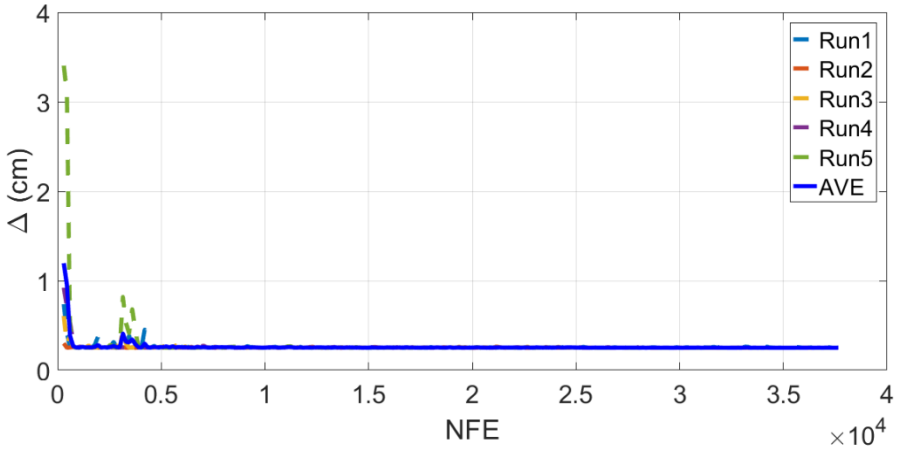

(a)

Figure 47. Convergence trends of design constraints (NFE: Number of function Evaluation)

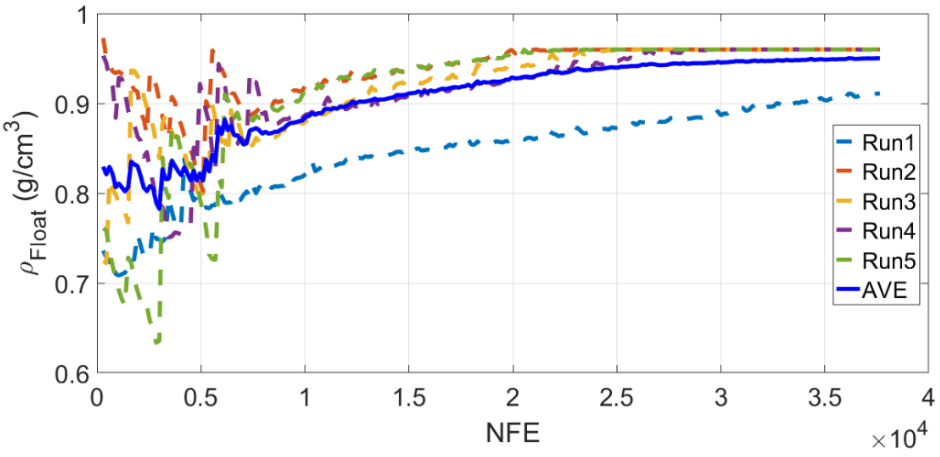

(b)

Figure 47 Continued

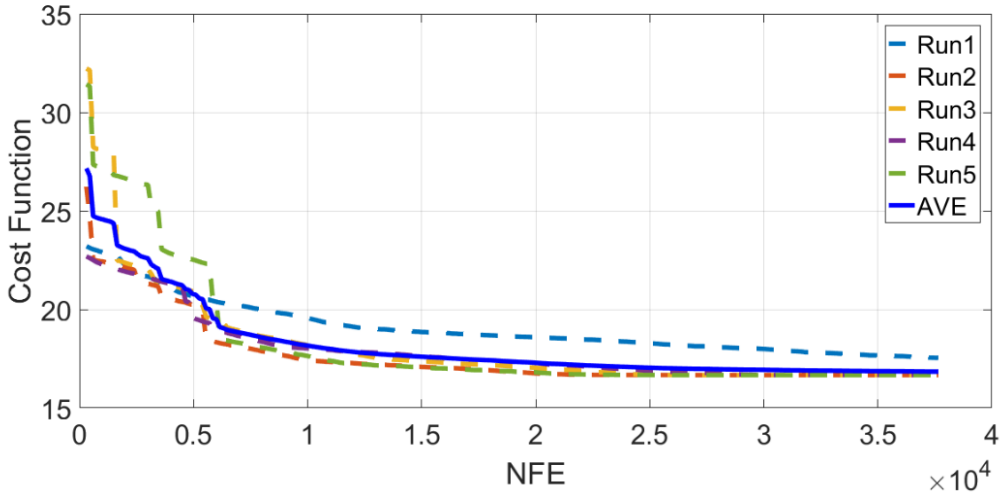

Figure 48. Convergence trend of the cost function (NFE: Number of function Evaluation)

The optimum values of design variable, constraints, and cost function obtained for different materials using bat algorithms (BA) and GRG algorithm are presented in tables 7 to 11.

Table 7. Optimal results obtained for PTFE (Teflon)

Analysis ID	**Constraints**		**Variables**				**Objective function**
Bat Algorithm	ρ_{float} (g/cm^3)	Δ (cm)	t (cm)	$L_{Cylinder}$ (cm)	X (cm)	$D_{Steel\ ball}$ (cm)	Best fit (cm)
Run 1	0.9759	0.2500	0.2000	31.5334	1.9913	1.9851	37.3476
Run 2	0.9599	0.2502	0.2000	33.0479	1.9795	1.9801	37.0075
Run 3	0.9484	0.2528	0.2000	35.7612	0.5000	2.0228	38.2840
Run 4	0.9600	0.2502	0.2000	33.4885	1.4885	1.9959	36.9742
Run 5	1.0150	0.2500	0.2000	29.5764	0.6866	2.0462	38.6711
AVE	0.9718	0.2506	0.2000	32.6814	1.3291	2.0060	37.6568
Best run	0.9600	0.2502	0.2000	33.4885	1.4885	1.9959	36.9742
GRG (Excel solver)	0.9600	0.2499	0.2000	29.6288	0.5000	1.8084	31.93715

Table 8. Optimal results obtained for PVC

Analysis ID	**Constraints**		**Variables**				**Objective function**
Bat Algorithm	ρ_{float} (g/cm^3)	Δ (cm)	t (cm)	$L_{Cylinder}$ (cm)	X (cm)	$D_{Steel\ ball}$ (cm)	Best fit (cm)
Run 1	0.9600	0.2506	0.2000	18.5715	0.5007	2.0422	21.1144
Run 2	0.9600	0.2502	0.2000	18.0356	1.1081	2.0100	21.1537
Run 3	0.9600	0.2504	0.2000	18.5730	0.5007	2.0421	21.1159
Run 4	0.9600	0.2507	0.2000	18.0594	1.0820	2.0114	21.1527
Run 5	0.9600	0.2506	0.2000	17.8325	1.3482	1.9975	21.1782
AVE	0.9600	0.2505	0.2000	18.2144	0.9079	1.9975	21.1782
Best run	0.9600	0.2506	0.2000	18.5715	0.5007	2.0422	21.1144
GRG (Excel solver)	0.9600	0.2499	0.2000	16.9535	0.5000	1.9143	19.3679

Table 9. Optimal results obtained for Acrylic

Analysis ID	**Constraints**		**Variables**				**Objective function**
Bat Algorithm	ρ_{float} (g/cm^3)	Δ (cm)	t (cm)	$L_{Cylinder}$ (cm)	X (cm)	$D_{Steel\ ball}$ (cm)	Best fit (cm)
Run 1	0.9600	0.2501	0.2000	16.2796	0.7856	2.0289	19.0949
Run 2	0.9599	0.2502	0.2000	16.5320	0.5011	2.0454	19.0785
Run 3	0.9600	0.2504	0.2000	16.5318	0.5018	2.0454	19.0836
Run 4	0.9600	0.2502	0.2000	15.8307	1.3176	1.9987	19.1470
Run 5	0.9600	0.2500	0.2000	16.1338	0.9564	2.0191	19.1093
AVE	0.9599	0.2501	0.2000	16.2615	0.8125	2.0275	19.1026
Best run	0.9599	0.2502	0.2000	16.5320	0.5011	2.0454	19.0785
GRG (Excel solver)	0.9599	0.2500	0.2000	15.3043	0.5000	1.9378	17.7400

Table 10. Optimal results obtained for Nylon

Analysis ID	**Constraints**		**Variables**				**Objective function**
Bat Algorithm	ρ_{float} (g/cm^3)	Δ (cm)	t (cm)	$L_{Cylinder}$ (cm)	X (cm)	$D_{Steel\ ball}$ (cm)	Best fit (cm)
Run 1	0.9597	0.2501	0.2000	16.0870	0.5008	2.0461	18.6340
Run 2	0.9599	0.2521	0.2000	16.0847	0.5019	2.0464	18.6330
Run 3	0.9600	0.2502	0.2000	15.9927	0.6001	2.0404	18.6332
Run 4	0.9600	0.2505	0.2000	16.0809	0.5009	2.0463	18.6281
Run 5	0.9298	0.2506	0.2006	16.7811	0.5018	2.0339	19.3168
AVE	0.9539	0.2507	0.2001	16.2053	0.5211	2.0426	18.76902
Best run	0.9600	0.2505	0.2000	16.0809	0.5009	2.0463	18.6281
GRG (Excel solver)	0.9600	0.2499	0.2000	14.9399	0.5000	1.9435	17.3835

Table 11. Optimal results obtained for LDPE

Analysis ID	**Constraints**		**Variables**				**Objective function**
Bat Algorithm	ρ_{float} (g/cm^3)	Δ (cm)	t (cm)	$L_{Cylinder}$ (cm)	X (cm)	$D_{Steel\ ball}$ (cm)	Best fit (cm)
Run 1	0.9111	0.2518	0.2012	15.0146	0.5004	2.0311	17.5461
Run 2	0.9600	0.2500	0.2000	14.1156	0.5010	2.0503	16.6669
Run 3	0.9600	0.2504	0.2000	14.1177	0.5002	2.0504	16.6685
Run 4	0.9598	0.2503	0.2000	14.11199	0.5003	2.0503	16.6704
Run 5	0.9600	0.2506	0.2000	14.1170	0.5007	2.0504	16.6680
AVE	0.9502	0.2506	0.2002	14.2954	0.4405	2.0465	16.8440
Best run	0.9600	0.2500	0.2000	14.1156	0.5010	2.0503	16.6669
GRG (Excel solver)	0.9599	0.2500	0.2000	13.3455	0.5000	1.9712	15.8168

For more comprehensive comparison, the optimization was implemented using cuckoo search (CS) algorithm, genetic algorithm (GA), and particle swarm optimization for the best selected material for design, i.e. low density polyethylene (LDPE) (Jalal and Goharzay 2019). Different geometries of the bottom weight, namely spherical, cylindrical, and conical were taken into account, the optimum results of which are presented in Tables 12, 13, and 14, respectively.

Table 12. Optimization results for the float with spherical weight

ID	ρ_{float} (g/cm^3)	Δ (cm)	t (cm)	$L_{Cylinder}$ (cm)	X (cm)	$D_{Steel\ ball}$ (cm)	Cost Function (cm)
CS							
Run 1	0.9630	0.2588	0.2003	14.0841	0.5070	2.0522	16.7116
Run 2	0.9594	0.2508	0.2001	14.1284	0.5027	2.0500	16.6811
Run 3	0.9584	0.2522	0.2002	14.0308	0.6381	2.0411	16.7100
Run 4	0.9606	0.2500	0.2001	14.1031	0.5068	2.0501	16.6748
Run 5	0.9603	0.2516	0.2001	14.0262	0.6029	2.0440	16.6803
AVE	0.9603	0.2527	0.2002	14.0745	0.5515	2.0475	16.6916
Best run	0.9594	0.2508	0.2001	14.1284	0.5027	2.0500	16.6811
GA							
Run 1	0.9600	0.2500	0.2000	14.1013	0.5168	2.0493	16.6673
Run 2	0.9600	0.2500	0.2093	13.6129	0.5168	1.9931	16.9903
Run 3	0.9600	0.2500	0.2000	13.4160	1.3410	1.9969	16.7539
Run 4	0.9601	0.2501	0.2007	13.8771	0.7969	2.0312	16.7063
Run 5	0.9599	0.2503	0.2001	13.5111	1.2288	2.0039	16.7438
AVE	0.9600	0.2501	0.2020	13.7037	0.8801	2.0149	16.7723
Best run	0.9600	0.2500	0.2000	14.1013	0.5168	2.0493	16.6673
PSO							
Run 1	0.9600	0.2501	0.2000	13.1279	1.7107	1.9740	16.8126
Run 2	0.9600	0.2502	0.2000	13.6739	1.0230	2.0169	16.7147
Run 3	0.9600	0.2501	0.2000	13.4473	1.3020	1.9993	16.7487
Run 4	0.9601	0.2501	0.2000	14.0044	0.6275	2.0422	16.6761
Run 5	0.9600	0.2502	0.2000	14.0195	0.6120	2.0431	16.6746
AVE	0.9600	0.2501	0.2000	13.6546	1.0550	2.0151	16.7253
Best run	0.9600	0.2502	0.2000	14.0195	0.6120	2.0431	16.6746
GRG method (Excel solver)							
	0.9600	0.2499	0.2000	13.3456	0.5000	1.9712	15.8168

Table 13. Optimization results for the float with cylindrical weight

ID	ρ_{float} (g/cm^3)	Δ (cm)	t (cm)	$L_{Cylinder}$ (cm)	X (cm)	D Steel cylinder (cm)	H Steel cylinder (cm)	Cost Function (cm)
				CS				
Run 1	0.9601	0.2619	0.2023	13.8586	1.1493	2.0391	1.3344	16.3448
Run 2	0.9594	0.2508	0.2005	14.0849	0.8895	2.4464	0.9643	16.0212
Run 3	0.9646	0.2521	0.2000	14.4051	0.5133	2.4747	0.9783	15.9933
Run 4	0.9614	0.2503	0.2000	14.0816	0.5521	1.7159	1.9505	16.6128
Run 5	0.9553	0.2509	0.2001	12.9739	2.4160	2.4124	0.8543	16.2443
AVE	0.9602	0.2532	0.2006	13.8808	1.1040	2.2177	1.2164	16.2433
Best run	0.9646	0.2521	0.2000	14.4051	0.5133	2.4747	0.9783	15.9933
				GA				
Run 1	0.9600	0.2546	0.2152	14.6966	0.5011	1.9828	1.4864	16.6841
Run 2	0.9600	0.4343	0.2188	14.9706	0.5006	1.7232	2.0031	17.4743
Run 3	0.9600	0.2500	0.3312	17.6016	0.5537	1.2966	3.1869	21.3423
Run 4	0.9600	0.2505	0.2036	13.4145	1.6392	1.8802	1.4849	16.5388
Run 5	0.9600	0.2500	0.2159	14.5204	0.7018	1.9579	1.4932	16.7154
AVE	0.9600	0.28788	0.23694	15.0407	0.7792	1.76814	1.9309	17.751
Best run	0.9600	0.2505	0.2036	13.4145	1.6392	1.8802	1.4849	16.5388
				PSO				
Run 1	0.9603	0.2503	0.2000	12.8690	1.9380	1.4803	2.2679	17.0840
Run 2	0.9600	0.2501	0.2002	13.7145	1.3292	2.2617	1.0737	16.1174
Run 3	0.9616	0.2505	0.2000	13.3556	1.2660	1.5110	2.3177	16.9918
Run 4	0.9600	0.2500	0.2000	13.7054	0.9821	1.6467	2.0245	16.7120
Run 5	0.9600	0.2500	0.2000	13.7054	0.9821	1.6467	2.0245	16.1959
AVE	0.9604	0.2502	0.2000	13.4700	1.2995	1.7093	1.9417	16.6202
Best run	0.9600	0.2501	0.2002	13.7145	1.3292	2.2617	1.0737	16.1174
				GRG method (Excel solver)				
	0.9599	0.2499	0.2000	13.6800	0.5000	2.5000	0.8505	15.0305

Table 14. Optimization results for the float with conical weight

ID	ρ_{float} (g/cm^3)	Δ (cm)	t (cm)	$L_{Cylinder}$ (cm)	X (cm)	D Steel cylinder (cm)	H Steel cylinder (cm)	Cost Function (cm)
CS								
Run 1	0.9565	0.2593	0.2017	13.7311	1.5134	2.4462	2.7227	17.9673
Run 2	0.9582	0.2504	0.2004	13.3772	1.8766	2.4997	2.5226	17.7763
Run 3	0.9593	0.2529	0.2008	13.6518	1.5209	2.4831	2.6437	17.8164
Run 4	0.9598	0.2506	0.2001	12.8755	2.4929	2.4841	2.4147	17.7831
Run 5	0.9624	0.2632	0.2014	14.0726	0.9952	2.4996	2.7505	17.8691
AVE	0.9592	0.2553	0.2009	13.5416	1.6798	2.4825	2.6108	17.8424
Best run	0.9582	0.2504	0.2004	13.3772	1.8766	2.4997	2.5226	17.7763
GA								
Run 1	0.9603	0.2500	0.2000	13.8023	1.2039	2.2225	3.3731	18.3842
Run 2	0.9600	0.2500	0.2025	14.2057	0.7792	2.1805	3.6348	18.6197
Run 3	0.9609	0.2514	0.2000	14.3420	0.5508	2.2286	3.5642	18.4770
Run 4	0.9600	0.2500	0.2009	13.4302	1.8035	2.1413	3.4302	18.5675
Run 5	0.9600	0.2500	0.2010	13.5347	1.5087	2.0502	3.8298	18.8732
AVE	0.9602	0.2503	0.2009	13.8630	1.1692	2.1646	3.5664	18.5843
Best run	0.9603	0.2500	0.2000	13.8023	1.2039	2.2225	3.3731	18.3842
PSO								
Run 1	0.9600	0.2500	0.2000	14.0414	1.0100	2.5000	2.7359	17.7573
Run 2	0.9600	0.2500	0.2000	14.3383	1.8749	2.5000	2.5247	17.7379
Run 3	0.9600	0.2500	0.2000	14.3698	0.6295	2.5000	2.8346	17.8338
Run 4	0.9602	0.2500	0.2002	14.2345	0.7850	2.5000	2.7943	17.8190
Run 5	0.9600	0.2500	0.2000	14.1075	0.9323	2.5000	2.7558	17.7956
AVE	0.9600	0.2500	0.2000	14.2183	1.0463	2.5000	2.7291	17.7887
Best run	0.9600	0.2500	0.2000	14.3383	1.8749	2.5000	2.5247	17.7379
GRG method (Excel solver)								
	0.9600	0.2499	0.2000	13.3058	0.9244	2.5000	2.4392	16.6694

Once the design and optimization of the float was implemented, the parts were made by machining and assembled, as shown in Figure 49. More details on the manufacturing process can be found in Jalal et al. (2019). However, due to complicacy of manufacturing through machining as well as the leaking issues, 3D printing a new manufacturing technology was considered as a solution.

In order to manufacture the float body using 3D printing, 4 types of materials, i.e. polypropylene filament, carbon fiber filament, standard resin, and high temperature resin were tested to come up with the best product that can sustain the VCMD conditions. The floats made from different materials are illustrated in Figure 50. All of the non-resin floats showed leaking issues and the resin made out of standard resins failed under higher temperature. The only design that survived the test conditions was the 3D printed float made from high temperature resin with higher thickness, as shown in Figure 51.

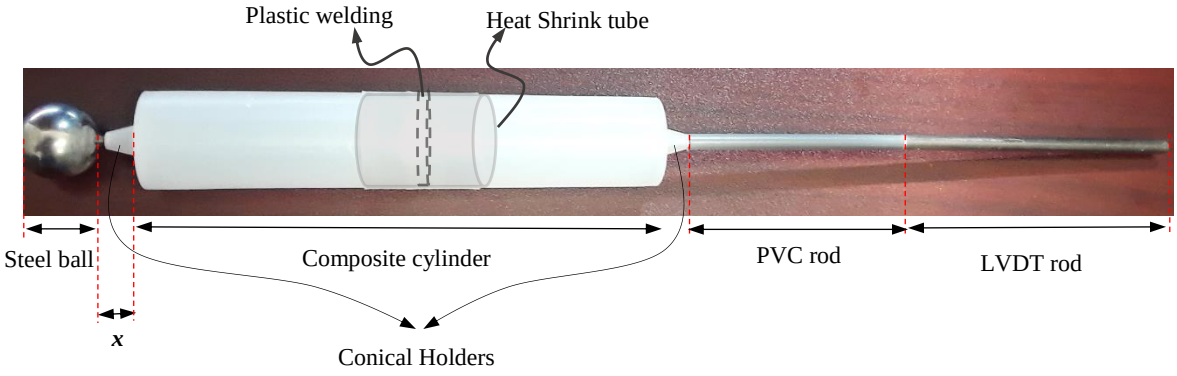

Figure 49. Details of the float made by machining

Figure 50. Different types of 3D printed floats along with the one made by machining

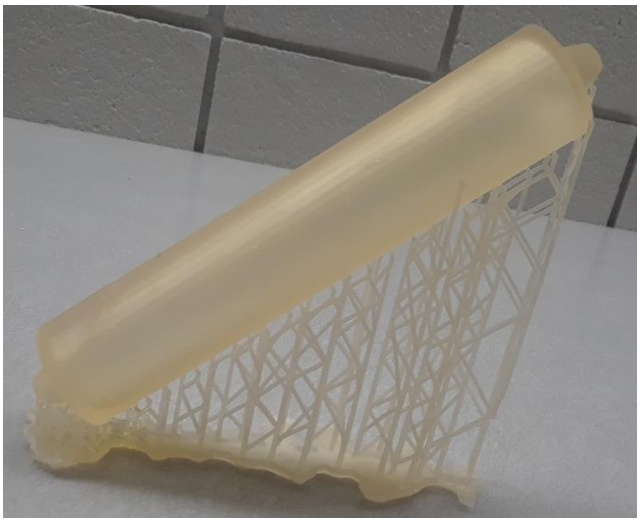

Figure 51. 3D printed float with high temperature resin with higher thickness

6.2. Results of Machine-Learning Predictions for Mortar Bar

As mentioned earlier in chapter 3, extensive mortar bar testing using AMBT with extended time and at two different temperature was carried out. Different mixes containing seven types of fly ash (FA) with different percentages were designed. An attempt was made to fully characterize

different FAs and identify the most influencing parameters of FA affecting ASR expansion (Mukhopadhyay et al., 2019). To quantify the type of FA in terms of the variables that can be introduced into the model, quite comprehensive assessment was made and three variables were selected including CaO, amorphous glass content, and available alkali (Na2Oe), and determined by XRF, XRD, and chemical test (ASTM C311), respectively. Once the data were collected, the models were constructed using 7 variables, namely aggregate CAE at 0.5N, aggregate CAE at 1N, Temperature (T), FA %, CaO%, amorphous phase%, available alkali (Na2Oe)%, and time. The following relationship shows the ASR expansion of mortar bars in terms of the influencing variable considered in this study:

$$ASR\ expansion\ (\%)_{Mortar\ bar} = f\ (CAE_{0.5N}, CAE_{1N}, T, FA\ \%, Amorph\%, CaO\%, Na_2O_e\%, t) \quad (6.1)$$

6.2.1. Performance Criteria

Different performance criteria are considered in this study to thoroughly assess the performance of the models including correlation coefficient (R), relative absolute error (RAE), mean absolute error (MAE), root relative square error (RRSE), root mean square error (RMSE), and coefficient of determination (R^2).

$$R = \frac{\sum_i (O_i - \bar{O})(t_i - \bar{t})}{\sqrt{\sum_i (O_i - \bar{O})^2 \sum_i (t_i - \bar{t})^2}} \quad (6.2)$$

$$RAE = \frac{\sum_i |t_i - O_i|}{\sum_i \left| t_i - \frac{1}{n}\sum_i t_i \right|} \quad (6.3)$$

$$MAE = \frac{1}{n}\sum_i |t_i - O_i| \quad (6.4)$$

$$RRSE = \frac{\sum_i (t_i - O_i)^2}{\sum_i (t_i - \frac{1}{n}\sum_i t_i)^2} \quad (6.5)$$

$$RMSE = \sqrt{\frac{1}{n}\sum_i (t_i - O_i)^2} \quad (6.6)$$

$$R^2 = 1 - \frac{\sum_i (t_i - O_i)^2}{\sum_i (t_i - \bar{t})^2} \quad (6.7)$$

where, $t_i, \bar{t}, O_i, \bar{O}, n$ are experimental value, average of experimental values, predicted value, average of predicted values, and number of samples, respectively.

6.2.2. Results of ANN Model

For the modeling purpose using ANN, first an attempt was made to find the optimal structure of the ANN model. Several parameters such as number of hidden layers, number of neuron in the hidden layers, type activation function, and learning algorithm were investigated to come up with the optimum ANN model.

6.2.2.1. Selection of Optimal ANN Architecture

On the one hand, the performance of an ANN model mainly depends on the network architecture, and on the other hand, one of the most difficult tasks in NN studies is to find this optimal network architecture, which is based on determination of numbers of optimal layers and neurons in the hidden layers by trial and error approach. However, this process is tedious and very time consuming. Therefore, for the initial screening process of finding optimal ANN model, MATLAB was used to facilitate the process of optimal model selection. However, the neural network in MATLAB randomly assigns the initial weights for each run each time, which considerably changes the performance of the trained NN, even if all parameters and NN architecture are kept constant. It can cause extra difficulties in the selection of optimal network architecture and parameter settings. Selection of the optimal training algorithm and transfer functions, based on the nature of the data being modeled, can also effect the NN performance which is another one may encounter in optimal model selection process. To overcome the trial

and error difficulty, a program was developed in MATLAB to automatically handle the trial and error process, which can be used to find out the best NN architecture.

The program tries various number of neurons in the hidden layers both for first and second hidden layers for a constant number of iterations several times and selects the best NN architecture with the minimum MAE (mean absolute error) or RMSE (root mean square error) of the simulated data. For instance, an NN architecture with 1 hidden layer and with 5 nodes is tested 10 times and the average error of 10 trials is stored, and then the number of nodes is increased to 6 and the process is repeated up to 20th neuron in the hidden layer. The flowchart of the whole process is shown in Figure 52.

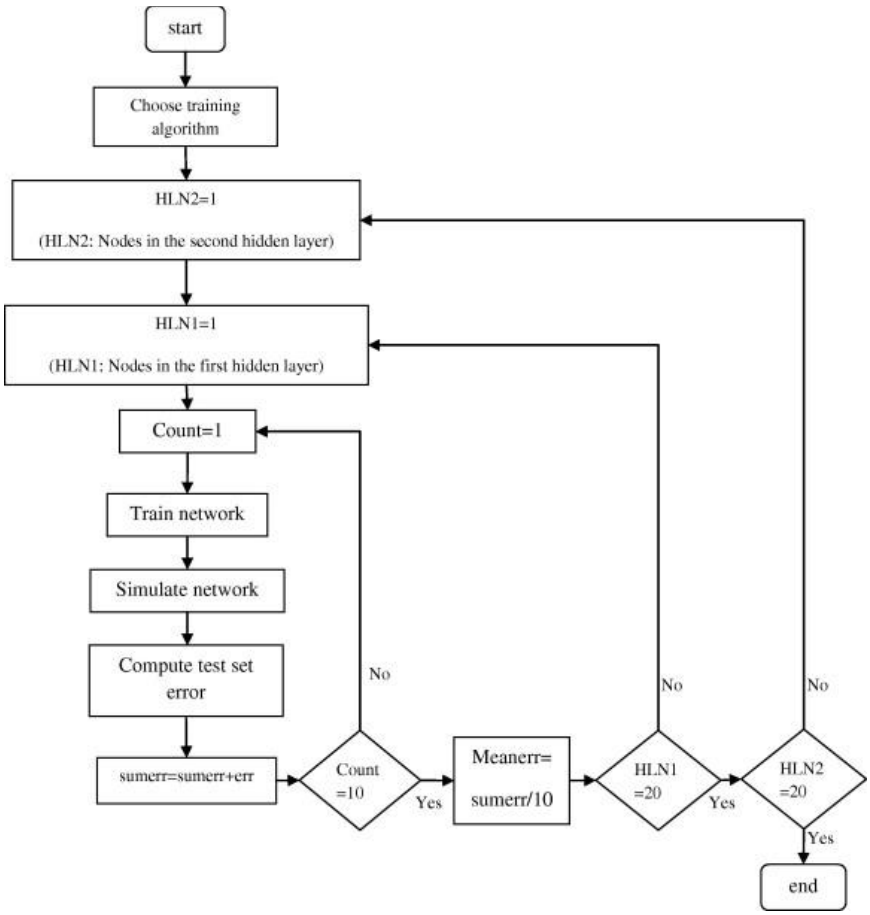

Figure 52. Flowchart of ANN architecture selection process

Besides, the process is implemented for different training algorithms and transfer functions. Therefore, the selection process starts with the simplest architecture of ANN consisting of one neuron in both hidden layers and finds the ANN model with the best performance among all different architectures, as shown in Figure 53.

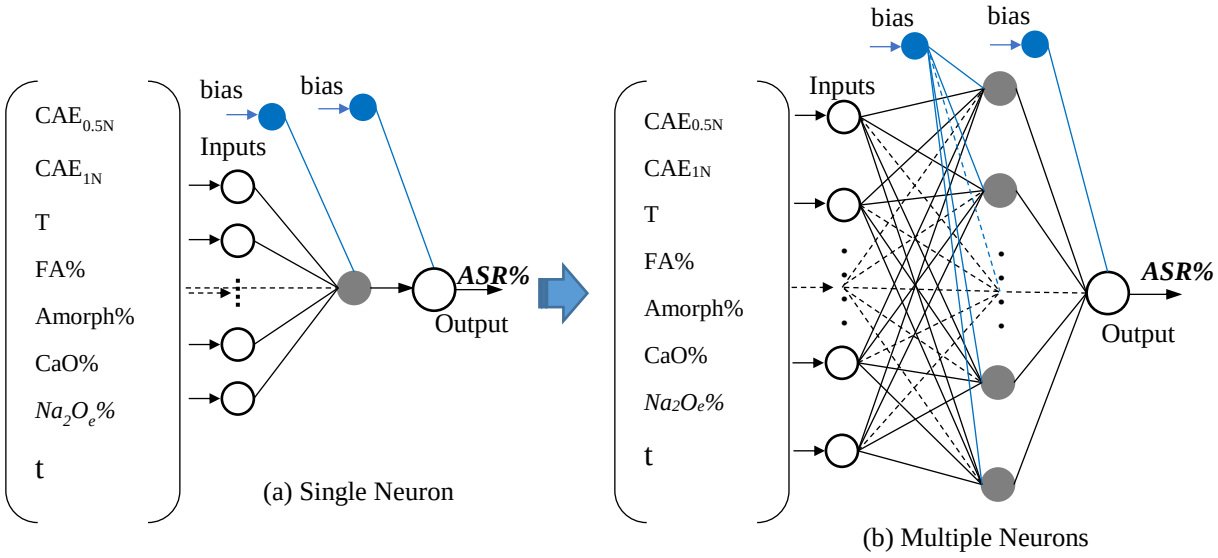

Figure 53. Schematic of ANN architectures in selection process

6.2.2.2. Results of Optimal ANN Selection Process

According to the selection process described earlier, the performance of the various ANN architectures were assessed. Among training algorithms, Levenberg-Marquardt back propagation (LMBP) was proved to be the best one. Among transfer functions, logsig was selected for the ANN model. The error of different architectures with double layer was evaluated as presented in Figure 54.

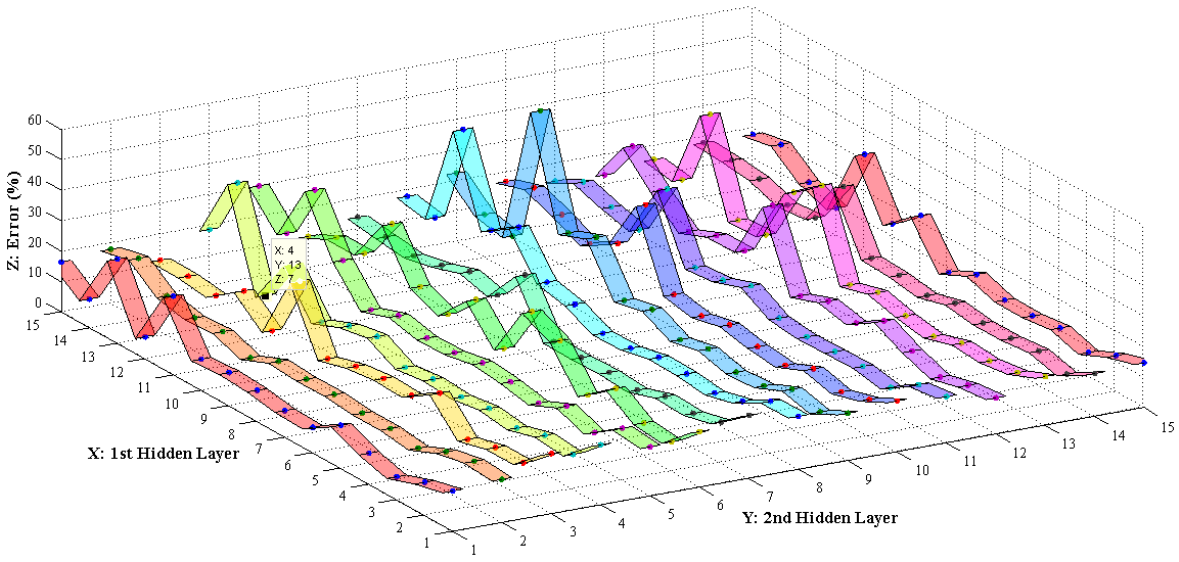

Figure 54. Error plot of the ANN architectures with two hidden layers

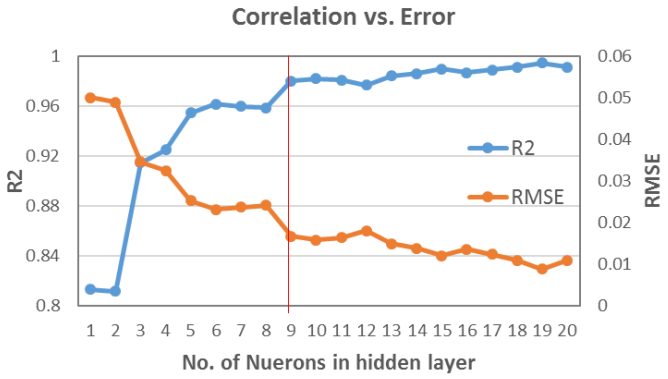

Figure 55. Correlation vs. RMSE for ANN architectures with single hidden layer

In this study, the network architecture used is called ANN 8-n-m-1, where the first digit is the number of input nodes, n is the number of nodes in the first hidden layer, m is the number of nodes in the second hidden layer, and fourth digit is the number of output nodes. Based on the model performance, the optimum architecture with two hidden layer was obtained as 8-4-13-1.

The performance of the ANN model with one hidden layer was also assessed, as shown in Figure 55, and the architecture 8-9-1 proved to have a comparable performance. Hence, due to close performance of the ANN architectures with single and double hidden layers but less complexity of the ANN with single hidden layer, it was chosen for the modeling in this study.

6.2.2.3.Optimal ANN Parameters and Performance Results

As determined in the previous step, the ANN model includes 8 nodes input layer, and one hidden layer including 7 neurons with hyperbolic logarithmic sigmoid function (logsig) activation function. BPLM is used as the training algorithm in this model. The output layer includes one node, which is the ASR expansion (%) of the mortar bar. The summary of the ANN model parameters is listed in Table 15.

Table 15. Parameters of optimal ANN model for mortar ASR expansion

No. of Nodes in input layer	8
No. of hidden layer	1
No. of neuros in hidden layer	9
No. of Nodes in output layer	1
Learning rate	1.6
Momentum rate	0.85
Train error goal	10e-5
Learning epochs	100

Once the ANN parameters were set, the model was trained, validated and tested by 60%, 20%, and 20% of the experimental datasets, respectively. Due to stochastic nature of the ANN, the modeling was implemented several times with different training, testing and validation datasets. Almost in all trials, the predicted values were in a very good agreement with experiment. The performance of the optimal ANN based on mean square error (MSE) is presented in Figure 56. One of the problems that is common in ANN models and can adversely affects their performance is called overfitting [39]. Validation sets are used to control the overfitting of the model by a process called early stopping. In this process, the iteration process is stopped when the performance on the validation set begins to decrease, even if the performance on the training set continues to increase under certain desired thresholds [39]. As is depicted in Figure 56, MSE is considered here as the network performance. It is noted from the figure that despite decreasing trend of training error, the training has stopped due to validation MSE getting constant. It is also noticed from the figure that the smallest error comes from training, and then validation, and after that test error, indicating the acceptable performance of the ANN model.

The results of train, test, and validation along with the correlation coefficient (R) are displayed in Figure 57. As it is observed from the figure, quite high correlation coefficients were obtained for train, validation, and test sets as 0.99, 0.98, and 0.96, respectively.

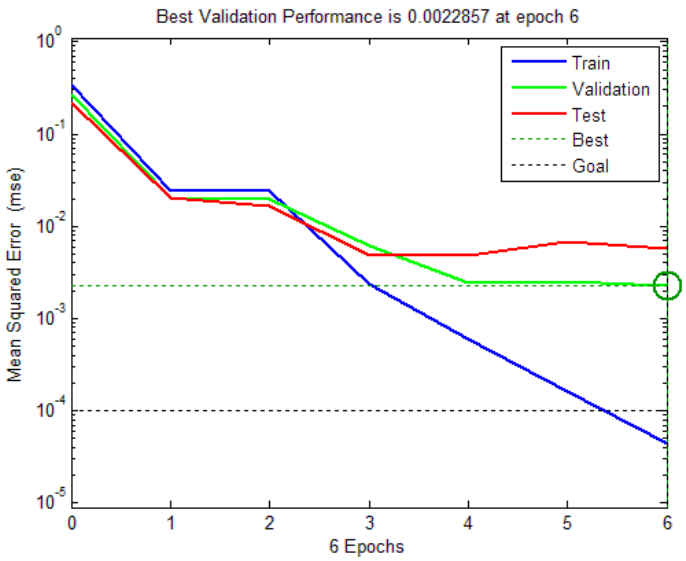

Figure 56. Performance of optimal ANN model

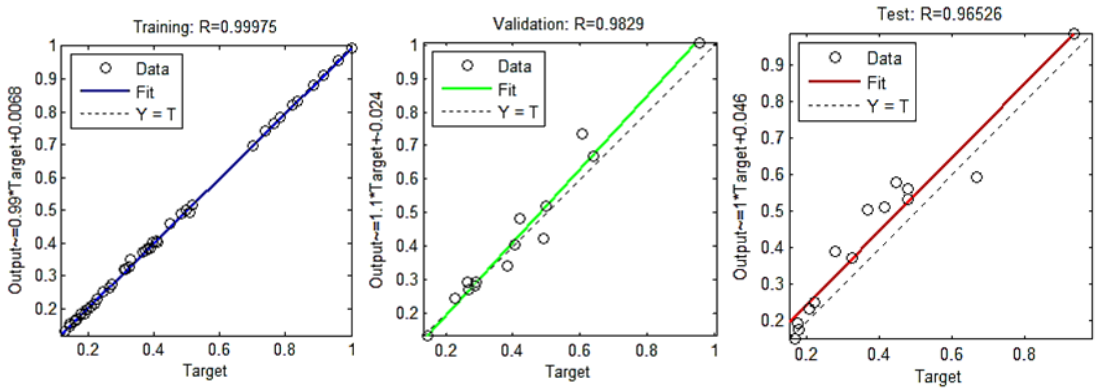

(a) (b) (c)

Figure 57. Performance of train, validation and test of ANN model

6.2.2.4.Closed-Form Formulation and Prediction Results

The final goal of this study is to find a closed-from formulation for compressive strength of the rubberized composite as a function of influencing variables through ANN model as below:

$$ASR\ expansion\ (\%)_{Mortar\ bar} = f\ (CAE_{0.5N}, CAE_{1N}, T, FA\ \%, CaO, Amorph, Na_2O_e, t) \quad (6.8)$$

All the inputs were normalized before being introduced into the model using the following equation:

$$X_{i\,(norm)} = \frac{X_i}{X_{max}} \tag{6.9}$$

The explicit equation of the proposed ANN model is obtained through the model optimum parameters, namely biases, the weights of input layer, the weights of hidden layer, and the output de-normalization.

The calculation starts in each neuron by the following equation:

$$(net)_i = \sum_{j=1}^{k} w_{ij}\, x_j + b_i \tag{6.10}$$

where, $(net)_i$ is the summation of k variables multiplied by their corresponding weights and its bias added. The logsig activation function that is used in ANN model in this study is given in Eq. (6.4)

$$f_{(x)} = \frac{1}{(1+e^{-x})} \tag{6.11}$$

By using Eqs. (6.3) and (6.4), the summation of $(net)_i$ is transformed and the model output is obtained as below:

$$f_{(net)} = \frac{1}{\left(1+e^{-(net(x))}\right)} \tag{6.12}$$

$$O_{norm} = f(Y_i) = \sum_{i=1}^{h} w_i\, f(net)_i + b \tag{6.13}$$

where, h is the number of neurons in the hidden layer and O_{norm} is the normalized output of the model. The final output of the model is obtained by de-normalizing the output of Eq. (6.13) :

$$O = Denorm(O_{norm}) \tag{6.14}$$

where, O is the final predicted output of the model. In this model, input vector is:

$$\begin{bmatrix} x_0 \\ x_1 \\ x_2 \\ x_3 \\ x_4 \\ x_5 \\ x_6 \\ x_7 \\ x_8 \end{bmatrix} = \begin{bmatrix} 1 \\ CAE_{0.5N} \\ CAE_{1N} \\ T \\ FA\% \\ Amorph \\ CaO \\ Na_2O_e \\ t \end{bmatrix} \quad (6.15)$$

The optimum weights and biases for the inputs to each neuron, $(net)_i$, are:

$$(net)_1 = 2.487 + 2.568CAE_{0.5N} + 2.734CAE_{1N} - 5.436T + 4.694FA\% + 5.848CaO - 16.611Amorph + 10.456Na_2O_e + 3.362t \quad (6.16)$$

$$(net)_2 = 1.582 + -21.171CAE_{0.5N} + -4.235CAE_{1N} + 18.349T - 19.696FA\% - 16.669CaO + 34.017Amorph - 13.427Na_2O_e - 2.863t \quad (6.17)$$

$$(net)_3 = -53.394 + 10.435CAE_{0.5N} - 40.394CAE_{1N} + 84.720T - 3.348FA\% - 170.985CaO - 316.874Amorph - 215.160Na_2O_e + 3.4878t \quad (6.18)$$

$$(net)_4 = -2.372 - 3.849CAE_{0.5N} - 2.796CAE_{1N} + 7.095T - 12.796FA\% + 4.545CaO - 1.367Amorph + 0.363Na_2O_e + 4.655t \quad (6.19)$$

$$(net)_5 = -13.316 - 10.553CAE_{0.5N} - 13.265CAE_{1N} + 24.094T - 43.371FA\% - 51.805CaO - 39.794Amorph - 30.530Na_2O_e + 83.292t \quad (6.20)$$

$$(net)_6 = -7.991 - 32.945CAE_{0.5N} - 14.407CAE_{1N} + 21.236T - 13.730FA\% - 27.006CaO + 8.284Amorph + 32.492Na_2O_e + 12.900t \quad (6.21)$$

$$(net)_7 = -3.801 - 1.501CAE_{0.5N} - 3.201CAE_{1N} + 3.769T - 2.762FA\% - 3.310CaO + 15.063Amorph - 11.083Na_2O_e - 0.840t \quad (6.22)$$

$$(net)_8 = -4.294 - 3.127CAE_{0.5N} - 4.286CAE_{1N} + 9.852T - 13.053FA\% - 0.813CaO + 16.405Amorph - 6.462Na_2O_e + 4.121t \quad (6.23)$$

$$(net)_9 = -9.707 - 0.387CAE_{0.5N} - 8.194CAE_{1N} + 10.279T - 4.003FA\% - 0.662CaO + 3.079Amorph + 2.351Na_2O_e + 22.303t \quad (6.24)$$

Applying the activation function in Eq. (15) and summation of $(net)_i$ in Eq. (16) will yield:

$$ASR(\%)_{norm} = -2.025 + 2.018\frac{1}{(1+e^{-net_1})} + 0.168\frac{1}{(1+e^{-net_2})} + 0.109\frac{1}{(1+e^{-net_3})} + 0.279\frac{1}{(1+e^{-net_4})} + 0.160\frac{1}{(1+e^{-net_5})} + 0.111\frac{1}{(1+e^{-net_6})} + 3.060\frac{1}{(1+e^{-net_7})} + 0.228\frac{1}{(1+e^{-net_8})} + 0.051\frac{1}{(1+e^{-net_9})} \quad (6.25)$$

By de-normalizing the output of Eq. (26), the final output of the model in this study as the predicted strength of the rubberized composite is obtained:

$$ASR(\%) = ASR(\%)_{norm} \times ASR(\%)_{max} = ASR(\%)_{norm} \times 0.607 \quad (6.26)$$

In order to evaluate the performance of the ANN formulation in predicting the strength of the rubberized composite, the predicted results versus the experimental ones for all datasets are plotted and compared in Figure 58, along with the coefficient of determination (R^2) and equation of the fit line. As is observed from the figure, R^2= 0.98 describes a very high correlation, indicating the fact that the prediction accuracy is pretty high, which in turn demonstrate the robustness of the ANN model and formulation. Since the performance of the model was already investigated to avoid overfitting, it can be said that the high correlation obtained herein is reliable and cannot be attributed to overfitting.

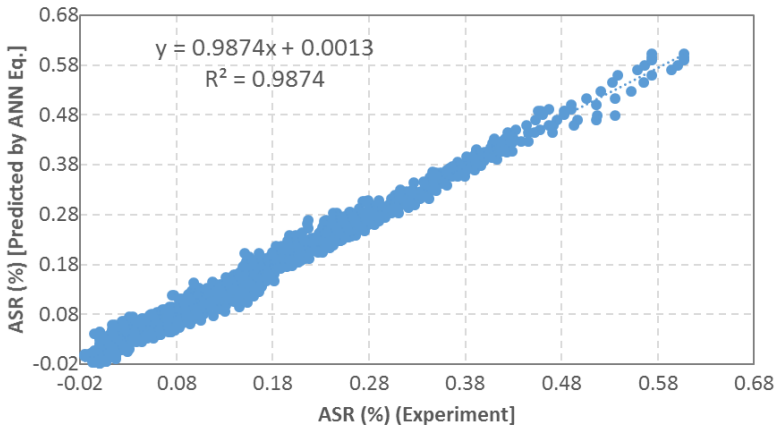

Figure 58. ANN equation vs. experiment for all ASR data

6.2.3. Results of GP Model

As described earlier in chapter 4, GP is one of the machine-learning techniques, by which a data-driven model with closed-form formulation can be derived. There are several genetic operators involved in GP, by controlling of which the accuracy and efficiency of the model can be enhanced. Since GP is somewhat slow when it comes to big data, time is also another factor that should be taken into account. Hence, multi-objective criteria such as fitness maximization, error minimization, and time optimization should be considered. The optimization approach of GP parameters to find the optimum model is presented in the following.

6.2.3.1. Multi-Objective Criteria

To find the best model in this study, multi-objective criteria were taken into account in order to:

(a) Maximize the fitness,

(b) Minimize the error

(c) Reduce the time to an optimum value

(d) Reduce the complexity to an optimum level

To address objectives (a) and (b), two new objective functions, namely OBJ_{cost} and OBJ_{fit}, are defined and evaluated in this paper as given below:

$Minimize\ (f_{cost})$

$$f_{cost} = OBJ_{cost} = \left(\frac{No._{Ts} + No._{Val}}{No._{All}}\right)\frac{(f_{Err})_{Tr}}{R^2_{Tr}} + \left(\frac{No._{All} - No._{Ts}}{No._{All}}\right)\frac{(f_{Err})_{Val}}{R^2_{Val}} + \left(\frac{No._{All} - No._{Val}}{No._{All}}\right)\frac{(f_{Err})_{Ts}}{R^2_{Ts}} +$$

$$(\Delta Err)_{Tr-Val} + (\Delta Err)_{Tr-Ts}, with\ Val\ \&\ Ts\ sets\ available \quad (6.27)$$

$$f_{cost} = OBJ_{cost} = \left(\frac{No._{Ts}}{No._{All}}\right)\frac{(f_{Err})_{Tr}}{R^2_{Tr}} + \left(\frac{No._{All} - 2No._{Ts}}{No._{All}}\right)\frac{(f_{Err})_{Ts}}{R^2_{Ts}} +$$

$$(\Delta Err)_{Tr-Ts}, with\ only\ Ts\ set\ available \quad (6.28)$$

$$f_{err} = Error\ Function = RMSE + MAE + RRSE + RAE \quad (6.29)$$

$$(\Delta Err)_{Tr-Val} = |(f_{err})_{Tr} - (f_{err})_{Val}| \quad (6.30)$$

$$(\Delta Err)_{Tr-Ts} = |(f_{err})_{Tr} - (f_{err})_{Ts}| \quad (6.31)$$

$Maximize\ (f_{fit})$

$$f_{fit} = OBJ_{fit} = \left(\frac{No._{Ts} + No._{Val}}{No._{All}}\right)\frac{R^2_{Tr}}{(f_{Err})_{Tr}} + \left(\frac{No._{All} - No._{Ts}}{No._{All}}\right)\frac{R^2_{Val}}{(f_{Err})_{Val}} + \left(\frac{No._{All} - No._{Val}}{No._{All}}\right)\frac{R^2_{Ts}}{(f_{Err})_{Ts}} -$$

$$(\Delta R^2)_{Tr-Val} - (\Delta R^2)_{Tr-Ts} \quad (6.32)$$

$$(\Delta R^2)_{Tr-Val} = |(R^2)_{Tr} - (R^2)_{Val}| \quad (6.33)$$

$$(\Delta R^2)_{Tr-Ts} = |(R^2)_{Tr} - (R^2)_{Ts}| \quad (6.34)$$

It should be noted that when there is just either validation or test set available, the term for which the dataset is not available is eliminated and the equation turns into Eq. (6.21).

To find the best model, either OBJ_{cost} or OBJ_{fit} can be selected to be minimized or maximized, respectively. In order to see which *OBJ* would lead to a better outcome, the sensitivity

of both should be evaluated which are elaborated in the following. The objectives (c) and (d) are governed by the parameter settings such as number of chromosomes, number of genes, head size and linking functions. Therefore, in order to assess the performance of the model based upon its parameter settings i.e. objective (d), design of experiment (DOE) was used to find the optimum values for the parameter settings in order to optimized objectives (a), (b), and (c), which is described in more details in the following section.

6.2.3.2.Objective Function Sensitivity Criteria

In order to evaluate the sensitivity of the each of aforementioned OBJs, one of the measures of dispersion such as Coefficient of Range (COR) can be used to assess the sensitivity of the objective function.

$$COR = \frac{f_{max} - f_{min}}{f_{max} + f_{min}} \times 100 \quad (6.35)$$

A similar parameter called "Percent Relative Range" (PRR) is defined and used in this study as given below. This parameter is used to better evaluate the sensitivity of the objective function to the optimum value.

$$PRR = \frac{f_{max} - f_{min}}{f_{max}} \times 100 \quad (6.36)$$

6.2.3.3.Optimization of Parameter Settings for GEP

Since there are several parameter settings that affect GEP performance in terms of fitness, time, and complexity, first the most influential parameter settings were selected which include number of chromosomes, number of genes, head size, and linking functions (Cevik 2008). Since there is no particular method to determine the suitable range of the parameters in GEP, the most

practical range of the parameters were selected based on the work of other researchers (Cevik, 2008).. In order to optimize the parameter settings and cut down on computation cost and time, design of experiment (DOE) method was employed to design the combination of GEP parameters and Taguchi method was applied to optimize the design and find the optimum values of each parameter.

Taguchi methodology for optimization can be divided into four phases: planning, conducting, analysis and validation. Each phase has a separate objective and contributes towards the overall optimization process. Taguchi's methods focus on the effective application of engineering strategies rather than advanced statistical techniques (Singh et al., 2002).

In order to predict the results of the experiment designed by Taguchi method, Eq. 6.30 is used:

$$\eta = \eta_m + \sum_{i=1}^{f}(\eta_i - \eta_m) \quad (6.37)$$

Where, η_m is the overall mean value of all Signal/Noise (S/N) ratios in all experimental runs, f is the number of factors, and η_i is the mean of S/N ratios corresponding a factor levels (Ross 1996, Dubey and Yadava 2007). In order to calculated the optimum results, the equation can be written as:

$$\eta_{opt} = \eta_m + \sum_{i=1}^{f}(\eta_{i-opt} - \eta_m) \quad (6.38)$$

where, η_{opt} is the mean of S/N ratios corresponding to the factors' optimum levels.

6.2.3.4.Multi-Objective Optimization

As mentioned earlier in the paper, two objective functions were defined as cost (OBJ_{cost}) and fitness (OBJ_{fit}), which the former should be minimized and the latter should be maximized. However, to consider the computation time in this study as one indicator of complexity, run time

of the models were calculated and another objective function, namely OBJ_{time} was also taken into account. Therefore, multi-objective optimizations of the time-cost and time-fitness were also implemented to come up with the most efficient GEP model. To do so, two new multi-objective cost functions (*MultiOBJ*) were defined to include OBJ_{cost} - OBJ_{time} and OBJ_{fit} - OBJ_{time} as two comparative multi-objective criteria of model performance. In order to form the multi-objective cost functions, first the normalized OBJ_{cost}, OBJ_{fit}, and OBJ_{time}, were calculated through the following equations:

$$NorOBJ_{time} = \frac{OBJ_{time} - OBJ_{time_{min}}}{OBJ_{time_{min}}} \times 100 \quad (6.39)$$

$$NorOBJ_{cost} = \frac{OBJ_{cost} - OBJ_{cost_{min}}}{OBJ_{cost_{min}}} \times 100 \quad (6.40)$$

$$NorOBJ_{fit} = \frac{OBJ_{fit_{max}} - OBJ_{fit}}{OBJ_{fit_{max}}} \times 100 \quad (6.41)$$

Then, the multi-objective cost functions (*MultiOBJs*) were defined as below which need to be minimized to find the most time-efficient and accurate model:

$$MultiOBJ_{fit-time} = NorOBJ_{fit} + NorOBJ_{time} \quad (6.42)$$

$$MultiOBJ_{cost-time} = NorOBJ_{cost} + NorOBJ_{time} \quad (6.43)$$

6.2.3.5. GP Prediction Results

Based on the optimum parameters, three different models were developed using GP with different complexity and accuracy. The equations of the developed models are given below and the variables as well as the coefficients of each are reported in Table 16:

GP I:

y = (((1.0/(d(0)))-(d(2)-(d(3)-d(5))))+(d(3)*Log(Log(G1C9))))

y = y * (1.0-((1.0-d(2))*gepTanh((Atn((1.0-Sqr(d(7))))-(1.0-Sqr(d(7)))))))

y = y * Exp((gep3Rt((((gep3Rt(G3C4)*(G3C8-d(5)))*(G3C4/G3C7/d(1)))-d(0)))+G3C9))

y = y * (d(5)+(d(7)+(1.0/((((1.0/(((d(2)/G4C1/G4C7)))+(gepTanh(G4C3)+d(6))) ^ 3)))))

y = y * (1.0/((((((G5C8+d(3))+gep3Rt(d(7)))/(1.0/((G5C4-d(6))))/Log(d(2)))-Atn(G5C3))))

(6.44)

GP II:

y = gepTanh(gepTanh(gepTanh(((G1C1 ^ 3)/((G1C6*d(1))*(G1C8+d(6)))/(d(3)-
G1C2)/(d(0)+d(3))))))

y = y * ((1.0-gepTanh(gep3Rt(gep3Rt(d(7)))))*((1.0/((1.0/(((d(2)-d(6))))))*(gep3Rt(d(7)) ^ 3)))

y = y * gep3Rt((((1.0-(1.0-(d(5) ^ 3)))-gep3Rt(((d(7) ^ 2)+(d(7)*G3C3*G3C1))))+d(0)))

y = y * (((1.0/(((1.0/((d(6)+(((d(4)-d(0))-d(0)) ^ 2))))-G4C1))) ^ 2) ^ 2)

y = y * gep3Rt(((((gep3Rt(d(4))-d(6))+(d(3)-d(2)))+(gep3Rt(d(4))+d(1)))-d(6))) (6.45)

GP III:

y = gep3Rt(((d(0)-gep3Rt(((d(0)*G1C9*d(0))+(d(7) ^ 2))))+(1.0-(1.0-(d(5) ^ 3)))))

y = y * ((1.0-gepTanh(gep3Rt(gep3Rt(d(7)))))*((1.0/((1.0/(((d(2)-d(1))))))*(gep3Rt(d(7)) ^ 3)))

y = y * gep3Rt((((((d(3)-d(2))+Atn(d(0)))+((d(4)/G3C5)-d(6)))+d(1))-d(6)))

y = y * gepTanh(gepTanh(gepTanh(((G4C4 ^ 3)/((d(1)*G4C6)*(G4C8+d(6)))/(d(3)-
G4C4)/(d(0)+d(3))))))

y = y * (((1.0/(((1.0/(((((d(4)-d(0))-d(0)) ^ 2)+d(6))))-G5C1))) ^ 2) ^ 2) (6.46)

Table 16. Variables and Coefficients of the GP I, II, and III models

GEP I										
G1C9	**G3C9**	**G3C4**	**G3C7**	**G3C8**	**G4C1**	**G4C7**	**G4C3**	**G5C3**	**G5C8**	**G5C4**
5.867	-6.944	-3.633	-0.942	11.856	3.664	-9.901	2.358	123.151	8.992	-9.951
GEP II										
G1C1	**G1C2**	**G1C6**	**G1C8**	**G3C3**	**G3C1**	**G4C1**				
-6.891	-7.352	9.529	5.313	6.580	-7.650	2.409				
GEP III										
G1C0	**G2C9**	**G4C4**	**G4C0**	**G4C6**	**G4C8**	**G5C1**	**G5C6**			
-2.504	8.265	-6.928	-6.767	9.424	4.850	2.376	1.564			
Variables										
d(0)	**d(1)**	**d(2)**	**d(3)**	**d(4)**	**d(5)**	**d(6)**	**d(7)**			
$AE_{0.5N}$	AE_{1N}	T	FA%	Amorph	CaO	Na_2O_e	t			

The plots of the predicted vs. experimental values of ASR (%) for three GP models are depicted in Fig 59.

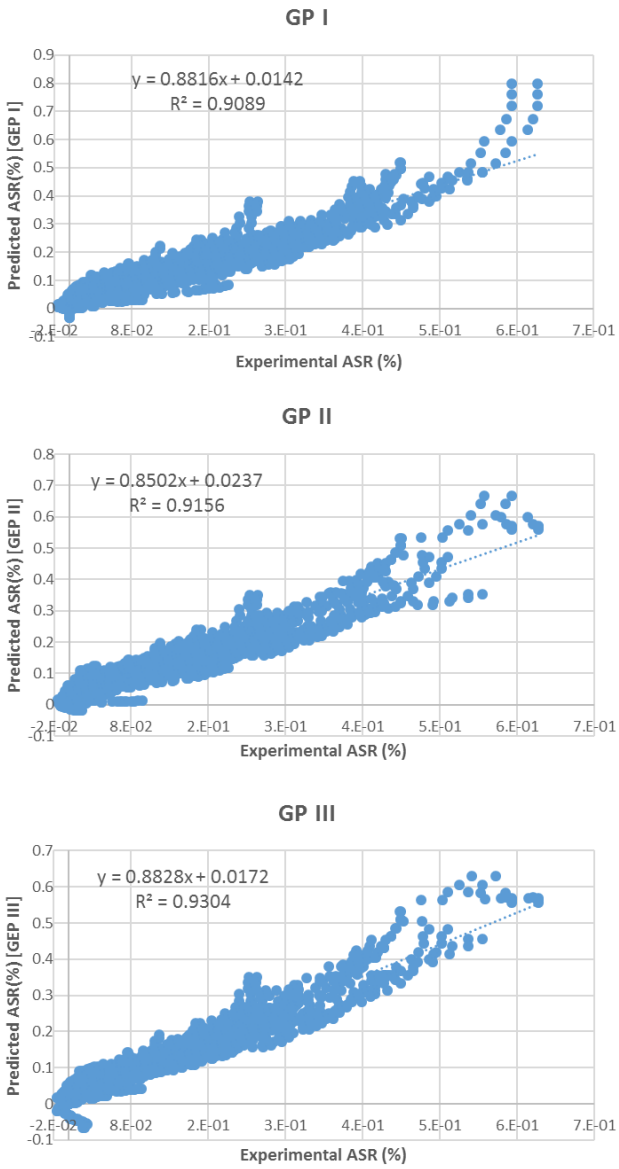

Figure 59. Prediction results along with the correlation of GPI, GP II, and GP III

For better performance demonstration and comparison of the models, the results of ASR prediction for a mix containing 30% of FA1 at 80° C is plotted in Figure 60 along with the experimental data points. It is observed that the GP models can well capture the ASR behavior based on the influencing variables.

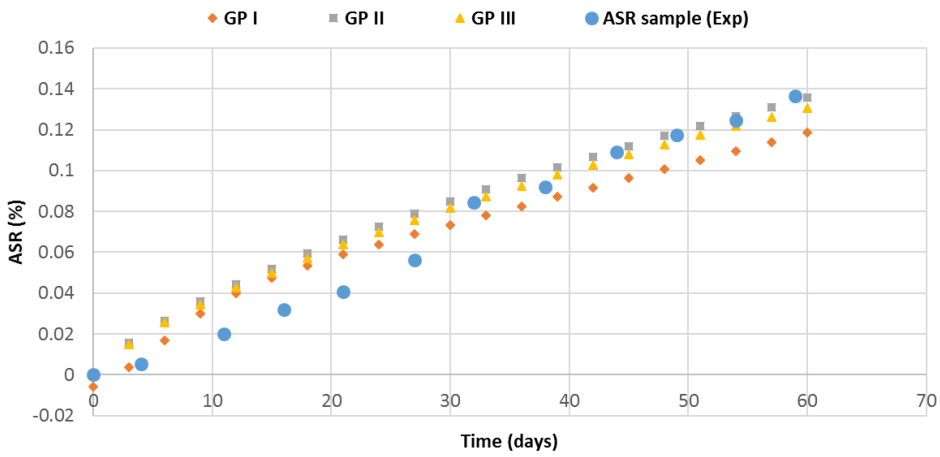

Figure 60. ASR prediction of GEP I, II, and III for a mix containing 30% of FA1 at 80° C

6.2.4. Results of ANFIS Model

Out of the total 2363 experimental datasets, training, validation, and testing datasets were randomly selected as 1183, 590, 590 datasets, respectively. There are two methods to construct the model in MATLAB Fuzzy Logic Toolbox [57], namely grid partition and subtractive clustering. With the number of inputs growing in the grid partition model, the membership function shows exponential growth, thereby leading to a paralyzed calculation system. By using the subtractive clustering method, it is easy to generate an input–output rule model without being computationally expensive [58-60]. In this study, grid partitioning was chosen for ANFIS modeling. Gaussian membership functions (MF) were employed in the model and two MF was used for each variable.

For training of the model in ANFIS, either back-propagation technique or hybrid-learning method can be used. The latter utilizes the gradient descent and the least-squares method to find a feasible set of antecedent and consequent parameters, which make it more efficient. Thus in this study, the later method was used to train the ANFIS model. Several trial runs were also performed and eventually 100 epochs were selected for training of the model.

The results of training, validation, and testing of the ANFIS model is presented in Figure 61. as is noted from the coefficient of determination (R2) in each plot, high correlations are observed in all training, validation, and testing phases.

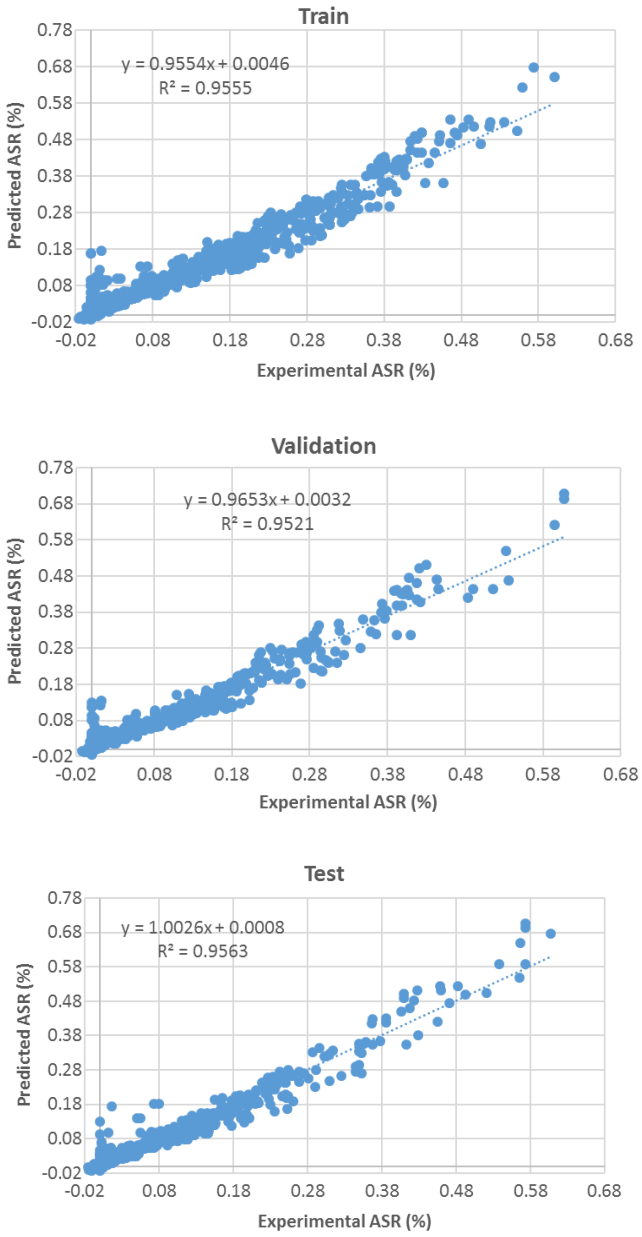

Figure 61. Results of training, validation, and testing of ANFIS model for ASR expansion of mortar samples

6.3. Results of Machine-Learning Predictions for Concrete Excluding Mortar Expansion

This section presents the results of prediction models for ASR concrete expansion based on ACCT. The modeling results of this section is divided into two categories, namely (a) concrete expansion prediction models independent of mortar expansion, and (b) concrete expansion prediction models based mortar expansion obtained from AMBT. The goal of the former is to develop the ASR prediction model for concrete based on influencing parameters identified in ACCT, thereby meeting the need for ASR prediction at the mix design phase without conducting the test. The aim of the latter is to examine the relationship between mortar bar and concrete expansion behavior more comprehensively, and study how ASR expansion of concrete can be derived from mortar expansion. Moreover, since this study deals with multi-scale assessment of ASR including aggregate, mortar, and concrete scales, this study can help reveal how including and excluding the mortar scale affects the accuracy and complexity of the machine-learning models.

To develop the models for ASR expansion of concrete based on ACCT and independent of mortar expansion, 9 variables were considered which are similar to those of mortar model except one additional variable that is alkali loading (AL). It should be mentioned that the levels of some variables are different from those of mortar based on the objective of the model, test requirements, and data availability. For example, two temperature such as 60°C and 38°C were taken into account. Besides, to provide a better possibility of subsequent comparison of concrete and mortar behavior, only the experimental data of concrete with non-reactive coarse and reactive fine were selected to develop the models. Presented in the following are the results of different models for ASR prediction of concrete independent of mortar behavior.

6.3.1. ANN Prediction Results for Concrete

As mentioned earlier, different training algorithms, transfer functions, number of hidden layers, and number of neuron in hidden layers were evaluated and the optimum ANN architecture based on lower prediction error and higher correlation was selected as 9-8-1 with *trainlm* training algorithm and *logsig* as the transfer function. In order to come up with the closed-form formulation, the coefficients of the equations used in the model were obtained which are presented in the following:

$$ASR(\%)_{norm} = 0.002 + 0.383\frac{1}{(1+e^{-net_1})} + 0.477\frac{1}{(1+e^{-net_2})} - 0.458\frac{1}{(1+e^{-net_3})} - 0.888\frac{1}{(1+e^{-net_4})} + 0.492\frac{1}{(1+e^{-net_5})} + 0.450\frac{1}{(1+e^{-net_6})} - 0.446\frac{1}{(1+e^{-net_7})} + 0.442\frac{1}{(1+e^{-net_8})} \quad (6.47)$$

where,

$$net(x) = \begin{bmatrix} net_1 \\ net_2 \\ net_3 \\ net_4 \\ net_5 \\ net_6 \\ net_7 \\ net_8 \end{bmatrix} = \begin{bmatrix} 17.979 & -13.449 & -23.061 & -25.042 & -4.919 & 1.609 & 19.665 & -14.061 & 32.596 & 39.268 \\ -4.708 & 53.317 & -20.244 & -32.099 & 31.722 & -26.148 & -1.248 & -1.673 & -26.209 & 48.197 \\ 53.977 & 10.321 & -25.707 & -35.864 & -18.216 & 3.634 & 26.809 & -20.868 & -48.193 & 52.701 \\ 10.016 & -8.683 & -7.398 & -21.851 & 6.886 & -15.190 & 2.605 & -0.418 & 19.560 & 33.436 \\ 9.526 & -14.245 & 8.773 & -17.318 & 3.317 & -9.914 & -4.379 & 1.348 & 6.205 & 24.742 \\ 13.219 & -15.856 & -13.478 & -5.279 & -8.898 & -15.451 & 35.4329 & -24.848 & 4.405 & 51.329 \\ -2.868 & -36.486 & -15.051 & -2.652 & 3.317 & -8.511 & 3.992 & 2.926 & 20.850 & 41.736 \\ 1.403 & 25.760 & 1.768 & -41.974 & 30.220 & 10.258 & -17.155 & -6.949 & -8.400 & 12.855 \end{bmatrix} \begin{bmatrix} x_0 \\ x_1 \\ x_2 \\ x_3 \\ x_4 \\ x_5 \\ x_6 \\ x_7 \\ x_8 \\ x_9 \end{bmatrix} \quad (6.48)$$

$$\begin{bmatrix} x_0 \\ x_1 \\ x_2 \\ x_3 \\ x_4 \\ x_5 \\ x_6 \\ x_7 \\ x_8 \\ x_9 \end{bmatrix} = \begin{bmatrix} 1 \\ CAE_{0.5N} \\ CAE_{1N} \\ T \\ FA\% \\ Amorph \\ CaO \\ Na_2O_e \\ AL \\ t \end{bmatrix} \tag{6.49}$$

$$ASR(\%) = ASR(\%)_{norm} * ASR(\%)_{max} \tag{6.50}$$

The predicted ASR expansion values versus experiment for different concrete mixes are plotted in Figure 62. It is seen form the plot the ANN model with 8 neurons yield a very high correlation. To evaluate the accuracy of the ANN model, a sample ASR expansion curve predicted by the model is compared with the experiment in Figure 63. it is observed that the ANN formulation can well capture the experimental ASR expansion curve.

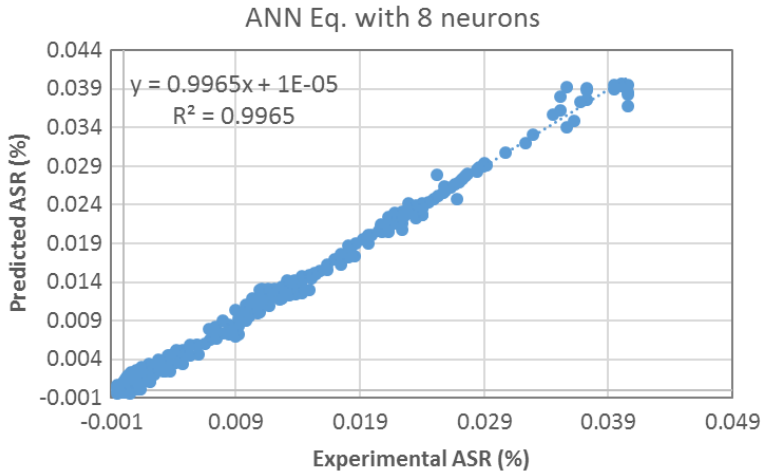

Figure 62. ANN prediction vs. experiment for concrete expansion independent of mortar expansion

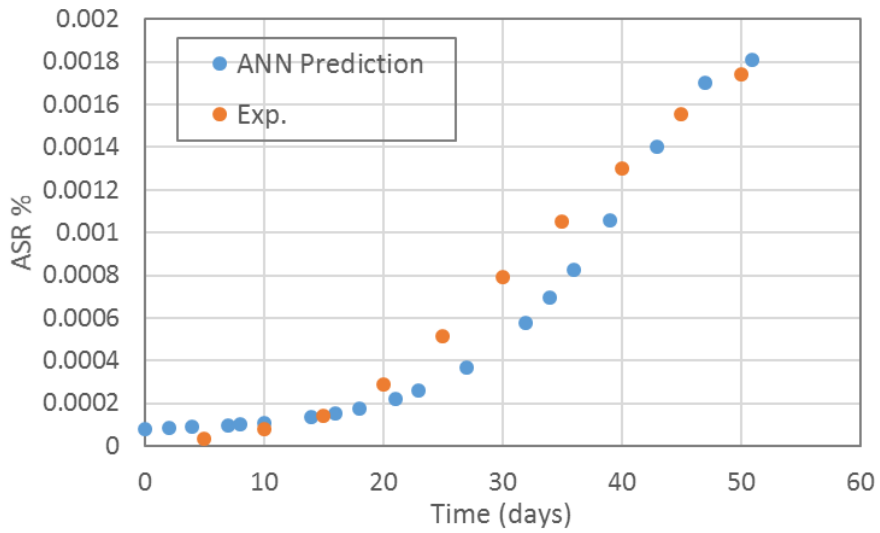

Figure 63. Prediction of ASR expansion for concrete with 20% F1 at 60C for El-Indio aggregate

6.3.2. GP Prediction Results for Concrete

The GP formulation for ASR expansion of concrete is given below, and the coefficients of the model are reported in Table 17. the prediction correlation of the train, test, and all datasets for concrete expansion independent of mortar is also displayed in Figure 64.

y = (((LN(LN(d(7)))*((d(7)*d(7))-(d(0)/d(7))))-Sqr((d(1) ^ 2)))+d(8))

y = y / (1.0-((d(2) ^ 2)/(Atn((d(1)-G2C9))-d(5))/(((G2C9*d(1))-d(7)) ^ 2)))

y = y / gepTanh(((((G3C3*G3C4)/Log(d(2)))-Atn((d(8) ^ 3)))+(gep3Rt(G3C9)+(d(7)*G3C6))))

y = y / (((((d(1)+d(4)) ^ 2) ^ (1/4))-d(2))-(gep3Rt((1.0-(G4C1+d(4))))-d(0)))

y = y / (d(7) ^ 3)

y = y / gep3Rt((d(2)-(Sqr((gep3Rt(G6C5) ^ 3))*gep3Rt(((d(4)+d(3))-(d(8)-d(4)))))))

y = y / (G7C5+(((1.0-G7C9) ^ 2)/(d(7)*(G7C4 ^ 3))/((d(7)*d(7))*Exp(d(5))*G7C7))) (6.51)

Table 17. Variables and Coefficients of the GP model for concrete

GP model coefficients										
G1C9	**G3C9**	**G3C4**	**G3C7**	**G3C8**	**G4C1**	**G4C7**	**G4C3**	**G5C3**	**G5C8**	**G5C4**
5.867	-6.944	-3.633	-0.942	11.856	3.664	-9.901	2.358	123.151	8.992	-9.951
GP model variables										
d(0)	**d(1)**	**d(2)**	**d(3)**	**d(4)**	**d(5)**	**d(6)**	**d(7)**	**d(8)**		
$AE_{0.5N}$	AE_{1N}	T	FA%	Amorph	CaO	Na_2O_e	AL	t		

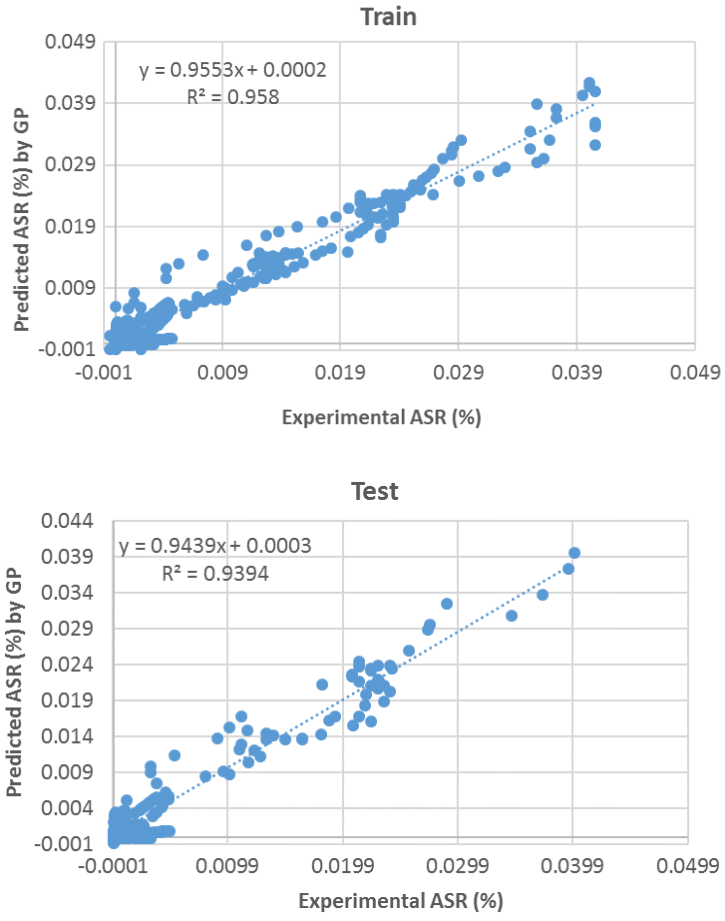

Figure 64. Prediction vs. experimental values of ASR expansion for train, test, and all datasets

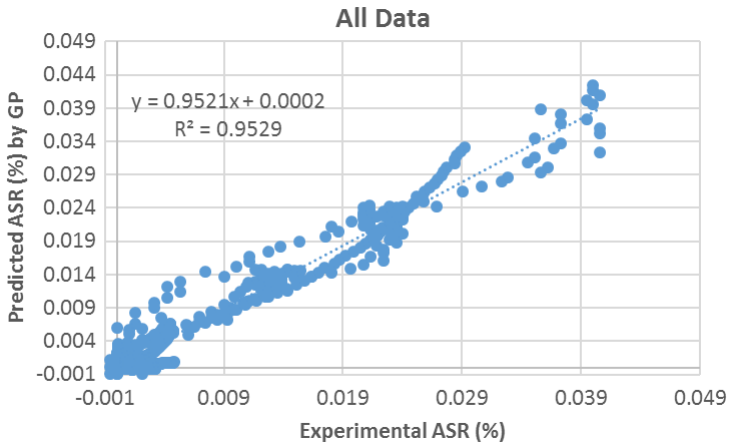

Figure 64 Continued.

6.3.3. ANFIS Prediction Results for Concrete

Prediction results of the ANFIS model developed for concrete expansion is presented in Figure 65. As it is observed from the plots, the prediction correlations relative to those of ANN and GP models are not high. It should be also noted that the correlations are lower than those of ANFIS model for mortar expansion. However, in order to assess the effect of influencing variables on concrete expansion in ANFIS model, the parametric study of the model was performed, the results of which are depicted in Figure 66.

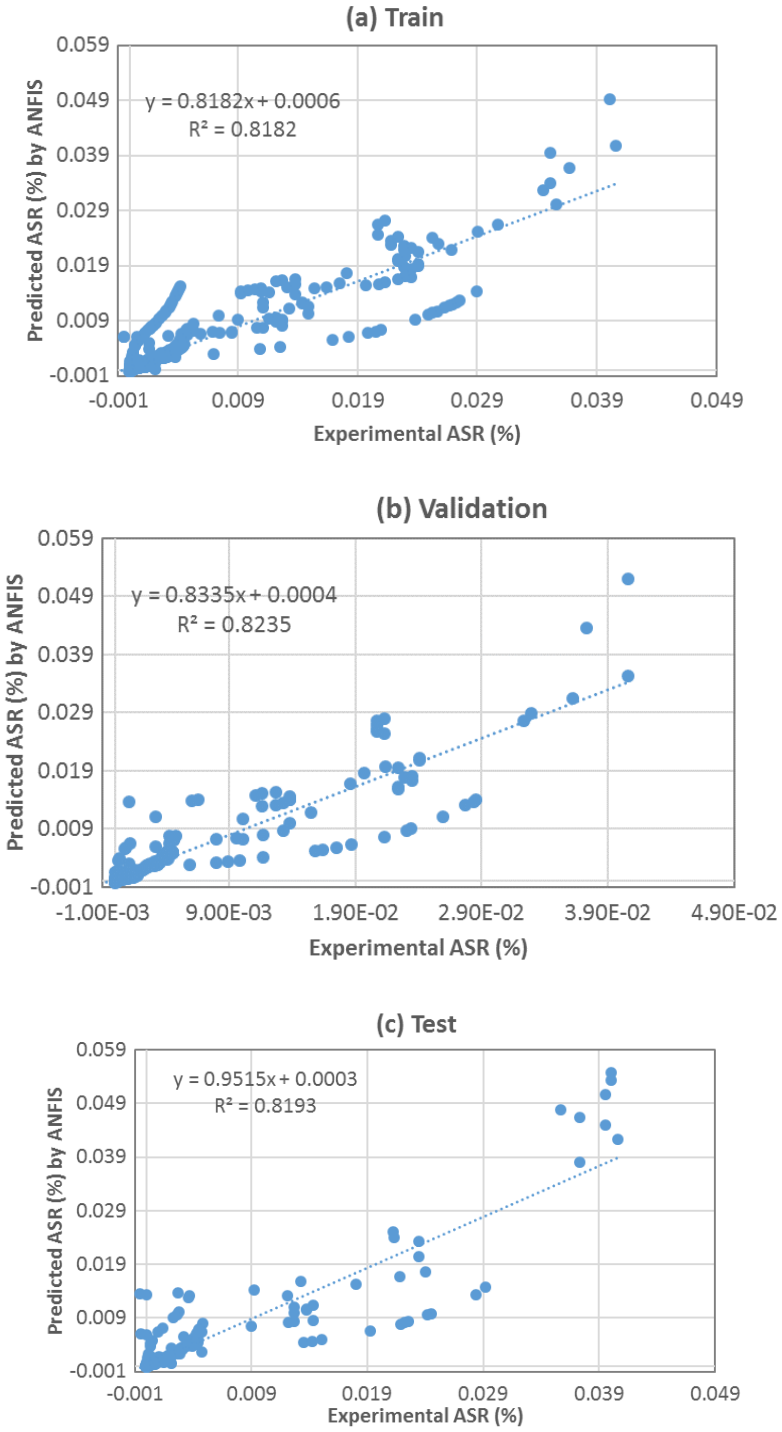

Figure 65. Prediction results of ANFIS model for train, validation, test ,and all datasets of concrete expansion

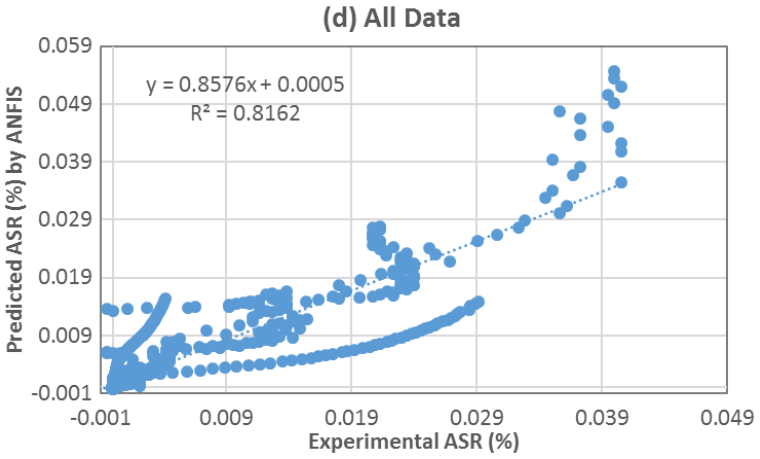

Figure 65 Continued

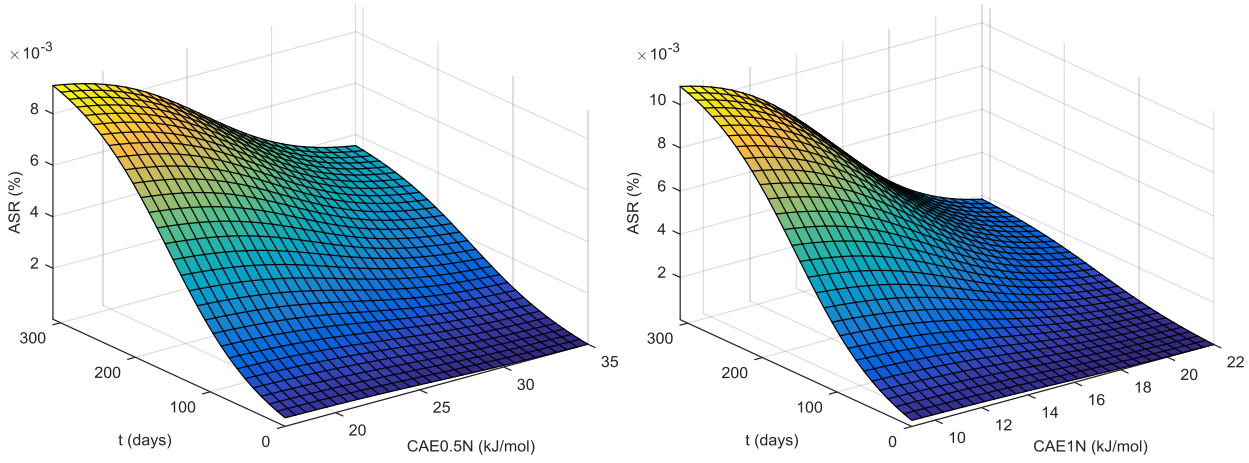

(a) (b)

Figure 66. Parametric study of ANFIS model for the effect of influencing variables on concrete expansion

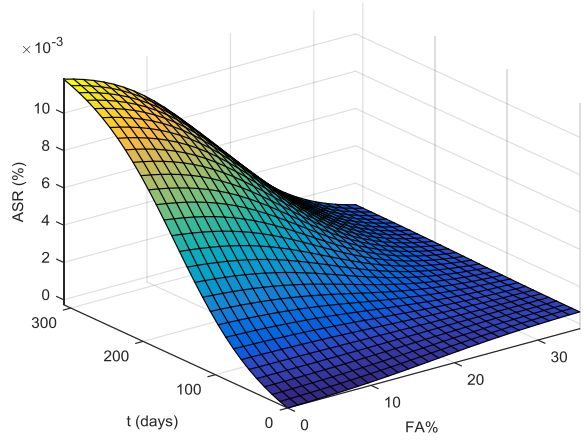
×10^-3
ASR (%)
t (days)
FA%

(c)

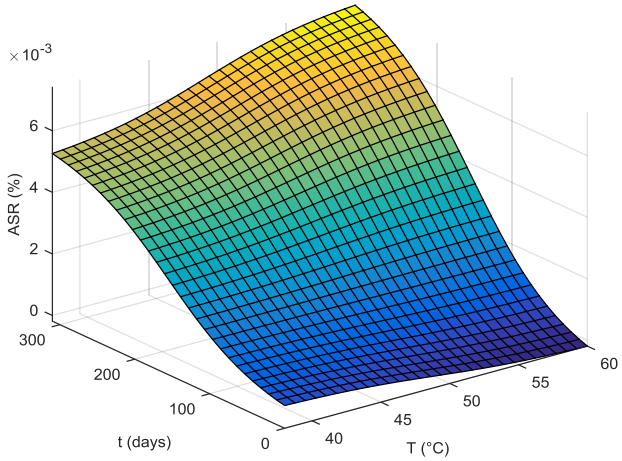
×10^-3
ASR (%)
t (days)
T (°C)

(d)

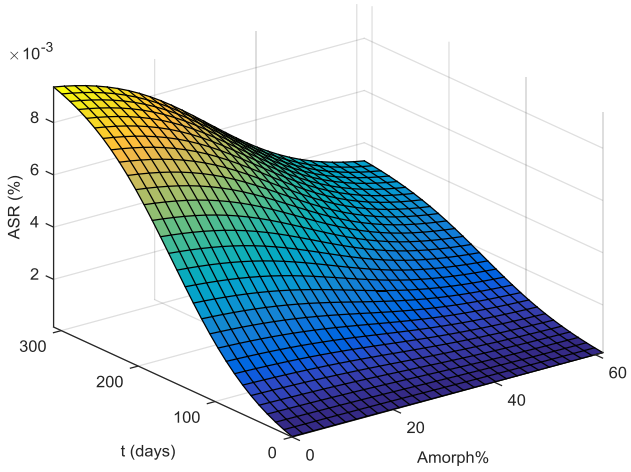
×10^-3
ASR (%)
t (days)
Amorph%

(e)

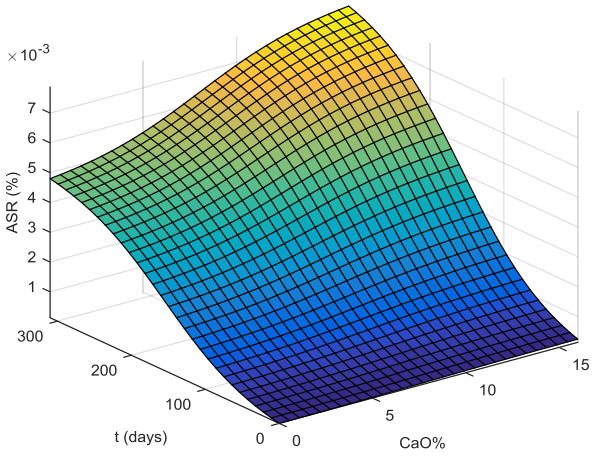
×10^-3
ASR (%)
t (days)
CaO%

(f)

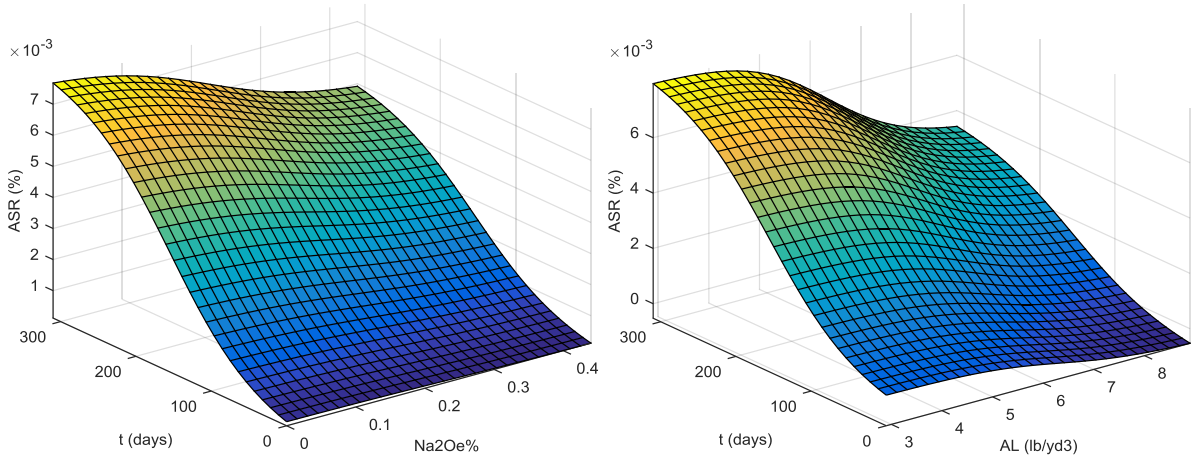

(g) (h)

Figure 66 Continued.

6.4. Results of Machine-learning Predictions for Concrete Including Mortar Expansion

As another complementary step of the multi-scale modeling of ASR expansion in concrete, model development using the results of VCMD, AMBT, and ACCT was undertaken, the results of which are presented in this section. To do so, the mix designs for which both ACCT and AMBT data were available, were considered, and the data of the tests conducted their standard temperature (80°C for AMBT, and 60°C for ACCT), were selected. Hence, since the purpose of this modeling was to derive the ACCT expansion models based on the influencing variables and AMBT results, the temperature variable was not considered for this model development. The variables taken into account include fine aggregates' CAE at 0.5N and 1N, FA percentage, FA type variables, i.e. Amorphous phase, CaO, and Na_2O_e, alkali loading, time, and mortar bar expansion (MBE). The results of ANN, GP, and ANFIS for ASR expansion of concrete based on mortar are presented below. In this section, to demonstrate that these models can help with the prediction of new,

missing, or noisy data, the results of an ACCT test with missing data (due to LVDT malfunctioning), was used to assess the robustness of the predicted results.

Regarding the concrete expansion prediction using mortar bar data, it should be pointed out that the corresponding mortar expansion data at each time should be available, which requires AMBT testing up to 60 days which is time-consuming and unfavorable. However, using the AMBT prediction model developed earlier, the needed mortar expansion data can be generated easily to be used in concrete ASR prediction model.

6.4.1. ANN Prediction of ACCT Based on AMBT

The equation of ANN model for concrete expansion based on mortar bar is given below. As is observed, the ANN model only comprises 3 neurons (net) in the hidden layer, and hence much less complex than the concrete model independent of mortar bar. By looking at the prediction vs. experiment plot in Figure 67, it is noted that even with less complexity of the model, prediction results show a very high accuracy with a correlation greater than that of concrete model independent of mortar bar.

To better assess the performance of the model, the ASR expansion of a concrete mix with missing data, which was not used in model construction is plotted versus predicted values by ANN model in Figure 68. It is observed that the ANN formulation can accurately predict the entire ASR curve including the missing data.

$$ASR(\%)_{norm} = -3.533 \times 10^{-06} + 0.105\frac{1}{(1+e^{-net_1})} + 0.459\frac{1}{(1+e^{-net_2})} + 0.474\frac{1}{(1+e^{-net_3})} \quad (6.52)$$

where,

$$net(x) = \begin{bmatrix} net_1 \\ net_2 \\ net_3 \end{bmatrix} =$$

$$\begin{bmatrix} -38.257 & 9.053 & -34.238 & 16.036 & -4.001 & -13.748 & 19.821 & 56.906 & 1.007 & 6.153 \\ 4.384 & -23.469 & 0.208 & 20.622 & -6.873 & -17.272 & -11.647 & 2.611 & 6.614 & 0.272 \\ 5.770 & -36.689 & -1.275 & -4.099 & -10.287 & -7.102 & -4.879 & 8.739 & 9.877 & 4.496 \end{bmatrix} \begin{bmatrix} x_0 \\ x_1 \\ x_2 \\ x_3 \\ x_4 \\ x_5 \\ x_6 \\ x_7 \\ x_8 \\ x_9 \end{bmatrix} \quad (6.53)$$

$$\begin{bmatrix} x_0 \\ x_1 \\ x_2 \\ x_3 \\ x_4 \\ x_5 \\ x_6 \\ x_7 \\ x_8 \\ x_9 \end{bmatrix} = \begin{bmatrix} 1 \\ CAE_{0.5N} \\ CAE_{1N} \\ FA\% \\ Amorph \\ CaO \\ Na_2O_e \\ AL \\ t \\ MBE \end{bmatrix} \quad (6.54)$$

$$ASR(\%) = ASR(\%)_{norm} * ASR(\%)_{max} \quad (6.55)$$

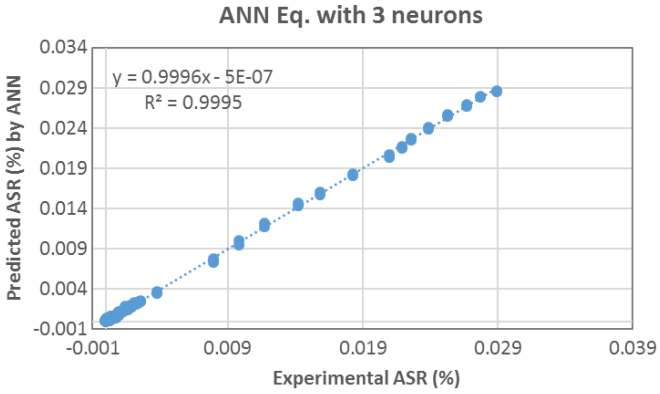

Figure 67. Predicted ASR by ANN formulation vs. experiment for all data points

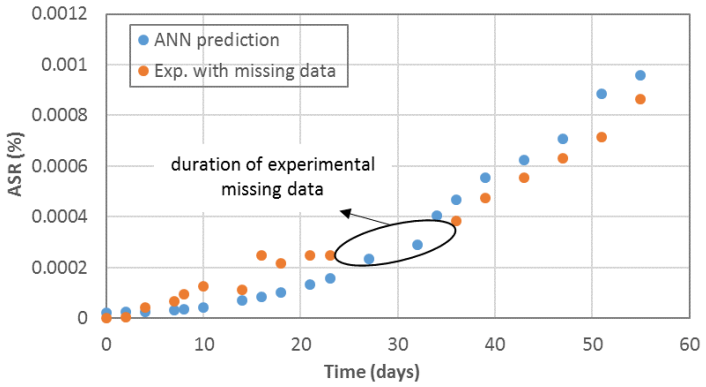

Figure 68. Comparison of predicted ACCT ASR curve with that of experiment for FA1, 30%, 60°C, AL=3.2 lb/yd^3

6.4.2. GP Prediction Results of ACCT Based on AMBT

Two different GP models were also developed to capture the ASR behavior of ACCT based on mortar bar expansion. As is seen from the equations below, the complexity of both GP I and GP II models are low, with the former using the multiplication (*), and the latter using summation (+) as the linking function. The variables' symbols and the confidents used in the equations are reported in Table 18. Figs. 69 and 70 respectively display the prediction correlations of all data points, and the ASR expansion prediction of the ACCT mix with missing data. As is clear from the plots, both models show a very high correlation and predict the ASR expansion very accurately. ASR expansion prediction at some later times than that of experiment is also presented in this figure.

GP I:

y=(1/((c1+((1/((1/(((d(0)+d(2))))))-(1-(d(2)+d(3)))))))

y=y*((1/(((((c4-d(2))^3)-(d(0)*c2*c3))/d(0))))+d(8))

y=y*(EXP((1/(((1-(c5*d(7)*d(7)))-((c6c7)^3)))))*d(8)) (6.56)

GP II:

TANH(((TANH((d(2)*d(7)))-TANH((d(7)+c2)))-c1))

y=y+TANH((((d(8))^(1/3)+(2*d(8)))-c3))+TANH((((d(2)+d(8))+(d(1)+c5))-c4))

y=y+TANH(((((d(4)+d(8))-(c6-d(5)))-(d(0)/d(1)))-d(2))) (6.57)

Table 18. Variables and Coefficients of the GP model for concrete

GP models Variables								
d(0)	**d(1)**	**d(2)**	**d(3)**	**d(4)**	**d(5)**	**d(6)**	**d(7)**	**d(8)**
$AE_{0.5N}$	AE_{1N}	FA%	Amorph	CaO	Na_2O_e	AL	t	MBE
GP I Coefficients								
c1	**c2**	**c3**	**c4**	**c5**	**c6**	**c7**		
-6.083	1.784	-6.042	-7.749	-1.262	7.021	-5.422		
GP II Coefficients								
c1	**c2**	**c3**	**c4**	**c5**	**c6**			
-4.269	-3.307	4.977	-3.161	-9.554	0.791			

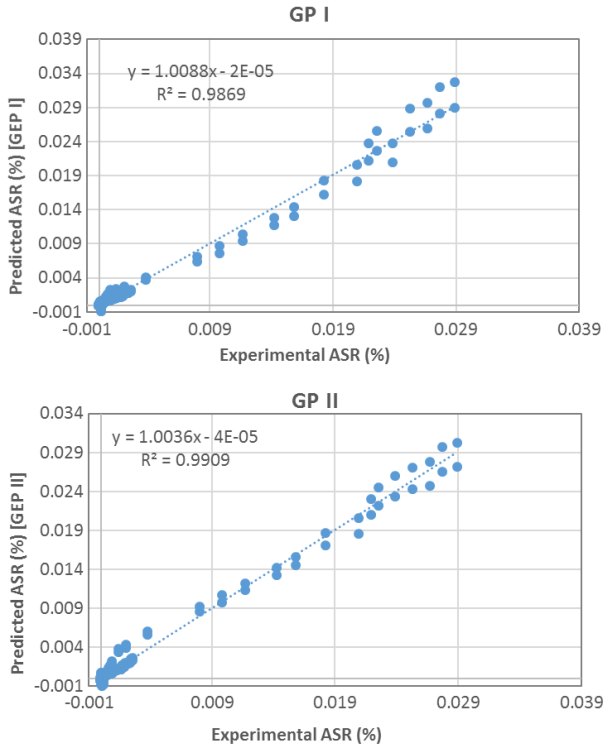

Figure 69. Prediction results of GP I and GP II models for concrete expansion based on mortar expansion

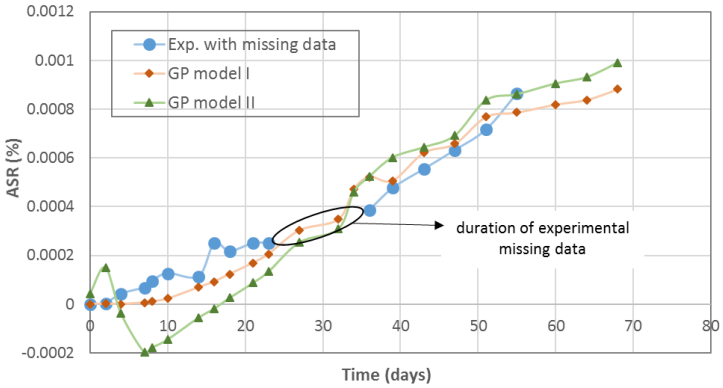

Figure 70. Comparison of predicted ASR curve by GP I and GP II with that of experiment for FA1, 30%, 60°C, AL=3.2 lb/yd^3

6.4.3. ANFIS Prediction Results of ACCT Based on AMBT

The results of the ANFIS model for train, validation, test and all data are presented in Figure 71. It is observed that the accuracy of the prediction is very high. It is worth mentioning that the prediction correlation of the ANFIS model obtained here for concrete expansion which includes the mortar expansion as a variable is much higher that of the ANFIS model that did not include the mortar expansion as a variable. However, it is noticed from Figure 72 that the ANFIS prediction of the missing data is not as good as those of ANN and GP models. Besides, the predicted expansion curve doesn't seem as smooth and uniform.

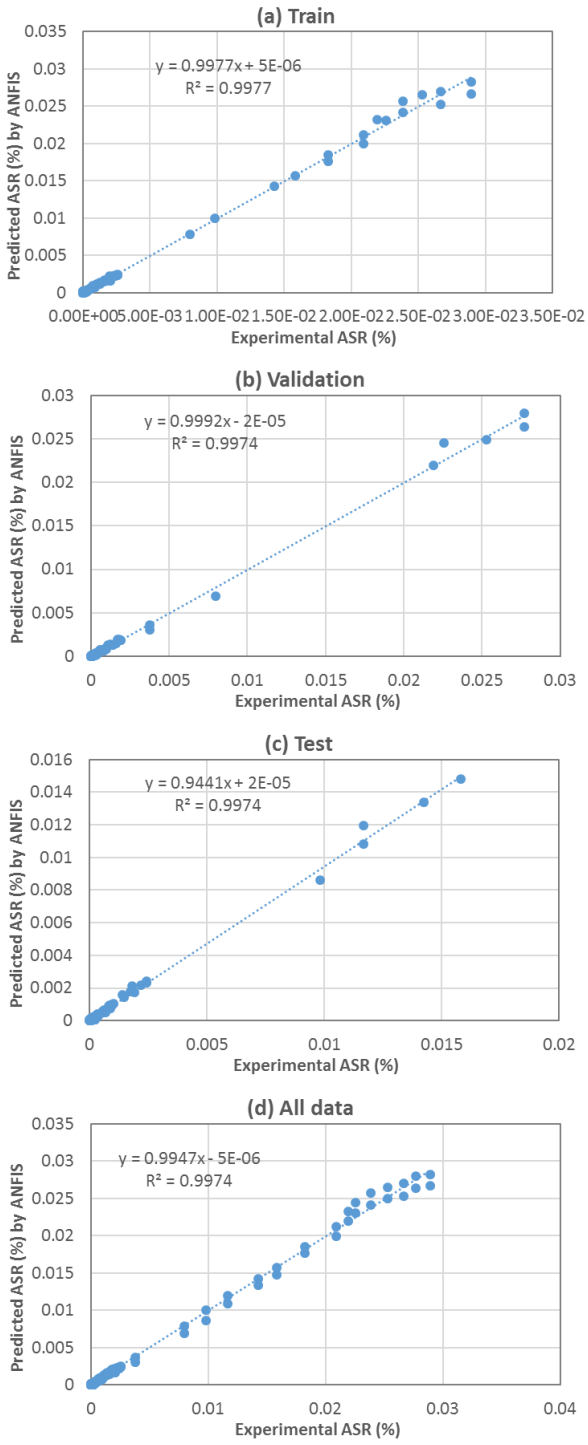

Figure 71. Prediction results of ANFIS model for concrete expansion based on mortar expansion

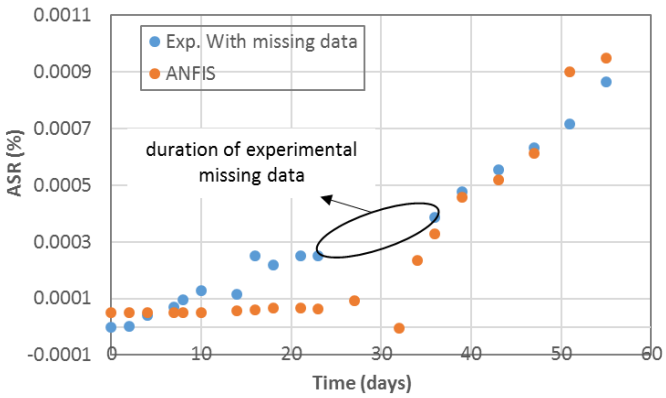

Figure 72. Comparison of predicted ASR curve by ANFIS with that of experiment for FA1, 30%, 60°C, AL=3.2 lb/yd^3

7. SUMMARY, CONCLUSIONS, AND RECOMMENDATIONS

This chapter presents a summary of the experimental and modeling work implemented in this research and draws conclusions. Recommendations for future research are suggested.

7.1. Summary

In this research, an extensive attempt was made to investigate ASR in different scales, namely aggregate, mortar, and concrete. To do so, multi-scale experimental assessment along with optimization and predictive modeling through machine-learning (ML) techniques were undertaken. For experimental assessment, several aggregates of different reactivity were tested to determine their compound activation energy (CAE) using VCMD, which is a test method established by former studies (Liu and Mukhopadhyay, 2014). However, in this research, an attempt was made to improve and facilitate the experimental setup and parameter estimation method. The former was achieved by design, optimization and 3D printing of a new float to enhance the data-logging system. The latter was obtained by developing a more user-friendly method in Excel for parameter estimation using Excel Solver. The CAEs of the new and old aggregates were calculated using the new method and compared with those of the previous model.

To assess ASR in mortar level, seven types of fly ash were characterized using XRD and XRF and the most influencing parameters were identified, namely amorphous phase%, CaO%, and Na_2O_e%. Then, the design of experiment (DOE) was employed to design different mixes containing different percentages of fly ash and aggregates of different CAEs, at two different temperatures, 60°C and 80°C. The ASR test based on ASTM C1260 was also conducted at an extended time up to 70 days, a duration similar to concrete testing.

To study the ASR behavior in concrete level, an accelerated concrete cylinder test (ACCT) was employed which incorporates the soak solution equal to pore solution, thereby minimizing the leaching in/out of the alkalis in concrete. In order to simulate the soak solution, pore solutions of cement paste of different mixes were extracted and characterized. Similar DOEs used for mortar mixes were used for concrete mixes with different levels of factors.

Once the data were collected from mortar and concrete tests, the most influencing variables from different scales were selected for the model development, namely CAE at 0.5N, CAE at 1N, temperature (T) fly ash percentage (FA%), fly ash type indicators (amorphous phase%, CaO%, Na_2O_e), and time. Three different types of predictive models using machine-learning techniques were developed, including Artificial Neural Network (ANN), Genetic Programming (GP), and Adaptive Neuro-Fuzzy Inference System (ANFIS). Closed-form formulations were derived for ANN and GP models and 3D parametric study was obtained from ANFIS. The models were evaluated based on performance criteria and the prediction comparisons were conducted on an ACCT experiment with missing data.

7.2. Conclusions

Based on the findings from this research, the following conclusions can be drawn:

- Two areas of improvement to the aggregate reactivity testing method, VCMD, were identified in this study for experimental and modeling: the data-logging system and parameter estimation. The former was improved by design, optimization and manufacturing a new float which was produced by 3D-printing technology. The latter was facilitated by developing a more user-friendly parameter estimation method in an excel spreadsheet. Both these improvements can lead to more accurate CAEs, despite being different from those obtained from the former method,

the new CAEs classify the aggregates and the reactivity categories the same as the previous method.

- Fly ash type is of huge importance in ASR mitigation and ASR predictive models. However, the type needs to be quantified in terms of indicators to be introduced into the model. The micro-scale characterization of several types of fly ash using XRF and XRD was implemented in this research and three parameters were found to be the most influential indicators, the amorphous phase, CaO, and Na2Oe. These parameters were also used in multiscale modeling of ASR in later steps of the research.

- As a part of the multiscale assessment and to develop machine-learning models for the first time in the ASR area, an extensive mortar bar test conforming ACTM C1260 was designed based on the DOE and conducted at extended time up to 70 days with different aggregate reactivity, temperature, fly ash type, and fly ash percentage. The optimum percentage of each fly ash type and most effective fly ash for ASR mitigation was concluded from the study. The mortar bar test also found how types of fly ash, temperature, and aggregate reactivity affect the ASR curve in a longer term.

- Since ASR behavior of the mortar bar is not close to that of concrete, and therefore does not represent the field, an accelerated concrete cylinder test (ACCT) was used to test several mixes based on DOE similar to that of the mortar bar. Influencing variables, such as fly ash type, percentage, aggregate reactivity, and temperature were found to differently and nonlinearly affect the ASR expansion of concrete. It was also observed that sample size does not affect the concrete expansion significantly.

- ACCT uses a soak-solution chemistry equal to pore solution with no alkali boosting mix design phase. Thus, the kinetics of the expansion is independent of the samples size due to

elimination of the concentration gradient and diffusion. Therefore, one of the great advantages of ACCT over CPT (ASTM C1293) and AMBT (ASTM C1260) is that there is not any thermal or mass diffusion involved in the expansion test.

- The machine-learning models, ANN, GP, and ANFIS, were used to develop the multiscale models for ASR and were validated for ASR mortar bar behavior for the first time to evaluate the accuracy and functionality of the theses techniques. It was found that all three models could capture the ASR mortar behavior based on the influencing variable.

- Once the models were validated for mortar bars, new sets of models were developed for ASR expansion of concrete. It was found that the models were able to predict the concrete expansion very well. However, by comparing the results of mortar models with those of concrete models, it is observed that the correlations of concrete models are lower than those of mortar model for GP and ANFIS. Besides, the complexity of the GP model developed for concrete was found to be higher than that of mortar.

- As the last part of multiscale modeling through machine-learning techniques, the concrete expansion models were developed by introducing the mortar bar expansion as a variable into the models. It was observed that the correlation of all models, ANN, GP, and ANFIS, were greatly improved. It was also found that the complexity of the ANN and GP models were less than that of the models developed for concrete independent of mortar expansion, confirming the role of scale effect on accuracy and performance of machine-learning techniques in multiscale modeling.

- Closed-form formulation of ANN and GP models was derived for the first time for ASR prediction. The models were implemented in an excel spreadsheet, which greatly facilitates the application of these models for design purposes.

- Comparison of the predicted ASR curve using ANN, GP and ANFIS with that of ACCT with missing data showed that not only can these models be used for ASR prediction at the time of mix design, but also they can be used for prediction of missing data. Nonetheless, it should be mentioned that the results in this research indicated that ANN and GP have better performance for prediction of missing data that that of ANFIS model.

7.3. Recommendations for Future Studies

Since machine-learning is a new approach in multiscale modeling, especially ASR and durability of infrastructures, there are several areas that can be explored for future research, which are recommended here.

- With availability of more petrography data on different types of aggregates, classification of aggregates in terms of reactivity can be performed by machine-learning classifiers such as GP and support vector machine (SVM).

- A more comprehensive mortar bar testing with wider range of aggregate reactivity is also recommended, from which more comprehensive machine-learning models can be developed.

- More comprehensive fly ash characterization as well as a more refined identification of fly ash indicators and statistical analysis are recommended.

- With availability of more data on ACCT at extended time, lower temperature and more aggregate reactivity levels, and fine-tuning the influencing variables, a more comprehensive model can be developed for concrete expansion prediction.

- To better scrutinize the mechanism of ASR expansion of mortar and concrete over time, the expansion difference between mortar and concrete can be also derived as ASR scale function in terms of influencing variable. It can help better correlate the expansion of mortar to that of concrete.

- Extended ASR multiscale prediction from lab scale (ACCT) to filed scale (exposure blocks) using ML techniques is also recommended for future studies.

- Parameters optimization of ANFIS and SVM is also recommended to enhance the prediction accuracy of theses ML techniques for ASR expansion.

REFERENCES

ACI Committee 221. (1998). State-of-the-art report on alkali-aggregate reactivity (Report No. ACI 221.1R-98). American Concrete Institute, Farmington Hills, MI, 31 pp.

Ahlstrom G., AASHTO Adopts Recommended Practice on Alkali-Silica Reactivity. HPC Bridge Views, (62) (2010).

Anderson JA. Cognitive and psychological computation with neural models. IEEE Trans Syst Man Cybern 1983;5(V.SMC-13):799–814.

Ashrafi, HR, Jalal, M, Garmsiri, K. Prediction of load–displacement curve of concrete reinforced by composite fibers (steel and polymeric) using artificial neural network. Expert Systems with Applications 2010; 37(12): 7663-7668.

ASTM Standard C1778,"Standard Guide for Reducing the Risk of Deleterious Alkali-Aggregate Reaction in Concrete." West Conshohocken, (2014), www.astm.org.

Barthelemy P, Bertolotti J, Wiersma DS (2008) A Le´vy flight for light. Nature 453:495–498.

Baykasoglu A, Gullub H, Canakci H, Ozbakir L. Prediction of compressive and tensile strength of limestone via genetic programming. Expert Syst Appl, 2008;35:111–23.

Bazant ZP., Steffens A., Mathematical model for kinetics of alkali-silica reaction in concrete, Cement and Concrete Research 30 (2000) 419-428.

Bleszynski R.F. and M.D. Thomas, Microstructural studies of alkali-silica reaction in fly ash concrete immersed in alkaline solutions. Advanced Cement Based Materials. 7(2) (1998), 66-78.

Blum C., Roli A. , Metaheuristics in combinatorial optimization: overview and conceptual comparison ACM Comput. Surv., 35 (3) (2003), pp. 268-308

Brown C, Liebovitch LS, Glendon R (2007) Le´vy flights in Dobe Ju/hoansi foraging patterns. Human Ecol 35:129–138.

Carrasquillo, R.L. and J. Farbiaz (1988). Alkali-Aggregate Reaction in Concrete Containing Fly Ash: Final Report. Center of Transportation Research, Research Report # 450-3F.

Charpin L., Ehrlacher A., A computational linear elastic fracture mechanics-based model for alkali–silica reaction, Cement and Concrete Research 42 (2012) 613–625.

Chatterji, S. (1989). Mechanisms of alkali-silica reaction and expansion. Proc., 8th Int. Conf. on Alkali-Aggregate Reaction in Concrete, Kyoto, p. 101-105.

Chong E.K.P., Zak S.H. , An Introduction to Optimization (Wiley-Interscience Series in Discrete Mathematics and Optimization) (third ed.), Wiley-Interscience (2008)

Colin, T., (2000). The Varienty of Life. Oxford University Press, Oxford.

Davis DE., Deschenes R, Hale JWM, Development of a Field Exposure Site for Predicting and Mitigating ASR, technical report, University of Arkansas, 2018

Diamond S. and Thaulow N., A study of expansion due to alkali—silica reaction as conditioned by the grain size of the reactive aggregate. Cement and Concrete Research. 4(4) (1974), 591-607.

Diamond S., Effects of two danish flyashes on alkali contents of pore solutions of cement-flyash pastes. Cement and Concrete Research. 11(3) (1981), 383-394.

Diamond, S. (1981). Effect of Two Danish Fly Ashes on Alkali Contents of Pore Solutions of Cement-Fly Ash Pastes. Cem. Concr. Res., Vol. 11, No. 3, p. 383-394.

Diamond, S. (1989). ASR—another look at mechanisms. Proceedings from 8th international Conference on Alkali-Aggregate Reaction (ICAAR). Kyoto, Japan, 83-94.

Drud A., CONOPT: A GRG code for large space dynamic nonlinear optimization problems, Mathematical Programming, 1985; 31 (1985): 153-191.

Dubey A. K., Yadava V.; Simultaneous Optimization of Multiple Quality Characteristics in Laser Beam Cutting Using Taguchi Method. International Journal of Precision Engineering and Manufacturing. Vol 8. No.4, 2007, pp. 10-15.

Duchesne J. and Bérubé M., The effectiveness of supplementary cementing materials in suppressing expansion due to ASR: another look at the reaction mechanisms part 2: pore solution chemistry. Cement and Concrete Research. 24(2) (1994), 221-230.

Dunstan E., The effect of fly ash on concrete alkali-aggregate reaction. ASTM Cement, Concrete and Aggregates. 3(2) (1981), 101-104.

Fathi M, Jalal M, Rostami S. Compressive strength prediction by ANN formulation approach for CFRP confined concrete cylinders. Earthquake and structures 2015; 8(5): 1171-1190.

Ferreira C. Gene expression programming in problem solving, in soft computing and Industry: recent applications; 2002

Ferreira C. Gene expression programming: a new adaptive algorithm for solving problems. Complex Syst 2001;13:87–129.

Flisch, A., et al. Industrial Computer Tomography in Reverse Engineering Applications. DGZfP-Proceedings BB 67-CD Paper 8, Computerized Tomography for Industrial Applications and Image Processing in Radiology, March 15–17, 1999, Berlin, Germany.

Folliard K.J., M.D.A. Thomas, B. Fournier, K.E. Kurtis, and J.H. Ideker (2007). The Use of Lithium to Prevent or Mitigate Alkali-Silica Reaction in Concrete Pavements and Structures.

Publication No. FHWA-HRT-06-133, Office of Infrastructure Research and Development, Federal Highway Administration: p. 47.

Fournier B. and Berube M-A., Alkali-aggregate reaction in concrete: a review of basic concepts and engineering implications. Canadian Journal of Civil Engineering. 27(2000), 147-191.

Fournier B., Berube M., and Rogers C., Canadian Standards Association (CSA) Standard Practice to Evaluate Potential Alkali Reactivity of Aggregates and to Select Preventive Measures against Alkali Aggregate Reaction in New Concrete Structures. 11th International Conference on Alkali Aggregate Reaction, Québec City, Canada. (2000) 633-642.

Fournier, B., Bérubé, M-A., Folliard, K.J., & Thomas, M.D.A. (2010). Report on the Diagnosis, Prognosis, and Mitigation of Alkali- Silica Reaction (ASR) in Transportation Structures 65 (Report No. FHWA-HIF-09-004). Federal Highway Administration, U.S. Department of Transportation, Washington DC, 154 pp.

Fournier, B., Bérubé, M-A., Thomas, M.D.A., Smaoui, N. & Folliard, K.J. (2004). Evaluation and Management of Concrete Structures Affected by Alkali-Silica Reaction - A Review. MTL 2004-11 (OP). Natural Resources Canada. Ottawa (Canada), 59 pp.

Garmsiri, K, Jalal, M. Multiobjective optimization of composite cylindrical shells for strength and frequency using genetic algorithm and neural networks. Science and Engineering of Composite Materials 2014; 21(4): 529-536.

Glasser F.P., Chemistry of the Alkali-aggregate Reaction, in The Alkali-Silica Reaction in Concrete. 1992, Blackie: New York. p. 30-53.

Glasser L. Dent and Kataoka N., The chemistry of ‘alkali-aggregate’reaction. Cement and Concrete Research. 11(1) (1981), 1-9.

Goharzay M, Noorzad A, Mahboubi Ardakani A, Jalal M. A Worldwide SPT-Based Soil Liquefaction Triggering Analysis Utilizing Gene Expression Programming and Bayesian Probabilistic Method. Journal of Rock Mechanics and Geotechnical Engineering 2017; 9(4): 683-693.

Goldberg D.E. , Genetic algorithms in search, optimization, and machine learning reading, Addison-Wesley, MA (1989)

Guthrie G D., Carey J.W, A thermodynamic and kinetic model for paste–aggregate interactions and the alkali–silica reaction, Cement and Concrete Research 76 (2015) 107–120.

Guzelbey I H., Cevikb A., Erklig A., Prediction of web crippling strength of cold-formed steel sheetings using neural networks, Journal of Constructional Steel Research, 2006; (62): 962–973.

HajiSotoudeh M, Jalal M, Effects of waste steel fibers on strength and stress-strain behavior of concrete incorporating silica nanopowder, Indian Journal of Science and Technology, 2013; 6 (10), 5411–5417.

Haykin S. Neural networks—a comprehensive foundation. New York: Macmillan College Publishing Company; 2000.

Helmuth, R. (1993). Alkali-silica reactivity: an overview of research (Report No. SHRP-C-342). Strategic Highway Research Program (SHRP), National Research Council, Washington, DC, 105 pp.

Herman, G. T., Fundamentals of computerized tomography: Image reconstruction from projection, 2nd edition, Springer, 2009.

Holland J.H. , Adaptation in natural and artificial systems, University of Michigan Press, Ann Arbor (1975)

Holland, J. H. (1992). Genetic algorithms. Scientific American, July, 114–116.

Hopfield JJ. Neural networks and physical systems with emergent collective computational abilities. Proc Natl Acad Sci 1982;79:2554–8.

Hou X., Kirkpatrick R.J., Struble L.J., and P.J. Monteiro, Structural investigations of alkali silicate gels. Journal of the American Ceramic Society. 88(4) (2005), 943-949.

Hou X., Struble L.J., and Kirkpatrick R.J., Formation of ASR gel and the roles of C-S-H and portlandite. Cement and Concrete Research. 34(9) (2004), 1683-1696.

https://www.solver.com/excel-solver-algorithms-and-methods-used.

Ideker, J. H., B. L. East, K. J. Folliard, M. D. Thomas, and B. Fournier (2010). "The current state of the accelerated concrete prism test." Cement and Concrete Research 40(4): 550–555.

Ideker, J.H., Bentivegna, A.F., Folliard, K.J., & Juenger, M.C.G. (2012). Do current laboratory test methods accurately predict alkali-silica reactivity? ACI Materials Journal, 109(4), 395- 402.

Jalal M , Grasley Z, Nassir N , Jalal H. Strength and dynamic elasticity modulus of rubberized concrete designed with ANFIS modeling and ultrasonic technique, Construction and Building Materials, 2020, 10.1016/j.conbuildmat.2019.117920.

Jalal M, AA Ramezanianpour, MK Pool, Split tensile strength of binary blended self-compacting concrete containing low volume fly ash and TiO2 nanoparticles, Composites Part B: Engineering, 2013; 55, 324-337.

Jalal M, Compressive strength enhancement of concrete reinforced by waste steel fibers utilizing nano SiO2, Middle East Journal of Scientific Research, 2012; 12 (3): 382-391.

Jalal M, Corrosion resistant self-compacting concrete using micro and nano silica admixtures, Structural Engineering and Mechanics, 2014; 51 (3), 403-412.

Jalal M, Influence of class F fly ash and silica nano-micro powder on water permeability and thermal properties of high performance cementitious composites, Science and Engineering of Composite Materials, 2013; 20 (1): 41-46.

Jalal M, M Fathi, M Farzad, " Effects of fly ash and TiO2 nanoparticles on rheological, mechanical, microstructural and thermal properties of high strength self compacting concrete", Mechanics of Materials, 2013; 61: 11-27.

Jalal M, Mansouri E, Effects of fly ash and cement content on rheological, mechanical, and transport properties of high-performance self-compacting concrete, Science and Engineering of Composite Materials, 2012; 19(4): 393-405.

Jalal M, Mansouri E, Sharifipour M, Pouladkhan AR, " Mechanical, rheological, durability and microstructural properties of high performance self-compacting concrete containing SiO2 micro and nanoparticles", Materials & Design, 2012; 34: 389-400.

Jalal M, Mirsayar M, Mukhopadhyay AK, “A Novel Multiscale Modeling Approach for Evaluation of the ASR in Concrete Structures”, Sixth International Conference on Durability of Concrete Structures (ICDCS2018), University of Leeds on 18-20 July 2018, Editor-in-Chief: PAM Basheer, 844-850.

Jalal M, Mukhopadhyay AK, Goharzay M. Bat algorithm as a metaheuristic optimization approach in materials and design: optimal design of a new float for different materials. Neural Computing and Applications 2018; DOI: 10.1007/s00521-018-3430-4.

Jalal M, Mukhopadhyay AK, Grasley Z. Design, manufacturing, and structural optimization of a composite float using particle swarm optimization and genetic algorithm. Proceedings of the Institution of Mechanical Engineers, Part L: Journal of Materials: Design and Applications 2019; 233 (7): 1404-1418.

Jalal M, Nassir N, Jalal H, Arabali P. On the strength and pulse velocity of rubberized concrete containing silica fume and zeolite: Prediction using multivariable regression models, Construction and Building Materials 2019; 223: 530-543.

Jalal M, Nassir N, Jalal H. Waste tire rubber and pozzolans in concrete: A trade-off between cleaner production and mechanical properties in a greener concrete. Journal of Cleaner Production 2019; 238: 117882.

Jalal M, Pouladkhan A, Harandi OF, Jafari D, "Comparative study on effects of Class F fly ash, nano silica and silica fume on properties of high performance self-compacting concrete" Construction and Building Materials, 2015; 94, 90-104.

Jalal M, Ramezanianpour AA, Pouladkhan AR, Tedro P, " Application of genetic programming (GP) and ANFIS for strength enhancement modeling of CFRP-retrofitted concrete cylinders", Neural Computing and Applications, 2013; 23(2): 455-470.

Jalal M, Ramezanianpour AA. Strength enhancement modeling of concrete cylinders confined with CFRP composites using artificial neural networks. Composites Part B: Engineering 2012; 43(8): 2990-3000.

Jalal M, Tahmasebi M, Assessment of nano-TiO2 and class F fly ash effects on flexural fracture and microstructure of binary blended concrete, Science and Engineering of Composite Materials, 2015; 22 (3), 263-270.

Jalal M, Transport properties of high-performance cementitious composites incorporating micro and nano SiO2 into the binder, Science and Engineering of Composite Materials, 2012; 19(4): 415-421.

Jalal M, Arabali P, Grasley Z, Bullard JW . Application of adaptive neuro-fuzzy inference system for strength prediction of rubberized concrete containing silica fume and zeolite Proc. Inst. Mech. Eng., Part L: J. Mater.: Des. Appl. 2019, 10.1177/1464420719890370

Jalal M. Soft computing techniques for compressive strength prediction of concrete cylinders strengthened by CFRP composites. Science and Engineering of Composite Materials 2015; 22(1): 97-112.

Jalal M., Moradi-Dastjerdi R., Bidram M., Big data in nanocomposites: ONN approach and mesh-free method for functionally graded carbon nanotube-reinforced composites, Journal of Computational Design and Engineerin, 2019, 6(2), 209-223.

Jalal, M, Goharzay, M. Cuckoo search algorithm for applied structural and design optimization: float system for experimental setups. Journal of Computational Design and Engineering. Journal of Computational Design and Engineering 2019; 6 (2): 159-172.

Jalal, M, Mansouri, E. Thermal and mechanical characteristics of cement nanocomposites. Science and Engineering of Composite Materials 2013; 20 (1): 35-40.

Jalal, M, Teimortashlu, E, Grasley, Z. Performance-based design and optimization of rheological and strength properties of self-compacting cement composite incorporating micro/ nano admixtures. Composites Part B: Engineering 2019; 163:497-510.

Jang, J.S.R. (1993), "ANFIS: adaptive-network-based fuzzy inference system", IEEE Transactions on Systems, Man, and Cybernetics, 23(3), 665-685.

Jang, J.S.R. and Sun. C.T. (1995), "Nuro-fuzzy modeling and control", Proceedings of the IEEE, 83(3).

Jodaei A, Jalal M, Yas MH, “Free vibration analysis of functionally graded annular plates by state-space based differential quadrature method and comparative modeling by ANN” Composites Part B: Engineering, 2012; 43 (2), 340-353.

Jodaei, A, Jalal, M, Yas, MH Three-dimensional free vibration analysis of functionally graded piezoelectric annular plates via SSDQM and comparative modeling by ANN. Mathematical and Computer Modelling 2013; 57(5): 1408-1425.

Kao C., Performance of several nonlinear programming software packages on microcomputers, Comput. Oper. Res. 25 (1998), no. 10, 807–816.

Kennedy, J., Eberhart, R.C.: Particle swarm optimization. In: Proceedings of IEEE International Conference on Neural Networks, Piscataway, New Jersey, USA, IEEE Press (1995) 1942–1948

Kim T., Olek J., Jeong H., Alkali–silica reaction: Kinetics of chemistry of pore solution and calcium hydroxide content in cementitious system, Cement and Concrete Research 71 (2015) 36–45.

Knudsen T. and Thaulow N., Quantitative microanalyses of alkali-silica gel in concrete. Cement and Concrete Research. 5(5) (1975), 443-454.

Kollek, S. Varma, and C. Zaris. Measurement of OH− concentrations of pore fluids and expansion due to alkali-silica reaction in composite cement mortars. Proceedings of the 8th International Congress on the Chemistry of Cement. (1986) 183-189.

Koza J.R. , Genetic programming: On the programming of computers by means of natural selection, MIT Press, Cambridge (MA) (1992)

Lawrence M. and Vivian H., The reactions of various alkalis with silica. Australian Journal of applied science. 12(1) (1961), 96-103.

Leemann A., Lothenbach B., The influence of potassium–sodium ratio in cement on concrete expansion due to alkali-aggregate reaction, Cem. Concr. Res. 38 (2008) 1162-1168.

Leemann A., Saout G. Le, Winnefeld F., Rentsch D., and Lothenbach B., Alkali–silica reaction: the influence of calcium on silica dissolution and the formation of reaction products. Journal of the American Ceramic Society. 94(4) (2011), 1243-1249.

Li C., A Comprehensive Mechanistic Study on Using Fine Lightweight Aggregate to Mitigate Alkali-silica Reaction, PhD dissertation, Oregon State University, 2016.

Liu KW, Mukhopadhyay AK, "A kinetic-Based ASR Aggregate Classification", Journal of Construction and Building Materials, 2014; 68: 525-534.

Liu SW, Huang JH, Sung JC, Lee CC. Detection of cracks using neural networks and computational mechanics. 12Comput Meth Appl Mech Eng 2002;191(25– 26):2831–45.

Malvar L., Cline G., Burke D., Rollings R., Sherman T., and Greene J., Alkali-silica reaction mitigation: state of the art and recommendations. Materials Journal. 99(5) (2002), 480-489.

Mehta P.K. and Menteiro P.J.M., Chapter 6 Hydraulic Cements, in Concrete: Microstructure, Properties, and Materials. 2006, McGraw-Hill. p. 203-252.

Mitchell, M. (1998). An Introduction to Genetic Algorithms. Massachusettss: The MIT Press.

Mukhopadhyay AK, Liu KW, Jalal M, An Innovative Approach to Fly Ash Characterization and Evaluation to Prevent Alkali-Silica Reaction, ACI Materials Journal, 2019; 116 (4): 173-181.

Mukhopadhyay AK, Liu KW, Jalal M. “Further validation of ASR testing and approach for formulating ASR - resistant mix: technical report” 2018. FHWA/TX-18/0-6656-01-R1, Texas A&M Transportation Institute, The Texas A&M University System, College Station, Texas.

Mukhopadhyay AK., Liu K, ASR TESTING: A New Approach to Aggregate Classification and Mix Design Verification, Technical Report, Texas A&M Transportation Institute, 2014.

Mukhopadhyay, A. K., Ghanem H., Shon C. S., Zollinger D., Gress D., and Hooton D. (2009). Mitigation of ASR in Concrete-Combined Materials Test Procedure. IPRF Report (DOT/FAA- 01-G-003-2, accessible at http://www.iprf.org/products/IPRF-03-2-Final%20Report-12.7.09.pdf)

Mukhopadhyay, A.K., Shon C., and Zollinger D. (2006). Activation Energy of Alkali-Silica Reaction and Dilatometer Method. In Transportation Research Record: Journal of Transportation Research Board, No. 1979, Transportation Research Board of the National Academies, Washington D.C., p. 1-11.

Multon S., Sellier A., Multi-scale analysis of alkali–silica reaction (ASR): Impact of alkali leaching on scale effects affecting expansion tests, Cement and Concrete Research 81 (2016) 122–133.

Munn C.J., Freitag S.A., Milestone N.B., Happy A., South W., Brown I., and Barnard D.P., TR3 Alkali silica reaction minimizing the risk of damage to concrete guidance notes and recommendation practicer. 2003, Cement & Concrete Association of New Zealand. p. 84.

Nixon, P.J. and I. Sims (1992). RILEM TC106 Alkali Aggregate Reaction–Accelerated Tests Interim Report and Summary of Survey of National Specifications. Proceedings of the Ninth

International Conference on Alkali-Aggregate Reaction in Concrete, Concrete Society, Slough, England, Vol. 2, p. 731–738.

Noel M.M. , A new gradient based particle swarm optimization algorithm for accurate computation of global minimum Appl. Soft Comput., 12 (1) (2012), pp. 353-359

Oltean M, Grosan C. A comparison of several linear genetic programming techniques. Complex Syst 2003;14:1–29.

Pavlyukevich I (2007) Le´vy flights, non-local search and simulated annealing. J Comput Phys 226:1830–1844

Payne RB, Sorenson MD, Klitz K, The Cuckoos. 2005, Oxford University Press, New York.

Pedneault, A., (1996). Development of Testing and Analytical Procedures for the Evaluation of the Residual Potential of Reaction, Expansion, and Deterioration of Concrete Affected by ASR. M.Sc. Memoir, Laval University, Québec City, Canada, p. 133.

Pignatelli R., Comi C., PJM Monteiro, A coupled mechanical and chemical damage model for concrete affected by alkali–silica reaction, Cement and Concrete Research 53 (2013) 196–210.

Ponce, J. M. and Batic O. R. (2006). Different manifestations of the alkali-silica reaction in concrete according to the reaction kinetics of the reactive aggregate. Cem. Concr. Res., 36, p. 1148–1156.

Poole A.B., Introduction to alkali-aggregate reaction in concrete, in The Alkali-silica Reaction in Concrete. 1992, Blackie & Van Nostrand Reinhold: New York. p. 1-29.

Pour-Ghaz, M., R. Pragg, J. Castro, and J. Weiss (2012). Can acoustic emission be used to detect alkali-silica reaction earlier than length change tests? In Proceedings of the 14th International Conference on Alkali-Aggregate Reaction in Concrete, Austin, TX.

Powers, T. C., & Steinour, H. H. (1955). An interpretation of some published researches on the Alkali-Aggregate Reaction, Part 1-the chemical reactions and mechanism of expansion. Journal of the American Concrete Institute, 26(6), 497-516.

Pramanik N., Kumar Panda R. (2009), Application of neural network and adaptive neuro-fuzzy inference systems for river flow prediction, Hydrological Sciences Journal, 54(2): 247-260.

Prezzi M., Monteiro P.J., and Sposito G., The alkali-silica reaction, Part I: use of the double-layer theory to explain the behavior of reaction-product gels. ACI Materials Journal. 94(1) (1997), 10-17.

Rajabipour F., Giannini E., Dunant C., Ideker J.H., and M.D. Thomas, Alkali–silica reaction: Current understanding of the reaction mechanisms and the knowledge gaps. Cement and Concrete Research. 76 (2015), 130-146.

Rao S. , Engineering Optimization: Theory and Practice New Age International (1996)

Rayment P., The effect of pulverised-fuel ash on the c/s molar ratio and alkali content of calcium silicate hydrates in cement. Cement and Concrete Research. 12(2) (1982), 133-140.

Reynolds AM, Frye MA (2007) Free-flight odor tracking in Drosophila is consistent with an optimal intermittent scale-free search. PLoS One 2:e354

Richard A. Deschenes Jr., Mitigation and Evaluation of Alkali-Silica Reaction (ASR) and Freezing and Thawing in Concrete Transportation Structures, PhD Dissertation, University of Arkansas, 2017.

Richardson, P., (2008). Bats. Natural History Museum, London.

Ross P. J.; Taguchi Techniques for Quality Engineering. Mcgraw-Hill International Editions, ISBN 0-07-114663-6. p. 329, 1996.

Rumelhart DE, Hinton GE, William RJ. Learning internal representation by error propagation. In: Rumelhart DE, McClelland JL, editors. Proceeding parallel distributed processing foundation, vol. 1. Cambridge: MIT Press; 1986.

Saouma VE., Martin RA., Hariri-Ardebili MA., Katayama T., A mathematical model for the kinetics of the alkali–silica chemical reaction, Cement and Concrete Research 68 (2015) 184–195.

Schwing K., Use of Fly Ash in the Mitigation of Alkali-Silica Reaction in Concrete, master of science, Oregon State University, 2010.

Shafaatian SMH., INNOVATIVE METHODS TO MITIGATE ALKALI-SILICA REACTION IN CONCRETE MATERIALS CONTAINING RECYCLED GLASS AGGREGATES, PhD Dissertation, Penn State University, 2012.

Shehata M.H. and Thomas M.D.A., The effect of fly ash composition on the expansion of concrete due to alkali–silica reaction. Cement and Concrete Research. 30(7) (2000), 1063-1072.

Shehata M.H., Thomas M.D.A., and Bleszynski R.F., The effects of fly ash composition on the chemistry of pore solution in hydrated cement pastes. Cement and Concrete Research. 29(12) (1999), 1915-1920.

Shehata, M.H. and M.D.A. Thomas (2000). The Effect of Fly Ash Composition on the Expansion of Concrete Due to Alkali Silica Reaction. Cem. Concr. Res., Vol. 60, No. 7, p. 1063-1072.

Shon, C. S., D.G. Zollinger, and S.L. Sarkar (2003). Application of Modified ASTM C 1260 Test for Fly Ash-Cement Mixtures, Journal of the Transportation Research Board 1834, p. 93- 106.

Shon, C. S., S.L. Sarkar, and D.G. Zollinger (2004). Testing the Effectiveness of Class C and Class F Fly Ash in Controlling Expansion due to Alkali-Silica Reaction Using Modified ASTM C 1260 Test Method, Journal of Materials in Civil Engineering Vol. 16, No. 1, p. 20-27.

Sibbick, R.G. and C.L. Page (1992). Threshold alkali contents for expansion of concretes containing British aggregates. Cem. Concr. Res., 22, p. 990–994.

Singh S., Shan H. S., Kumar P.; Parametric Optimization of Magnetic-Field- Assisted Abrasive Flow Machining by the Taguchi Method, Quality and Reliability Engineering International, pp. 273- 283, 2002.

Standard Practice for Laboratory Testing to Demonstrate the Effectiveness of Supplementary Cementing Materials and Lithium-based Admixtures to Prevent Alkali-silica Reaction in Concrete, in A23.2-28A. 2004b, Canadian Standards Association: Mississauga, ON, CA. p. 327-330.

Standard Test Method for Determination of Length Change of Concrete Due to Alkali-Silica Reaction, in ASTM C 1293-08b, A. International, Editor. 2008, ASTM International: West Conshohocken, PA. p. 7.

Standard Test Method for Determining the Potential Alkali-Silica Reactivity of Combinations of Cementitious Materials and Aggregate (Accelerated Mortar-Bar Method), in ASTM C 1567. 2008, ASTM International: West Conshohocken, PA. p. 6.

Stanton T.E., (2008), A tribute to "expansion of concrete through reaction between cement and aggregate". ACI Special Publication. 249.

Stanton, T. E. (1940). Expansion of concrete through reaction between cement and aggregate. Proceedings American Society of Civil Engineers, 66(10), 1781-1811.

Stark, D. (1991). Handbook for the identification of alkali silica reactivity in highway structures (Report No. SHRP-C/FR-91-101). Strategic Highway Research Program, National Research Council, Washington, DC, 49 pp.

Stark, D. C. (1980). Alkali-silica reactivity: some reconsiderations. Cement, Concrete, and Aggregates, 2(2), 92-94.

Suratgar AA, Tavakoli MB, Hoseinabadi A. Modified Levenberg–Marquardt method for neural networks training. World Acad Sci Eng Technol 2005;6:46–8.

Swamy, R. N., & Al-Asali, M. M. (1988b). Expansion of concrete due to alkali-silica reaction. ACI Materials Journal, 85(1), 33-40.

Teimortashlu E, Dehestani M, Jalal M. 2018, Application of Taguchi method for compressive strength optimization of tertiary blended self-compacting mortar, Construction and Building Materials, 190: 1182-1191.

Thomas M., Fournier B., and Folliard K.J., Alkali-aggregate Reactivity (AAR) Facts Book. 2013.

Thomas M., The effect of supplementary cementing materials on alkali-silica reaction: A review. Cement and Concrete Research, (2011), 1224-1231.

Thomas M., The role of calcium hydroxide in alkali recycling in concrete. Materials Science of Concrete Special, (2001), 225-236.

Thomas M.D., Fournier B., and Folliard K.J., Report on determining the reactivity of concrete aggregates and selecting appropriate measures for preventing deleterious expansion in new concrete construction. 2008.

Thomas, M., Fournier, B., Folliard, K., Ideker, J., & Shehata, M. (2006a). Test methods for evaluating preventive measures for controlling expansion due to alkali–silica reaction in concrete. Cement and Concrete Research, 36(10), 1842-1856.

Topcu, I.B., and Sarıdemir, M. (2008), "Prediction of mechanical properties of recycled aggregate concretes containing silica fume using artificial neural networks and fuzzy logic", Computational Materials Science, 42 (1), 74-82.

van den Bergh F., An Analysis of Particle Swarm Optimizers. PhD thesis, University of Pretoria, 2001.

Vazinram, F, Jalal, M, Foroushani MY. Effect of nano ZnO2 and lime water curing on strength and water absorption of concrete. International Journal of Materials and Product Technology 2015; 50:356-365.

Walia N., Singh H., Sharma A. (2015), ANFIS: Adaptive Neuro-Fuzzy Inference System-A Survey, International Journal of Computer Applications, 123 (13):3 2-38.

Yang X.S. , Nature-Inspired Metaheuristic Algorithms (second ed.), Luniver Press (2010)

Yang X.S., Deb S., Cuckoo Search via Le´vy Flights, World Congress on Nature & Biologically Inspired Computing, 2009; 210-214.

Yang X.S., Optimization and metaheuristic algorithms in engineering X.-S. Yang, A.H. Gandomi, S. Talatahari, A.H. Alavi (Eds.), Metaheuristics in Water, Geotechnical and Transport Engineering, Elsevier, Oxford (2013), pp. 1-23.

Yang, X. S., (2010). A New Metaheuristic Bat-Inspired Algorithm, in: Nature Inspired Cooperative Strategies for Optimization (NISCO 2010) (Eds. Cruz, C.; Gonz´alez, J. R.; Pelta, D. A.; Terrazas, G), Studies in Computational Intelligence Vol. 284, Springer Berlin, pp. 65–74.

APPENDIX A

A.1. Comparison plots of model fit for VCMD and modified VCMD

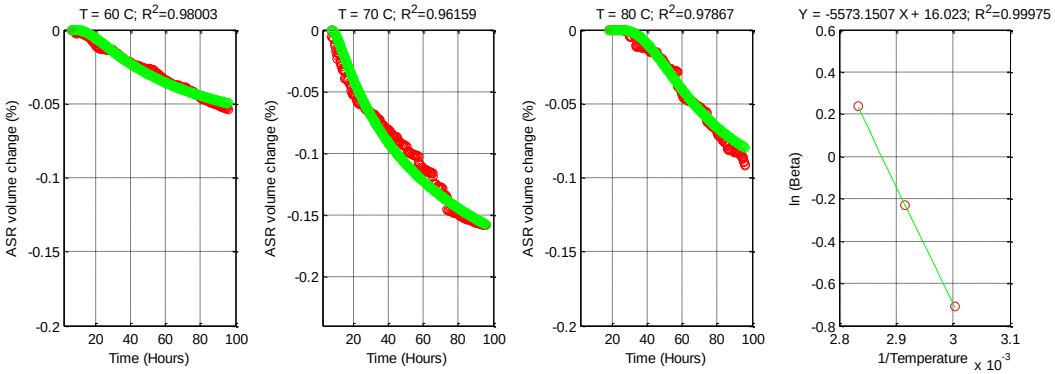

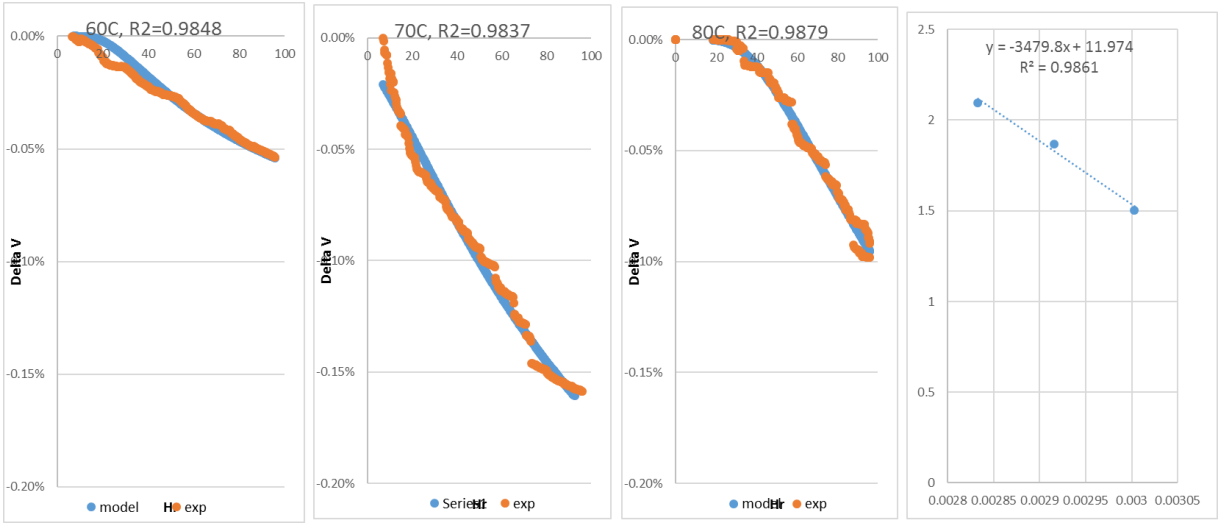

(a)

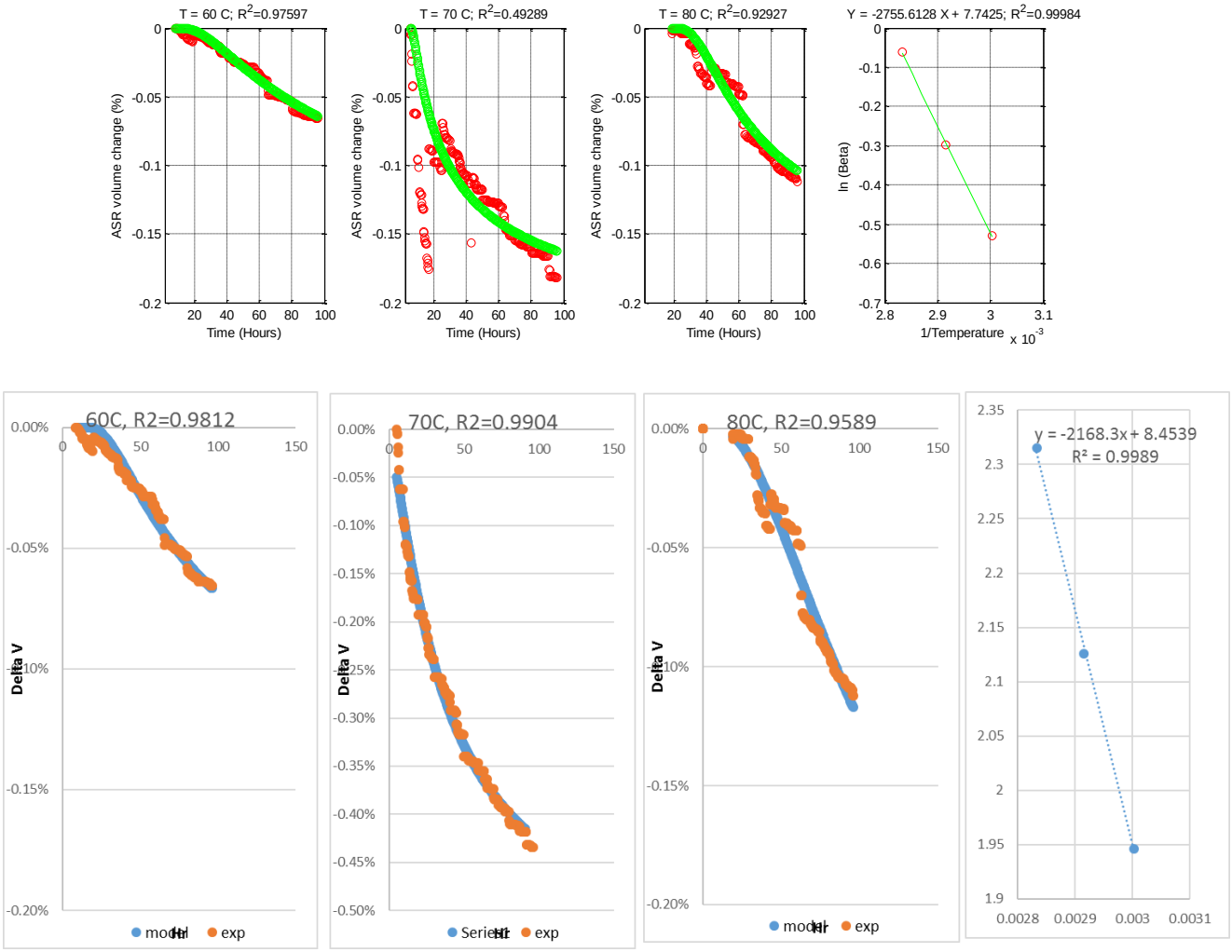

(b)

Figure A.1.1. Results for fine aggregate 1 (FA1) at (a) 0.5N, and (b) 1N

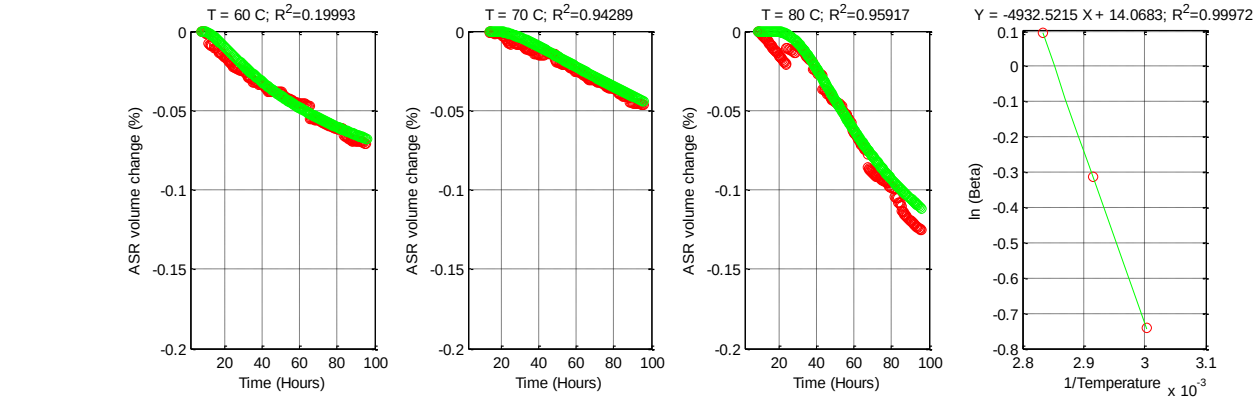
T = 60 C; R2=0.19993
T = 70 C; R2=0.94289
T = 80 C; R2=0.95917
Y = -4932.5215 X + 14.0683; R2=0.99972
ASR volume change (%)
Time (Hours)
ln (Beta)
1/Temperature
x 10-3

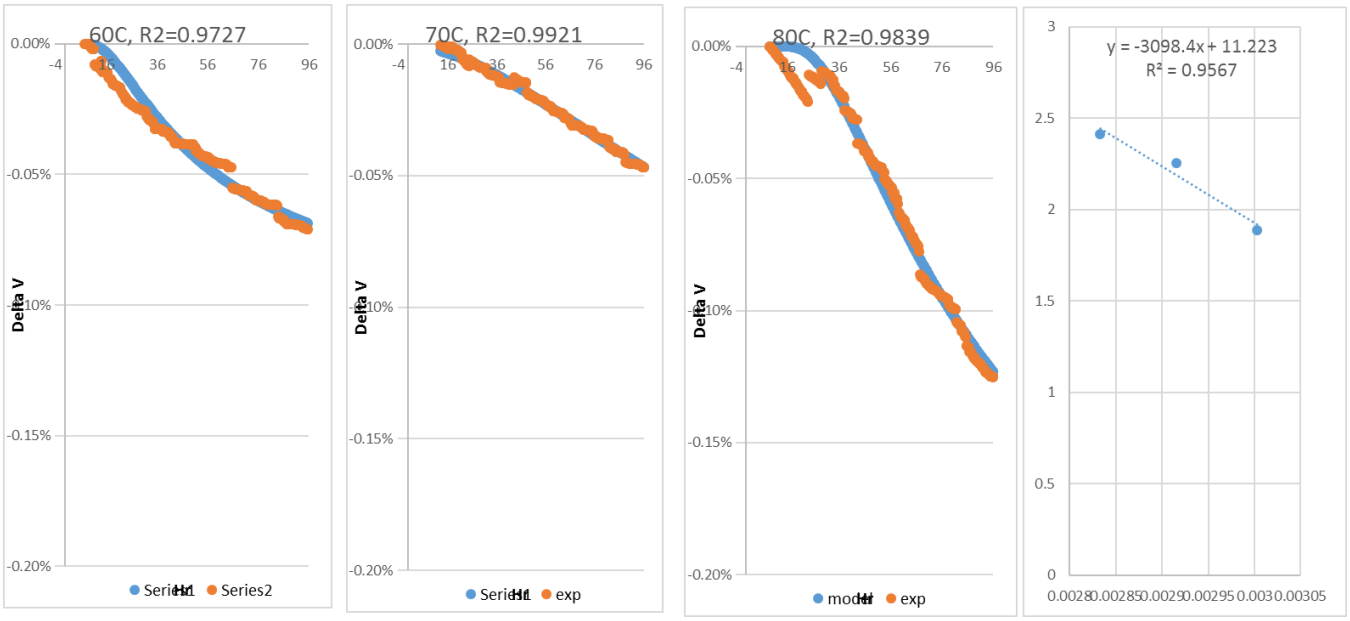
60C, R2=0.9727
70C, R2=0.9921
80C, R2=0.9839
Delta V
Series1
Series2
exp
model
y = -3098.4x + 11.223
R² = 0.9567

(a)

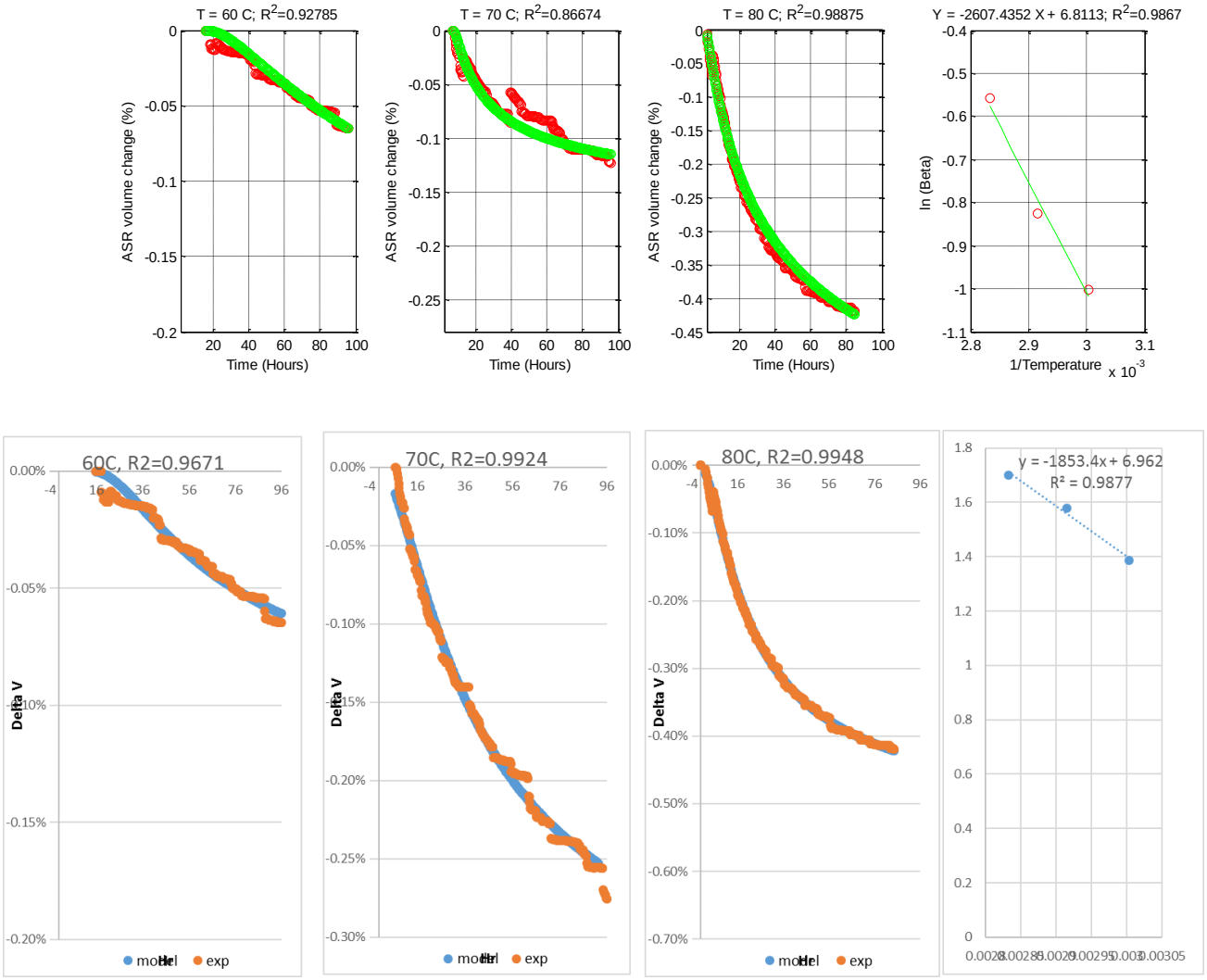

(b)

Figure A.1.2. Results for FA2 at (a) 0.5N, and (b) 1N

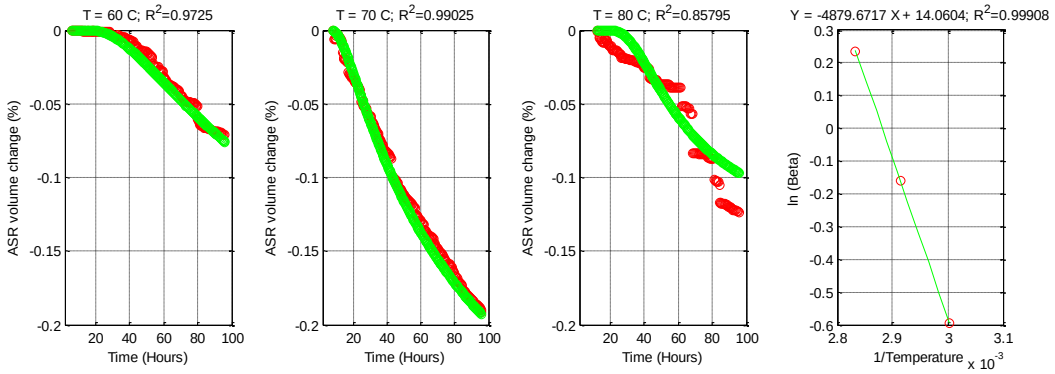
T = 60 C; R2=0.9725
T = 70 C; R2=0.99025
T = 80 C; R2=0.85795
Y = -4879.6717 X + 14.0604; R2=0.99908
ASR volume change (%)
Time (Hours)
ln (Beta)
1/Temperature x 10-3

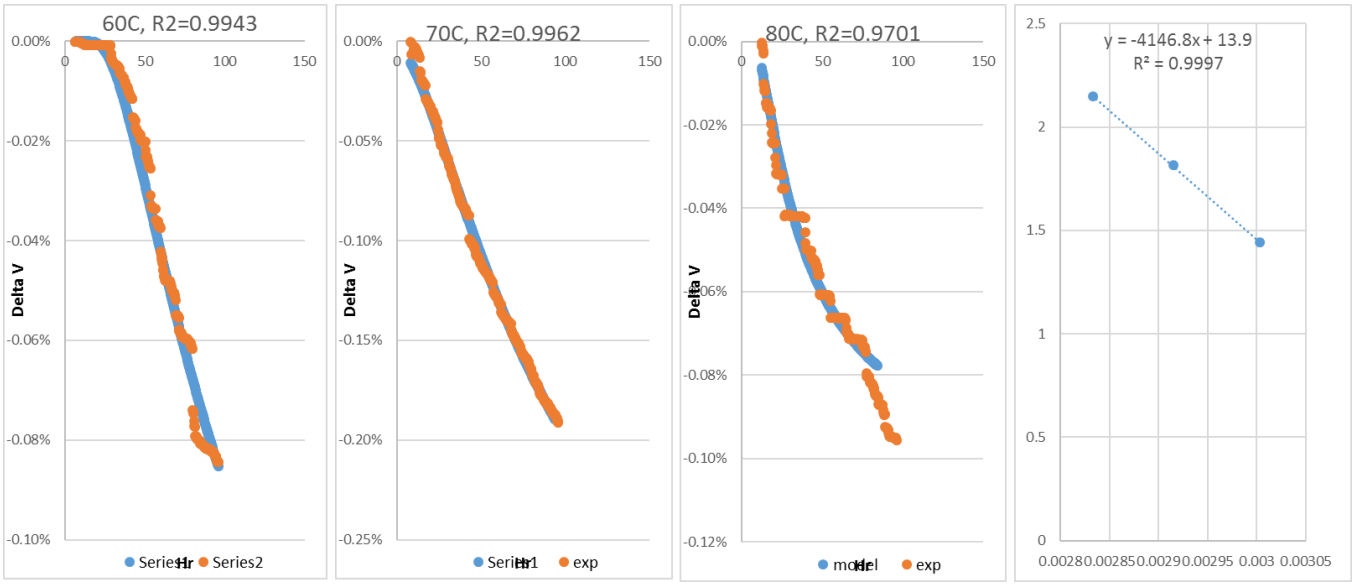
60C, R2=0.9943
70C, R2=0.9962
80C, R2=0.9701
Delta V
Series1
Series2
exp
y = -4146.8x + 13.9
R² = 0.9997

(a)

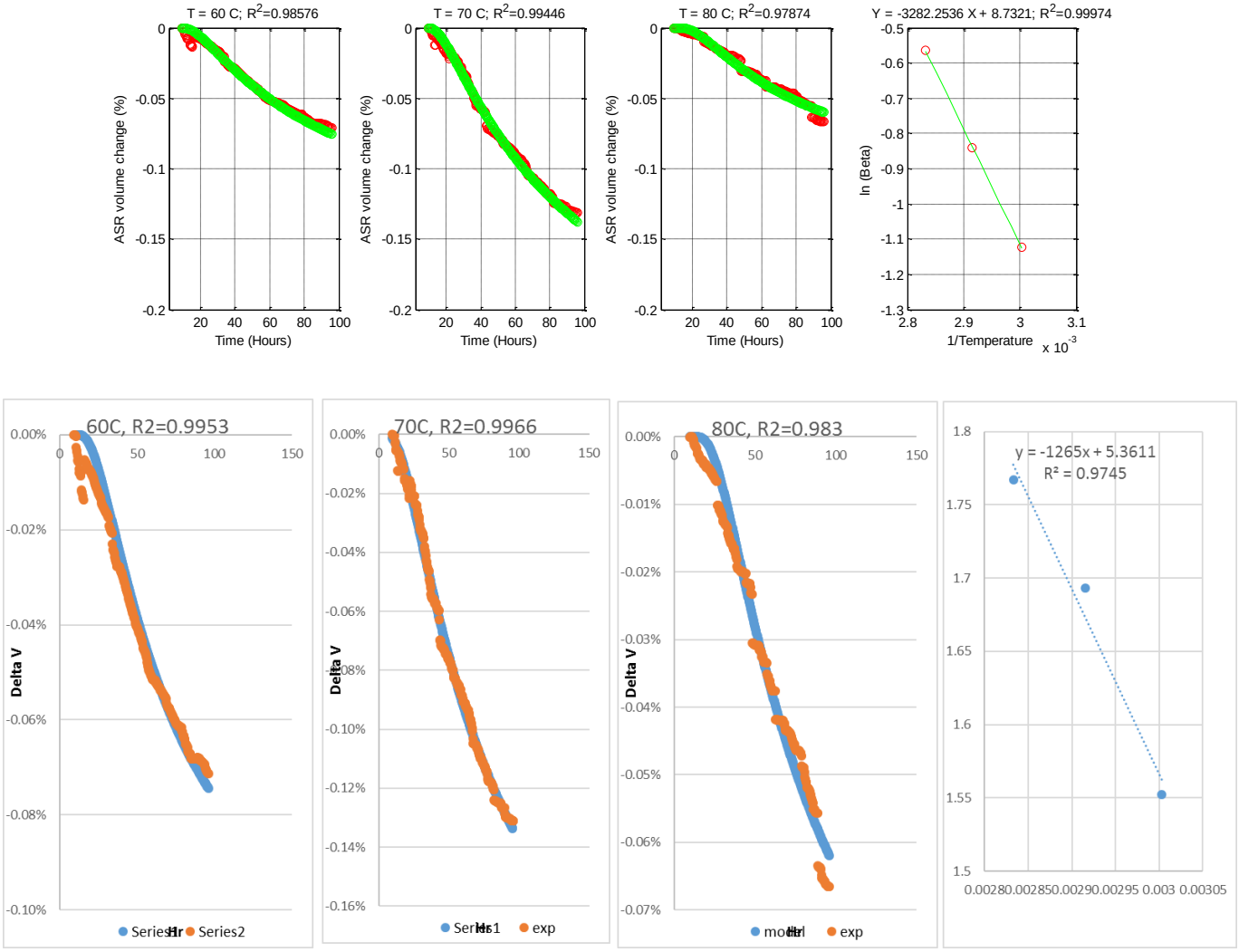

(b)

Figure A.1.3. Results for FA3 at (a) 0.5N, and (b) 1N

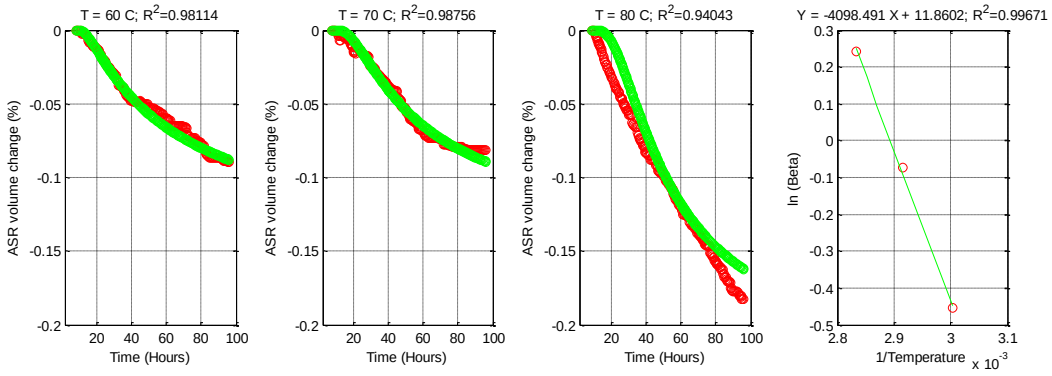
T = 60 C; R2=0.98114
T = 70 C; R2=0.98756
T = 80 C; R2=0.94043
Y = -4098.491 X + 11.8602; R2=0.99671
ASR volume change (%)
Time (Hours)
ln (Beta)
1/Temperature
x 10-3

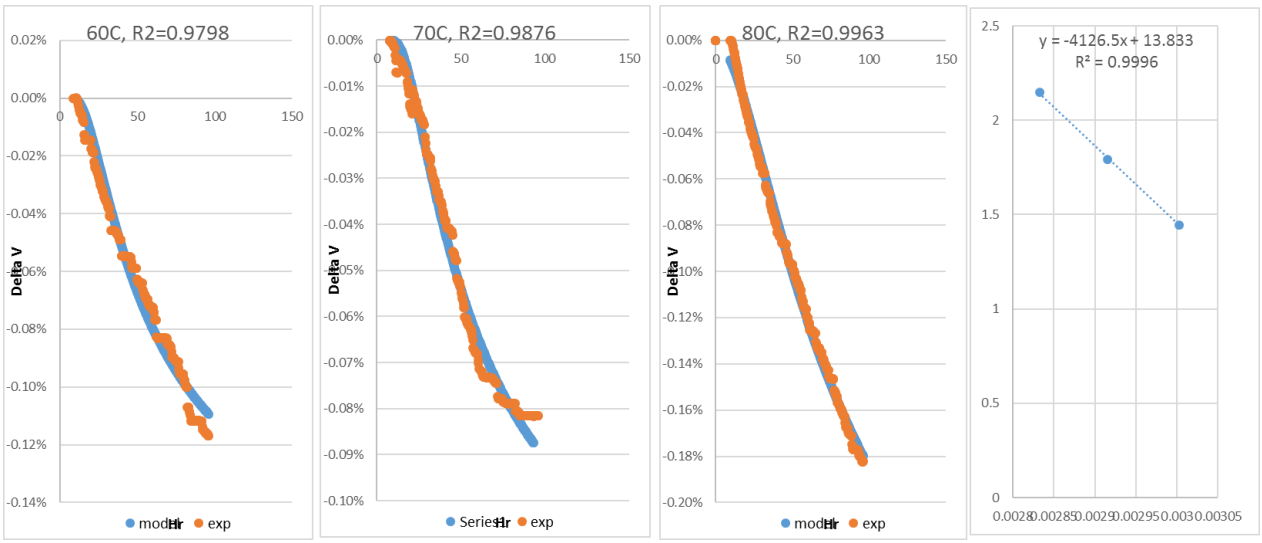
60C, R2=0.9798
70C, R2=0.9876
80C, R2=0.9963
Delta V
exp
y = -4126.5x + 13.833
R² = 0.9996

(a)

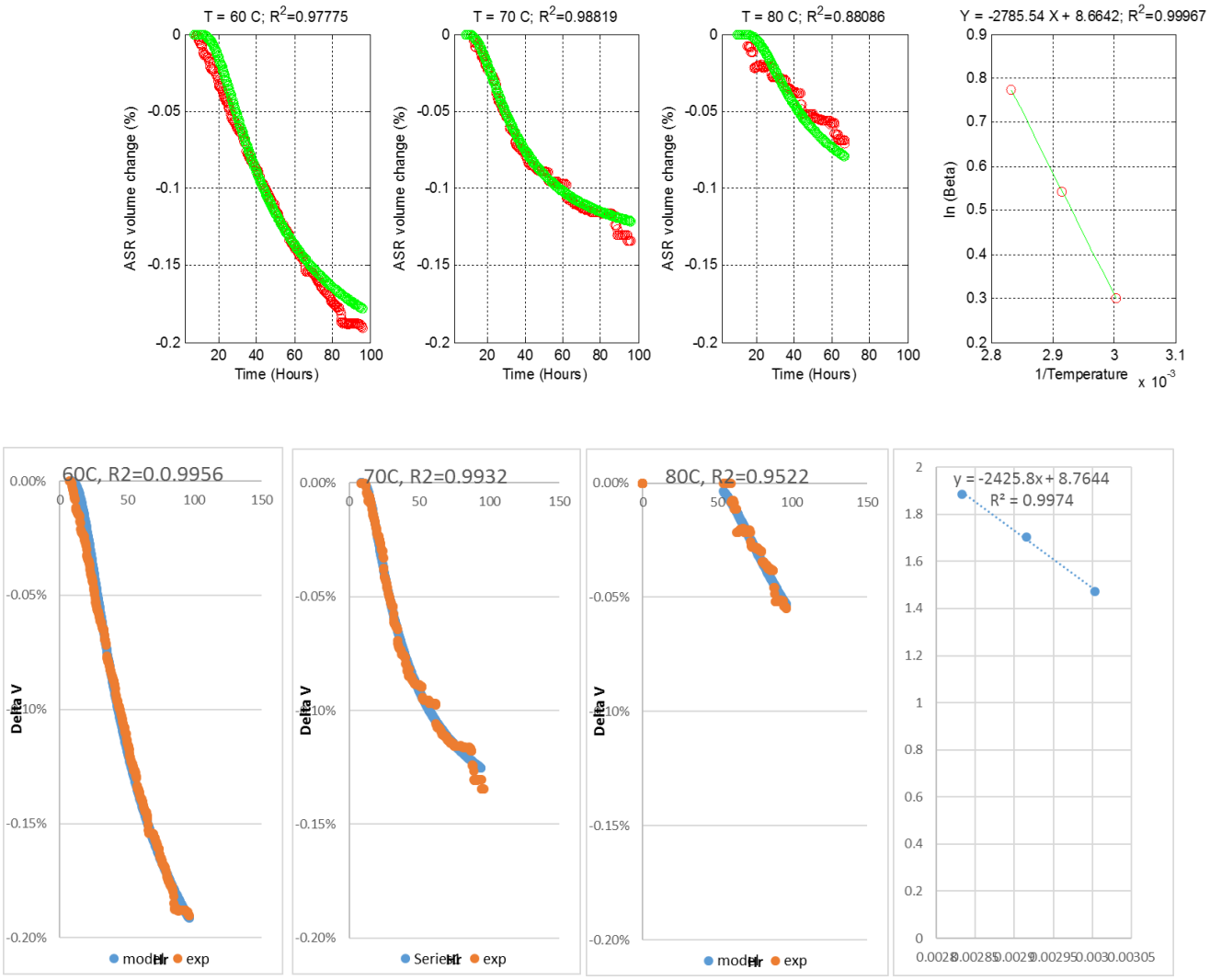

(b)

Figure A.1.4. Results for CA1 at (a) 0.5N, and (b) 1N

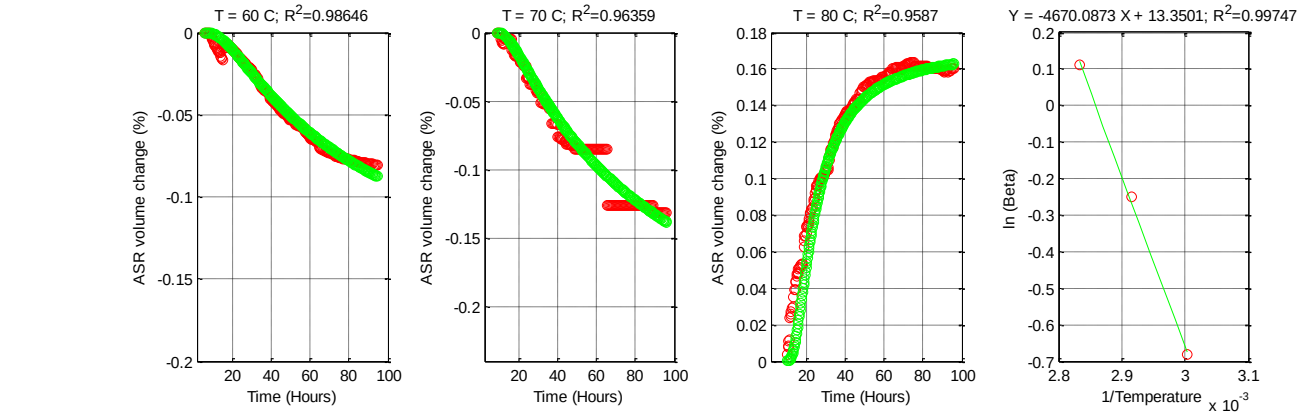
T = 60 C; R2=0.98646
T = 70 C; R2=0.96359
T = 80 C; R2=0.9587
Y = -4670.0873 X + 13.3501; R2=0.99747
ASR volume change (%)
Time (Hours)
ln (Beta)
1/Temperature
x 10-3

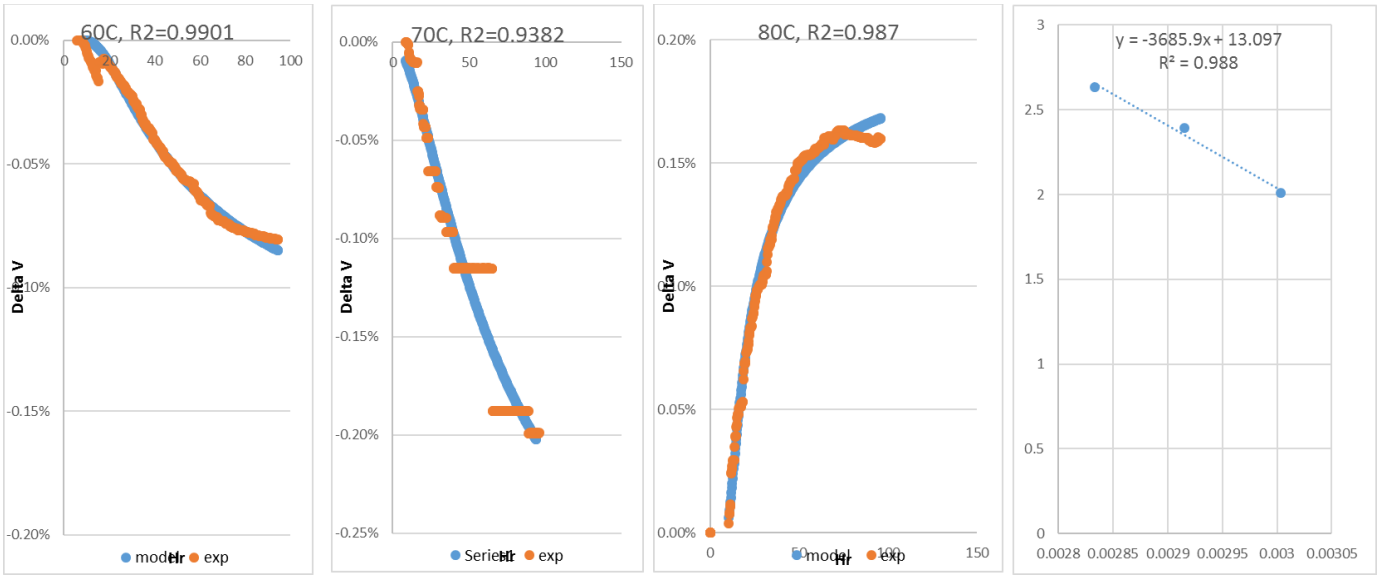
60C, R2=0.9901
70C, R2=0.9382
80C, R2=0.987
y = -3685.9x + 13.097
R² = 0.988
Delta V
Hr
model
exp
Series1

(a)

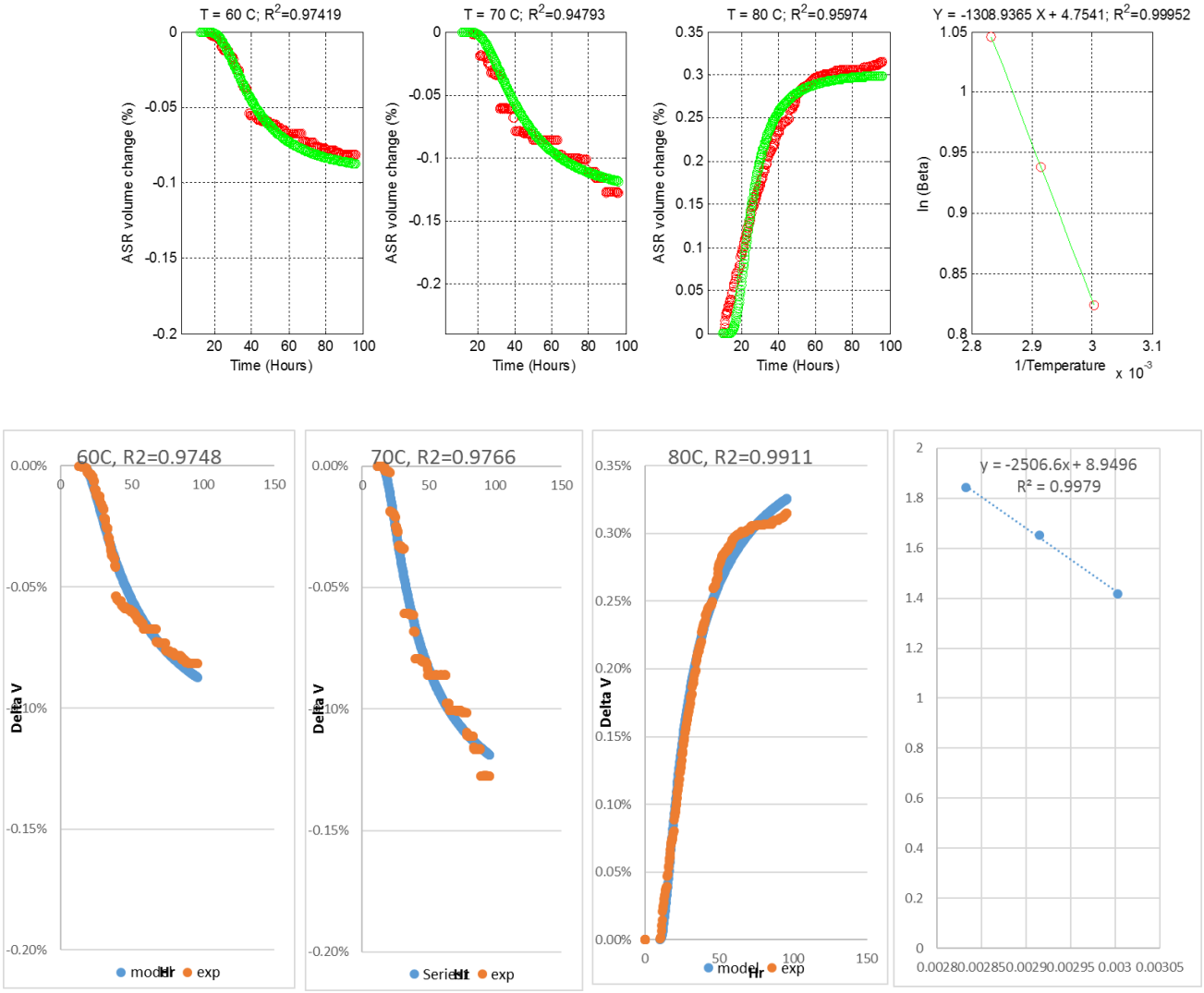

(b)

Figure A.1.5. Results for CA2 at (a) 0.5N, and (b) 1N

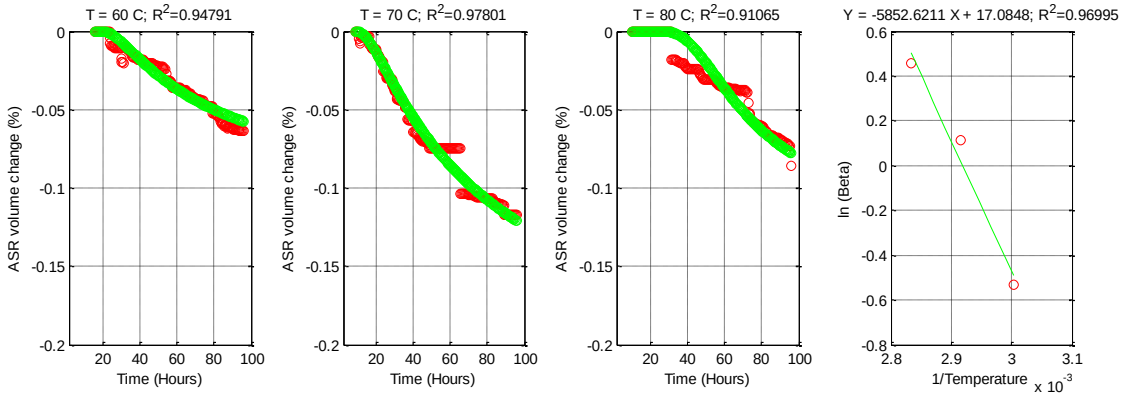
T = 60 C; R2=0.94791
T = 70 C; R2=0.97801
T = 80 C; R2=0.91065
Y = -5852.6211 X + 17.0848; R2=0.96995
ASR volume change (%)
Time (Hours)
ln (Beta)
1/Temperature
x 10-3

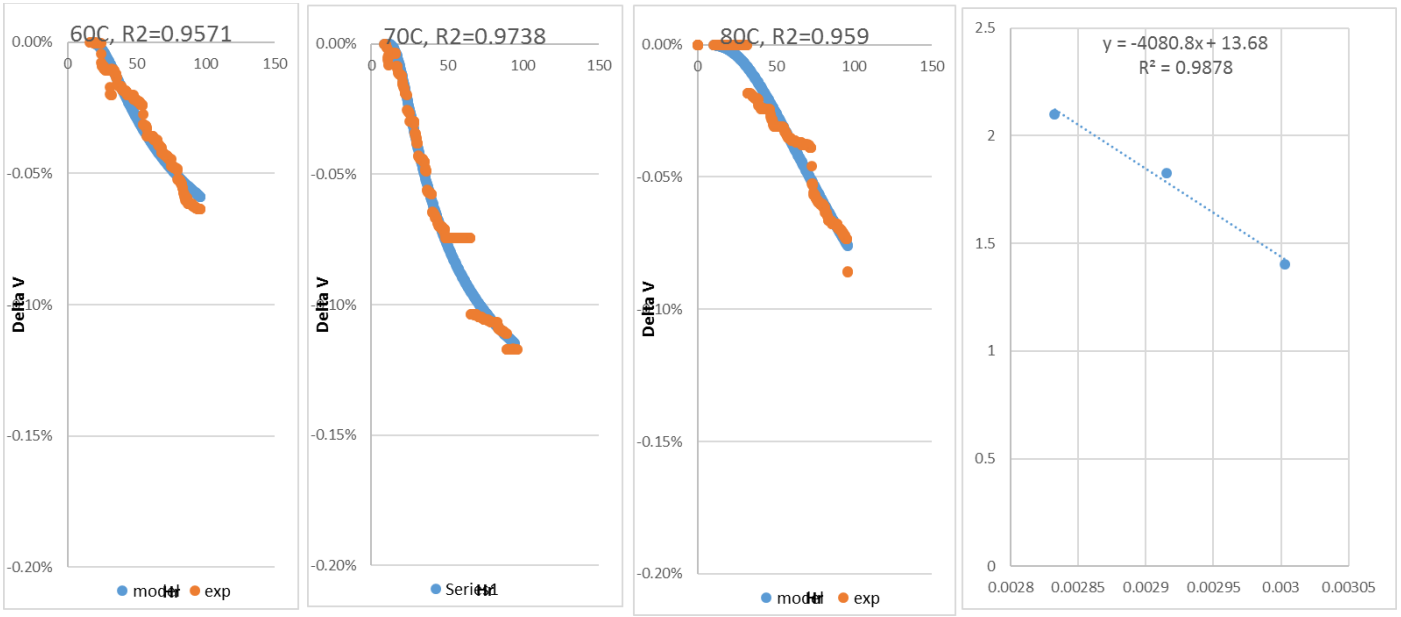
60C, R2=0.9571
70C, R2=0.9738
80C, R2=0.959
Delta V
exp
y = -4080.8x + 13.68
R² = 0.9878

(a)

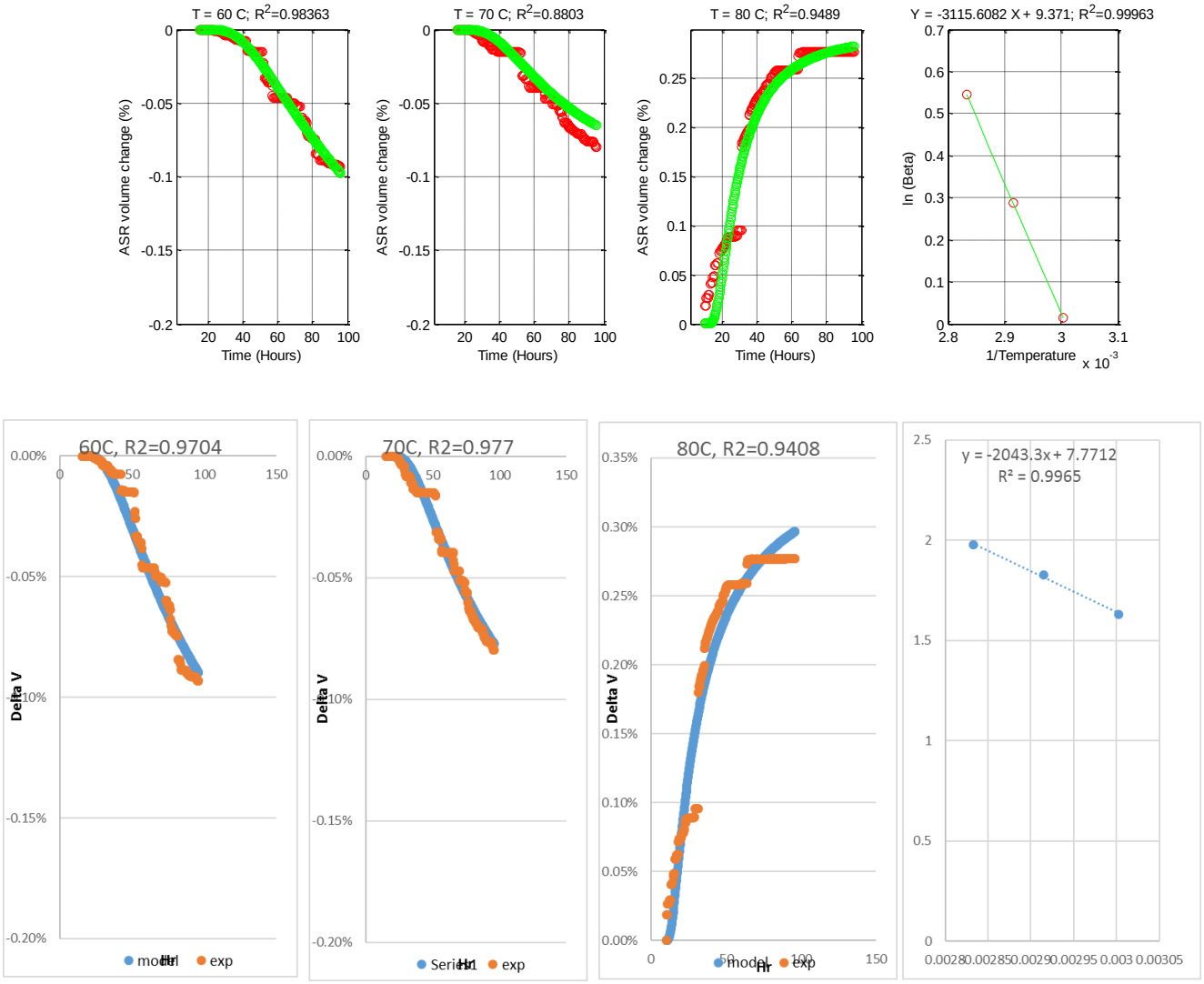

(b)

Figure A.1.6. Results for CA3 at (a) 0.5N, and (b) 1N

.

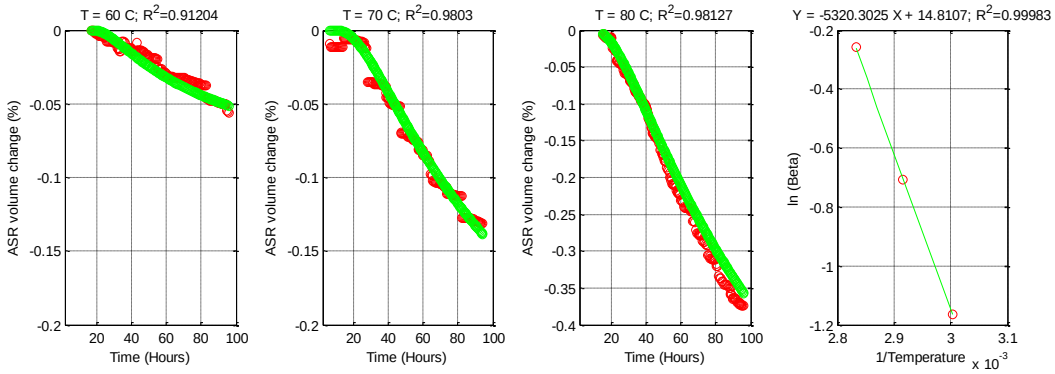
T = 60 C; R2=0.91204
T = 70 C; R2=0.9803
T = 80 C; R2=0.98127
Y = -5320.3025 X + 14.8107; R2=0.99983
ASR volume change (%)
Time (Hours)
ln (Beta)
1/Temperature x 10-3

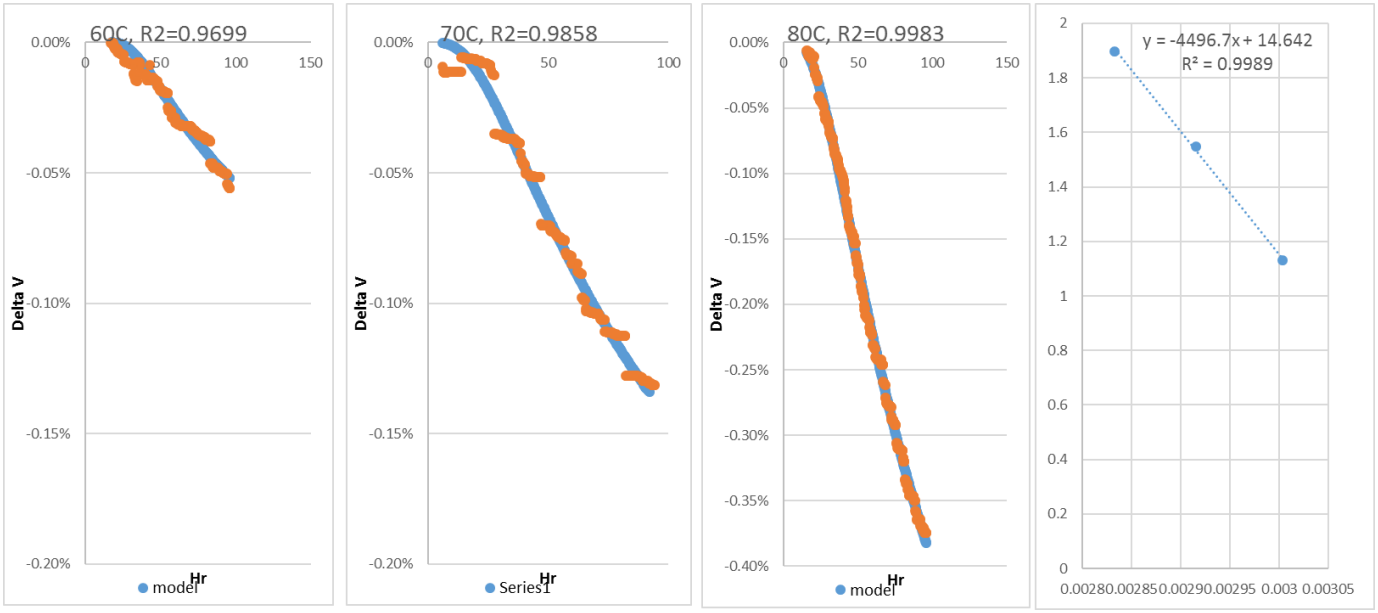
60C, R2=0.9699
70C, R2=0.9858
80C, R2=0.9983
Delta V
Hr
model
Series1
y = -4496.7x + 14.642
R² = 0.9989

(a)

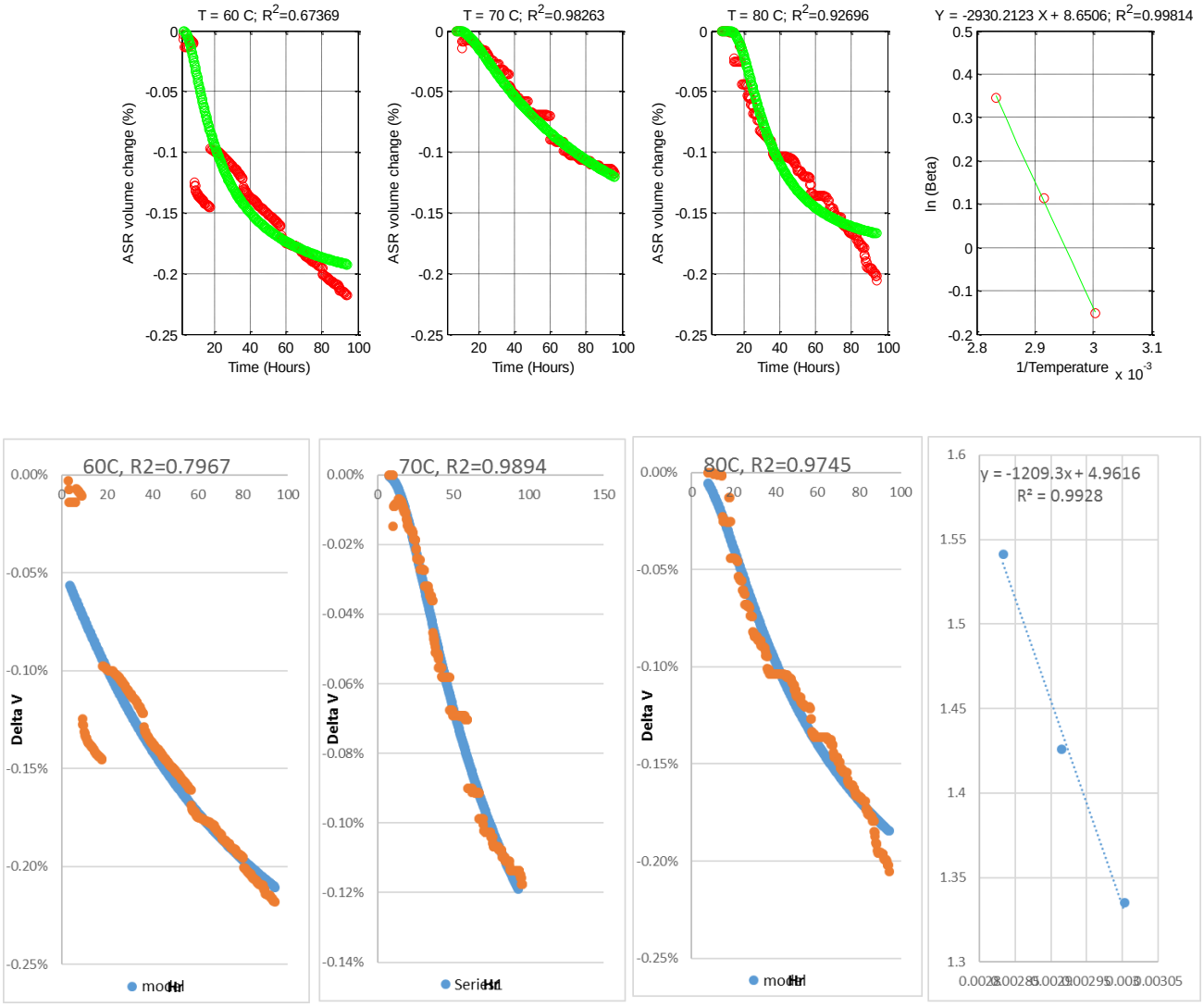

(b)

Figure A.1.7. Results for CA4 at (a) 0.5N, and (b) 1N

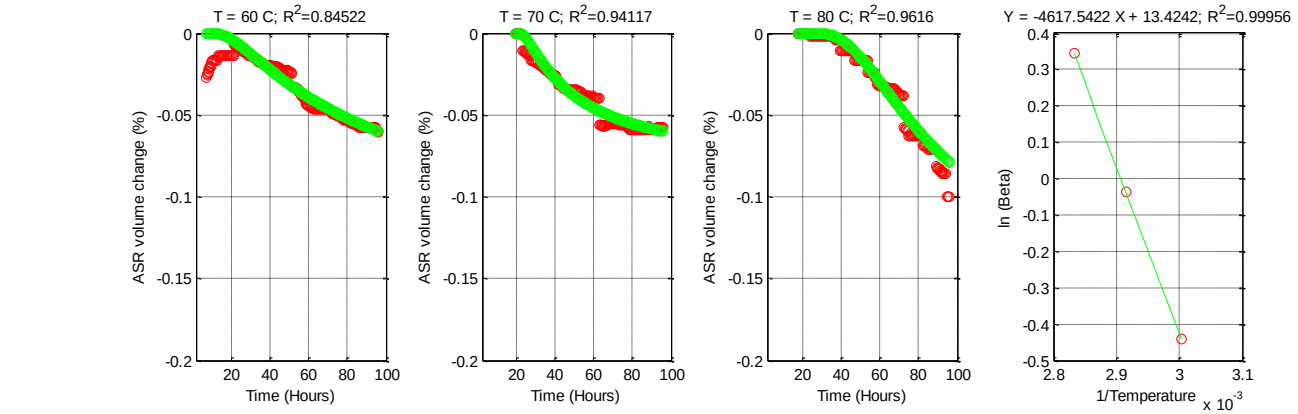
T = 60 C; R2=0.84522
T = 70 C; R2=0.94117
T = 80 C; R2=0.9616
Y = -4617.5422 X + 13.4242; R2=0.99956
ASR volume change (%)
Time (Hours)
ln (Beta)
1/Temperature
x 10-3

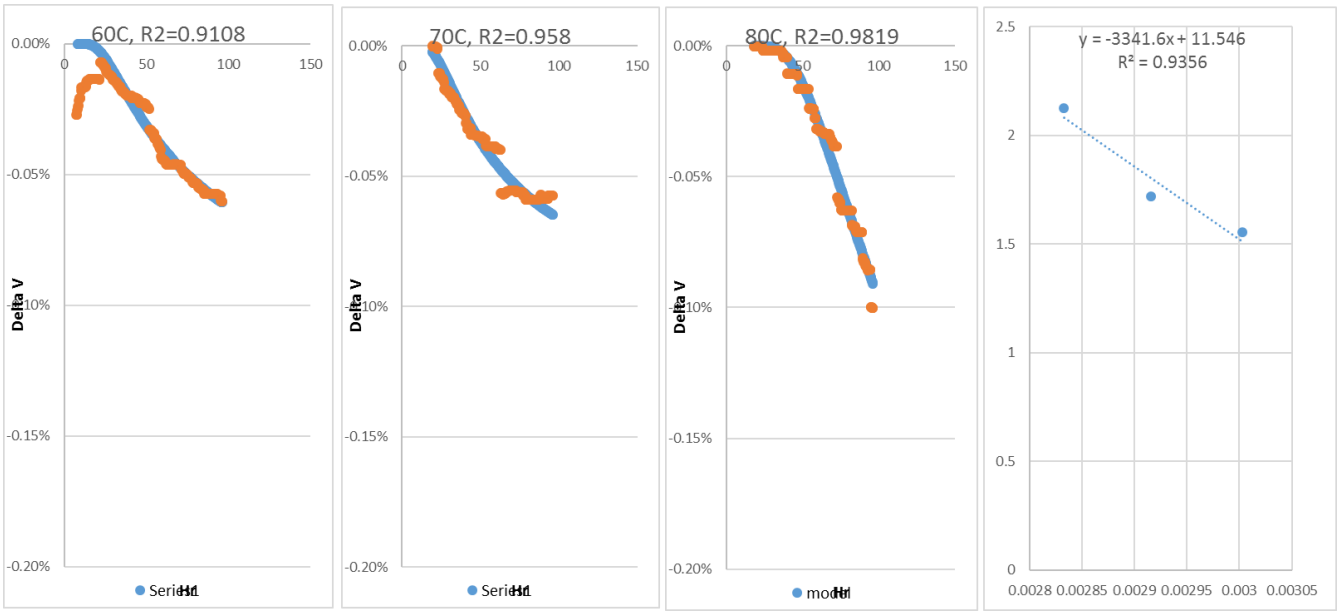
60C, R2=0.9108
70C, R2=0.958
80C, R2=0.9819
Delta V
y = -3341.6x + 11.546
R² = 0.9356

(a)

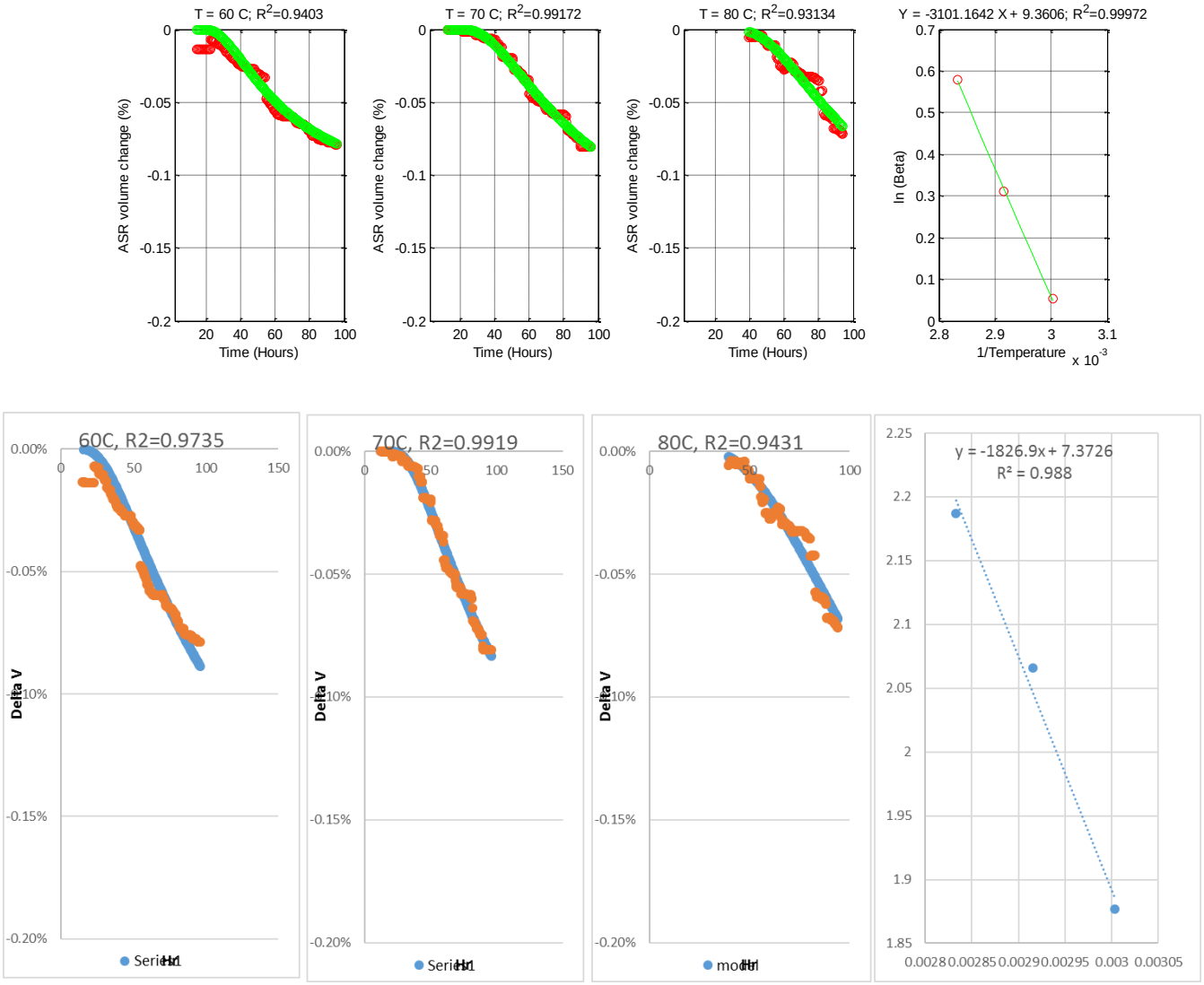

(b)

Fig. A.1.9. Results for CA5 at (a) 0.5N, and (b) 1N

A.2. Results of ACCT testing

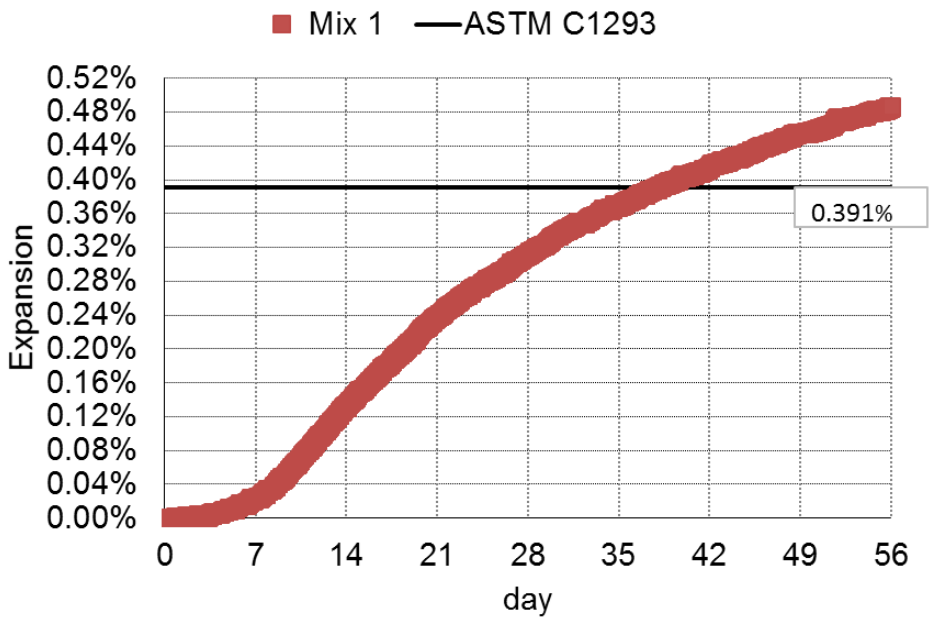

Figure A.2.1. Expansion curve of ACCT (Mix 1) over time at alkali level of 4.5 lb/cy

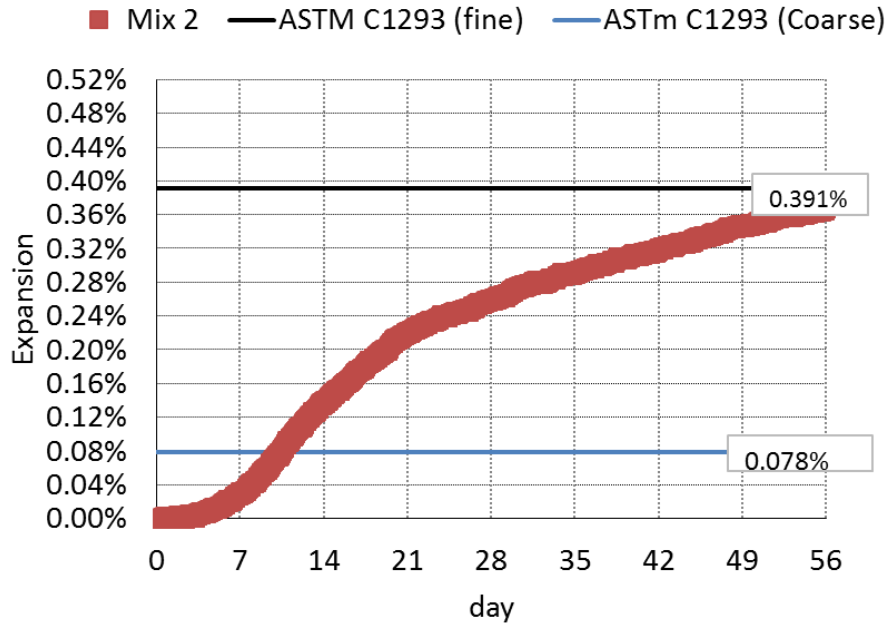

Figure A.2.2. Expansion curve of ACCT (Mix 2) over time at alkali level of 4.5 lb/cy

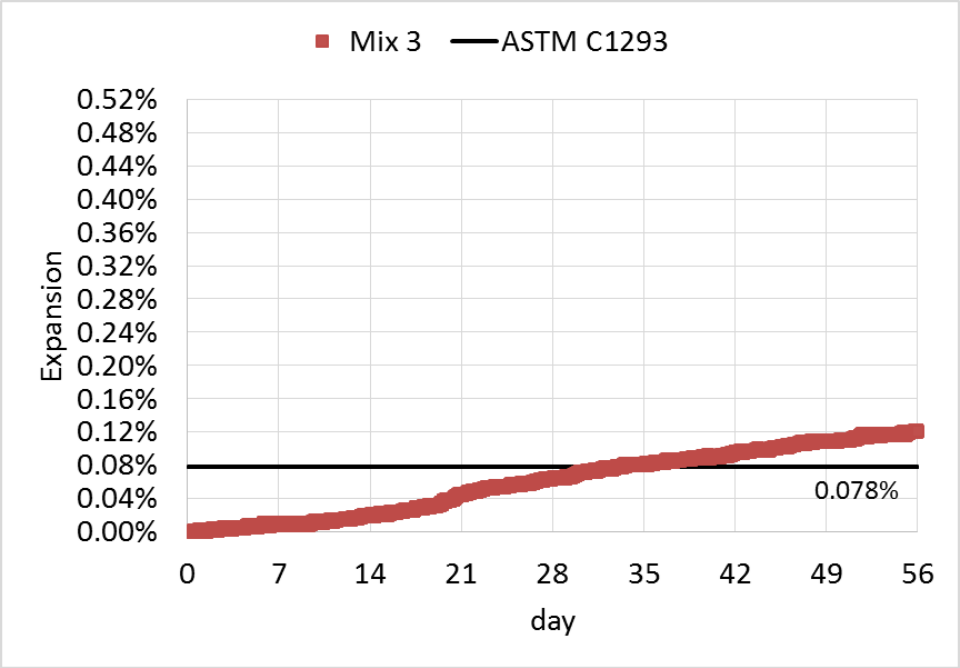

Figure A.2.3. Expansion curve of ACCT (Mix 3) over time at alkali level of 4.5 lb/cy

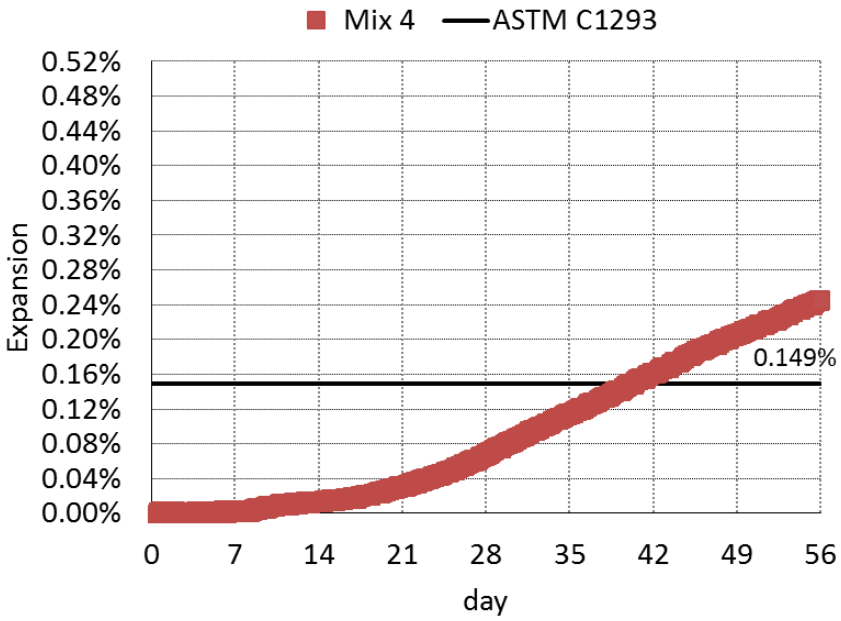

Figure A.2.4. Expansion curve of ACCT (Mix 4) over time at alkali level of 4.5 lb/cy

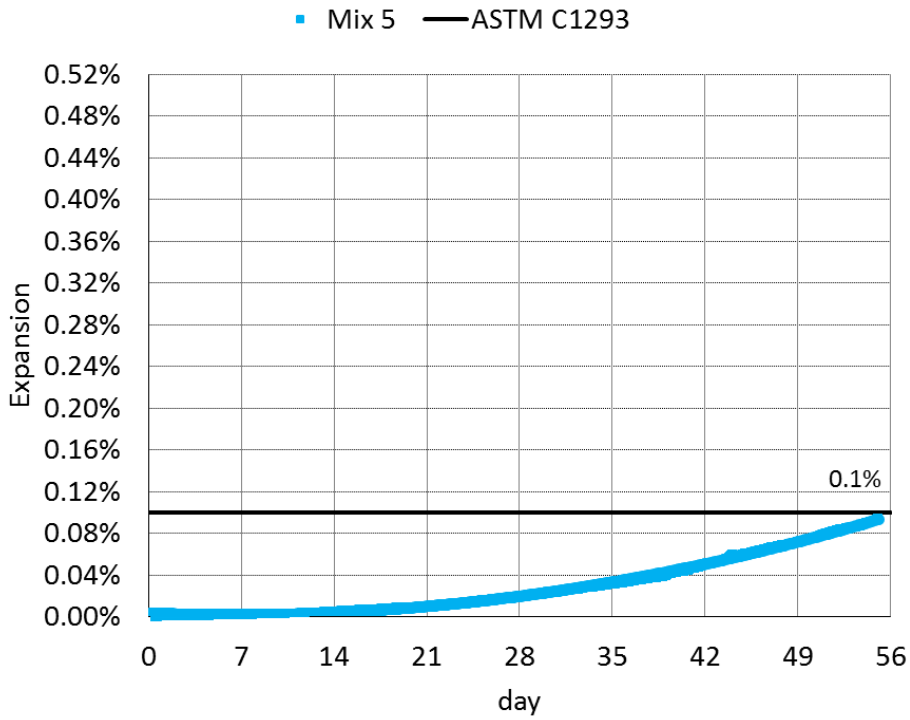

Figure A.2.5. Expansion curve of ACCT (Mix 5) over time at alkali level of 4.5 lb/cy

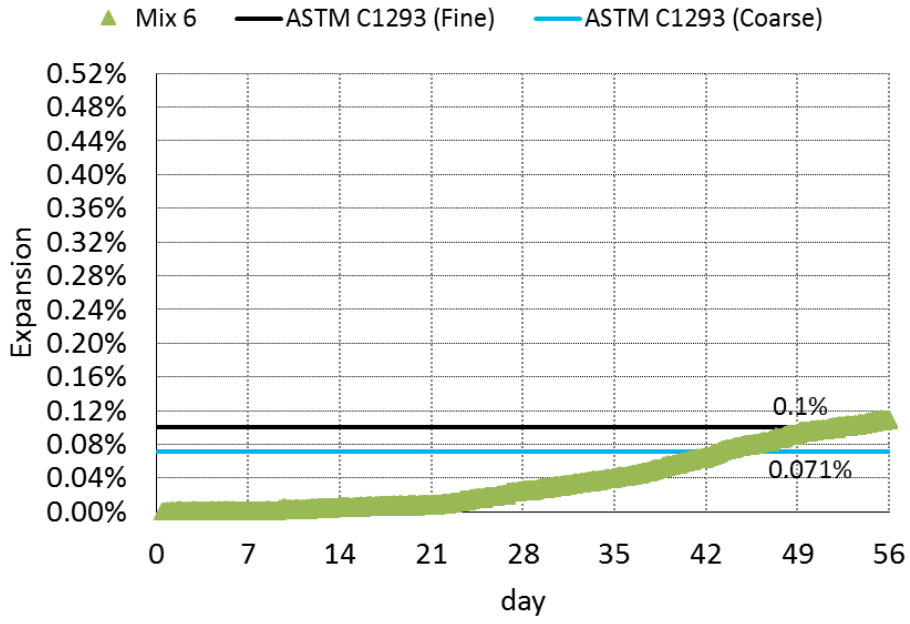

Figure A.2.6. Expansion curve of ACCT (Mix 6) over time at alkali level of 4.5 lb/cy

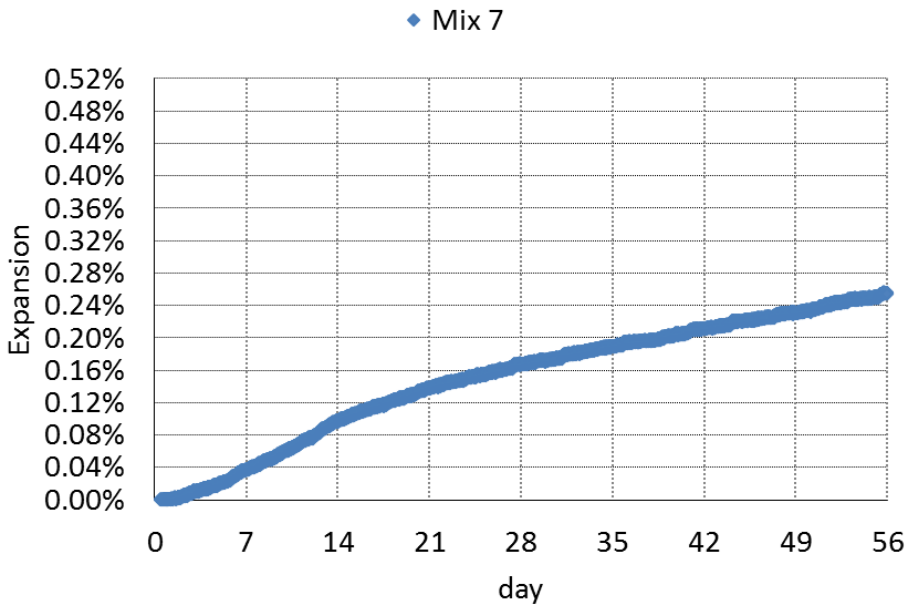

Figure A.2.7. Expansion curve of ACCT (Mix 7) over time at alkali level of 4.5 lb/cy

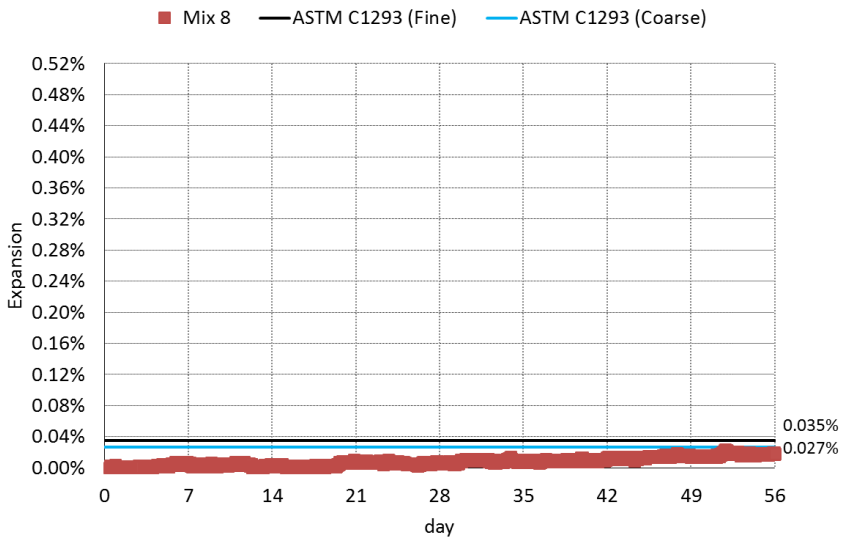

Figure A.2.9. Expansion curve of ACCT (Mix 8) over time at alkali level of 4.5 lb/cy

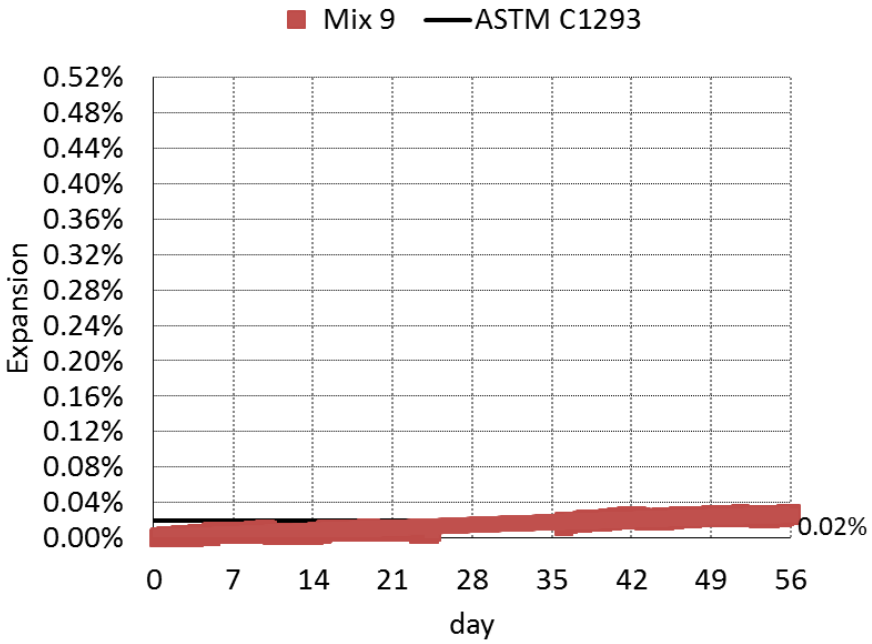

Figure A.2.10. Expansion curve of ACCT (Mix 9) over time at alkali level of 4.5 lb/cy